Linkage between mechanical properties and phase transformations in a 301LN austenitic stainless steel

by

David Maréchal

B. Eng., INP Grenoble, France, 2004

A THESIS SUBMITTED IN PARTIAL FULFILLMENT OF
THE REQUIREMENTS FOR THE DEGREE OF

DOCTOR OF PHILOSOPHY

in

The Faculty of Graduate Studies

(Materials Engineering)

THE UNIVERSITY OF BRITISH COLUMBIA

(Vancouver)

April 2011

Abstract

In this work, the deformation mechanisms of an austenitic stainless steel (grade 301LN) have been investigated with particular attention on the strain-induced phase transformations from austenite to ϵ and α' martensites. The average grain size of this alloy was varied in the range 0.5–28 µm, and two strain paths, namely uniaxial tension and simple shear, were analyzed. At the macroscopic level, the work-hardening response was examined in relation to the formation of ϵ and α' martensites, followed by X-ray phase quantification and Feritscope measurements. At a microscopic level, the microstructures after deformation were investigated using electron back-scatter diffraction, energy-dispersive X-ray spectroscopy and transmission electron microscopy. It was found that the grain size refinement was responsible for a change in nucleation mechanisms of α'-martensite, thereby affecting the macroscopic volume fraction of α'-martensite. The switch from tension to shear was not found to affect the mechanisms of formation of ϵ and α' martensites, but significantly reduced the work-hardening, an effect too large to be attributed to the slight reduction of the kinetics of α' volume fraction. The stresses borne in the α'-martensite were quantified using a novel method based on the magnetomechanical effect. These stresses, together with the determination of the intrinsic constitutive laws of austenite and α'-martensite, were used to design a one-dimensional physically-based model of the work-hardening in this alloy. This model, based on the "dynamic composite" effect of the formation of fresh α'-martensite in austenite, successfully predicted the measured stress-strain behaviour in tension, as well as the tensile instabilities encountered in this class of materials.

Table of Contents

Appendices

List of Tables

List of Figures

Chapter 1

Introduction

Car manufacturers are continuously seeking to decrease vehicle weight and emissions [1], while improving crash performance (energy absorption). As a consequence, there is demand for high-strength materials that permit reduced thickness without compromised formability or crashworthiness. Similar demands are also made in other applications [2]. A range of strengthening methods including grain size reduction [3], solid solution strengthening [4], precipitation hardening [5, 6] and texture optimisation [7] have been explored in this context. Another strengthening approach is the use of composite microstructures where the properties of the parent phase are reinforced by a harder phase, an approach used in pearlitic and dual-phase (DP) steels [8]. Recent developments have led to the commercialization of multiphase **TRIP** (Transformation Induced Plasticity) and **TWIP** (TWinning Induced Plasticity) steels in which phase transformations and twin formation represent the reinforcing "phase". These materials are particularly complex since the microstructure evolves strongly with plastic deformation.

According to Figure 1.1, stainless steels displaying the TRIP effect offer an impressive combination of mechanical and physical properties compared to high-performance carbon steel grades. The main weakness of the stainless steels is, however, in the areas of formability, cost and "experience". Improvements in these three areas would allow for the expansion of the markets for austenitic stainless steels. The lack of "experience" noted above refers, in large part, to the inability to predict with high precision the mechanical behaviour of these steels using physically-based models, a gap which inhibits the development of solutions to improve the formability of these materials, e.g. finite element simulations [9]. Consequently, there is a need for new physically-based models that predict the mechanical properties and

their variations with controlled parameters, such as temperature, strain rate, stress state and strain path as well as with microstructure, e.g. grain size, texture and dislocation density.
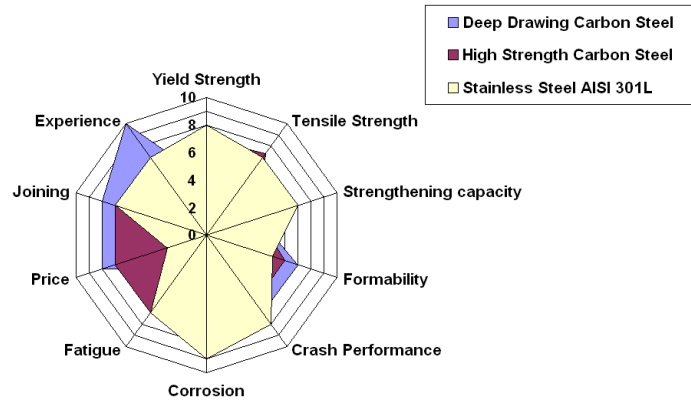
Figure 1.1: Relative performances of three generations of steels. Reproduced from Schmitt [2].

While there is a relatively large pre-existing literature surrounding the mechanical behaviour of austenitic stainless steels, there remain basic questions about the physical processes coupling the strain-induced martensitic phase transformation and plastic deformation. Recent work has questioned whether this transformation is driven by stress or by plastic strain [10] while other work has focused on how microstructural parameters such as grain size can be used to control mechanical response in these materials [11, 12]. With the advent of new experimental techniques, there is an opportunity to examine some of these questions with the aim of developing more physically-based models that couple the microstructure, deformation and phase transformations.

In this work, the strain-induced martensitic phase transformations occurring in an austenitic stainless steel (grade 301LN) have been studied experimentally. Material provided by ArcelorMittal Stainless Steel has been further processed by rolling and annealing to achieve materials with grain

sizes as small as D=500 nm. Starting from these materials, mechanical testing has been performed at room temperature with a fixed strain rate in both uniaxial tension and simple shear. These results are meant to complement results obtained on the same grade under uniaxial tension but where strain rate and test temperature have been varied [13, 14]. Experimentally, the material has been characterized with an eye to linking the microstructural evolution during plastic deformation with the strain-induced transformations occurring in this material. The bulk mechanical response of the material has been analyzed treating the material as a sort of "dynamic composite". A new method for estimating the load transfer between the two phases based on the magnetomechanical effect has been developed and compared to measurements of lattice strains made in a previous study by neutron diffraction.

This thesis starts by a review of the literature, aiming at clarifying the effect of strain-induced phase transformations on the mechanical properties of austenitic stainless steels. It continues by describing the methods used in the initial processing of the as-received material. Following this, the macroscopic mechanical properties and phase fractions are presented. This is followed by a description of the microstructural evolution with strain. A magnetic method for estimating the fraction of the macroscopic stress carried by the α'-martensite phase is next presented and used to develop a simple physically based model for the bulk mechanical response. In all cases, this work is specifically linked to i) the starting austenite grain size and ii) the imposed strain path (shear and tension).

Chapter 2

Literature Review

Austenitic stainless steels are relatively mature materials, being widely used in practical applications. There is, therefore, a large amount of literature describing the behaviour of this class of materials. In the specific case of the TRIP effect in austenitic stainless steels, periods of active research into the details of the strain-induced martensitic transformations alternated with periods of lower activity. In the past 10 years, there has been growing interest in returning to the basic questions of the mechanisms of the strain-induced martensitic transformation induced by increased demand for these materials as well as by the availability of new experimental techniques for probing the material response. This literature review seeks to describe the literature most relevant to the work done in this Ph.D. thesis and, in particular, focuses on new developments in the field over the past 10–15 years. The reader interested in a more detailed overview of the behaviour of austenitic stainless steels is directed to the reviews found in the literature [15–17].

2.1 Austenitic Stainless Steels: Stable and Metastable Phases

Stainless steels are iron-based alloys containing between 10.5% to 30% chromium by weight [18, 19]. The chromium content is responsible for the high resistance to oxidation and corrosion, due to the formation of a passive chromium oxide film on the sample surface, in the presence of oxygen. The two most common stainless steel families are ferritic stainless steels and austenitic stainless steels. Ferritic stainless steels have chromium as the primary alloying addition and the state of the material at room temperature is

the stable body centered cubic (bcc) ferrite (α) phase. Austenitic stainless steels are alloyed so as to allow for the retention of the high temperature face centered cubic (fcc) austenite (γ) phase to room temperature. Nickel is the most common fcc-stabilizing element, although other fcc-stabilizing elements (e.g. manganese, copper) may partially replace nickel in some alloys [18, 20]. The interstitial elements, namely carbon and nitrogen, also increase the stability of austenite relative to ferrite. The use of carbon to stabilize austenite is avoided as chromium carbide formation depletes grain boundaries of chromium, leading to enhanced intergranular corrosion (sensitization) [16]. Instead, nitrogen has been used as an alloying element providing austenite stabilization, solid solution strengthening and increased corrosion resistance in various austenitic stainless steel grades [21]. An example of the nitrogen-alloyed steels is the grade AISI 301LN, which has a nitrogen content ranging from 0.1 to 0.2 wt %.

The retention of austenite at room temperature does not imply that it is the most thermodynamically stable phase at this temperature. Indeed, for all austenitic stainless steels at room temperature and ambient pressure, the α-ferrite is the stable phase. The addition of austenite stabilizers (e.g. nickel) lowers the free energy of austenite relative to ferrite. This is most easily seen if one considers the free energy difference between austenite and ferrite as a function of nickel content of the steel, cf. Figure 2.1(a). The temperature at which the free energy of austenite and ferrite are equal (the T_0 temperature) is important in this context, since the driving force for the $\gamma \rightarrow \alpha$ transformation increases with undercooling below T_0. As one can see from Figure 2.1(b), increasing nickel additions lower the T_0 temperature, thus reducing the driving force for the $\gamma \rightarrow \alpha$ transformation at a fixed temperature (e.g. room temperature). Moreover, as T_0 decreases, so do the kinetics of diffusion required to transform γ to α by diffusional mechanisms. If T_0 is low enough, the combination of lowered driving force for transformation and the slow rate of transformation can "trap" the material in a metastable γ state.

A third phase, denoted as ϵ, also plays an important role in the deformation response of austenitic stainless steels. This phase has a hexagonal
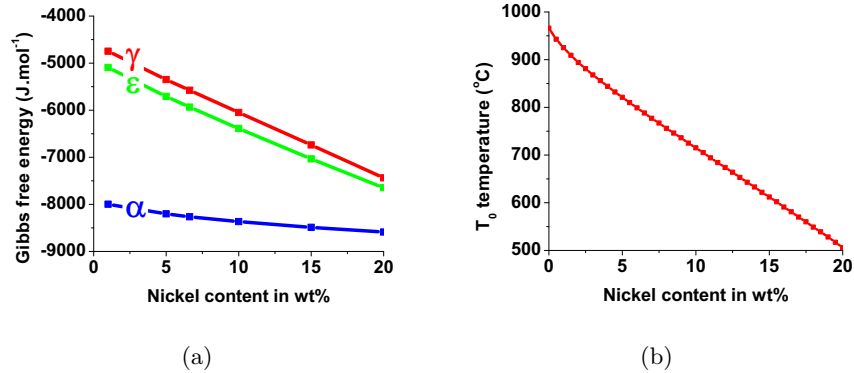
Figure 2.1: Relative stability of phases predicted by Thermo-Calc [22] using the composition corresponding to the 301LN stainless steel studied in this work (cf. composition in chapter 4) at atmospheric pressure. (a) Evolution of the Gibbs free energy of fcc (γ), hcp (ϵ) and bcc (α) phases at room temperature, (b) Evolution of the T_0 temperature with variable nickel content.

close-packed (hcp) crystal structure and is the equilibrium phase only at high pressure [23–25], although it is often observed to form during the plastic deformation of austenitic stainless steels at ambient temperature and pressure. Figure 2.1 (a) illustrates that, at room temperature and at atmospheric pressure, the hcp ϵ phase has an energy intermediate between bcc α and fcc γ phases.

The formation of ϵ, as well as deformation twinning, during the plastic straining of austenitic stainless steels has been linked to the low stacking fault energy (SFE) of austenitic stainless steels. In this regard, there is a close association with stacking faults, ϵ and twins [1].

Table 2.1 compares typical values of the intrinsic SFE of face centered cubic materials [2]. In comparison to most metals, the intrinsic stacking fault energy of austenitic stainless steels is low, being between 6 and 60 mJ.m^{-2}

---

[1] See references [26, 27] for a detailed discussion on partial dislocations and stacking faults in fcc crystals.

[2] An extensive survey of the stacking fault energy and its dependence on composition and temperature for austenitic steels has been carried on recently by Bracke [28].

[29]. The stacking fault energy of austenitic stainless steels is strongly affected by the composition [30–32]. For example, carbon is known to strongly increase the SFE, while nitrogen and silicon decrease it [32]. Also notable is the strong temperature dependence of the SFE in austenitic stainless steels compared to other pure fcc metals [33].

Material	301LN	316L	304	Ag	Cu	Ni	Al
SFE (mJ.m^{-2})	14	14	17	22	78	90	166
Reference	[34]	[28]	[30]	[35]	[35]	[30]	[35]

Table 2.1: Experimentally-determined stacking fault energies (SFE) of various fcc materials at room temperature. All measurements were obtained from observation of dissociated triple nodes, except in 301LN where X-ray diffraction line broadening was used.

The intrinsic SFE has a direct relation to the stability of fcc-austenite relative to hcp-ϵ. A single intrinsic stacking fault results in a two atomic layer thick crystal having hcp packing [36, 37]. On the basis of this geometric relationship, it has been proposed that the free energy difference between the fcc and hcp phases can be related to the intrinsic SFE as [38]:

$$SFE = 2\rho\Delta G_{fcc\rightarrow hcp} + 2\sigma_{fcc/hcp} \qquad (2.1)$$

where ρ is the molar surface density of the austenite [3], $\Delta G_{fcc\rightarrow hcp}$ is the Gibbs Free energy difference in transforming one mole of fcc crystal to one mole of hcp crystal, and $\sigma_{fcc/hcp}$ is the surface energy of the hcp plate. Other, more detailed, models for the SFE have been advanced, for example that described by Ferreira [39] for the Fe-Cr-Ni system.

Simple models of the stacking fault energy have been used in an attempt to predict the strain-induced deformation response of low-SFE steels. Notable is the work of Allain *et al.* who have constructed maps allowing for the correlation between composition, test temperature and deformation mech-

---

[3] The molar surface density can be determined from the lattice parameter a, by: $\rho = \frac{4}{\sqrt{3}} \frac{1}{a^2 \aleph}$ where $\aleph$ is Avogadro's number.

anism (e.g. ϵ formation, deformation twinning, only slip) in Fe-Mn based steels [38].

2.2 Deformation-Induced Martensitic Phase Transformations in Austenitic Stainless Steels

2.2.1 Ferrous Martensites in Austenitic Stainless Steels

As noted in section 2.1, austenitic stainless steels retain the fcc crystal structure at room temperature owing to the fact that the kinetics of the diffusional phase transformation from γ to α are too slow at temperatures where the driving force for the transformation is large enough. This leaves the material in a **metastable** state with respect to the thermodynamically stable α phase. While diffusion may be too slow to allow for the transformation from γ to α (or to the intermediate ϵ phase), another option for the transition exists. A martensitic transformation can lead to the transformation from γ to ϵ or α without the need for long-range diffusion. In contrast to a diffusive phase transformation, a martensitic transformation is characterized by its displacive character, the motion of atoms being governed by a homogeneous shearing of atoms at velocities close to the speed of sound [40, 41].

Ferrous martensites are most commonly associated with the spontaneous formation of the martensitic phase (e.g. body centered tetragonal α' martensite from austenite in carbon steels) when the steel is cooled below a certain temperature, known as the martensite start (or M_s) temperature [42]. In most cases, the martensite is formed at velocities close to the speed of sound as soon as the material is cooled below this temperature. The volume fraction of martensite increases with undercooling below the M_s temperature until the transformation is complete at the martensite finish (or M_f) temperature. While this **thermal** martensite [43] is most common, there are other steels that exhibit a time dependence to the fraction of martensite formed when cooled below the M_s temperature. The kinetics of this **isothermal** martensitic transformation are typically linked to the difficulty in the nucleation of martensite plates [44–46]. This can be understood based on the fact that a large energy barrier must be overcome in order to form ferrous martensite. In a plain carbon steel, this barrier is on the order of $\sim$ 1 kJ.mol^{-1} [47].

On the microscopic scale, the martensitic phase transformation from γ to α' can be described on the basis of a uniform and homogeneous strain of the crystal lattice. The Bain correspondence between the γ and α' lattices is often used to describe a pathway between these two phases [48]. This relation, schematically shown in Figure 2.2, assumes that one α' lattice can arise from γ, provided it is contracted along one of the $\langle 100 \rangle_\gamma$ directions and expanded along the two other $\langle 100 \rangle_\gamma$ directions.
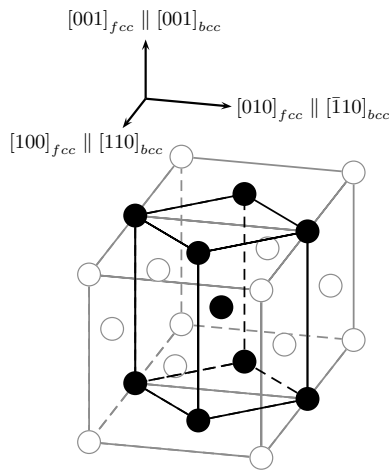
Figure 2.2: The Bain correspondence between the fcc unit cell (light gray) and the tetragonally distorted bcc unit cell (black).

In the case of pure iron taken at room temperature, the Bain expansion is 20% while the Bain contraction is 12%. The magnitude of these distortions depends on the composition of the alloy, increasing strongly with the carbon content. The Bain model, while giving the correct lattice correspondence between the α and γ lattices, does not predict properly the crystallographic orientation relationship between the two phases [49, 50]. This requires a more detailed understanding of the mechanism of nucleation and growth of martensite, which will be described in section 2.2.3.

While the $\gamma \rightarrow \alpha'$ transformation is the most well-known martensitic transformation in steels, it is also possible to form ϵ from γ as a martensitic transformation. As noted in Equation 2.1, a stacking fault has the equivalent

stacking sequence as a two atomic layer thick plate of hcp crystal. Thus, one way to obtain a thin plate of ϵ-martensite is by the passage of a Shockley partial dislocation on every other parallel {111} plane. A small contraction normal to the {111} plane is also necessary since ϵ-martensite is more dense than austenite [51].

In the case of austenitic stainless steels, an M_s temperature below 4K is common for the $\gamma \rightarrow \alpha'$ transformation [52]. Therefore, thermal martensite is not readily obtained even though a significant driving force exists. There is, however, the possibility to trigger the martensitic transformation by either: (i) modifying existing nucleation barriers by reducing their activation energy, or (ii) increasing the number of nucleation sites with low activation barriers.

One of the common ways of modifying existing nucleation sites by lowering the activation barrier is through the application of an applied stress. The work of Patel and Cohen showed how stress could effect the M_s temperature of thermal martensite [47]. As shown in Figure 2.3, the effect of stress state on the transformation can increase or decrease the M_s temperature.
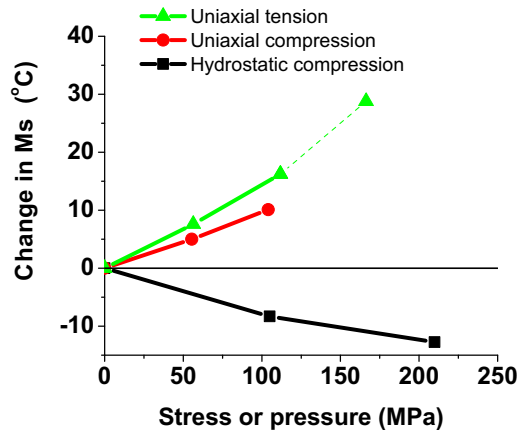
Figure 2.3: Change in the M_s temperature as a function of the loading condition. Adapted from the work of Patel and Cohen [47].

Patel and Cohen argued that this effect could be explained based on the

mechanical work done in the transformation of γ to α'. In this argument, the mechanical work (or interaction energy) done by the phase transformation corresponds to:

$$U_{inter} = \sigma\epsilon + \tau\gamma \tag{2.2}$$

where σ is the component of the macroscopic stress acting normal to the martensite plate, and τ is the shear stress acting parallel to the shear direction of the plate. The strains denoted as ϵ and γ are the normal strain and shear strain accompanying the martensitic transformation. In the case of the steels studied by Patel and Cohen, the values of ϵ and γ were taken to be 0.04 and 0.20 respectively. The value of the interaction energy based on this calculation was 0.86 J.mol^{-1} per MPa of applied (tensile) stress [47]. Using a linear temperature-dependence of the free energy difference between austenite and martensite and under the assumption of a constant activation energy for martensite nucleation (taken to be 837 J.mol^{-1}), Patel and Cohen obtained a variation of the M_s temperature with tensile stress equalling:

$$\frac{dM_s}{d\sigma} = 0.15°C.MPa^{-1} \tag{2.3}$$

which corresponds well to the experimental measurements shown in Figure 2.3.

In some materials the deformation temperature is close to, but slightly above, M_s. In this instance, the imposition of a stress in the elastic regime can be enough to induce a **stress-assisted** martensitic phase transformation [53]. This form of transformation is made use of in shape memory alloys where deformation induces the martensitic transformation which can be subsequently removed by heating the material to a temperature where γ is the stable phase [54–56]. In the case of ferrous alloys, the most common stress-assisted martensitic transformation occurs in the Fe-Mn-Si system where thin ϵ martensite plates can form under an elastic applied stress [57], consistent with the Patel and Cohen model as defined by Equation 2.2.

If the testing temperature is sufficiently above the M_s temperature, the stress required to induce the martensitic transformation can be above the

yield stress of the alloy. In this case, the martensitic transformation occurs during plastic deformation. Beyond the possible effect of the applied stress on the activation barrier for martensite nucleation, plastic deformation can also serve to create nucleation sites not present in the as-annealed material [47, 58, 59]. Martensite formed concurrently with plastic deformation is said to be **strain-induced** [43].
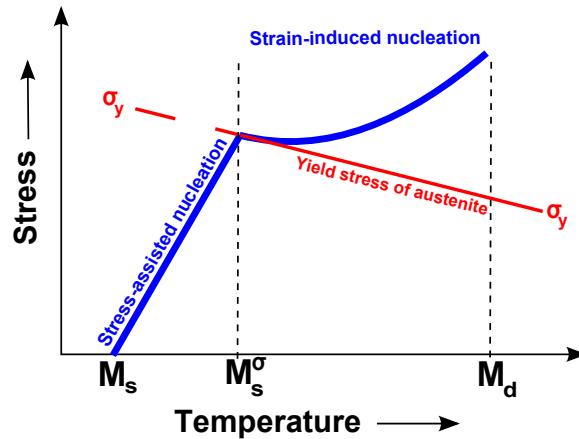
Figure 2.4: Schematic representation of the interrelationships between stress-assisted (below M_s^σ) and strain-induced (above M_s^σ) martensitic transformations. The blue curve indicates the onset temperature for the $\gamma \to \alpha'$ martensitic transformation. In the absence of stress, this onset corresponds to M_s. When a stress is superimposed, the onset temperature is increased in agreement with Equation 2.3. Above the yield stress of austenite, new nucleation sites are formed by plastic deformation. Plot adapted from the work of Olson and Cohen [60].

The dependence of the M_s temperature with stress is schematically illustrated in Figure 2.4. This plot also shows how the yield stress of the austenite changes with temperature and therefore how the dependence of the M_s temperature changes with stress. All points lying above the blue line indicate conditions where martensite will form. The M_s^σ temperature is defined as the corresponding M_s temperature at the yield stress of the austenite. On the other end of the plot, the M_d temperature corresponds to the temperature above which no strain-induced transformation will occur.

2.2.2 Techniques Used to Measure Martensite Content in Austenitic Steels

To understand the relationship between deformation and martensitic phase transformation, it is necessary to have experimental techniques capable of quantifying the fraction of the microstructure they occupy. Several such methods are available, the most important having been recently reviewed by Talonen [61]. Some of the characteristics of these techniques are detailed in Table 2.2.

Technique	Probed volume	Advantages	Disadvantages
Magnetic measurements (permeability or force)	Bulk	High accuracy	Magnetic saturation not always reached, Edge effects, Calibration needed
Neutron diffraction	Bulk	High penetration depth (~ 20 mm)	Need access to large facility
X-ray diffraction	Surface layer	Fast and relatively easy	Small penetration depth (~ 10 µm), Texture effects
Metallography / SEM / EBSD	Surface layer	Spatial information	Phase recognition is not straightforward
Mössbauer	Thin foil	High accuracy	sensitive to chemistry

Table 2.2: Review of the techniques used to quantify phase fractions of α'-martensite.

Phase fractions from X-ray diffraction (XRD) and neutron diffraction can be estimated from the ratios of the intensities of Bragg peaks (e.g. Dickson's method [62]) or from whole pattern Rietveld fitting [63, 64]. A drawback of these techniques is that intensities of the diffraction peaks are dependent upon crystallographic orientation and that peak overlap can influence peak fitting. Various techniques to reduce these effects have been proposed [65, 66].

Measurement of the α' phase based on magnetic probes have been used with good results [4]. Measurements of α' fraction by saturation magnetiza-

---

[4] Both austenite and ϵ-martensite being paramagnetic, the ferromagnetic α'-martensite is the only phase that can be detected by magnetic sensors.

tion [67], magnetometer [68], SQUID [69] and Feritscope [68] or equivalent devices [70] have been used extensively, while magnetic force measurements or Satmagan measurements [61] are less common.

Finally, direct measurement of the phase fractions by microscopy (optical, SEM, EBSD) have also been attempted (e.g. [71]). These techniques are limited, however, by the difficulty of resolving the fine scale phases (particularly ϵ martensite) and by the poor statistical sampling of the microstructure by these techniques.

2.2.3 Mechanisms of Formation of Strain-Induced Martensite in Austenitic Stainless Steels

In the case of austenitic stainless steels, the martensitic transformations are typically observed to occur during plastic deformation and thus are **strain-induced** according to the definition given in 2.2.1. It is common in these steels for both ϵ-martensite and α'-martensite to form during straining. Moreover, it is common for ϵ-martensite to participate in the nucleation of α'-martensite. The result is a complex relationship between microstructure, plastic deformation and martensite fraction.

Most recent work supports the view that the strain-induced $\gamma \rightarrow \epsilon$ transformation precedes the formation of α'-martensite and that the ϵ-martensite is important in the nucleation of α'. The strain-induced ϵ-martensite forms in the shape of thin plates, as illustrated in Figure 2.5.

As noted in section 2.1, the structure of ϵ-martensite is consistent with a stacking fault lying on every second $\{111\}_\gamma$ plane. This results in the Burgers orientation relationship [73]:

$$\{111\}_\gamma // \{0001\}_\epsilon \tag{2.4}$$

$$\langle \bar{1}\bar{1}0 \rangle_\gamma // \langle 2\bar{1}\bar{1}0 \rangle_\epsilon \tag{2.5}$$

which leads to only four distinguishable variants of ϵ-martensite [50, 74, 75].

One obvious mechanism for the formation of ϵ-martensite is the coordinated motion of $a/6 \langle 112 \rangle$ Shockley partial dislocations. The similarity
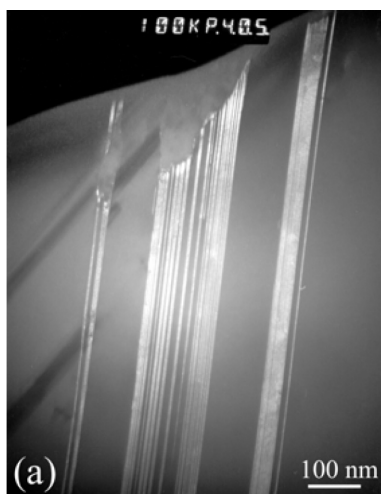
Figure 2.5: Plates of ϵ-martensite in grade 304L after a 5% tensile strain at $-196°$C. Reproduced with permission from [72].

between the structure of an ϵ-plate and a deformation twin is illustrated in Figure 2.6. While a twin can be described as a stacking fault on every adjacent $\{111\}_\gamma$ plane, a plate of ϵ-martensite only requires a stacking fault on every second plane. This has led to the hypothesis that the formation of ϵ-martensite is similar to the mechanism of formation of deformation twins [51]. Rémy and Pineau have suggested that there is a continuous transition from deformation twining to ϵ-martensite formation with decreasing stacking fault energy [75, 76].

Recently, new experimental work has provided further clues as to the differences between the nucleation of twins and ϵ-martensite [77]. The dislocation structure in an Fe-Mn-Al-Si alloy was studied over a range of temperatures where the deformed structure contained twins or ϵ-martensite. In this experiment, it was found that, under conditions where ϵ-martensite was formed, extrinsic stacking faults were observed in the material. In contrast, under conditions where twinning was observed, intrinsic stacking faults were observed. This contradicts theories that have proposed that intrinsic stacking faults are precursors for ϵ-martensite while extrinsic stacking faults are precursors for twinning (e.g. [78, 79]).

16

(a) Twin

(b) ϵ-martensite

Figure 2.6: Schematic representation of (a) a twin, (b) a thin plate of ϵ-martensite. The atoms belonging to a {100} plane prior to the transformation are underlined to help visualize their motion.

It has been experimentally observed in many cases [79, 80] that plates of ϵ-martensite are often imperfect and composed of thinner ϵ-layers separated by retained austenite, which itself may or may not be twinned [28, 38]. Such complex structures, as shown in Figure 2.7, may explain why much of the early microscopy on austenitic stainless steels referred to the fine plate-like packets of stacking faults as "shear bands" (e.g. [81]) rather than as ϵ-martensite or as deformation twins.

Figure 2.7: TEM Micrograph of an α' martensite island formed within an ϵ-band. Reproduced with permission from [28]

The formation of ϵ is a very localized process, associated with the pres-

17

ence of wide stacking faults [45, 78, 82]. Though the formation of ϵ-martensite is still not well understood, some mechanisms have been proposed. Notable models include pole mechanisms (e.g. Seeger [83]) and deviation based mechanisms (e.g. Fujita *et al.* [84]), the latter mechanism being consistent with the idea that the nucleation of ϵ requires some overlapping of stacking faults [37]. In all of these cases, the formation of ϵ-martensite is traced to the existence of extended stacking faults rather than by nucleation at grain or twin boundaries [85].

There has also been a suggestion that the formation of ϵ-martensite may respect the Schmid law, in that it occurs at a critical value of the resolved shear stress on some slip system of the austenite. In a 301 grade, Hedström determined that the austenitic grains which form ϵ-martensite were those with highest Schmidt factor on the $\{111\}_\gamma [1\bar{2}1]_\gamma$ slip systems [86]. The same slip systems were found to verify the Schmid law for the apparition of mechanical twins [28, 87] in Fe-Mn steels.
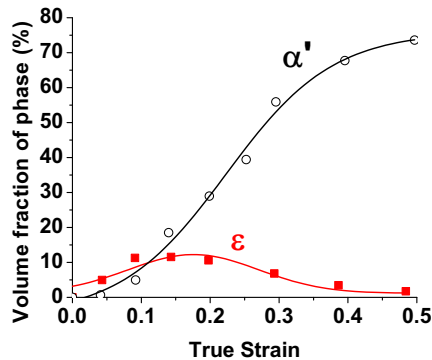
Figure 2.8: Evolution of the fraction of ϵ and α' martensites formed during room-temperature tensile deformation of grade 301. The volume fractions were measured by X-ray diffraction [88].

While ϵ-martensite is often found as an important feature of the microstructure in austenitic stainless steel deformed to low levels of strain, Figure 2.8 illustrates that it never exceeds a small fraction of the total volume of the microstructure [88]. After only a few percent plastic strain, it

is typically found that the volume fraction of α'-martensite significantly exceeds that of ϵ martensite. In these steels, the α' phase is comparable to the body centered tetragonal (bct) thermal martensite obtained by quenching of carbon steels [89–92], though the interstitial content (i.e. carbon plus nitrogen) of austenitic stainless steels tends to be low meaning that the tetragonality of the martensite is nearly zero [17, 93].

While the volume fraction of α' is found to greatly exceed that of ϵ-martensite, the formation of the former is often linked to the existence of the latter. In particular, it is very common to observe the nucleation of α' on ϵ-martensite plates as well as at the intersection between ϵ-martensite plates as illustrated in Figure 2.9.
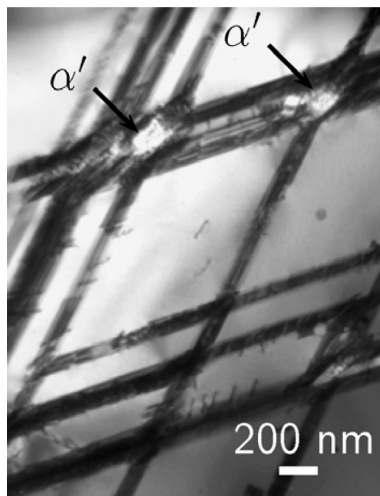
Figure 2.9: Nucleation of α' in grade 316 after a 5% tensile strain at $-196°$C. The dark fault bands are associated with ϵ-martensite while α' martensite is highlighted at some, but not all, intersections. TEM micrograph reproduced with permission from [72].

Venables was the first to describe this mechanism of nucleation in austenitic stainless steels [94]. There has been some controversy about whether ϵ appears as an intermediate to α' [33, 60, 95] or if it is generated to accommodate plastic strains [95, 96], although the current opinion tends to favour the concept that ϵ-martensite forms prior to α' [72].

Besides nucleation at ϵ intersections, α' has been observed to nucleate heterogeneously on other deformation-induced defects (cf. Table 2.3). Similar to the nucleation at ϵ intersections, other researchers have observed the nucleation of α' at the intersection of deformation twins [82, 97–102]. Other variations include the proposal for the formation of α' at the intersection between a plate of ϵ and a deformation twin [103] or an annealing twin [72], or at the intersection of two stacking faults [104]. Twin boundaries have generally been proposed to be less effective nucleation sites than ϵ-martensite [72, 105].

Intersecting features are not always a necessary condition: some researchers have observed the nucleation of α' to take place within a single ϵ plate [106, 107]. Martensite formation at grain boundaries has been much less reported with the only observations being made in grades displaying higher nickel content than traditional commercial stainless steels [33, 108, 109] or in submicron austenitic grains obtained after Equal Channel Angular Pressing (ECAP) [110]. Finally, there has been the proposal that α' can form directly from slip in the austenite [95, 111].

Type of Nucleation	Reference
Intersection between two ϵ plates	[94, 97, 112–115]
Intersection between two deformation twins	[82, 97–102, 116]
Intersection between ϵ and a deformation twin	[103]
Intersection between ϵ and an annealing twin boundary	[72, 117]
Nucleation within a single ϵ plate	[106, 107]
Grain Boundary nucleation from γ	[33, 108, 109, 118]
Direct nucleation from γ	[95, 96, 111]

Table 2.3: Review of the mechanisms of α' nucleation observed in austenitic stainless steels.

A physically-based model capable of explaining the apparent relationship between ϵ-martensite plates and the nucleation of α'-martensite was first proposed by Olson and Cohen [60]. Olson and Cohen reflected upon the double shear model for α'-martensite from γ, first proposed by Bogers and

Burgers [119]. Bogers and Burgers showed that the homogeneous shearing of the fcc lattice on two different $\{111\}_\gamma$ planes, illustrated in Figure 2.10, can produce a strain equivalent to the Bain strain.

(a)   (b)
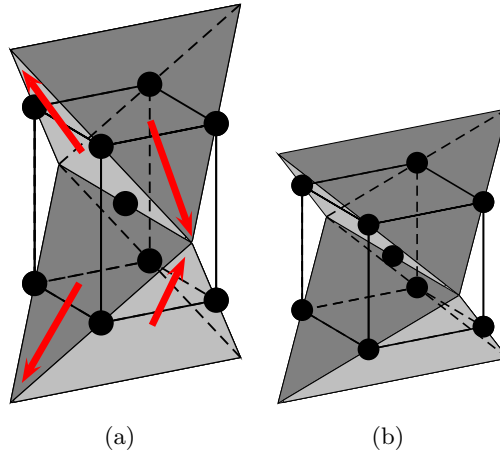
Figure 2.10: The distorted bcc unit cell extracted from Figure 2.2, plotted showing $\{111\}_{fcc}$ planes (i.e. two Thompson tetrahedra). If the material is homogeneously sheared on the $\{111\}$ planes as shown by the arrows in (a), then one approximately obtains the Bain strain leading to a bcc lattice as in (b).

The shears required to give the Bain strain are $a_{fcc}/12 \langle 112 \rangle$ (half the twinning shear) on one set of $\{111\}$ planes and $a_{fcc}/18 \langle 112 \rangle$ (one third the twinning shear) on a second set of $\{111\}$ planes. Olson and Cohen made the link between this concept and the presence of α' at ϵ intersections, noting that the first shear given above corresponds exactly to that caused by an ϵ plate, while the second is consistent with the strain-induced formation of a **faulted** ϵ plate. This model therefore requires that two ϵ plates, one perfect and the other faulted, must intersect in order to generate strains at the intersection which, in a continuum sense, give the Bain strain. While the Olson-Cohen model is a continuum model, recent molecular dynamics simulations have shown that the martensitic transformation can occur at the intersection between the bands, even when the discreteness of the crystal lattice is considered [105, 120]. Moreover, the atomistic models indicate

that a variety of different ϵ and faulted ϵ intersection combinations can lead to conditions resulting in the martensitic transformation. One feature of this model which appears at odds with the generally accepted experimental results is that the γ/α' orientation relationship obtained from this model (Pitsch) differs from that observed experimentally (Kurdjumov-Sachs) [120].

In the case of strain-induced martensite, there has been little discussion regarding the relative importance of nucleation versus growth. In most models for the evolution of strain-induced martensite nucleation, the kinetics are assumed to be only limited by nucleation. However, experimentally, one can see that the growth of strain-induced ϵ and α' is not the same in all directions [121]. In the work of Spencer [72], careful attention was paid to the morphology of martensite in the early stages of formation under conditions where nucleation occurred at the intersection between ϵ-martensite plates. In this condition, the α'-martensite clearly had a preference to grow along the prior ϵ plates rather than normal to the plates. This was also observed in molecular dynamics simulations, where the growth was observed to be nearly isotropic when the orientation relationship was Pitch but anisotropic with particularly fast growth along ϵ bands when the α' had a Kurdjumov-Sachs orientation relationship [105].

A final point regarding the concept of the potential importance of martensite growth relative to nucleation for the kinetics of strain-induced martensitic transformations relates to the concept of **mechanical stabilization**. The concept of mechanical stabilization relates to the fact that dislocations ahead of a martensite interface will retard the motion of the austenite/martensite interface. In the model of Chatterjee et al. [122], the retarding force from a density of dislocations in austenite was presumed to arise from the stress to move dislocations past one another. When the density of dislocations is high enough that the force required to move dislocations is higher than the driving force for the martensite interface, the martensite will not be able to move further and the remaining austenite is considered to be stabilized mechanically. Chatterjee *et al.* applied this concept to explain the fact that a maximum of 50–60% strain-induced martensite could be formed in a 316L stainless steel that had undergone severe

plastic deformation. It was found, in this case, that the effects of mechanical stabilization were not important until large strains ($\epsilon \approx 2$–3). Conversely, in a crystal-plasticity-based study, it was found that a relatively small level of prestrain (7.5% strain in the austenitic grain) was sufficient to fully suppress the phase transformation due to austenite stabilization [123].

2.3 Factors Influencing the Rate of Strain-Induced Martensitic Transformation in Austenitic Stainless Steels

Given the complex nature of the strain-induced martensitic transformations in austenitic stainless steels, it is not surprising that the rate of transformation is sensitive to a large number of parameters. Some of these parameters are intrinsic to the microstructure of the material (e.g. grain size, dislocation density) while other factors are intrinsic to the test conditions (e.g. test temperature, strain rate, stress state, strain path).

One important microstructural feature that impacts on martensitic transformations is austenite grain size. The effect of grain size on the stability of **thermal** martensite can be observed as a variation of M_s temperature with grain size. For both thermal $\gamma \to \alpha'$ [124] and $\gamma \to \epsilon$ [125, 126] martensitic transformations, grain size refinement leads to a reduction in the M_s temperature. It is possible, in fact, to completely suppress the α' martensite transformation via grain size refinement [127, 128].

The strain-induced ϵ-martensite obtained in Fe-Mn steels shows similar characteristics. Hamada *et al.* [129] showed that the $\gamma \to \epsilon$ transformation could be suppressed by reducing the grain size from 40 µm to 10 µm. These authors proposed that the presence of numerous $\Sigma 3$ twins in small grains could impede the motion of the partial dislocations and be an obstacle to the growth of the ϵ-martensite platelets. Alternatively, they also suggested that large austenitic grains may allow for the formation of stacking faults along a large number of planes. Thus, the probability of finding nucleation sites (for ϵ) formed by the overlapping of faults is higher in larger grains.

The literature on metastable austenitic stainless steels provides a much less complete set of data for the effect of grain size on transformation kinetics and mechanical response. The range of grain sizes for which data exists in the literature ranges principally between 10 and 200 µm, though a small number of experiments on materials with smaller grain sizes have been recently reported [110, 130]. The trend in the literature is for grain size

refinement to promote the stability of γ with respect to the strain-induced formation of both ϵ [131] and α' [132, 133] martensites. The reduction of the rate of transformation to α' with decreasing grain size has been observed directly by Nohara [134], Leal [135], Gonzales [136], Jeong [137], Varma [138] and Pétein [139]. There are, however, cases where exceptions to this behaviour have been observed. For example, in grade 304, an increase in the rate of transformation to α' with decreasing grain size has been observed [140, 141]. Examples of these two contradicting behaviours are represented in Figure 2.11.

(a)   (b)
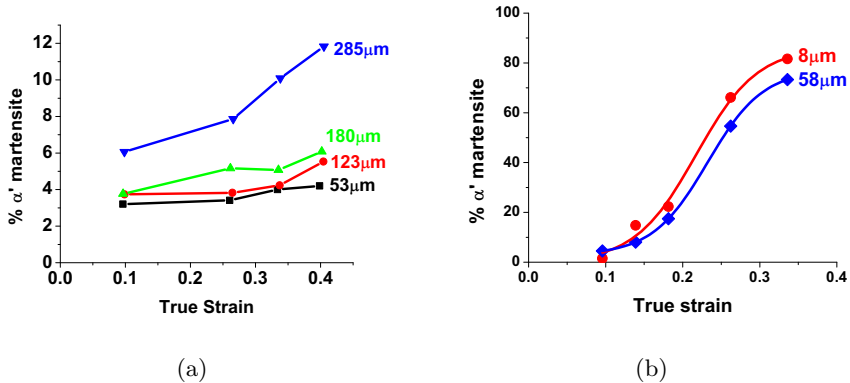
Figure 2.11: Illustration of two different behaviours of the transformation kinetics as a function of grain size. Grade 304 deformed in tension (a) at room temperature [138] and (b) at $-50°$C [141].

There are few mechanisms that have been proposed to explain this trend. In particular, there have been no attempts to separate the grain size dependence of the $\gamma \rightarrow \epsilon$ and $\epsilon \rightarrow \alpha'$ transformation. This is linked to the uncertainty, in many cases, of the mechanism of formation of α', i.e. is it formed directly from austenite, or does it require ϵ as a precursor?

One attempt to rationalize a grain size dependence of the $\gamma \rightarrow \alpha'$ transformation mechanism is found in the work of Yang *et al.* [118]. They observed that coarse austenite grains (~ 40 µm) would form α' at intersections of shear bands (ϵ-martensite, deformation twins, stacking faults), whereas in submicron austenitic grains, α' would preferentially nucleate at grain bound-

25

aries. No quantitative attempt to link the rate of transformation to grain size was attempted in this work, however.

Another example of the importance of starting microstructure comes from experiments where metastable stainless steels have been subjected to pre-strain under one set of test conditions, followed by a second straining under different conditions. Spencer imposed tensile strain of 10% at $-196°$C on alloy 316L [72]. This pre-strained material was subsequently allowed to return to room temperature and the tensile deformation continued. While normally the rate of formation of α'-martensite at room temperature is low in this alloy, after pre-straining at $-196°$C, it was observed that the rate of transformation at room temperature was extremely high (cf. Figure 2.12). In fact, the rate of transformation at room temperature, just following the temperature change, was found to be the same as that at $-196°$C just before the test was stopped. Inversely, when pre-straining was conducted first at room temperature followed by testing at $-196°$C, the subsequent formation of α' at low temperature resulted in the formation of a Lüders-like band which propagated through the material [72] [5]. Observation indicated that the amount of the α'-martensite within the localization band was higher than that outside of the band. The conclusion drawn from these results was that the rate of α'-martensite transformation is sensitive to the microstructure formed by plastic deformation, and thus to the presence of forest dislocations and other deformation-induced defects. This phenomenon is not well-understood, and has only been accounted for in quantitative kinetic models in a semi-empirical form based on the concept of austenite stabilization [123].

Aside from microstructural effects on the strain-induced transformation, bulk mechanical testing conditions can also have notable effects on the transformation kinetics. One of the most important parameters, with regards to the strain-induced martensitic transformation to α'-martensite is the effect of test temperature. Figure 2.13 illustrates the reduction in the rate of formation of α' with increasing temperature in a 301LN stainless steel. This observation is consistent with a wide range of other alloys, e.g. [134, 142–

---

[5] Refer to section 2.5.1 for more details about this behaviour.
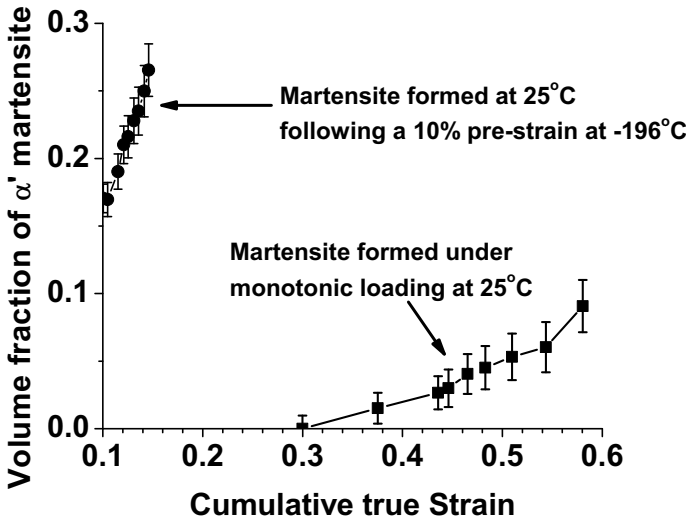
Figure 2.12: Evolution of martensite volume fraction in 316L stainless steel during room-temperature deformation and after a $-196°$C prestrain. Adapted from [72].

146]. The decreasing rate of transformation with increasing temperature can be understood in relation to the reduction in the driving force for transformation ($\gamma \rightarrow \epsilon$ and $\gamma \rightarrow \alpha'$) and the associated rise in the stacking fault energy of the austenite (linked to the formation of ϵ-martensite), with increasing temperature, as described in section 2.1. For instance, in grade 304, increasing the temperature from 20°C to 80°C reduces $\Delta G^{\gamma \rightarrow \alpha'}$ by 300 J.mol^{-1} and $\Delta G^{\gamma \rightarrow \epsilon}$ by 150 J.mol^{-1} while increasing the stacking fault energy by 4 mJ.m^{-2} [33].

The strong influence of temperature on the transformation kinetics can also be seen in an indirect way if one performs tests at elevated strain rates. While most metals exhibit relatively low strain rate sensitivity, stainless steels are an exception. This rate sensitivity is a direct effect of deformation-induced sample heating, which overwhelms the possible intrinsic effects of strain rate on mechanical response even for relatively moderate increases in strain rate. In this case the sample heating comes from the energy dissipated

27
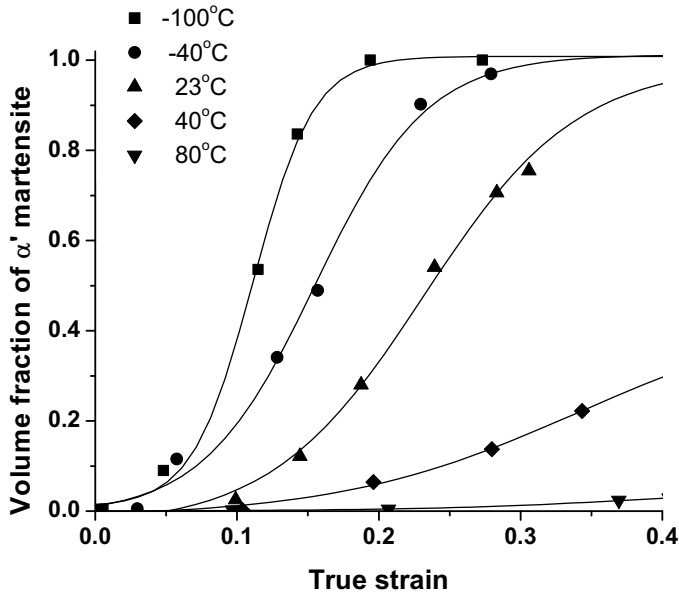
Figure 2.13: Effect of deformation temperature on the $\gamma \rightarrow \alpha'$ kinetics of grade 301LN. Adapted from [146].

by the motion of dislocations **and** the latent heat of the phase transformation(s). As an example of the sensitivity of austenitic stainless steels to this effect, Figure 2.14 shows that increasing the strain rate by one order of magnitude (from 1.3×10^{-3} s^{-1} to 1.3×10^{-2} s^{-1}) during the tensile testing of grade 204M causes a 50°C increase of sample temperature at the end of a uniaxial tensile test. As illustrated, this rise in temperature is enough to reduce the rate of transformation in half [14, 147, 148].

While there have been some reports that increasing strain rates promote the formation of microscopic shear bands (e.g. ϵ-martensite) [68, 97, 149, 150], this effect is best seen at low strains. It is not clear whether this effect continues to be important at larger strains as the effects of self-heating described above tend to dominate the material response.

As noted above, the influence of imposed stresses (and stress state) on the

28

(a)   (b)
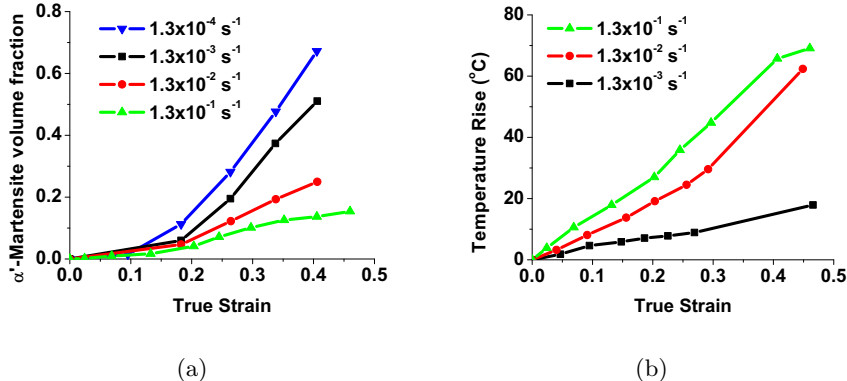
Figure 2.14: Effect of strain rate in grade 204M (a) on the $\gamma \rightarrow \alpha'$ kinetics, (b) on the sample temperature. Adapted from [148]

formation of thermal martensite are well known and documented. In the case of strain-induced martensitic transformations, the effects are more complex owing to the path dependence of plastic deformation. It is therefore often difficult to deconvolute the effects arising from the transformation being stress-assisted and/or from the plastic strains generating different nucleation sites depending on the strain path.

Though this topic is complex, there have been a number of studies examining and comparing the mechanical response and transformation kinetics for different modes of mechanical loading. Unfortunately, there are many conflicting results that make a definitive correlation difficult.

As an illustration of the confusion regarding the effects of stress state and deformation path, one can compare the effects of uniaxial tension and compression found in the literature. Powell [153] and Lebedev [151] showed that the rate of the $\gamma \rightarrow \alpha'$ transformation was higher in uniaxial tension than either in compression or torsion. Contradicting these results are the results of Iwamoto [152] and Kato [154], who observed that compression resulted in the formation of more α' than did tension. Iwamoto rationalized their observations based on differences in texture evolution between tension and compression [152].

(a)

(b)
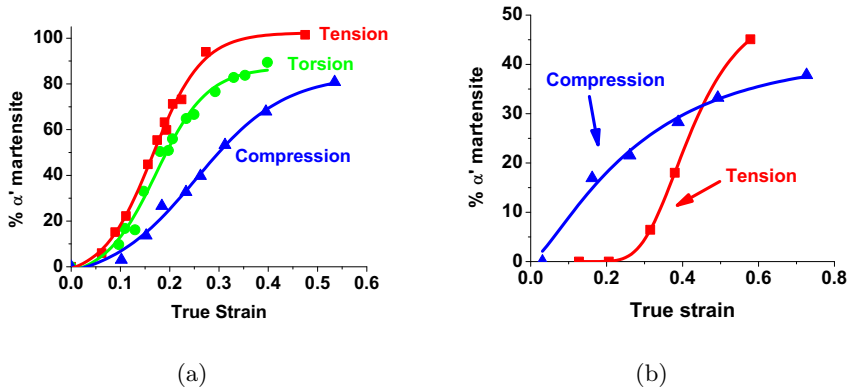
Figure 2.15: (a) Grade 304 deformed at $-196°$C along 3 different paths, at a constant loading rate. The α' fraction was measured by X-ray diffraction [151]. (b) Difference between tension and compression performed at room temperature on grade 304. This difference is attributed to the deformation-induced anisotropy [152].

Hecker found that the use of the Von Mises equivalent strain was appropriate to compare test data ranging from biaxial tension to uniaxial tension in terms of α' formation. It was found that α' started to form at lower strains under biaxial stresses [68], consistent with the observation that the intersection of "shear bands" (e.g. ϵ-martensite, twins, bundles of stacking faults) started at a lower strain along that path [97]. The observation of enhanced transformation at crack tips [155] suggests that the $\gamma \rightarrow \alpha'$ transformation is accelerated for high values of the stress triaxiality. Experiments performed over a wide range of stress states suggest a complex dependence, with an increase in the rate of the $\gamma \rightarrow \alpha'$ martensitic transformation for stress states varying from simple shear to uniaxial tension [146, 151, 156], as illustrated in Figure 2.16.

The trend from uniaxial tension to equibiaxial tension is not definitive however, with reports of decreasing [146, 151, 157] and increasing transformation rate [156]. Equibiaxial tests are often achieved using cup drawing, a complex non-uniform state of deformation [158]. It is possible that the use of such complicated, non-monotonic, non-proportional deformation

(a)   (b)
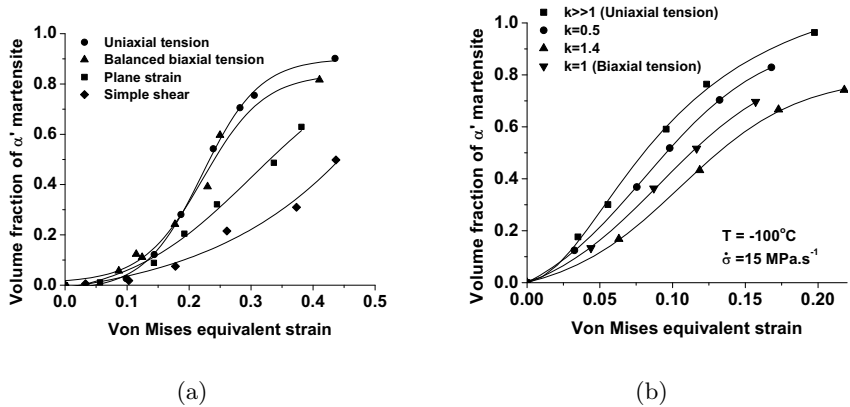
Figure 2.16: Kinetics of two austenitic stainless steels for different loading combinations. (a) Grade 301LN Quantification of kinetics by saturation magnetic measurements. Adapted from [146]. (b) $18-10$ austenitic stainless steel for various ratios of principal stresses (denominated by k). Adapted from Lebedev [151].

paths adds extra degrees of complexity that make their direct comparison against monotonic, proportional loading routes (e.g. uniaxial tension, uniaxial compression or shear) impossible. Recent work has started the task of examining the effects of controlled non-monotonic deformation paths on the strain-induced transformation behaviour [158, 159], however, without a proper understanding of the physical mechanisms linking the deformed state to the rate of martensitic transformation, a physical understanding of these results is very difficult.

As a final comment on the relationship between the imposed deformation path and strain-induced martensitic transformation, there has been recently a return to the application of the Patel and Cohen model (described in section 2.2.3) in an attempt to explain the observation of **variant selection** of α'-martensite. It is observed in metastable stainless steels that, out of the 24 possible crystallographic variants of α'-martensite that could form with a Kurdjumov-Sachs orientation relationship, only a small fraction are actually observed. As with the Patel and Cohen model described above for thermal martensite and stress-induced martensite, the most favourable

crystallographic variants of ϵ-martensite and α'-martensite could be determined based upon the interaction energies calculated between the shape change associated with each martensite variant and the imposed stress state [10, 50, 160]. It has been shown, however, that the application of these models requires arbitrary cutoffs to be applied so as to limit the number of predicted variants. In a recent publication [161], the number of these cutoffs has been reduced through simple geometrical arguments consistent with experimental observations. Further, in this work, it has been shown that the variant selection can be made without the need to calculate the interaction energy. Such predictions could be improved further if the exact mechanism(s) of transformation could be better understood.

2.4 Modelling of the Kinetics of the Strain-Induced Phase Transformations

In the previous section, it has been shown that the strain-induced martensitic transformations depend in a complex, and not well-understood way, on a number of microstructural and test parameters. In order to build physical models for the transformation kinetics and subsequently the mechanical response of these materials, one must attempt to capture at least the basic physical observations consistent with experiments. To date, many of the models proposed in the literature for the kinetics of the strain-induced martensitic transformations have been **empirical** in nature. Table 2.4 lists some of the more common empirical models applied in the literature for capturing the volume fraction of α' as a continuous function of strain. Such models rely on their fitting parameters to empirically capture the effects of variables such as temperature, strain rate, grain size and strain path. Such models do not, however, allow for the complex behaviours illustrated in section 2.3 where path changes must be accounted for. It is also important to note that the role of the $\gamma \rightarrow \epsilon$ transformation is not explicitly accounted for in these models.

Reference	Model	Year
Ludwigson-Berger [162]	$f^{\alpha'} = \frac{1}{1+\frac{1}{k\epsilon^P}}$	1969
Gerberich [163]	$f^{\alpha'} = A\epsilon^{\frac{1}{2}}$	1970
Guimaraes [164]	$f^{\alpha'} = 1 - \exp(-k_g\epsilon^z)$	1972
Sugimoto [165]	$f^{\alpha'} = 1 - \exp(-k_s\epsilon)$	1992
Pychmintsev [166]	$f^{\alpha'} = 1 - \exp(-(k_s - \beta_h P_h)\epsilon)$	2002
Shin [167]	$f^{\alpha'} = f^{\alpha'}_{sat}(1 - \exp(-\beta(\epsilon - \epsilon_0)^n))$	2003

Table 2.4: Empirical models used to describe the volume fraction of strain-induced α'-martensite. All parameters are determined from fitting.

2.4.1 Review of the Olson-Cohen Model for Transformation Kinetics

The most widely used physically based model is that of Olson and Cohen [81]. The Olson and Cohen (O-C) model is based on the assumption that the transformation kinetics are dictated by the rate at which nucleation sites for α' are formed. It is assumed in this model that the nucleation sites are formed via plastic deformation, thus giving the link to the degree of plastic strain.

In the development of the O-C model, the nucleation sites for α' were described as being "shear band intersections". Neither the nature of these fault band intersections (i.e. whether they are ϵ plates or some other planar feature induced by deformation), nor their specific mechanism of formation are described explicitly by the model. Instead, it is simply assumed that the volumetric rate of formation of fault bands is constant with strain. Taking into consideration the evolution of the fraction of austenite then gives the rate of shear band formation as:

$$\frac{df^{sb}}{d\epsilon} = \alpha(1 - f^{sb}) \tag{2.6}$$

where f^{sb} is the volume fraction of shear bands and α is their rate of formation, assumed constant with strain. It is expected that this parameter should depend upon stacking fault energy and strain rate, since both influence the formation of planar faults. The $(1 - f^{sb})$ term accounts for the fact that the fraction of non-faulted material is reduced as straining continues.

From Equation 2.6, the number of shear bands per unit volume can be calculated assuming a constant volume per shear band ($\bar{v}^{sb}$). The number of shear band intersections is thus calculated from geometry as,

$$N_v^I = K(N_v^{sb})^n \tag{2.7}$$

where K is a constant that depends on the austenitic grain size (D). Quantitative stereology predicts that $K = \frac{\pi^2 D^2}{16}$ and $n = 2$ for shear bands that are randomly oriented "thin" plates. Olson and Cohen argued that,

as shear bands tend to align parallel to each other, they can no longer be considered randomly oriented, which would lead to a different value for n. They finally chose $n = 4.5$ from fitting the experiments of Angel [142].

It is assumed in the O-C model that there is a probability, p, that an intersection of shear bands will give rise to the nucleation of α'-martensite. Thus, the number of shear band intersections is related to the number of α' nuclei as,

$$dN_v^{\alpha'} = p \cdot dN_v^I \tag{2.8}$$

In this case, the probability p should be related to the chemical driving force for the $\gamma \to \alpha'$ transformation. Olson and Cohen assume a Gaussian distribution of these probabilities with the chemical driving force (therefore with temperature). The cumulated distribution is:

$$P = \frac{1}{\sqrt{2\pi}} \int_{-\infty}^{g} \exp\left[-\frac{1}{2} \left(\frac{p - \bar{p}}{s_p} \right)^2 \right] dp \tag{2.9}$$

where $\bar{p}$ and s_p represent the mean and the standard deviation of the distribution, determined by best fit.

Finally, one obtains the following equation for the volume fraction of α'-martensite (f'_α) as a function of the true plastic strain ϵ:

$$\frac{df^{\alpha'}}{d\epsilon} = \bar{v}^{\alpha'} \frac{dN_v^{\alpha'}}{d\epsilon} (1 - f^{\alpha'}) \tag{2.10}$$

where $\bar{v}^{\alpha'}$ is the critical nucleus size for the nucleated martensite.

After integration, this leads to:

$$f^{\alpha'} = 1 - \exp(-\beta(1 - \exp(-\alpha\epsilon))^n) \tag{2.11}$$

with

$$\beta = PK \frac{\bar{v}^{\alpha'}}{(\bar{v}^{sb})^n} \tag{2.12}$$

One can directly link the parameter β with the saturated volume fraction

of α' (f_{sat}) attained as true strain tends to infinity,

$$\beta = -\ln(1 - f_{sat}) \tag{2.13}$$

The maximum rate of nucleation of α'-martensite, is itself a function of both α and β.

The importance of ϵ-martensite as a potential site for the nucleation for α' was demonstrated in section 2.2.3. While the physical basis for the O-C model is far more sound than that of the models presented in Table 2.4, it remains that the basic model for the formation of "shear bands" in the O-C model is itself largely empirical. The hypothesis of constant rate of nucleation of shear bands has never been validated. This makes it difficult to link nucleation of α' with experimental volume fraction of ϵ-martensite. Olson and Cohen themselves pointed out that their choice for the α parameter does not match the volume fraction evolution of ϵ-martensite experimentally determined by Guntner and Reed [168].

2.4.2 Influence of External Parameters on the Olson-Cohen Model

Although the O-C model succeeds in reproducing the sigmoidal shape of the monotonic martensite fraction curve with strain and provides a significant physical basis, its basic formulation requires extension to consider the effects resulting from changes in microstructure and testing conditions, as presented in section 2.3.

As an example, consider the influence of grain size on the transformation kinetics for α'. Assuming α and n not to depend upon grain size, the grain size dependence predicted by the O-C model comes from the fact that β is proportional to D^2. This dependence is shown in Figure 2.17, for some conventional values of α and n. According to this plot, decreasing the austenitic grain size tends to decrease the saturated volume fraction of α'. This effect has been discussed by Iwamoto [169] and is consistent with the argument advanced in section 2.3 that grain refinement makes the austenite more stable. Unfortunately, however, there is little experimental data in the
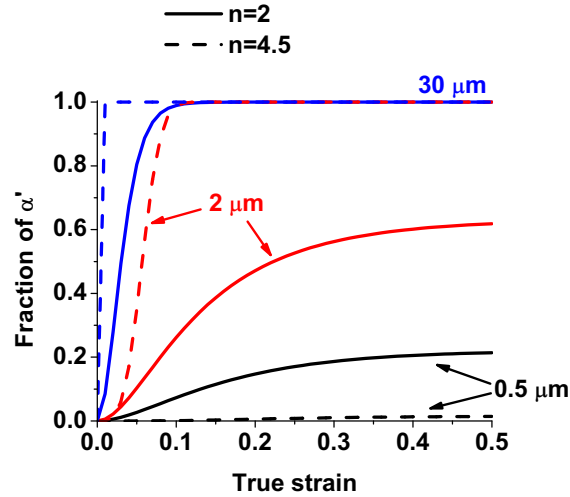
Figure 2.17: Illustration of the grain size dependence on the Olson-Cohen equation, with $\alpha = 8$. The sensitivity of the grain size dependence increases when n is changed from 2 ("theoretical value") to 4.5 ("Olson and Cohen value").

literature with which to compare the O-C predicted grain size dependence of the transformation rate. However, if one considers typical values of n used to fit in the limit of large grain sizes (above 10 µm), then one can see that the grain size dependence would be predicted to be very significant. Such a large grain size dependence does not seem to have been reported in the literature.

Yet, the model of Olson and Cohen could be reinterpreted to observe the opposite dependence upon grain size. It is implied by Olson and Cohen that the shear bands cross the entire grain, meaning that $\bar{v}^{sb} = tD^2$ where t is the thickness of the shear bands. Substituting this into Equation 2.12 gives a grain size dependence of $\beta \propto \frac{D^2}{D^{2n}}$. Thus, for $n > 1$, the O-C model would predict an increasing rate of transformation with decreasing grain size, in contradiction with Figure 2.17 and in contradiction with most experiments presented in section 2.3.

From the perspective of building physical models, one would like to be

able to directly predict the results for different alloy compositions without having to resort to re-fitting of parameters for each composition change. Moreover, a model incorporating directly the thermodynamics of the phases could be valuable for alloy design. Olson and Cohen noted, for example, that substitution of chromium and manganese by nickel could help reducing the strong temperature-sensitivity of the kinetics of nucleation of α', based on qualitative trends they observed in their model fit to experiments. In the O-C model, the chemical composition only appears indirectly through the fitting parameters (namely α, β and n), making the comparison/modelling of the kinetics of two different grade of steels difficult. Related to composition is the temperature dependence of the material behaviour, which affects both the driving force for the transformation as well as the mechanisms of plasticity (via stacking fault energy). Since α is expected to vary inversely with the stacking fault energy and β is linked to $\Delta G^{\gamma \to \alpha'}$, both α and β should decrease with temperature, as illustrated in Figure 2.18.
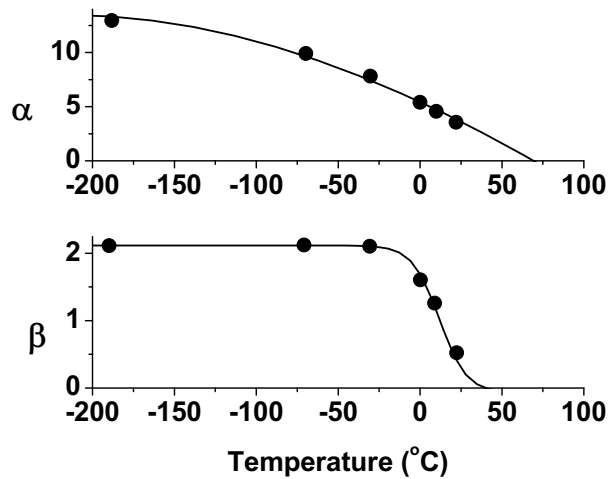
Figure 2.18: Illustration of the temperature dependence on the two Olson-Cohen parameters (namely α and β). Adapted from [81].

The O-C model attempts to directly link the rate of transformation to nucleation sites formed due to plasticity (shear band intersections). One

would expect that such features formed via plasticity should have an effect as well on the flow stress and the work-hardening of the austenite. There has been, however, no attempt to make a direct link between these two features of the material response. Related to this is the fact that the O-C model is not well-suited to capture effects arising from non-monotonic testing. If the O-C model is used in its integrated form (Equation 2.11), then there is no ability to deal with behaviours such as that presented in Figure 2.12 where straining is continued at a higher temperature after a pre-strain performed at a lower temperature. In this case, a more sophisticated linkage between the strain-induced nucleation sites, the mechanical behaviour of the austenite and the transformation kinetics of α' would be needed.

As with the effect of composition and temperature, the influence of stress state on the rate of transformation was not explicitly outlined in the original O-C model. However, the observations presented in section 2.3 relating to variant selection and the stress dependence of the M_s temperature indicate that stress state should be explicitly incorporated into a model of α' kinetics. In this direction, the O-C model has been refined by Stringfellow to include the effect of triaxiality [6] [170, 171]. Stringfellow assumes a distribution of potencies for "shear band intersections" to form α', this distribution being a function of temperature and triaxiality through a parameter g, which represents a net thermodynamic driving force:

$$g = g_0 - g_1 T + g_2 \Sigma - g_3 \Sigma^3 \tag{2.14}$$

where g_0, g_1 and g_2, g_3 are dimensionless constants, T is the temperature, and Σ is the triaxiality. In the case of high triaxiality ratios, as can be found in crack tips, Stringfellow recommends using the last term in Σ^3, which can be ignored otherwise.

The driving force defined by Equation 2.14 is the basis for the distribution of the probability that an intersection forms α'-martensite. In parallel

---

[6] The triaxiality is defined here as the ratio of the volumetric and deviatoric stress invariants: $\Sigma = \frac{-p}{\bar{\sigma}}$ where p is the hydrostatic pressure and $\bar{\sigma}$ the Von Mises equivalent stress.

to Equation 2.9, Stringfellow wrote the cumulative probability as:

$$P = \frac{1}{\sqrt{2\pi}} \int_{-\infty}^{g} \exp\left[-\frac{1}{2} \left(\frac{g' - \bar{g}}{s_g} \right)^2 \right] dg' \tag{2.15}$$

with $\bar{g}$ and s_g the mean and the standard deviation of the distribution, determined by best fit. This probability is proportional to the β parameter which appears in Equation 2.11.

Stringfellow mentions an attempt to model the full stress tensor, instead of simply the triaxiality, but this resulted in too much transformation at high levels of stress, an effect attributed to the difficult propagation of α' when the austenite work-hardens.

It is worth comparing the Stringfellow model to the Patel-Cohen model mentioned in section 2.2.1. While the Stringfellow model predicts that uni-axial compression lowers the rate of transformation (cf. Figure 2.19), the Patel-Cohen model shows that both uniaxial tension and uniaxial compression favour the transformation (cf. Figure 2.3). This difference comes from the fact that the shear component is not taken into account by Stringfellow, while it often dominates in the Patel-Cohen model. This observation questions the relevance of the triaxiality as unique parameter to describe complex stress states. Another scalar variable, known as the Lode parameter, was proposed to complement the triaxiality [139].

Based on the fact that compression would form more shear bands at low strains, Iwamoto, Tomita and Tsuta refined the Stringfellow model by adding the triaxiality ratio into the rate of increase of shear bands [152]. To do this, the α parameter which appears in Equation 2.11 was written as:

$$\alpha = \alpha_1 + \alpha_2 T + \alpha_3 T^2 - \alpha_4 \Sigma \tag{2.16}$$

in which $\alpha_4 = 0$ returns the Stringfellow model.

As noted by Serri *et al.*, there is a drastic difference between the kinetics predicted either by Stringfellow or by Iwamoto [172]. Iwamoto's model tends to delay the formation of shear bands in equibiaxial tension, an observation contrary to the experimental data presented in Figure 2.16.
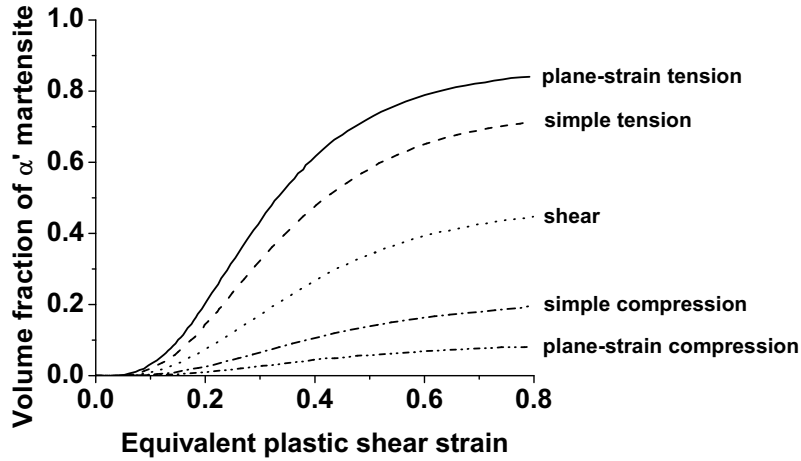
Figure 2.19: Illustration of the stress state dependence on the Stringfellow model. Adapted from [171].

The rate of the strain-induced phase transformation might as well have a stress-dependence. Despite some recent work [159], this issue remains unresolved at present.

To summarize, in all models of the $\gamma \rightarrow \alpha'$ transformation kinetics, the influence of grain size on the kinetics of the $\gamma \rightarrow \alpha'$ phase transformation is treated in the same way as originally proposed in the O-C model, yet this trend has never been systematically studied experimentally. Many studies have considered changes of strain path via the triaxiality ratio. This parameter only accounts for variations of the hydrostatic stress. Despite abundant amount of data relating to changing strain paths, the incorporation of the shear components into a model of the $\gamma \rightarrow \alpha'$ transformation kinetics has not advanced significantly since the work of Patel and Cohen (1953) [47].

2.5 Mechanical Response of Austenitic Stainless Steels

The strain-induced martensitic phase transformations described above results in a microstructure that evolves strongly during plastic deformation. As the microstructure evolves from being fully austenitic to containing a mixture of α'-martensite, ϵ-martensite and austenite, the bulk mechanical properties of the material vary as well. This evolution creates a material whose properties are not necessarily given by a volume fraction weighted combination of the properties of the individual phases in bulk form. One can also incorporate the synergistic effects arising from one phase on the others (e.g. the accumulation of transformation-induced dislocations in austenite due to the formation of α'-martensite), as well as other complex features, such as the size and morphology of the martensitic phases. Despite there being a significant amount of experimental data published in the literature (see for instance the surveys of Powell [153] and Llewellyn [17]) on the bulk mechanical response of metastable austenitic stainless steels, our basic understanding of the physical origins of the mechanical response remains a complex and challenging topic.

2.5.1 Bulk Mechanical Response

In most fcc metals, the yield stress is weakly dependent upon temperature, with the main variation coming from the temperature-dependence of the shear modulus (μ) [173]. In contrast, austenitic stainless steel present a high-temperature dependence of yield stress, as one can see in Figure 2.20.

Despite this strong temperature dependence of the yield strength, the grain size dependence of yield stress is found to generally follow the Hall-Petch relation [175, 176] for grain sizes ranging from approximately 1 µm upwards. Some measurements for the Hall-Petch parameters of different stainless steels are given in Table 2.5 and compared to the Hall-Petch constants for other fcc metals. The important feature of Table 2.5 is that there can be a large dispersion in the values given for the Hall-Petch slope, this
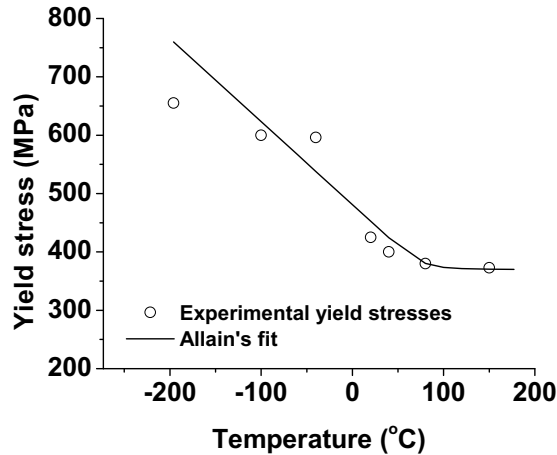
Figure 2.20: Effect of the temperature on the yield stress (determined by 0.2% offset method) of a 301LN stainless steel. The experimental data points are from Nanga [14], fitted with the equation proposed by Allain for austenitic Fe-Mn-C steels [174].

feature being a reflection of the difficulty to reproduce grain size measurements.

Beyond yield, the evolution of the flow stress with deformation (the work-hardening) is sensitive to a large variety of parameters including strain rate, test temperature and deformation path. The dependency on these variations are often largely determined by the way in which the test parameters change the rate of transformation. The uniaxial tension stress-strain curves of a 316L stainless steel are plotted as a function of test temperature in Figure 2.21(a) [72]. The stress-strain curve at $177°C$ represents the behaviour of a fully austenitic material as neither α' nor ϵ-martensite form at this temperature. One may also note that, at this temperature, serrations in the stress-strain curve appear at higher stresses. These serrations are a common feature in many austenitic steels (stainless as well as non-stainless alloys [87]) and are associated with dynamic strain-aging. Various explanations for the dynamic strain-aging in austenitic steels have been proposed

Material	Ref.	Friction stress σ_0 (MPa)	Hall-Petch slope k_y (MPa.μm$^{1/2}$)
301LN	[177]	252	274
304	[178]	220	492
316L	[179]	200	116
316L	[180]	164	621
316L-modified	[181]	144	580
Copper	[182]	26	110
Nickel	[183]	15	238

Table 2.5: Hall-Petch parameters determined at room temperature for various fcc materials.

(e.g. [184, 185]), though this is still an active area of research.

The TRIP effect manifests itself in this material for temperatures below 25°C. The effect of the transformation to α' can be recognized from the inflection in the stress-strain curve and the consequent increasing rate of work-hardening, at intermediate levels of strain. The effect of the appearance of strain-induced martensite can be more easily seen in a plot of work-hardening rate as presented in Figure 2.21(b).

(a)   (b)
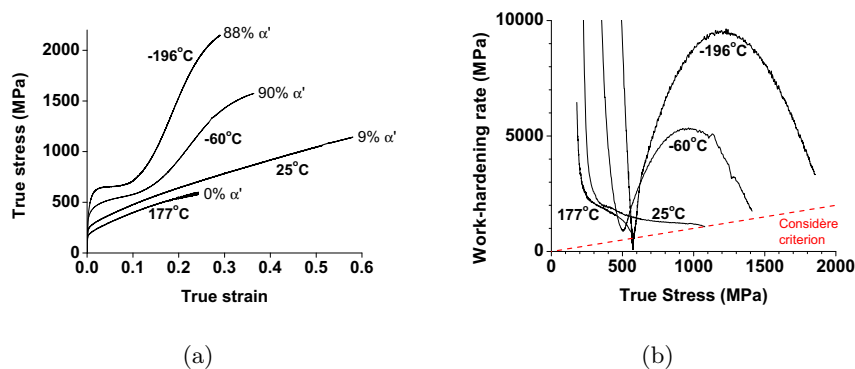
Figure 2.21: Effect of the temperature on the tensile curves of a 316L stainless steel. Adapted from Spencer [72].

One of the benefits of the increasing rate of work-hardening is that it

allows for the onset of strain localization in tension, as determined by the Considère criterion,

$$\frac{\partial \sigma}{\partial \epsilon} \leq \sigma \qquad (2.17)$$

to be suppressed until high strains and stresses. This results in materials that have very large combinations of uniform elongation and ultimate tensile strength.

Figure 2.22 illustrates that a similar behaviour is exhibited by grade 301LN [186]. In this alloy, however, the formation of α' during straining becomes significant at higher temperatures compared to alloy 316L, a consequence of the lower stability of austenite in this alloy. For temperatures below -40°C, Figure 2.22 shows the presence of an upper yield point and a lower yield point, as well as a long plateau of $\sim 10\%$ strain. It was observed that this corresponds to the formation of a Lüders-like band during deformation. Only the volume swept by the band in which strain localization occurs was found to form α'-martensite. Similar behaviour was obtained in the condition described in section 2.3 and whose tensile curve is reproduced in Figure 2.23, in which the material was pre-strained at a certain temperature and then was reloaded at a lower temperature [72]. Additionnally, such discontinuous yielding has also been reported in submicron-grained 304 or 316 grades, and the magnitude of the Lüders strain was found to increase when the temperature was lowered from 25°C to -196°C [187]. The explanation of this phenomenon is not well understood [187], although recent work has suggested the possibility that the strong increase of yield stress with decreasing temperature may lead to the yield stress rising above the level necessary to initiate a truly stress-assisted martensitic transformation [10].

The role that grain size plays in modifying the work-hardening response of austenitic stainless steel is also complicated by the fact that grain size impacts both the mechanical response of austenite as well as the kinetics of martensitic transformation, as seen from section 2.3. In the case of stable austenitic stainless steels, several researchers [179, 180, 188, 189] have taken an empirical approach to explaining the grain size dependence through an **extended** Hall-Petch expression where the Hall-Petch parameters are taken
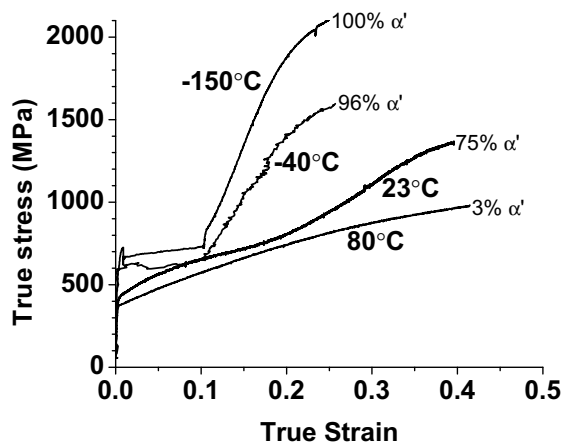
Figure 2.22: Effect of the temperature on the tensile curves of a 301LN stainless steel. Adapted from Nanga [14].

to be strain-dependent. A more physical approach to understanding the grain size dependence of the work-hardening rate of alloy 316L (in which no martensitic transformation occurred under the testing conditions) was performed by Feaugas and Haddou [190]. In this work, the grain size dependence of the work-hardening rate was attributed primarily to an increase in the long-range stresses arising from dislocation pile-ups at grain boundaries. Accordingly, it was argued that the grain size dependence, and therefore kinematic hardening, is higher for lower stacking fault energy alloys. This is in qualitative agreement with a recent model proposed for the grain size dependent work-hardening of fcc metals [191].

Varying the strain path has an effect on the stress-strain response of austenitic stainless steels. The reason for this change in stress-strain behaviour has been attributed to different reasons, e.g. variation of transformation kinetics (cf. section 2.3) and different texture evolution [152, 157]. Two examples of strain path dependence of the stress-strain behaviour of austenitic stainless steels are given in Figure 2.24. Very often, the relative position of the stress-strain curves is consistent with the measured kinetics, the grades forming more α' at a given equivalent strain experiencing higher hardening
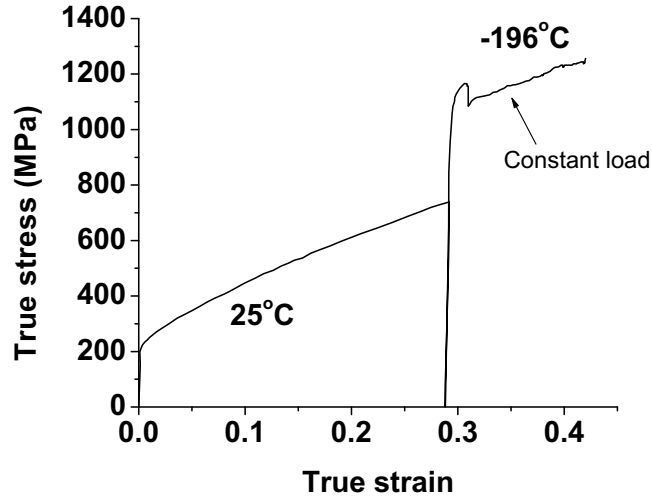
Figure 2.23: Tensile behaviour of 304L pre-strained at 25°C and further deformed at -196°C. The reloading at -196°C was associated with the propagation of a band in which the strain was localized. Adapted from Spencer [72].

[151]. This is evident when comparing Figure 2.16 to Figure 2.24. In Figure 2.24(a), shear and tension initially display similar work-hardening before diverging for an equivalent true strain of ∼18%, whereas the difference between strain path manifested itself much earlier (almost after yielding) in Figure 2.24(b). This inconsistency also appears in the rate of the kinetics, and can be observed when comparing Figure 2.16(a) and Figure 2.16(b).

2.5.2 The Intrinsic Mechanical Response of Austenite and Martensite

One of the most common methods for analyzing the bulk mechanical response of metastable stainless steels is to consider the bulk response as coming directly from the weighted response of each of the individual phases. This requires a knowledge of the mechanical response for each of the phases present in the microstructure.

47
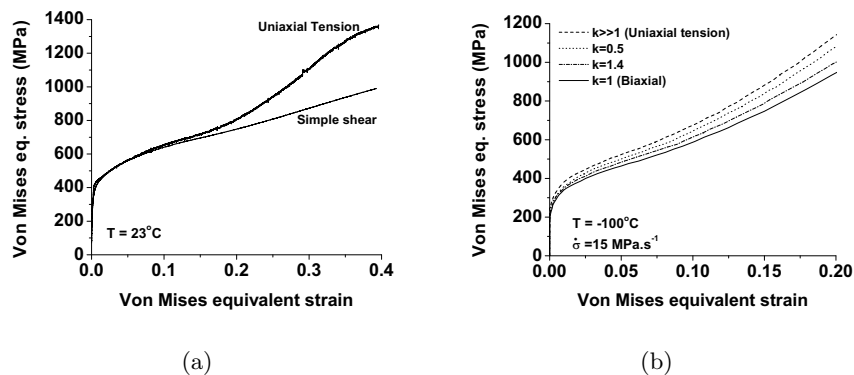
Figure 2.24: Stress-strain curve of two austenitic stainless steels for different loading combinations. (a) 301LN adapted from Nanga [146], (b) 18-10 austenitic stainless steel for various ratios of principal stresses (denominated by k). Adapted from Lebedev [151].

Although ϵ-martensite is formed in many austenitic stainless steels, its contribution has largely been ignored in descriptions of the bulk mechanical response of these materials. This is normally justified based on the fact that ϵ-martensite represents only a small fraction of the microstructure [192]. A recent study by Hedström [86] combined uniaxial tensile experiments with X-ray diffraction to monitor the elastic strain in ϵ-martensite during in-situ straining experiments. Over the relatively small range of plastic strains studied it was found that the ϵ-martensite had a very low work hardening rate (Figure 2.25).

While there are few systematic studies examining the relationship between the presence of ϵ-martensite and mechanical properties in austenitic stainless steels , there are a large number of studies aimed at correlating the bulk mechanical response with the presence of α'-martensite. In order to understand the relative contributions to the overall work-hardening rate coming from austenite and α'-martensite, several experiments have been performed in an attempt to directly assess (for a given deformation and level of martensite) the stresses carried by each of the phases. The stress-strain response of austenite in the absence of martensite is not directly measurable
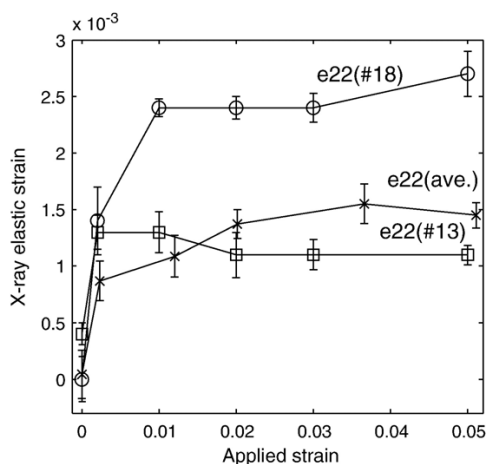
Figure 2.25: Measured elastic strain evolution along the tensile direction plotted for two individual austenite grains (13 and 18), along with the average X-ray elastic strain. Grain 13 transformed fully to ϵ-martensite. Reproduced from Hedström [86].

for conditions where the strain-induced transformations occur, since straining of the austenite affects the phase transformation. One possibility is to perform mechanical tests at temperatures where no strain-induced martensitic transformations are observed (e.g. [193]) and infer the response of the austenite at lower temperatures. Of course, the strong temperature sensitivity of the stacking fault energy (among other properties) for these steels makes this extrapolation difficult. Similarly, it is not possible to measure directly the bulk mechanical response of the martensitic phase since it is only formed by straining of the austenite. It is, however, possible to make **indirect** measurements that provide estimates for the stress borne by the austenite and/or martensite phases.

In the work performed by Spencer *et al.*, neutron diffraction was used to measure the elastic lattice strains in alloy 316L [72, 194]. In this case, 316L test coupons were pre-strained at -196°C so as to obtain a significant fraction of α'-martensite, then tensile tests were continued at room temperature under neutron irradiation for diffraction experiments. By continuing the testing at room temperature, the fraction of martensite in the

microstructure was found to not vary significantly beyond the first few percent strain. In these experiments, the load partitioning in the case of a **static** phase fraction could be estimated. As shown in Figure 2.26, it was observed that α'-martensite represents a strong reinforcing phase (i.e. having a higher yield strength than the austenitic matrix) but that the phases exhibited significant plastic co-deformation. Moreover, the apparent rate of work-hardening arising from the α'-martensite was only slightly higher than the macroscopic work-hardening rate. This implies that the strong increase in work-hardening rate associated with the TRIP effect comes not from an intrinsically high work-hardening rate of the α'-martensite but instead, from the contribution of the evolution of the phase fraction to the work-hardening.
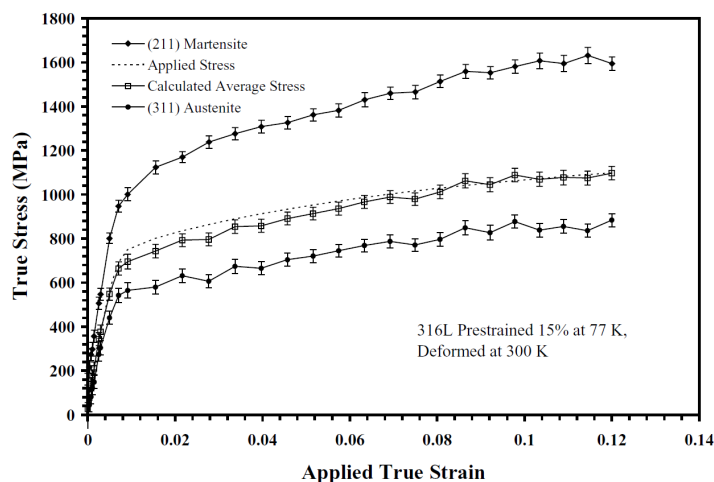
Figure 2.26: Stress level in austenite and α'-martensite phases measured by neutron diffraction in grade 316L. Reproduced from Spencer [112].

Other diffraction based studies of the stresses borne by the two phases have been carried out using neutron and X-ray diffraction under conditions where the phase fraction evolves with strain. One example is represented in Figure 2.27, from the work of Talonen [34]. In this case, one observes first that the diffraction-based estimate of the stress borne by the austenite matches the macroscopic stresses over the range of strains where austenite

is the only phase present. Once the fraction of α' becomes significant however, the macroscopic flow stress is seen to evolve away from the austenite flow curve. While it is impossible to make quantitative comparisons between these results and those from the work of Spencer (Figure 2.26), due to differences in the testing methodology and alloy, one can note that the observed hardening rates for the α'-martensite measured in both cases are similar, as are the hardening rates for the austenite. These results are also very similar to those obtained under similar conditions by Berrahmoune [195] using X-ray diffraction, and to the neutron diffraction measurements performed by Dufour [13].
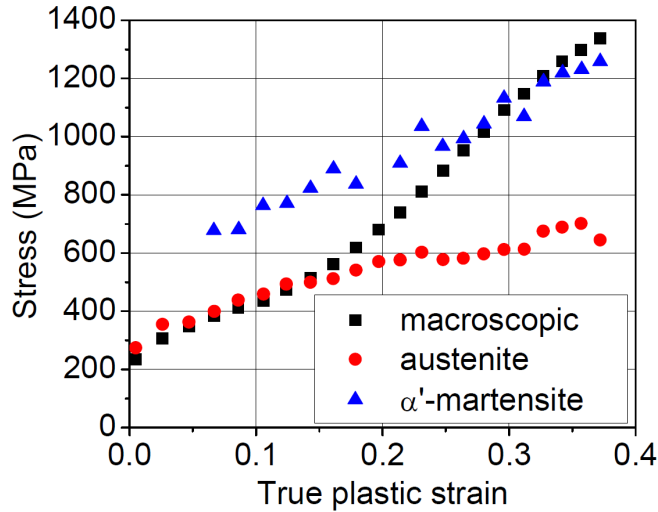
Figure 2.27: Stress level in austenite and α'-martensite phases measured from X-ray diffraction stress measurements in grade 301LN. Reproduced from Talonen [34].

Further analysis of such diffraction based data can be used to give deeper insight into the deformation behaviour of the two phases. Talonen [34] used the results of peak broadening from X-ray diffraction measurements in an attempt to estimate the dislocation density in the austenite and α'-martensite phases in a 301LN alloy. Figure 2.28, from this work, shows the total flow stress as well as the stress in the austenite phase as measured

from diffraction peak shifting versus the square root of dislocation density in austenite.
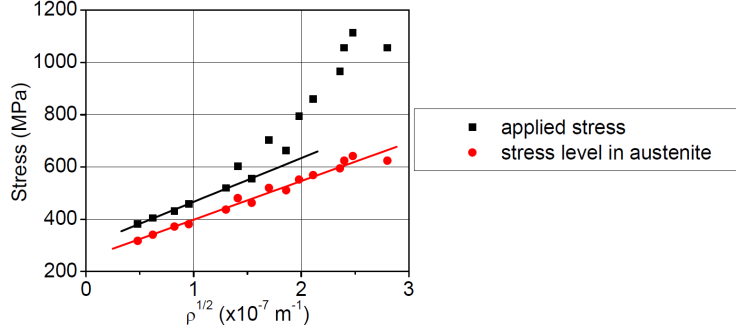
Figure 2.28: Stress level in the austenite phase of grade 301LN, measured by X-ray diffraction as a function of square root of dislocation density of austenite determined by Integral Breadth Method. Reproduced from Talonen [34].

The results show that the Taylor equation relating flow stress to dislocation density:

$$\sigma = \sigma_0 + \alpha_T \mu b \sqrt{\rho} \tag{2.18}$$

appears to be well obeyed for the austenite phase. Similar estimations of the dislocation density where made for the α' phase resulting in a high dislocation density ($\rho_{\alpha'} \approx 6-14\times10^{14}$ m^{-2} compared to $\rho_{\gamma} \approx 1-6\times10^{14}$ m^{-2} for austenite) which did not vary substantially with plastic strain. This dislocation density is similar to that found by Narutani [196] and is consistent with the qualitative TEM observations by Spencer [72] who explained the high dislocation density in the martensite as likely being a consequence of dislocations in the prior austenite being incorporated into α' during the transformation. Yet, one must be careful with the interpretation of these results. Beyond the difficulties of dislocation density estimates from peak broadening in simple single phase materials, the interpretation of peak broadening in the α' phase here are complicated by the fact that the α' forms progressively with strain, meaning that the α' has a large and continuous distribution of plastic strains.

These results give the overall view that both austenite and α' phases undergo significant plastic co-deformation. However, the α' phase is seen to deform with a significantly higher flow stress than the austenite, though the apparent work-hardening rate of the two phases is similar.

2.5.3 Modelling of the Overall Mechanical Response of Austenitic Stainless Steels

As noted above, it is common to interpret the overall mechanical response of austenitic stainless steels as that of a composite having a dynamically evolving phase fraction. According to this approach, the overall response of the material may be predicted, provided constitutive laws for the phases can be identified and a scheme for homogenization (i.e. the method to define the stress and strain partitioning between phases) can be selected. Among the different studies that have sought to model the mechanical response of metastable austenitic stainless steels, the approaches can be generally separated into those coming from a mechanics or a materials background.

Mechanics-based models for the mechanical response of austenitic stainless steels are very prevalent in the literature owing to practical application of these models in simulations for the forming and in-service mechanical properties of these materials. The general approach, in this case, is to develop tensorial expressions for the yield surface and its expansion with strain. Sophisticated homogenization schemes (e.g. tangent [197] or secant [198] self-consistent approaches, Mori-Tanaka [199, 200], or finite element simulation) can be used to obtain the net response based on the constitutive laws of the individual phases. The constitutive models for the individual phases, as well as the transformation kinetics in these models, however, tend to include many empirical fitting parameters such that the behaviour laws can be made to coincide with experimental results for a wide range of experimental observations.

An example of this type of approach is given by the work of Iwamoto and Tsuta's [169], which aims to describe both the transformation kinetics and the mechanical response of metastable stainless steels as a function of

temperature, strain rates and grain size. In this model, constitutive laws for each phases are described by:

$$\bar{\sigma}_I = \bar{\sigma}_{0(I)} \left[\frac{\dot{\bar{\epsilon}}_I^{pslip}}{\dot{\epsilon}_y} \right]^m$$

$$\sigma_{0(I)} = \sigma_{y(I)} + C_{1(I)} \left\{ 1 - \exp\left(-C_{2(I)} \bar{\epsilon}_{(I)}^{pslip} \right) \right\}^{C_{3(I)}}$$

$$\sigma_{y(a)} = C_{4(a)} \exp\left(-C_{5(a)} T \right) + k_y \left(\frac{d}{d_0} \right)^{-1/2}$$

$$\sigma_{y(m)} = C_{4(m)} \exp\left(-C_{5(m)} T \right) \tag{2.19}$$

where I can be replaced by "a" in case of austenite and "m" in case of martensite, where m is the strain rate sensitivity exponent and where $C_{1(I)}$ to $C_{5(I)}$ are material constants. The kinetics of the phase transformation to α'-martensite are described by the Tomita-Iwamoto model [201] presented in section 2.4.2, including strain rate sensitivity. The homogenization is performed using a finite element simulation. To account for any arbitrary stress state, a yield function needs to be defined. In this particular case, the following has been used:

$$\bar{\sigma} = \sqrt{3 \left(J_2 - \kappa \frac{J_3}{J_2^{1/2}} \right)} \tag{2.20}$$

One can separate the work-hardening into an isotropic component (obeying the yield function above) and a kinematic component. In the case of the Iwamoto-Tsuta model, the hardening has been assumed to be purely isotropic (as in many of the mechanics based models) though the presence of phases having different flow stresses will necessarily result in stress partitioning and a kinematic hardening component [158].

As an illustration of the fit between experiment and model, the calibrated Iwamoto model is shown in Figure 2.29 illustrating its ability to capture the experimentally observed grain size dependence of the mechanical response.

Such a model has the advantage of not making particular assumptions on how the stresses and/or strains are partitioned. However, 24 fitting
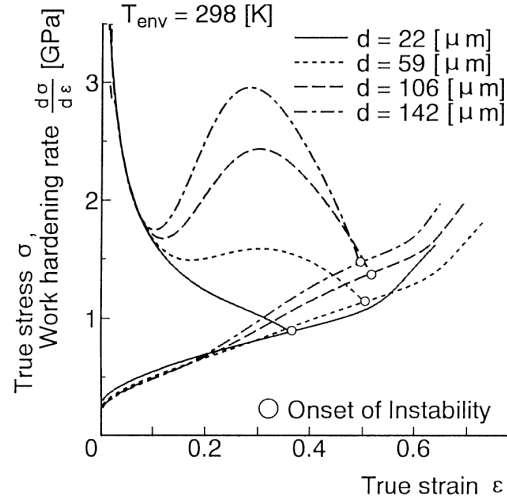
Figure 2.29: Simulated true stress and work-hardening curves obtained for room-temperature tension in various austenitic grains. Reproduced from [169].

parameters need to be estimated from experiments, with no explicit reference to the deformation microstructures or many of the other physically-based observations described in previous sections of this review.

An alternative approach, often less rigorous in terms of mechanics, is to use simple one-dimensional materials-based modelling approaches in which the constitutive laws are more generally physical in nature and attempt to explicitly account for microstructure. These models may use simpler homogenization laws than the mean-field approaches described above. For instance, many authors [58, 112] have used the assumption of uniform strains, the so-called Taylor assumption, which constitutes the upper-boundary of homogenization.

As noted above, the behaviour of austenite appears to obey the Taylor equation implying the dominance of forest hardening. A popular approach to predicting the evolution of dislocation density is via the Kocks-Mecking and Kocks-Mecking-Estrin equations [202]. In the Kocks-Mecking model, the evolution of the dislocation density is modeled as being associated with

a dislocation storage term and an annihilation term. In the Kocks-Mecking-Estrin model, the Kocks-Mecking equation is expanded to include a second storage term associated with the storage of geometrically necessary dislocations due to plastic strain gradients. This approach has been successful in describing the work-hardening in many fcc materials [202] and has been also shown to reproduce the work-hardening rate in stable grades of stainless steels [203] as well as in TWIP steels [204]. In the latter case, deformation twins substantially increase the work-hardening rate, and increase the density of obstacles to planar slip (so-called dynamic Hall-Petch effect). The presence of these boundaries increases the rate of geometrically necessary dislocation storage, while also introducing strong kinematic hardening [205, 206].

An example of the Kocks-Mecking-Estrin approach applied to both the austenitic and martensitic phases is in the work of Bouquerel *et al.* [207]. In this model, the austenitic grain size is considered strain-dependent,

$$d_\gamma(\epsilon) = d_\gamma^{init}(1 - f_{\alpha'})^{1/3} \qquad (2.21)$$

and the dislocation density evolution in austenite is represented by:

$$\frac{1}{M}\frac{d\rho}{d\epsilon} = \frac{1}{b}\left(\frac{1}{d_\gamma(\epsilon)} + k\sqrt{\rho}\right) - f\rho \qquad (2.22)$$

where k and f are the two Kocks-Mecking parameters representing the rate of accumulation of statistically stored dislocations and the dynamic recovery respectively. In this model, it was assumed that the accumulation of geometrically necessary dislocations dominated over statistically stored dislocations.

The stress-strain curve of the martensite is described by the Rodriguez and Guttierez relation [208] which is an integrated version of the Kocks-Mecking model:

$$\sigma_{\alpha'} = \sigma_0 + \alpha M\mu\sqrt{b}\sqrt{\frac{1 - \exp(-Mk_2\epsilon)}{k_2\Lambda}} \qquad (2.23)$$

where Λ is the mean-free path between dislocations within martensite, α is a geometrical constant close to 0.33 and k_2 is an adjustable parameter. The kinetics of the $\gamma \rightarrow \alpha'$ phase transformation is given by the O-C model. The stress of the composite material is estimated from a Gladman-type mixture law,

$$\sigma = \sigma_\gamma (1 - f_{\alpha'}^2) + \sigma_{\alpha'} f_{\alpha'}^2 \tag{2.24}$$

with the Taylor assumption (i.e. equal strain) for the strain partitioning.

The outputs of the model are represented in Figure 2.30.
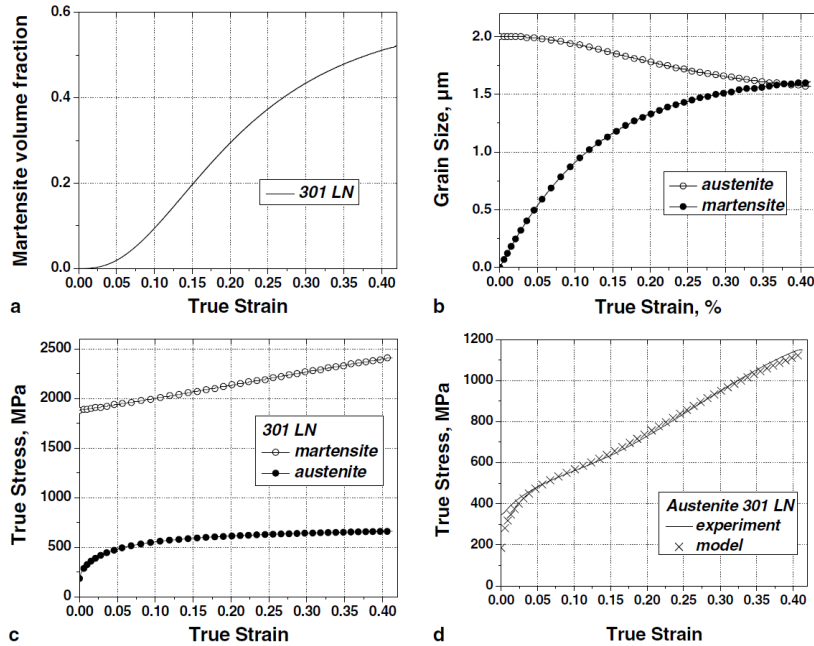
Figure 2.30: (a) Evolution of the volume fraction of martensite with strain for the 301LN stainless steel during tensile testing at 20°C. (b) Evolution of the calculated austenitic and martensitic grain size during the tensile test. (c) Simulated stress-strain curves for the martensitic and austenitic constituents. (d) Experimental and modelled stress-strain curves. Reproduced from [207].

Such a model has the advantage of describing the stress-strain relation of the two constituents via the same micro-mechanical approach, and it

considers the scale reduction in both the austenite and the martensite in terms of generating geometrically necessary dislocations. Moveover, unlike other models which consider the martensite to be a purely elastic phase, the martensite phase in this model is considered to contribute to the mechanical response via plastic co-deformation with the austenite matrix. A criticism of this approach, however, is that it considers that the martensite can be described as a uniform phase, having the same properties throughout. This does not appear consistent with the fact that the fraction of martensite is evolving with plastic strain implying that there should be a range of properties for the martensite present for any given level of imposed plastic strains.

Other models highlighting the importance of geometrically necessary dislocations in the strengthening of austenitic stainless steels have also been proposed (cf. section 2.2.3) [123]. Talonen performed measurements of the chord length distributions of α' in grade 301LN [34] after different levels of strain. His results, reproduced in Figure 2.31 show that, although the α' nuclei are initially small, large clusters start appearing very early in the course of the deformation. Those measurements can be used to construct a model of dispersion hardening, based on the generation of geometrically necessary dislocations in the austenite [34, 109].

Talonen estimated the density of geometrically necessary dislocations accumulated in the austenite phase assuming that the α'-martensite is a rigid (non-deforming) phase [34]. The martensite islands were assumed cubic shaped, of volume L^3, L being the chord-length presented in Figure 2.31. The density of geometrically necessary dislocations is then given by:

$$\rho_G = \frac{4 f_{\alpha'} \Delta \epsilon}{bL} \tag{2.25}$$

with b the Burgers vector of the geometrically necessary dislocations.

Talonen found reasonable agreement between the density of geometrically necessary dislocations and the dislocation densities estimated from X-ray diffraction (Figure 2.28). The fundamental difficulty with this approach is that the rate of generation of geometrically necessary dislocations depends
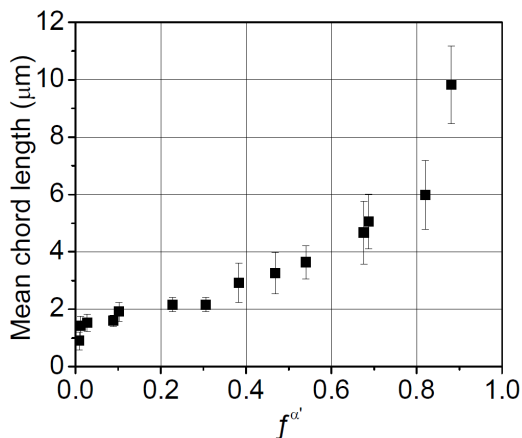
Figure 2.31: Mean chord length of α'-martensite islands in 301LN steel as a function of α'-martensite volume fraction. Reproduced from [34].

on the assumption of how much plastic strain is accomplished by the α' and austenite phases. The assumption that the α' phase is a rigid phase is not supported by the diffraction based data shown above (Figure 2.26 and Figure 2.27) nor from in-situ TEM observations where significant dislocation activity in the α' phase has been observed [72]. Indeed, it has been suggested that the partitioning of strain between the austenite and α' phases might be related to a percolation threshold, below which most of the imposed strain is carried by austenite and above which most strain is carried by α'-martensite [34, 109].

While describing the mechanical behaviour of austenite appears to be possible within well-established physically based methodologies (e.g. Kocks-Mecking-Estrin), defining a constitutive law for the strain-induced α'-martensite is much more difficult. As noted above, many studies have simply assumed that the α'-martensite acts as a rigid (or purely elastic), phase though experimental measurements are at odds with this assumption. Further, as discussed by Spencer [72], owing to the fact that the α' phase forms progressively with strain, the α' formed at one level of strain is formed into a very different environment compared to α' formed at another level of strain.

59

For instance, the first α' forms into austenite having a much lower density of dislocations compared to the α' formed at larger strain.

Spencer has highlighted the composite nature of the material, as well as the influence of stress and strain partitioning between the two phases on kinematic hardening [72]. In this work, the role of the transformation strain, i.e. the shape change associated with transforming austenite to α' (and ϵ) martensite, was noted as:

$$d\epsilon_{applied} = d\left(\epsilon^{\gamma\to\epsilon}f_\epsilon\right) + d\left(\epsilon^{\gamma\to\alpha'}f_{\alpha'}\right) + (1 - f_{\alpha'})d\epsilon^{\gamma+\epsilon} + f_{\alpha'}d\epsilon^{\alpha'} \quad (2.26)$$

where $\epsilon^{\gamma\to\epsilon}$ and $\epsilon^{\gamma\to\alpha'}$ correspond to the transformation strains associated with the transformation from austenite to ϵ and α'-martensite respectively. The terms f_i represent the volume fraction of the various phases ($i = \alpha', \epsilon, \gamma$). Finally, the strain associated with deformation in the austenite and ϵ-martensite are considered together ($\epsilon^{\gamma+\epsilon}$). If the rate of transformation is very high, then it was argued that the first two terms could dominate leading to a very low work-hardening rate. In this case, it has been argued that the transformation strain could explain the observation of Lüders like behaviour described above [72].

An equal strain assumption for the plastic response of the austenite and α' phase was made leading the net work-hardening rate:

$$\frac{\partial \sigma}{\partial \epsilon} = f_{\alpha'}\frac{\partial \sigma_{\alpha'}}{\partial \epsilon} + (1 - f_{\alpha'})\frac{\partial \sigma_\gamma}{\partial \epsilon} + \frac{\partial f_{\alpha'}}{\partial \epsilon}(\sigma_{\alpha'} - \sigma_\gamma) \quad (2.27)$$

One of the important points arising from this equation is that it highlights the role of the rate of phase transformation $df_{\alpha'}/d\epsilon$ on the work-hardening rate.

In summary, many mechanics based models have been proposed to explain the mechanical response of austenitic stainless steels. These generally are capable of incorporating the effects of stress state, but have a weak physical basis when it comes to the constitutive laws of each phase, especially in terms of linkage to actual microstructures. Moreover, many of these models are based upon purely isotropic models despite experimental measurements

that show large internal stresses. On the other hand, more physical models have been developed, which capture important microstructural aspects of the TRIP effect. One issue is that those are not easy to couple with the mechanical models mentioned above. What is missing is a way to describe simply the dependence of the mechanical properties of the composite towards simple variables such as temperature, strain rate, grain size and strain path. This approach already exists - with degrees of accuracy subject to discussion - in some kinetics models (e.g. O-C, Stringfellow, Iwamoto-Tsuta) but is almost non-existent in a unified theory of work-hardening in this class of dynamic materials.

2.6   Summary of the Literature Review

This review has highlighted the link between microscopic deformation mechanisms, strain-induced phase transformations and the macroscopic response of metastable austenitic stainless steels. The low stability of austenite with respect to ϵ and α' martensites means that both phase transformations are often observed during straining. There is substantial evidence suggesting that the microscopic mechanisms of plasticity are directly linked to both the ϵ and α' transformations. The exact way in which these two phase transformations are linked to the plastic deformation of the material is, however, still open for debate. At the microscopic scale, the link between starting microstructure and the strain-induced transformations is still poorly understood. For instance, as far as grain size is concerned, the conflicting trends which have been reported from experiments have generally confused attempts to provide physically-based models.

With respect to the bulk mechanical response, there have been a large number of experiments performed to examine the effect of strain path, stress state as well as the influence of microstructure. However, these experiments are, again, often at odds with one another. This is directly linked to the uncertainty regarding the material behaviour at the microscopic scale. These discrepancies impact on the ability to develop physically based models for the plastic response of the material, though recent experiments aimed at identifying the mechanical response of the austenite and martensite individually appear to be promising for developing new understanding.

Chapter 3

Scope and Objectives

In the previous chapter, the complex mechanical response of austenitic stainless steels was highlighted. In particular, this review has pointed to several aspects that remain poorly understood. In some cases there is a general lack of literature, in other areas the existing literature is contradictory.

This project has aimed to study both the macroscopic mechanical response and the microstructural response of a particular industrially supplied grade of metastable austenitic stainless steel (AISI 301LN). The deformation considered in this work was carried out at low homologous temperature and at low strain rates along monotonic strain paths. Within this study, two primary variables have been investigated. First, the grain size of the material has been varied over almost two orders of magnitude. As noted in the literature review, grain size affects both the strain-induced phase transformations as well as the intrinsic mechanical response of austenite. To date, there is little systematic work in the literature that has investigated this relationship. The second parameter that has been varied in this study is the mode of deformation. Mechanical testing has been performed in both uniaxial tension as well as in simple shear at various grain sizes in order to help establish the strain path dependence of the mechanical response. Tension and shear have been chosen for this study due to the fact that both strain paths can be achieved uniformly in a relatively simple experimental route on sheet samples. Materials tested under these conditions have been characterized using electron microscopy, X-ray diffraction and magnetic measurements to deduce the strain-induced evolution of the microstructure.

This project fits within a larger framework organized by the stainless steel manufacturer ArcelorMittal, whose aim is to develop models for the phase transformations and mechanical properties of these stainless steels.

Related to the project carried out here, a second study [14] at **École des Mines de Paris** has studied the same material but has focused on the influence of temperature and strain rate on the mechanical response of the same grade.

Based on the results of these experiments, and with reference to the literature, the main objective of this thesis has been to advance the state-of-the-art in physically based modelling of the mechanical response of these materials. In particular, this requires the incorporation of grain size and strain path effects on (i) the evolution of the deformation microstructures, (ii) the nucleation of ϵ-martensite and α'-martensite, (iii) the kinetics of the phase transformations and (iiii) the stresses carried by individual phases. The modelling work detailed in chapter 8 has relied on previous formulations [204, 206], to which significant extensions were made to account for the experimental results obtained as a part of this work.

Chapter 4

Processing and Characterization of 301LN Sheet to Develop Grain Sizes in the Micrometer to Nanometer Range

4.1 Introduction

As a first step in the experimental program of this thesis, it was necessary to modify the microstructure of the as-received stainless steel sheet so as to obtain a range of grain sizes. These materials would then serve as the starting materials for experiments on the link between microstructure and mechanical properties in this alloy. There have been a number of recent studies describing routes for generating materials having a sub-micron grain size in austenitic stainless steels [181, 209, 210] by α'-**martensite reversion**. While the goal of this work is not to study the mechanisms for this strong grain size refinement, we have used a route similar to that in other studies. The reader with interest in the mechanisms of grain size refinement via martensite reversion is directed to recent literature [211–215].

This chapter begins by introducing the experimental procedures used to i) generate the microstructures for further testing, and ii) characterize these microstructures. Following this, the material received from ArcelorMittal Stainless Steel is described in terms of its chemistry and microstructure.

This is followed by a description of the thermo-mechanical processing routes used to achieve different grain sizes. The microstructures of the as-processed materials are described with a particular emphasis on the grain size distribution. Finally, the presence of secondary phases and solute segregation in the processed microstructures are examined.

4.2 Experimental Methodology: Materials Characterization

4.2.1 Quantification of α'-Martensite Content via Feritscope Measurements

In this work, a Feritscope MP30E (*Fischer*) was used to determine the volume fraction of α'-martensite. The Feritscope is a commercially available device that has been developed for the non-destructive measurement of the ferrite content in austenitic and duplex steels in the range of 0.1 to 80% α-Fe [216]. This probe has been used extensively in the past for measuring the fraction of α'-martensite in austenitic stainless steels (see e.g. the review in reference [61]). The principle of measurement used by the Feritscope is illustrated schematically in Figure 4.1.
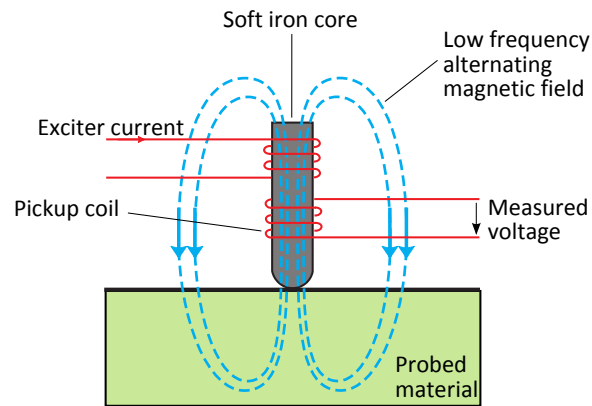
Figure 4.1: Schematic of the magnetic induction measurement performed by a Feritscope.

A low frequency alternating magnetic field is generated by a coil surrounding the soft iron core of the probe. A second 'pickup' coil has an induced current due to the field generated by the first coil. When the probe is brought into contact with a ferromagnetic sample, the magnetic field is modified resulting in a change in induced current in the 'pickup' coil. The resulting change in voltage across the pickup coil is proportional to the ferromagnetic content of the sample. In the case of austenitic stainless steels, both the austenite and ϵ-martensite are paramagnetic, meaning that only ferromagnetic α' martensite contributes to the resulting signal. To obtain a quantitative measure of the volume fraction of α'-martensite, the voltage change needs to be calibrated against standards of known α' martensite contents. Because the magnetic permeability depends upon chemical composition (especially carbon content, e.g. [217, 218]), it is important to prepare calibration standards from the specific material under study. In this work, a set of calibration standards were prepared from the 301LN alloy, by pre-deforming samples then quantifying the α' martensite content by X-ray diffraction. This calibration method, including the preparation of the calibration standards, is detailed in Appendix A.

Correction curves describing the effect of the specimen thickness and proximity to the sample edge are provided by the manufacturer [216]. These corrections are not necessary for samples thicker than 0.6 mm and as long as the probe is placed no closer than 5 mm from the edge of the sample. The geometry of all the samples used in this study was chosen with these dimensions in mind, so that these effects would be negligible. Feritscope readings were made with the probe in contact with the specimen, perpendicular to its surface. Measurements were made with samples in the unloaded state so as to avoid the influence of stress on the magnetic susceptibility (the so-called Villari effect, or magnetomechanical effect [219, 220]). A detailed evaluation of the magnetomechanical effect will be described in chapter 7.

4.2.2   Materials Characterization by Electron Microscopy

Samples for scanning electron microscopy (SEM) and back-scattered electrons (BSE) observation were first prepared by mechanical polishing with SiC emery paper to 1200 grit followed by polishing using 6 μm and 1 μm diamond paste. Electropolishing was next performed using a solution of 90 vol.% acetic acid and 10 vol.% perchloric acid at room temperature. This solution was found to give good results when electropolishing was performed at room temperature with a current density of ~ 50 mA/cm^2. Water cooling was used to ensure that the temperature of the electropolishing solution did not exceed 25°C. After electropolishing, the specimen was first cleaned with distilled water to remove residues of acetic/perchloric acid, then with denatured alcohol, before being dried by a flow of compressed air.

To ensure that the mechanical preparation did not induce deformation-induced martensite on the sample surface, back-scattered electron contrast in the SEM was used to ensure the absence of α'-martensite on the polished surface of as-recrystallized (fully austenitic) samples. It was found that short polishing times (2 minutes) were sufficient to remove the deformed layer induced by mechanical polishing in small grain size samples, while longer electropolishing times (6 minutes) were required in coarse grain sized samples.

Two scanning electron microscopes were used in this study, depending on the spatial resolution required. The first one was a tungsten-filament Hitachi S-570. Higher resolution imaging was achieved with a JEOL JSM-7000F SEM equipped with a Field Emission Gun (FEG). Imaging by back-scattered and forescattered electron detectors was used as a technique for illustrating the microstructure. For quantitative measurements of micro-texture, electron back-scattered diffraction (EBSD) systems were attached to each of the SEMs used. In the lower resolution Hitachi microscope, an *HKL Channel5 Flamenco* acquisition system was used providing a spatial resolution of ~ 1 μm, whereas the JEOL FEG SEM was equipped with an *Oxford INCA Crystal* acquisition system. For data collected from both microscopes and EBSD systems, data post-processing was conducted using

HKL Channel5 software (*Oxford Instruments*).

The EBSD acquisition allows for indexing of different phases based on their crystal structure. While in later chapters multiple phases will be indexed, here only austenite was considered during acquisition. The as-measured EBSD maps were cleaned by first performing a **wild spike** removal. This process changes isolated pixels that are misoriented by more than 6–7° from their eight neighbours to being non-indexed. Following this, **noise reduction** was applied to remove non-indexed points. This cleaning consists of attributing to a non-indexed pixel an orientation calculated from the mean orientation of the neighbouring points. Noise reduction was performed until no non-indexed points remained. Great care was exercised to ensure that no artifacts were created during this cleaning procedure.

In order to visualize the results, band contrast maps were used. Band contrast is a measure of the quality of the Kikuchi pattern recorded by the EBSD acquisition system at each point of measurement [221]. This band contrast is sensitive to defects, e.g. grain boundaries which tend to give low band contrast [106], as well as to crystallographic orientation of the grain. Also plotted, are the position of grain boundaries. These boundaries are calculated based on a misorientation of more than 2° between adjacent EBSD points.

Energy dispersive spectroscopy (EDS) and wavelength dispersive spectroscopy (WDS) were performed in order to estimate the heterogeneity in chemical composition. The chemical analysis was only qualitative. It was carried out in the FEG-SEM described above, using a Si (Li) detector with a super atmospheric supporting thin window (SATW) (*Oxford Instruments*). EDS maps, with dimension 512×430, were acquired with the software *INCA Energy*. The acquisition was run for 170 minutes with a step size of ~ 0.1 µm.

In order to investigate the role of other phases in the recrystallized microstructures, thin foils for transmission electron microscopy were prepared by mechanical polishing using 600 and 1200 grit emery paper to a thickness of 100 µm. Circular samples were subsequently punched from the sheet and jet-polished using a Struers Tenupol 2. The polishing solution used was the

same as that described above, i.e. a solution of 10 vol.% percholoric acid and 90 vol.% acetic acid. The thinning was performed at room temperature, under an imposed voltage of 9 V corresponding to a current of ~ 0.1 A. The thin foils were subsequently examined in a Hitachi H-800 Transmission Electron Microscope (TEM) operating at 200 kV.

4.3 Experimental Methodology: Materials Processing

4.3.1 Cold Rolling of As-Received Sheet

In section 2.3, it was shown that temperature and strain rate have an important effect on the rate of martensite formation. Therefore, a preliminary study was done to determine the relationship between rolling conditions (temperature and strain rate) and α'-martensite volume fraction, the latter being monitored by the Feritscope. This preliminary study is important since the deformation-induced martensite formed during rolling affects the grain size after annealing [178, 181, 209, 222, 223]. Conventional rolling was performed on a laboratory mill (*Stanat*, model TA-215) equipped with 105 mm diameter rolls. Two different schedules were followed for rolling the materials. Room temperature rolling ("RT-rolling") was performed using kerosene as a lubricant. Rolling was also performed with no lubrication on material that was cooled to $-196°$C in a liquid nitrogen bath prior to each pass. This processing route will be denominated as "cryorolling" in the following. For most experiments, samples having initial dimension of ~ 150 mm $\times$ 50 mm $\times$ 2.1 mm were used. Rolling was always performed parallel to the industrial rolling direction of the sheet.

Figure 4.2 shows that higher amounts of α'-martensite can be obtained by cryorolling. Also, the α'-martensite content formed during RT-rolling was lowered with the angular speed of the rolls (an effect due to higher sample heating at high velocities). This effect was not observed during cryorolling. In order to achieve the widest range of grain sizes upon annealing, both RT-rolling and cryorolling were used with an angular speed of 51.4 rpm to

a total reduction of 62% (from 2.1 mm to 0.8 mm thickness). This was accomplished in 15 passes for the RT-rolled material and in 30 passes for the cryorolled material. In both cases the largest reduction per pass possible was attempted.
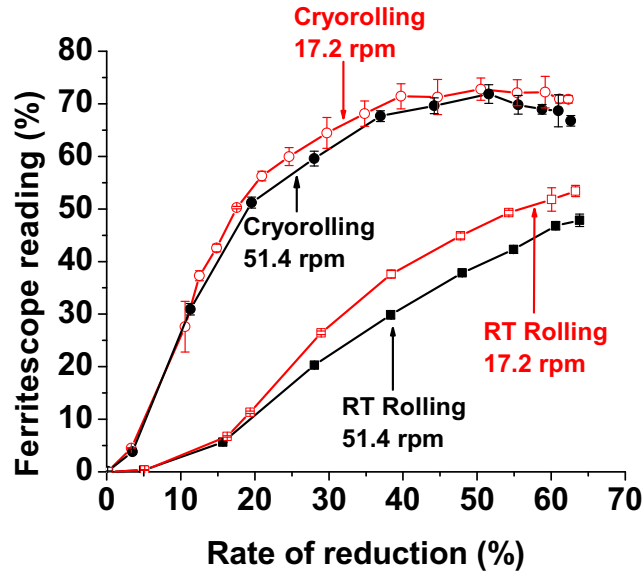
Figure 4.2: Magnetic signal measured by Feritscope during RT-rolling and cryorolling, for two angular rotations. The Feritscope signal is proportional to the volume fraction of α'-martensite, as described in Appendix A.

4.3.2 Post-Rolling Annealing Treatments

Rolled materials were isothermally annealed in a tube furnace under flowing argon. Two annealing times were chosen, namely 3 minutes and 30 minutes, and the annealing temperature was varied between 800°C and 1050°C. After the furnace temperature was stabilized at the desired temperature, the sample was manually inserted. The initial heating rate of the sample was measured to be 17°C.s^{-1} and the target temperature was reached in the sample after 70 seconds. After heat treatment, the samples were cooled in

air. A very thin chromium oxide layer formed on the sample surface and was removed by polishing.

4.4 As-Received Material

The work presented here was focused on an AISI 301LN austenitic stainless steel provided by the ArcelorMittal Stainless Steel Research Centre in Isbergues France. The nominal composition of this grade is given in Table 4.1. Low carbon and high nitrogen contents are also characteristics of this grade (hence the "LN" denomination).

Element	C	N	Cr	Ni	Mn	Si	Cu	Mo	Co
wt.%	0.022	0.107	17.33	6.62	1.77	0.53	0.24	0.21	0.14

Table 4.1: Nominal composition (in wt.%) of the grade used in this study.

The material was received as cold rolled and recrystallized sheets 2.1 mm thick. The state of surface was 2D, meaning that there has been no skin-pass operation after annealing and pickling. An EBSD map illustrating the microstructure of the as-received steel is presented in Figure 4.3. The material had a relatively uniform and equiaxed grain size $D = 10$ µm. A small amount of δ-ferrite (less than 1 vol.%) was found in the as-received material, similar to what had been previously reported for this grade [181].

4.5 Generation of Materials With Varying Grain Sizes

The first step in this thesis was to generate a range of grain sizes, the goal being to span as wide a range of sizes possible (from sub-micron to tens of microns). After a series of preliminary annealing experiments, a set of five annealing conditions were decided upon to generate materials having grain sizes ranging from 0.5 µm to 28 µm. These annealing conditions are given in Table 4.2.

Figure 4.3: Band contrast EBSD map of as-received 301LN, plotted to also reveal grain boundaries (misorientation > 2°, black lines). The map was acquired on the plane containing the rolling direction (RD) and normal direction (ND) of the sheet.

The grain sizes resulting from these five different thermo-mechanical processing routes were characterized by electron backscatter diffraction (EBSD). Although the as-measured maps were of high quality (more than 75% points indexed for the low-resolution EBSD system and more than 90% indexed for the high-resolution EBSD system), some cleaning of the data was required as described above. Representative EBSD band contrast maps including grain boundaries (black lines) from each of the conditions given in Table 4.2

Condition	Rolling procedure	% Reduction	Annealing temperature	Annealing time
A	Cryorolling	62% - 30 passes	800°C	3 minutes
B	Cryorolling	62% - 30 passes	850°C	3 minutes
C	Cryorolling	62% - 30 passes	950°C	3 minutes
D	Cryorolling	62% - 30 passes	1050°C	3 minutes
E	RT rolling	62% - 15 passes	1050°C	30 minutes

Table 4.2: Thermo-mechanical procedure used to generate the five conditions of grain size studied in this thesis.

are shown in Figure 4.4.

For each condition, the EBSD data was analyzed to determine the grain size. Grains were reconstructed from the EBSD data by grouping together touching measurement points having a misorientation of less than 2°. The size of each of these grains was quantified as its equivalent area diameter (EQAD), i.e. the diameter of a circle having an area equal to that of the measured grains. Grains in contact with the edge of the measurement frame were not considered for grain size estimation. In this grain reconstruction, any grains smaller than 3 pixels were discounted. The removal of these clusters was checked visually to ensure that they did not represent a realistic grain. The mean grain size, as well as other characteristics of the grain size distribution, measured in this way for these five conditions, is given in Table 4.3. To be consistent with industrial practice, two different assumptions were made regarding the inclusion of annealing twin boundaries in the grain size measurement. In a first measurement, any grains separated by annealing twins were combined so as to neglect the annealing twin boundary when calculating grain size (^{a} in Table 4.3). In the second method, annealing twins were considered as being equivalent to grain boundaries and thus used to define the grain size (^{b} in Table 4.3). For the purposes of this thesis, the latter definition of grain size is used.

The measured EQAD grain size distributions are illustrated in Figure 4.5. The distributions are observed to be well represented by log-normal distributions (straight lines in Figure 4.5 (a) to (e)) and appear to be self-similar when the grain size is normalized by the average grain size (Figure 4.5(f)).

While the number average grain size distributions presented above appear to give self-consistent results, Figure 4.4 (a) and to a lesser extent (b) give the impression of having a wide size distribution. Similar observations have been previously made on nanocrystalline austenitic stainless steels and have been linked to the nucleation of new grains in regions containing α'-martensite versus austenite [11, 139]. It is known that the number size distribution as plotted in Figure 4.5 tends to suppress the importance of a small number of large grains within a microstructure [224]. As an alternative

(a) Condition A

(b) Condition B

(c) Condition C

(d) Condition D

(e) Condition E

(f)
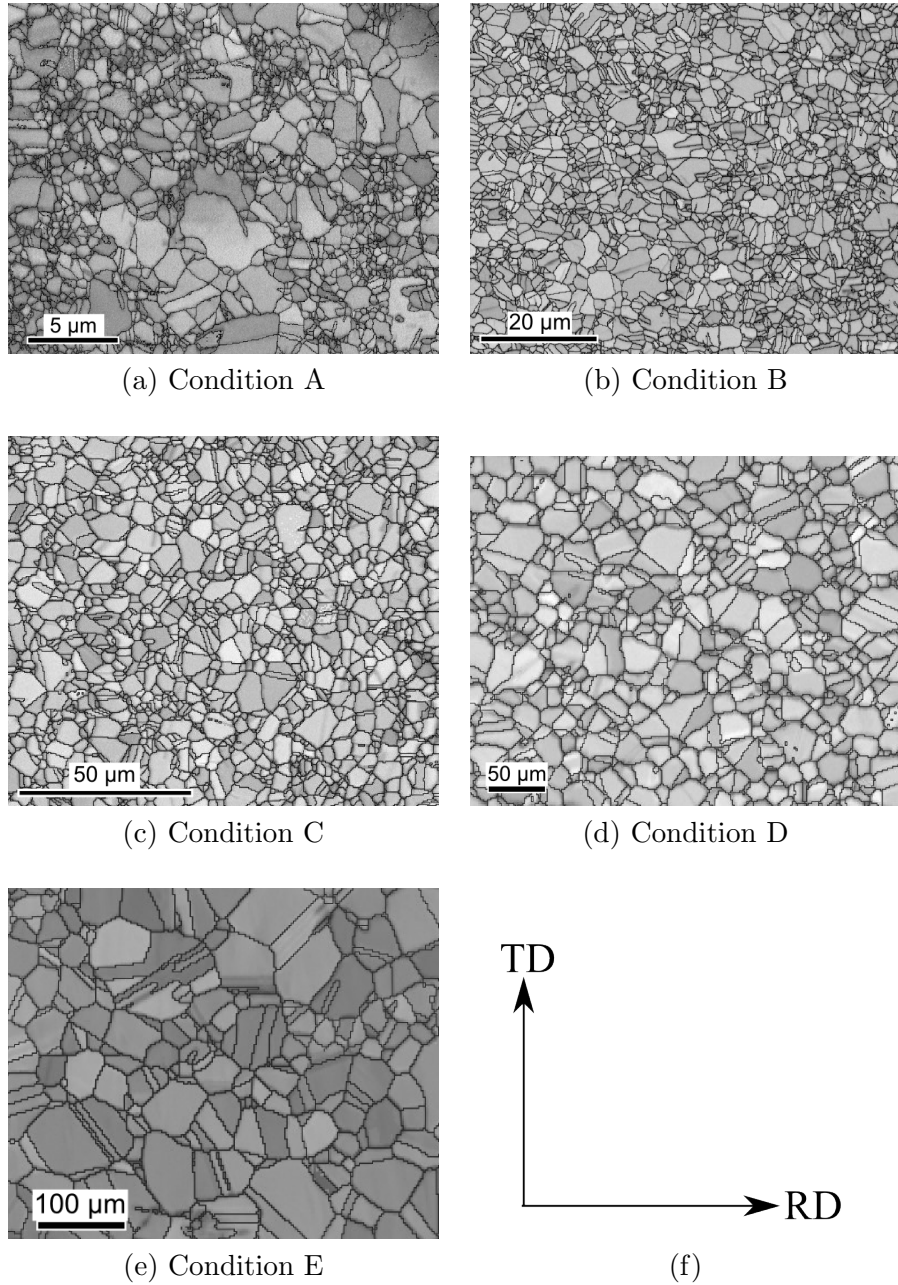
Figure 4.4: Band contrast EBSD maps including grain boundaries (misorientation $> 2°$, black lines). The conditions A – E correspond to the annealing conditions in Table 4.2. The average grain sizes from these samples are given in Table 4.3.

Condition	A	B	C	D	E
Step size	0.06 µm	0.12 µm	0.5 µm	1.5 µm	2.5 µm
Average grain size (^{a})	0.70 µm	1.4 µm	2.4 µm	19 µm	43 µm
$ASTM$ number (^{a})	17.8	15.6	13.6	11.2	6.0
Average grain size (^{b})	0.52 µm	0.91 µm	2.2 µm	14 µm	28 µm
$ASTM$ number (^{b})	18.6	14.7	13.7	9.0	7.7
Standard deviation of the distribution (^{b})	0.4 µm	0.7 µm	1.6 µm	8 µm	18 µm
Number of grains analyzed (^{b})	2 000	11 000	2 500	3 000	1 500
Proportion of twin boundaries	20%	30%	15%	30%	38%

Table 4.3: Description of the five grain size distributions, characterized by EBSD. The average grain sizes and $ASTM$ numbers are given both (^{a}) without and (^{b}) with twin boundaries. The $ASTM$ number was calculated as $ASTM = 3.322 \times \log(N_a) - 2.95$, N_a being the number of grains per mm^2. The proportion of twin boundaries as defined in this table is the ratio of twin boundaries over total amount of boundary (grain boundaries and twin boundaries).

to Figure 4.5, Figure 4.6 presents the distribution under the form of an area fraction. These histograms are normalized by the mean of the distribution to enable comparison of the widths, and clearly indicate that the widest distributions appear in both 0.5 µm and 0.9 µm conditions of grain size. It is also evident that the distributions, while wide, are not bimodal.
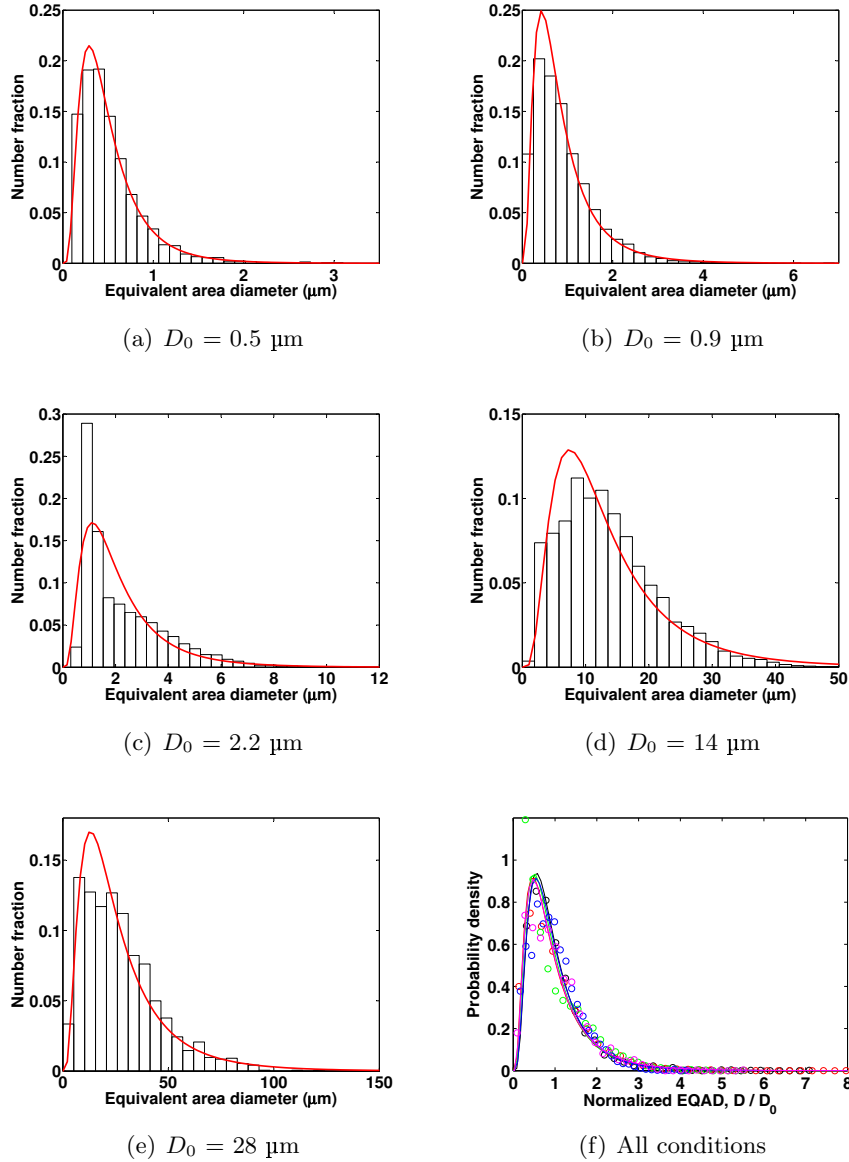
Figure 4.5: (a) to (e): Histograms of the grain size distributions in terms of number fraction, as a function of the equivalent area diameter (EQAD). (f) Superimposition of the five grain size distributions, represented as a function of the EQAD (D) normalized by the average of the distribution (D_0). The dots correspond to the classes represented by the histograms in (a) to (e).

(a) $D_0 = 0.5$ μm

(b) $D_0 = 0.9$ μm

(c) $D_0 = 2.2$ μm

(d) $D_0 = 14$ μm

(e) $D_0 = 28$ μm
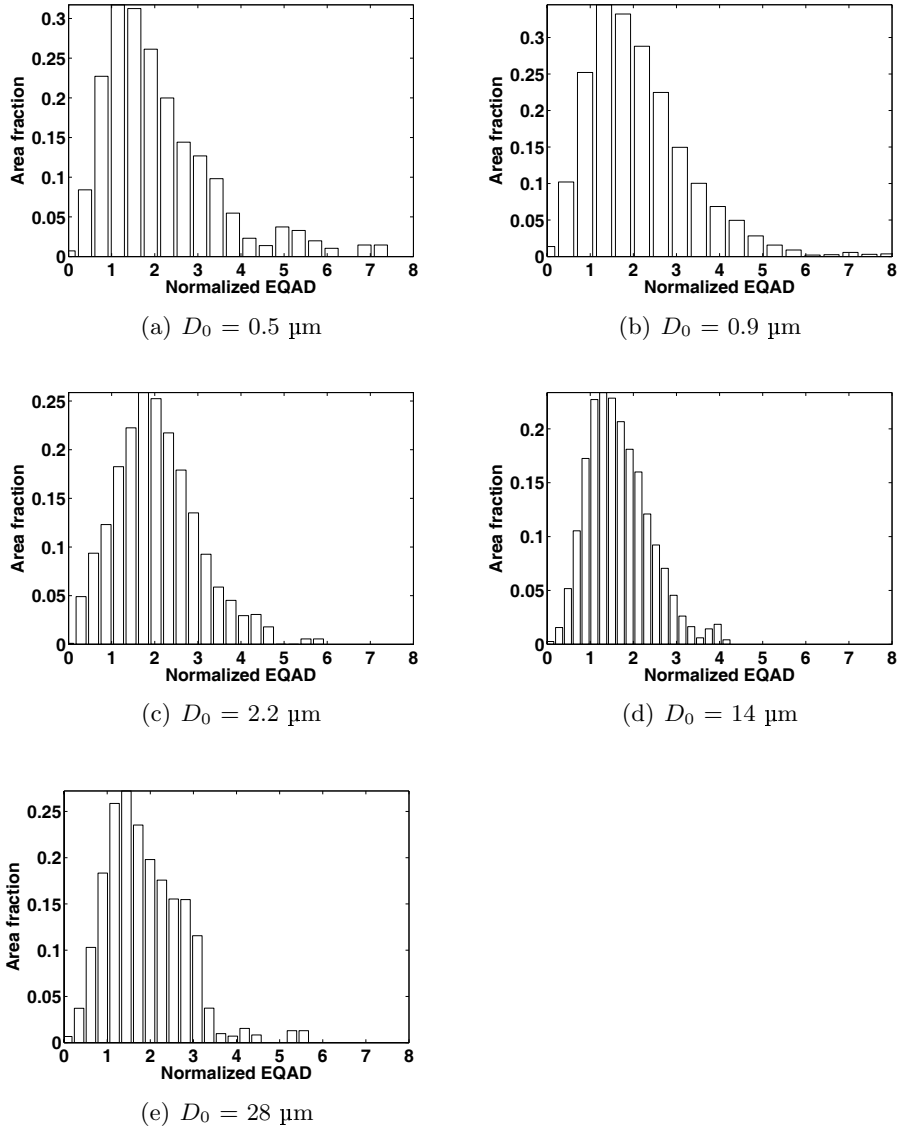
Figure 4.6: (a) to (e): Histograms of the grain size distributions in terms of area fraction, as a function of the normalized EQAD (D/D_0).

4.6 Presence of Other Phases in the Recrystallized Microstructures

While to this point, this thesis has focused on three phases, austenite, α'-martensite and ϵ-martensite, other phases may exist in 301LN, in the form of precipitates. Transmission electron microscopy analysis was made on the materials processed by the thermo-mechanical route described above. It was found (Figure 4.7) that nanometric second phase precipitates existed in the material annealed at 800°C, whereas these precipitates were not found in any of the other processed materials. This observation is consistent with that of Rajasekhara *et al.* [177] who, also in a 301LN stainless steel, identified these precipitates formed at low annealing temperatures as Cr_2N precipitates.

Figure 4.7: Bright field TEM image of a sample annealed for 3 minutes at 800°C resulting in a D=0.5 µm average grain size, illustrating the presence of chromium nitride precipitates. Such precipitates were not found in samples annealed at higher temperatures.

In normal practice, nitrides are not formed in the 300 series austenitic stainless steels, owing to the high solubility of nitrogen [21, 225]. However, 800°C is much lower than the temperatures normally used for the processing of these grades. In the work of Rajasekhara *et al.* [177], it was estimated that the amount of nitrogen contained in nitrides was 0.01 wt.% after annealing at 800°C.

4.7 Solute Segregation

Given the importance of alloying elements like nickel and nitrogen in determining the stability of austenite, and therefore the mechanical response of the material studied, it was attempted to quantify the chemical homogeneity of the material studied. In this case, materials having been processed via route A above (800°C, 3 minutes) were subjected to energy dispersive spectroscopy (EDS) and wavelength dispersive spectroscopy (WDS) analyses in the SEM. These analyses were performed on the plane containing the rolling and normal directions of the sheet. Given the low annealing temperature and the short annealing time, it is believed that this sample would represent the segregation pattern exhibited by the as-received material. EDS analysis of alloying elements Cr, Mn, Si did not reveal any specific pattern of segregation on the scale of the sample thickness. Higher sensitivity to chemical heterogeneities was achieved using WDS on detection of chromium and nitrogen, and confirmed the absence of heterogeneities. However, EDS analysis of nickel did indicate segregation as bands parallel to the rolling direction as illustrated in Figure 4.8. The intensity ratio characteristic of the Ni $K\alpha_1$ electronic transition could vary by 25% from within the segregation bands to oustide the bands. Once related to the nominal nickel content, this intensity ratio enables rough quantification of the nickel within the segregation. The level of nickel could thus vary by $\pm$ 1.3 wt.% around its average value (6.62 wt.%). It was found, that this segregation pattern could be seen in backscatter electron (BSE) images in the SEM. Figure 4.8 shows that the regions of segregation appear brighter than the surroundings. It is, finally, worth noting that the spacing of the segregation bands is on the order of 0.5 μm. This spacing is similar to the average grain size in the finest-grained material, indicating that the effect of segregation may lead to more heterogeneous behaviour in these microstructures. In larger grain size materials, all grains should be expected to contain regions of high and low nickel content.
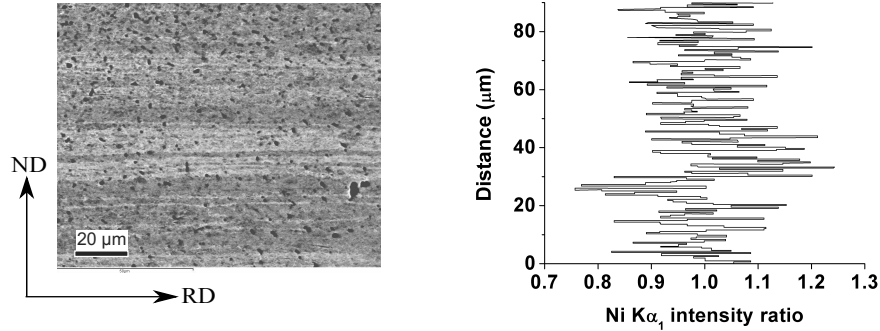
Figure 4.8: The segregation of nickel as seen with back-scattered electrons imaging in the SEM. The correspondence between the lighter coloured bands and regions of nickel enrichment can be seen when compared to the EDS line scan.

4.8 Summary

In this chapter, the preliminary processing of the as-received material has been described. It has been found that materials having mean grain sizes between 0.5 µm and 28 µm could be formed by a combination of conventional rolling and annealing. These results are in good agreement with previous work on the recrystallization behaviour of the same alloy [181]. It has been shown that, while the grain size distribution appears self-similar, and consistent with a log-normal distribution, there are deviations at the smallest grain sizes associated with the presence of some larger grains in the microstructure. Also, it has been shown that in the material with smallest grain size, chromium nitride precipitates are present and that segregation on the scale of the grain size exists. These factors will be returned to when the deformation microstructures of this material are discussed.

Chapter 5

Macroscopic Characterization of the Mechanical Properties and Phase Fraction

5.1 Introduction

In this chapter, the macroscopic mechanical behaviour of the alloy (grade 301LN) is described. In particular, the behaviour in uniaxial tension and simple shear will be compared for samples having the grain size range described in the previous chapter. These mechanical properties are, in turn, related to the evolution of the average content of ϵ and α'-martensites measured using the Feritscope described in the previous chapter.

5.2 Experimental Methods

5.2.1 Uniaxial Tensile Testing

Tensile coupons were machined by electro-discharge machining, prior to annealing. The geometry of the tensile coupons (Figure 5.1) is different from the ASTM [7] standard [226]. It was found that, for the standard geometry, the high rate of work-hardening of the material resulted in plasticity spreading from the gauge section into the head of the sample. The sample was therefore re-designed to ensure that at maximum force, the stress in the grip

---

[7] the American Society for Testing and Materials.

section (head) was lower than the yield stress of the material in the largest grain size condition.
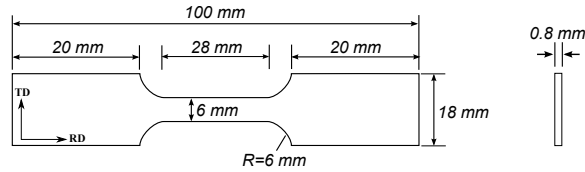
Figure 5.1: Geometry of the flat tensile test coupons used in this study.

Room-temperature tensile tests were conducted in displacement control using a computer-controlled servohydraulic load frame. The tensile axis was always parallel to the rolling direction. Strains were measured with an axial extensometer of 12.5 mm gage length. The rate of data acquisition was 2 points per second.

As noted in section 2.3, the strain rate sensitivity of austenitic stainless steels can be high, particularly when the rate of phase transformation results in large heating of the sample. Therefore care was taken in the selection of strain rate such that the temperature rise in the sample was not significant. After different trials, it was found that a cross-head speed of 0.04 mm.s^{-1} was adequate for this purpose. Considering the geometry of the coupons, this corresponds to a nominal strain rate of 1.4×10^{-3} s^{-1}. The temperature rise in the specimen was monitored on test samples having a K-type thermocouple welded in the center of the gauge section. It was observed that the temperature increased with strain, but that the temperature change never exceeded 10°C. Tests were also performed at lower strain rates (down to 4×10^{-5} s^{-1}) and it was found that the stress-strain response of the material was not significantly different from that of the sample tested at 1.4×10^{-3} s^{-1}.

Uniaxial tension was also performed at 80°C. These tests were conducted in a small (5 kN capacity) screw-driven Instron load frame where the sample could be fully immersed in a constant temperature bath. For these tests, a stirred bath of water heated with a hot plate was used and the temperature was monitored with a thermometer. The geometry of the samples was the

same as those for room temperature testing (Figure 5.1) as was the imposed displacement rate. Because classical extensometers could not be used at this elevated temperature, displacement of cross-head was used to calculate strain in the sample, a correction being made for the machine stiffness. The stiffness correction was performed so as to ensure consistency of the elastic modulus of the samples.

5.2.2 Testing in Simple Shear

Simple shear was performed at the **3S-R laboratory, Institut National Polytechnique de Grenoble, France**, the setup being illustrated in Figure 5.2. A detailed description of this testing setup can be found elsewhere (cf. [227–230]).

1	sample
2	fixed grip
3	movable grip
4	upper frame part
5	lower frame part
6	LVDT
7	load frame
8	frame
9	computer
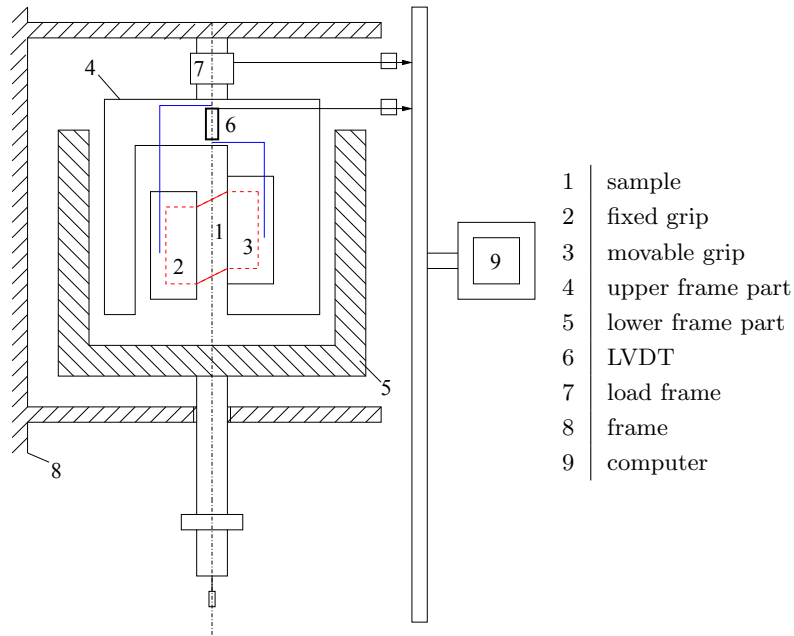
Figure 5.2: Schematic overview of the shear testing apparatus.

The test coupons for shear were rectangular (25 mm × 18 mm × 0.8 mm) with a 3 mm-large gauge area, as illustrated in Figure 5.3. The displacement of one side of the coupon relative to the other was monitored by

a Linear Variable Differential Transformer (LVDT), and used to calculate shear strains.

(a) Before deformation
(b) After deformation
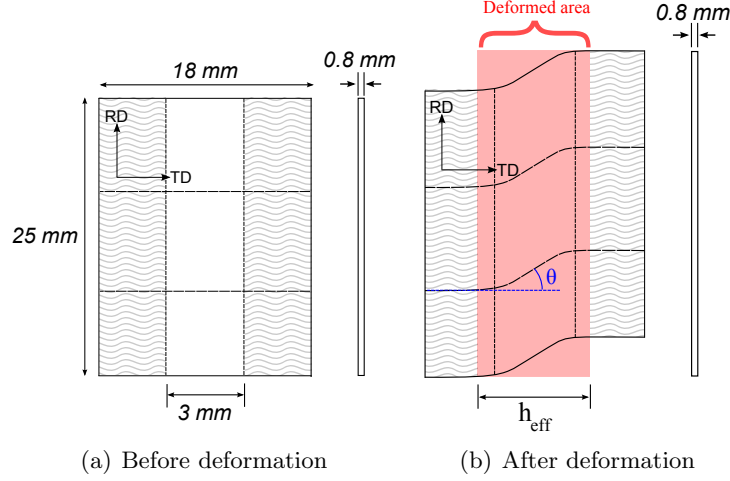
Figure 5.3: Geometry of the flat shear test coupons used in this study. The shear angle is defined by θ. While the distance out of the grips is set to be 3 mm, the deformation actually occurs on a larger width represented by h_{eff}.

It is known that this testing procedure results in shear strains that are not fully homogeneous across the width of the gauge area. Thus, a correction to the width of the deformed region of the sample is conventionally used [229]. This correction uses the shear angle measured from fiducial lines inscribed on the sample (θ in Figure 5.3 (b)), after unloading of the coupon. In this case the fiducial lines were made using a fine point marker. The final shear strain (γ) was calculated from θ according to:

$$\gamma = \frac{1}{2}\tan\theta \tag{5.1}$$

This correction was found to reproduce the shear strains measured on other samples using digital image correlation in previous work [229] as well as in samples of austenitic stainless steel observed in this thesis. The shear tests were performed with the direction of the shear parallel to the rolling direction, at a cross-head speed of 3×10^{-3} mm.s^{-1}, which after correction

corresponds to $\dot{\gamma} \approx 2.9 \times 10^{-4}$ s^{-1}. In order to compare to uniaxial tension, it can be useful to express this strain rate using the Von Mises equivalent strain. This equivalent strain rate is $\dot{\bar{\epsilon}} \approx 3.3 \times 10^{-4}$ s^{-1}, which is 4 times smaller than the one imposed in tension.

5.2.3   Phase Quantification by X-Ray Diffraction

In order to complement the Feritscope measurements presented in section 4.2.1 for the quantification of α'-martensite, and to estimate the amount of ϵ-martensite, X-ray diffraction spectra were analysed by means of Rietvieldt refinement (see [63, 64]).

For tensile samples, a Bruker D8 advance diffractomer equipped with the Cu K$_\alpha$ radiation was used. The acquisition of the diffraction spectra is documented in reference [139].

For shear samples, a PANalytical X'Pert PRO goniometer was used with a monochromatic Co K$_\alpha$ radiation. The diffractometer operated under a voltage of 45 kV and an intensity of 35 mA. A 1 mm beam size was used with a step of 0.033°/s. Samples were carefully positioned so that only the uniformly strained portion of the sample was analysed. In order to reduce the effect of crystallographic texture, the coupons were placed on a rotating sample holder and scans were summed up for different radial angles χ. Twelve scans were performed for χ varying from 0° to 55° (by steps of 5°) and the sum of these scans was considered. The Rietveld analysis was performed with X'Pert software. The corresponding space groups were imposed for the three phases: γ-austenite, α'-martensite and ϵ-martensite. Both the volume fractions and the lattice parameters (Table 5.1) were used as fitting parameters in the refinement. It was ensured that, at the end of the refinement, the converged values of the lattice parameters were reasonable.

Lattice parameter	γ	α'	ϵ
a	3.61 Å	2.86 Å	2.54 Å
c	-	-	4.16 Å

Table 5.1: Initial values of the lattice parameters used in the Rietveld analysis. Those were taken from the X-ray diffraction work of Pétein [139].

5.3 Mechanical Properties of 301LN in Uniaxial Tension

The tensile response of 301LN at room temperature is shown in Figure 5.4. While this figure shows only one curve per condition, a minimum of two tensile tests were performed up to failure to confirm reproducibility, and many other tests, performed to variable levels of strain, justify the confidence in these measurements. The stress-strain curves in Figure 5.4 have been stopped after the onset of necking, the onset of necking corresponding well to the Considère criterion. This is despite the fact that the phase transformation causes volume to not be conserved during the test.

Several of the characteristics of the material in tension are given in Table 5.2. The variation of 0.2% offset yield stress with grain size (including twin boundaries) obeys a Hall-Petch relation ($\sigma = \sigma_0 + k_y D^{-1/2}$) with a friction stress of σ_0=230 MPa and a Hall-Petch slope of k_y=312 MPa.µm$^{-1/2}$. Discontinuous yielding was observed for grain sizes in the range of 2.2 µm to 28 µm. This is consistent with previous observations on the yielding behaviour for similar grain sizes in grades 304 and 316 [187]. The discontinuous yielding in these steels has previously been attributed to a low initial number of mobile dislocations per grain, leading to a high yield stress associated with the nucleation of dislocations from grain boundaries [187].
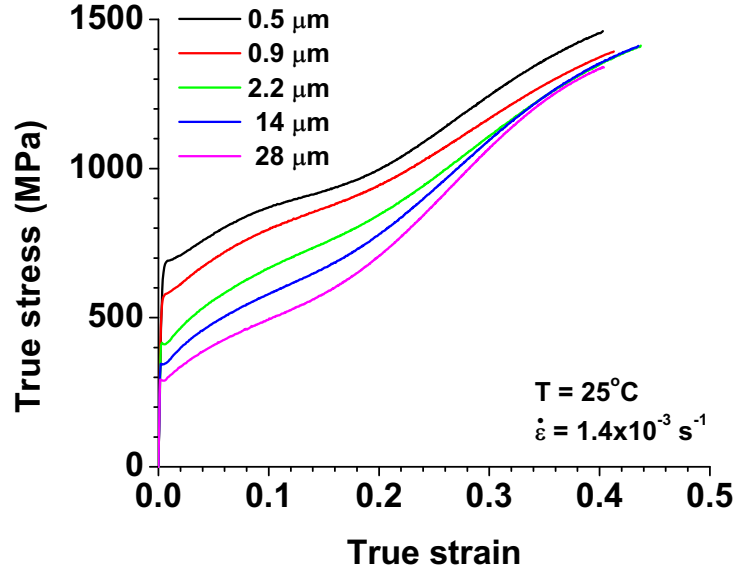
Figure 5.4: Stress-strain curves obtained in uniaxial tension at room temperature.

Average grain size	Yield stress	True stress at necking	True strain at necking
D=0.5 µm	676 MPa	1460 MPa	0.403
D=0.9 µm	593 MPa	1393 MPa	0.413
D=2.2 µm	409 MPa	1412 MPa	0.437
D=14 µm	334 MPa	1411 MPa	0.435
D=28 µm	280 MPa	1339 MPa	0.404

Table 5.2: Tensile characteristics of the five grain size conditions.

In contrast to the yield strength, the ultimate tensile strength and uniform elongation were not found to vary strongly for grain sizes between 0.5 µm to 28 µm. The fact that, unlike yield stress, the tensile strength has a weak grain size dependence suggests that the hardening behaviour of the
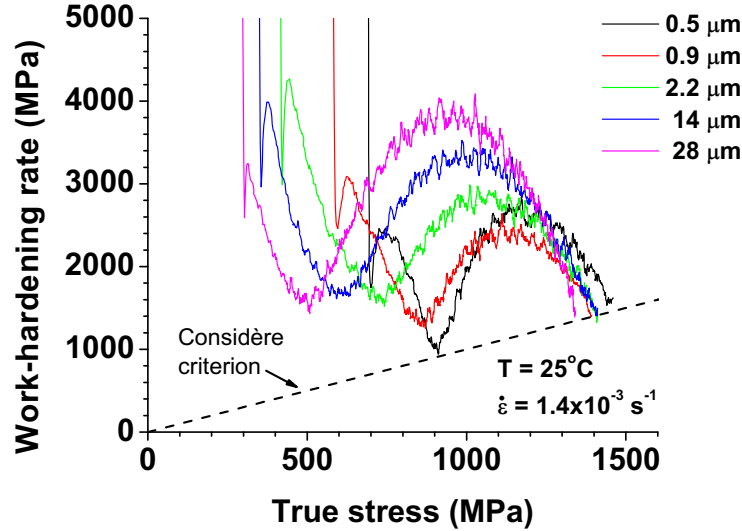
Figure 5.5: Work-hardening curves obtained under uniaxial tension. The onset of plastic instability (Considère criterion) is represented by the dashed line.

material is strongly grain size dependent, with the larger grain size having the higher hardening rate. This is indeed observed in the work-hardening curves, presented in Figure 5.5, these having been obtained by numerical differentiation of the stress-strain curves. In all but the D=0.5 μm condition, an increase in austenitic grain size corresponds to a higher maximum rate of work-hardening. The maximum rate of work-hardening are in good agreement with those measured by Talonen also on a 301LN alloy under similar conditions of temperature and strain rate [150].

The work of Nanga [146, 186] on a similar steel grade showed that very little α'-martensite was formed in tension at a temperature of 80°C. Therefore, in order to collect information on the behaviour of austenite with little or no formation of α'-martensite, tensile tests were carried out at 80°C (Figure 5.6).
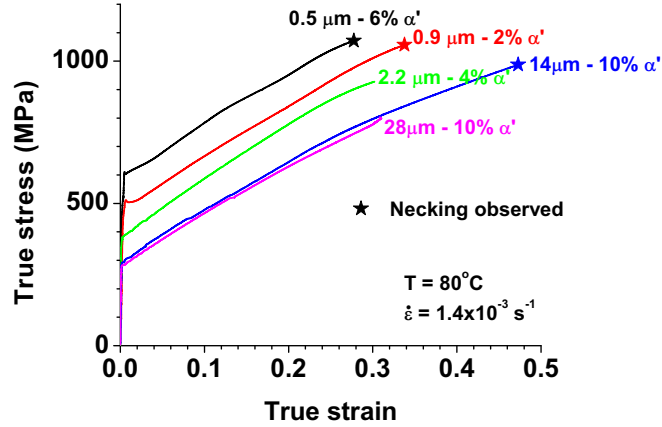
Figure 5.6: Stress-strain response of grade 301LN under uniaxial tension at 80°C. The tensile tests were not conducted to failure. The maximum fraction of α' formed during uniform deformation of the sample is indicated as determined from Feritscope measurements.
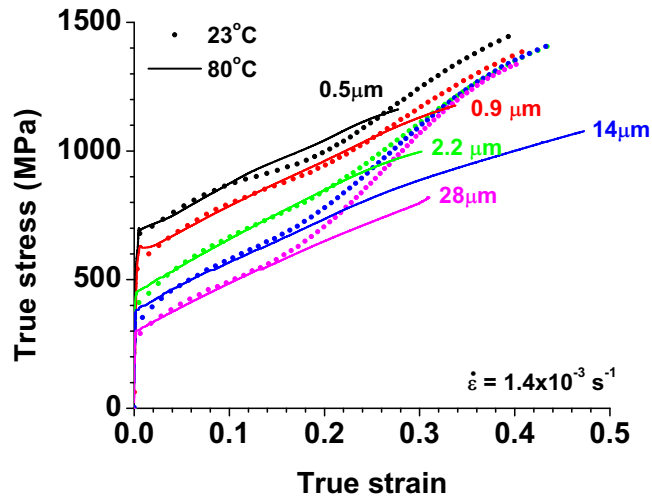
Figure 5.7: Comparison of the tensile tests performed at 23°C (from Figure 5.4) and at 80°C (from Figure 5.6). In the latter, the yield stress was corrected to be at the same level as that measured at 23°C.

In order to compare these elevated temperature tests with those performed at room temperature, it is necessary to correct for the temperature-dependence of the yield stress. The comparison is shown in Figure 5.7, for which the yield stresses obtained at 80°C were adjusted to match the yield stresses obtained at 23°C.

In the case of tensile tests performed at elevated temperature, the fraction of martensite formed outside of the neck was measured at the end of the test using a Feritscope. It can be seen that while some α'-martensite was formed during testing, the fraction formed is low. This is consistent with the mechanical response of these samples in that they appear qualitatively similar to the response obtained in stable austenitic grades.

An important feature of Figure 5.7 is that the grain size dependence of the work-hardening of austenite is low, i.e. all samples show similar hardening.

5.4 Mechanical Properties of 301LN in Simple Shear

The stress-strain response of 301LN in simple shear is presented in Figure 5.8 for three conditions of grain size. It was impossible, in this case, to observe the presence of discontinuous yielding. This may be due to the different characteristics of the load frames used in tension and shear testing. In these tests, the stress-strain curves plotted only up to the point where the strains remained relatively uniform within the gauge section.

In order to compare these deformation curves to those obtained in uniaxial tension, Von Mises equivalent strains and stresses were calculated according to:

$$\bar{\epsilon} = \frac{2}{\sqrt{3}}\gamma \tag{5.2}$$

$$\bar{\sigma} = \sqrt{3}\tau \tag{5.3}$$

These are plotted alongside the tensile results in Figure 5.9.
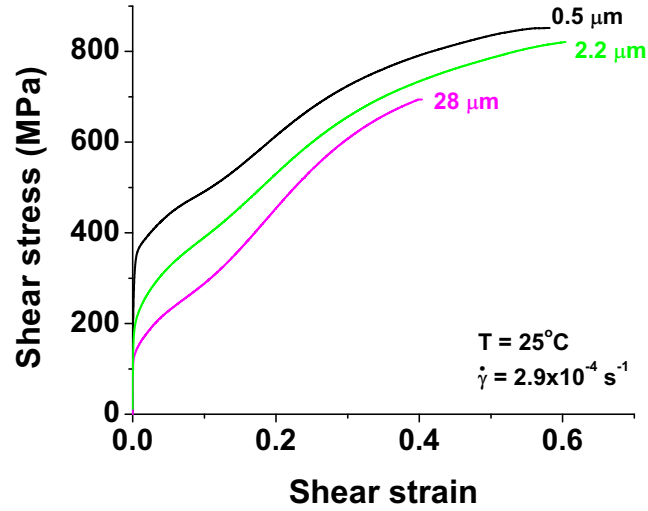
Figure 5.8: Stress-strain curves obtained under simple shear, at room-temperature.

Figures 5.9 and 5.10 show that, while at small to intermediate levels of strain the stress-strain responses are nearly equivalent in these two strain paths, at higher strains the work-hardening rates are higher in uniaxial tension than in simple shear. The divergence between the curves for a given grain size are observed at true strains between 0.2 to 0.25.

Figure 5.9: Comparison of the stress-strain curves from uniaxial tension and simple shear tests.
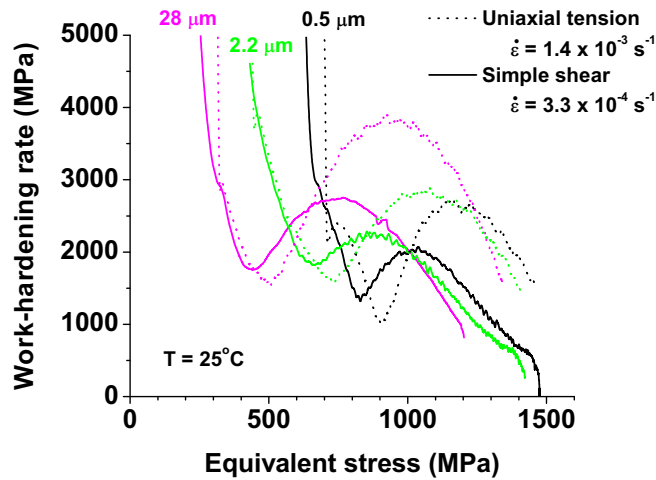
Figure 5.10: Comparison of the work-hardening curves from uniaxial tension and simple shear tests.

5.5 Quantification of the Volume Fractions of Strain-Induced Martensitic Phases

5.5.1 Quantification of ϵ martensite

Figure 5.11 shows the diffraction spectrum of the 0.5 µm grain size condition at various levels of strain, compared to the 28 µm grain size condition. These results are qualitatively similar to the results obtained in previous studies particularly with respect to the grain size dependence of ϵ-martensite formation with refinement of grain size [139]. No evidence of ϵ-martensite could be found for the smallest grain sized materials in this study. In coarse grained samples, the maximum volume fraction of ϵ-martensite also remained small, with a maximum of $2.4\% \pm 0.6\%$ observed for a true strain of 0.1.
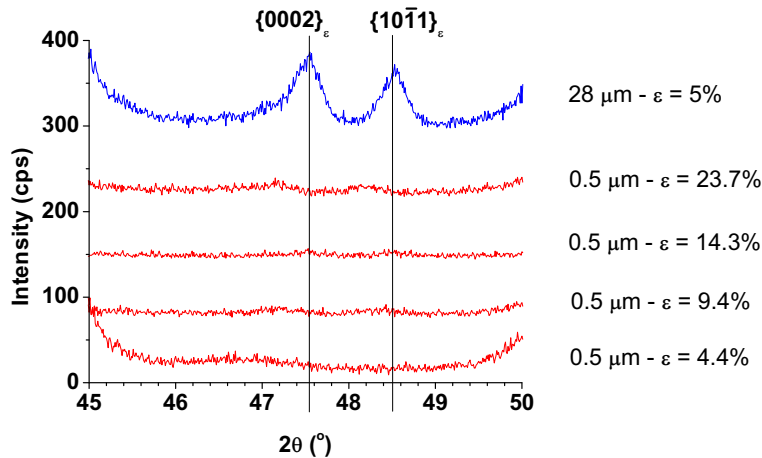
Figure 5.11: X-ray diffraction spectra representing the $\{0002\}_\epsilon$ and $\{10\bar{1}1\}_\epsilon$ peaks for four conditions of strain in the 0.5 µm condition. A comparison towards the 28 µm condition is presented.

5.5.2 Quantification of α' martensite

The evolution of α'-martensite was monitored by Feritscope, according to the protocol described in section 4.2.1. For room-temperature uniaxial ten-

sion, the tests were interrupted in increments of 0.03 true strain. Six measurements at different locations within the gauge length were performed in the unloaded state. The as-measured Feritscope numbers were then converted to volume fraction α'-martensite using the calibration in Appendix A. The average of these measurements appears in Figure 5.12, with the error bars representing the maximum and minimum of the Feritscope readings within the same sample. Each test was repeated twice and the variation in Feritscope readings were found to be smaller between two tests than between measurements within the same sample. The deviation between measurements increased with strain, being less than 0.1% at low strains and from 1% to 3% at high strains.
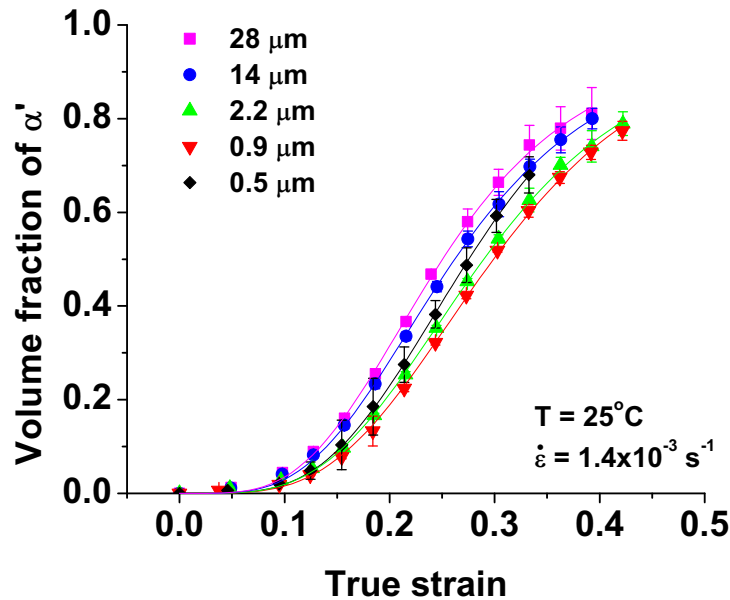
Figure 5.12: Evolution of the volume fraction of α'-martensite with strain determined by Feritscope measurements made after room-temperature uniaxial tension. The error bars represent the spread in Feritscope measurement on a single sample. The solid lines correspond to sigmoidal fits drawn to guide the eyes.

The experimental measurements displayed in Figure 5.12 show a global trend suggesting a slow down of the kinetics with refinement of the austenitic grain sizes, with the exception of the $D=0.5$ µm condition, for which the kinetics is accelerated. This non-monotonic effect can also be seen in Figure 5.13 which shows the value of the maximum rate of formation of α' as a function of grain size. Such non-monotonic trend cannot be described by the usual Olson-Cohen model [81] detailed in section 2.4. Indeed, it has been shown in section 2.4.2 that grain size refinement could be interpreted to slow down ($\beta \propto D^2$) or accelerate ($\beta \propto D^{2(1-n)}$) the formation of α'-martensite, but always monotonically. Moreover, as mentioned in Figure 2.17, the original grain size dependence postulated by Olson and Cohen (i.e. $\beta \propto D^2$) is far too strong to capture the experimental saturation fractions of α'-martensite presented in Figure 5.12. This non-monotonic grain size effect will be revisited in section 6.6, in relation with observed mechanisms of nucleation for both ϵ-martensite and α'-martensite.
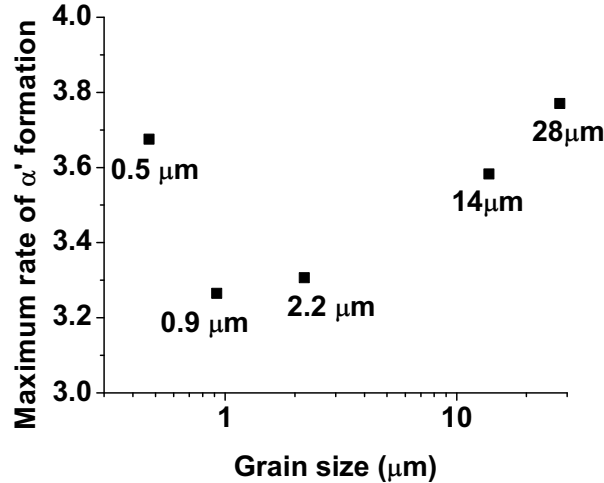
Figure 5.13: Maximum rate of formation of α'-martensite as a function of the initial austenite grain size.

Considering the samples deformed in shear, due to the small dimensions

of the gauge section of shear coupons, the Feritscope was not suitable for measurements in these samples. Instead, X-ray diffraction was performed with the experimental protocol described in section 5.2.3. Each measurement was performed on a different coupon. These measurements appear in Figure 5.14. Because the correction applied from the shear angle measured post-mortem could vary significantly from one sample to another, it was not possible to reproduce the same shear strain for different condition of grain size. One can observe larger scatter in the volume fractions under shear when compared to tension, a scatter of the order of the variation of volume fractions with grain size. Therefore, from these results, it is not possible to definitively comment on the grain size dependence of the transformation kinetics in simple shear.
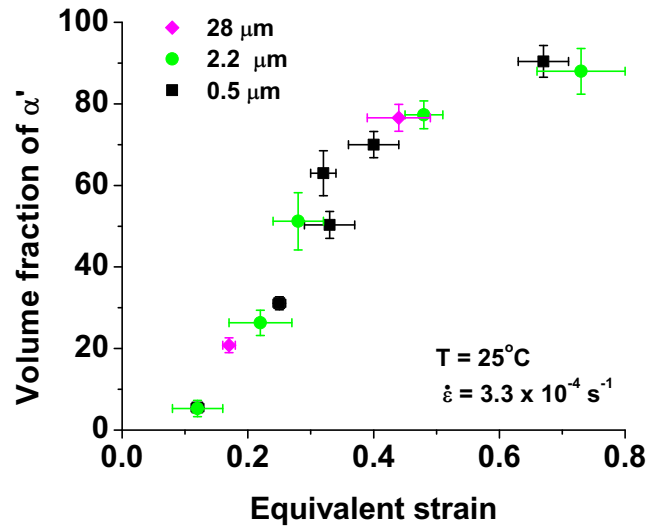
Figure 5.14: Evolution of the volume fraction of α'-martensite in simple shear as measured from X-ray diffraction.

Figure 5.15 compares the α' volume fractions measured in simple shear and in uniaxial tension as a function of Von Mises equivalent strain. These plots suggest a dependence of the fraction of α' with the strain path. Similar

to the stress-strain curves presented above, it is observed that the fraction of α'-martensite formed in tension and shear are similar over the first $\epsilon \sim$ 0.2–0.3. Beyond this level of strain, the fraction of α'-martensite in simple shear are systematically lower than those in uniaxial tension. This effect on the kinetics is the one observed in Figure 2.15 (a) [151] but not in Figure 2.19 [170].
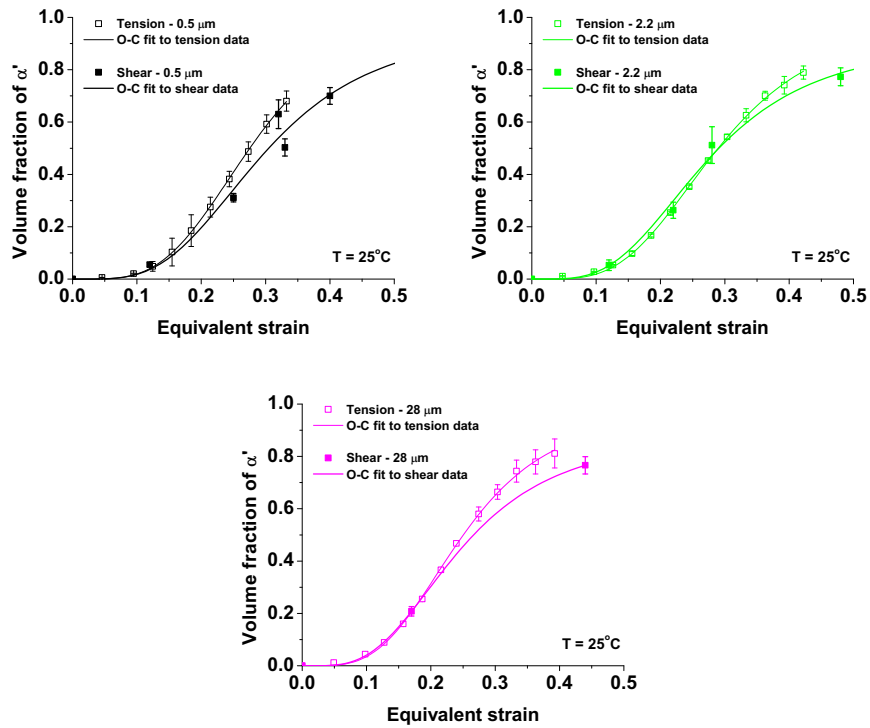
Figure 5.15: Comparison of the volume fraction of α'-martensite in simple shear, compared to the one measured in uniaxial tension as a function of Von Mises strain. The solid lines are drawn to guide the eyes.

5.6 Relationship between Mechanical Response and Volume Fraction of Phases

Consistent with previous studies, this work shows only a very small fraction of ϵ-martensite formation during tensile testing. This is not particularly surprising given the discussion in section 2.2.3 regarding the tendency for the α'-martensite transformation to be preceded by ϵ-martensite. The other important point is illustrated in Figure 5.11 which shows that the grain size strongly affects the formation of ϵ-martensite. This trend is consistent with the reported increase in the M_s temperature for the $\gamma \rightarrow \epsilon$ phase transformation when the grain size is increased, in various austenitic stainless steels [125, 126, 131]. This trend will be further discussed in chapter 6.

While it is difficult to make definitive correlations between mechanical response and ϵ-martensite fraction owing to the low volume fraction of this phase, relationships between the formation of α'-martensite and mechanical response can be made. To assist in describing this relationship below, the work-hardening response of the alloy is divided into three stages, those are represented in Figure 5.16. Note that the three stages defined here are not meant to have any relationship to the stages of work-hardening typically used to describe the behaviour of single crystals.
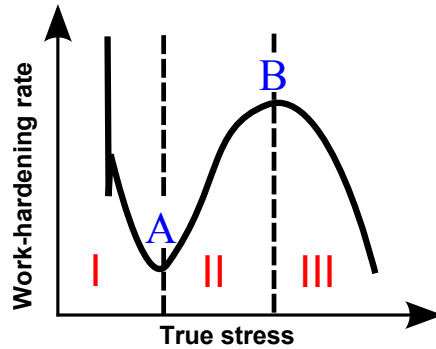
Figure 5.16: Schematic of the work-hardening behaviour in stainless steels, defining the three stages of work-hardening at room temperature.

The work-hardening within **stage I** is seen to be similar to the work-

hardening of stable austenitic grades that do not undergo phase transformation. Figure 5.7 showed that the work-hardening behaviour observed during this stage was very close to that observed at 80°C where little transformation occurred. Some authors have commented on a rapid decrease in stage I work-hardening and have related this to the rapid formation of ϵ-martensite [141, 168], or to the nucleation of α' at shear bands [111, 231]. The end of **stage I** is marked by a minimum of work-hardening (noted "A" in Figure 5.16).

Stage II work-hardening is the stage which accounts for the inflection in the stress-strain curve, typical to materials exhibiting pronounced TRIP effect. The end of this stage II is marked by a maximum of work-hardening (noted "B" in Figure 5.16). With the exception of the $D=0.5$ μm condition, the most intense work-hardening peaks were found in the conditions of grain size displaying the highest rates of α' formation. This suggests a strong link between the rate of formation of α'-martensite and the rate of work-hardening.

Some authors have considered α'-martensite as an ideally plastic phase. Under such an assumption, once formed, the α'-martensite would always carry the same stress ($\sigma_{\alpha'}$). Assuming the volume fraction of ϵ being small enough to be neglected, the true stress of this dynamic composite material would then be given by a simple rule of mixtures (consequence of mechanical equilibrium) between only γ and α':

$$\sigma = \sigma_\gamma(1 - f_{\alpha'}) + \sigma_{\alpha'} f_{\alpha'} \tag{5.4}$$

which can be rewritten as:

$$\sigma = \sigma_\gamma + f_{\alpha'}(\sigma_{\alpha'} - \sigma_\gamma) \tag{5.5}$$

Equation 5.5 would result in a linear dependence of the true stress of the composite as a function of the volume fraction of α'. Such a plot is presented in Figure 5.17. It can be seen that the flow stress does scale with the fraction of α'-martensite but that the relationship is not linear. Similar

feature was observed in simple shear. This observation suggests that, while the rate of transformation plays a very important role in the macroscopic work-hardening response of the material, one cannot reasonably assume a perfect plastic response for the α'-martensite. This point will be discussed in more detail in chapter 7 and chapter 8.
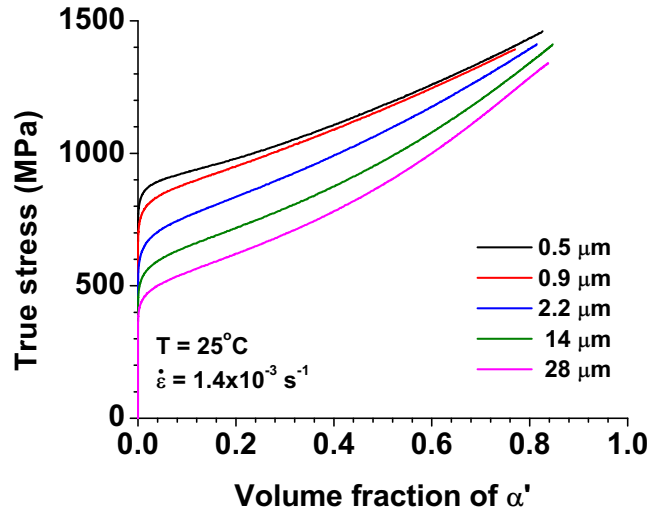
Figure 5.17: Flow stress obtained under uniaxial tension at room-temperature as a function of the volume fraction of α'.

One can use similar reasoning in an attempt to estimate the flow stress in the α' phase, recalculated from the macroscopic mechanical equilibrium:

$$\sigma_{\alpha'}^{theo} = \frac{\sigma - (1 - f_{\alpha'})\sigma_\gamma}{f_{\alpha'}} \qquad (5.6)$$

In this case, the behaviour of the austenite is estimated from the stress-strain response measured at 80°C, during which less than 10% of α' was formed.

The variation of this theoretical stress in α'-martensite is plotted against applied true strain in Figure 5.18. It is important to note that the x-axis of this graph represents the **macroscopic** strain which is different from the

strain carried by the α'-martensite. The difference between these strains is related to the way in which strains must be partitioned through the microstructure.
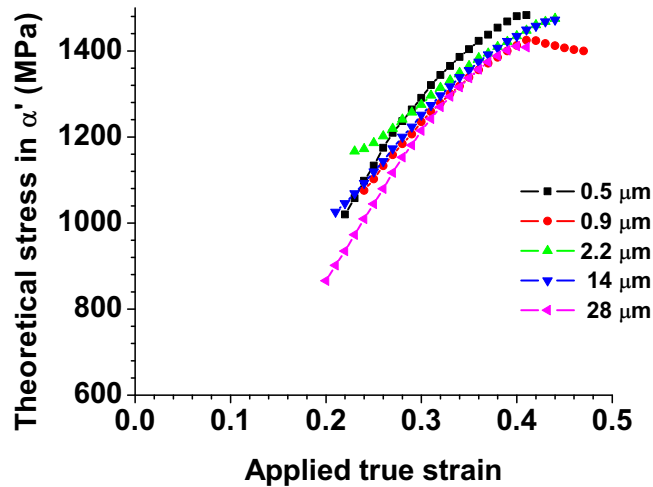
Figure 5.18: Average theoretical stress in α' as a function of applied true strain.

In this plot, the theoretical stresses below true strains of ~ 0.2 are subject to large scatter. This is because $f_{\alpha'}$ appears in the denominator in Equation 5.6, and a small scatter in the volume fraction of α'-martensite results in a large scatter of the theoretical stress. For this reason, the calculated values corresponding to an α' volume fraction below 30% have not been plotted. Despite this limitation, this plot shows that the (theoretical) mechanical behaviour of α' is nearly independent of the austenite grain size. This is an important point that will be revisited when a model for the mechanical behaviour of the material is proposed in chapter 8.

5.7 Summary

In this chapter, the mechanical response of grade 301LN has been described for tension and shear tests performed at room temperature. It has been

found that the rate of formation of α' is important for determining the macroscopic work-hardening response of the material. The reduction of the rate of α'-martensite with decreasing grain size explains (at least partially) the reduction in macroscopic hardening. This is reflected in the relatively weak variation of the ultimate tensile strength with grain size compared to the strong grain size dependence of yield stress with grain size. Also observed here is the fact that testing in simple shear results in a lower rate of transformation compared to tension, particularly at higher strains. While the response in the two strain paths (when compared on the basis of Von Mises equivalent stress and strain) are nearly equivalent for $\epsilon \sim 0.2$–0.3, above this level of strain the rate of $\gamma \rightarrow \alpha'$ transformation slows more quickly in shear than it does in tension, leading to a lower rate of work-hardening in shear.

Chapter 6

Characterization of the Deformed Microstructures

6.1 Introduction

In the last chapter, the mechanical properties and phase transformation from austenite to α'-martensite were explored from a macroscopic point of view. The close link between the transition to α'-martensite and the work-hardening rate of the material was illustrated and discussed in relation to previous work. In this chapter, the details of the autenite to ϵ-martensite and (particularly) α'-martensite transformation are examined at the microscopic scale in order to provide an understanding of the relationship between plasticity in austenite and the rate of formation of the martensitic phases. Also, the apparent grain size dependence of the transformation kinetics are explored. The main tool used for the microstructural observations is electron backscatter diffraction (EBSD). The EBSD technique provides sufficient resolution to allow for identification of all three phases (although not all with the same ease) while providing a more statistically reliable overview of the microstructure compared to transmission electron microscopy. This chapter begins by focusing on the transformations and microstructure evolution during straining for the material with the largest (28 µm) grain size. Following this, observations on the two finest grain sizes are presented (0.5 µm and 2.2 µm) and compared against the behaviour of the coarse grained material. Finally, a comparison will be made between the microstructures of samples deformed in tension and in shear.

6.2 Experimental Techniques and Representation Convention

High-resolution EBSD maps were measured using the FEG-SEM described in chapter 4. The experimental procedure (sample preparation, data treatment) is the same as previously described in section 4.2.2, the one difference being that EBSD patterns were indexed considering fcc austenite, bcc α'-martensite and hcp ϵ-martensite as possible phases. The EBSD maps presented in this chapter have not been cleaned so that unindexed points would still be visible. This avoids the possible creation of false information in the deformed microstructure. The *HKL* wild spike extrapolation procedure [232] was used to remove single pixels corresponding to wrongly indexed points [8].

To represent the microstructures resulting from EBSD maps, a convention has been adopted in this chapter to display austenite using band contrast maps. While this does not provide explicit information on orientations, it does allow one to identify features such as grain boundaries and planar, deformation-induced, bands. The α'-martensite has been shown superimposed on the austenite band contrast maps as orientation maps with colours corresponding to the Inverse Pole Figure (IPF) code shown in Figure 6.1. The colour on the maps corresponds to the crystallographic direction aligned parallel to the rolling direction (RD) of the sample, also parallel to the tensile direction or the shear direction. Finally, ϵ-martensite, when present, has been plotted as being red. As will be seen, very little amount of ϵ-martensite has been indexed and therefore its presence will be explicitly noted in any of the maps presented.

Trace analysis was performed on EBSD maps using a script written in *MATLAB*. This script reads in EBSD data and allows one to compare crystallographic traces identified manually by the user on the map with crystallographic planes and directions. In particular, this script has been used in an attempt to identify $\{111\}_\gamma$ planes associated with planar features

---

[8] As mentioned in section 4.2.2, wrongly indexed points (or wild spike) are defined within the *HKL* software to be single pixels that have a misorientation higher than 6–7° with all surrounding points.
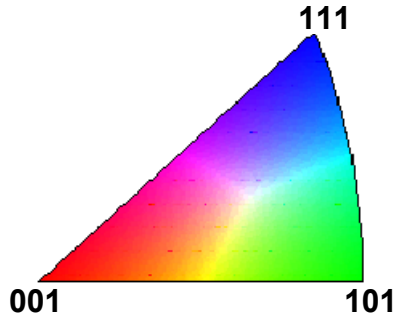
Figure 6.1: Inverse pole figure, coloured corresponding to crystallographic direction parallel to sample direction. This colour scheme is used in all following EBSD maps for plotting the orientation of α'-martensite. In this chapter, the α'-martensite maps have been coloured using the rolling direction (RD) as the sample direction in this scheme.

observed on the maps. A criterion of less than 2° angular difference between experimental and theoretical traces was used to determine which $\{111\}_\gamma$ plane coincided to the observed trace. This allowed, in all cases, for an unambiguous determination of the plane.

The Schmid factor of a particular slip system was analysed using the information from trace analysis. The systems considered are $\{111\}_\gamma \langle 211 \rangle_\gamma$ for the apparition of ϵ-martensite and $\{111\}_\gamma \langle 110 \rangle_\gamma$ for the apparition of α'. The Schmid factor (m) was calculated as:

$$m = \frac{(\sigma n)}{\|\sigma\|} \cdot b \tag{6.1}$$

where σ is the macroscopic stress tensor, n the slip plane normal and b the slip direction on the slip plane. For each $\{111\}_\gamma$ plane, there are three possible $\{110\}_\gamma$ or $\{112\}_\gamma$ slip directions, and consequently three possible Schmid factors. Since the slip direction cannot be unambiguously determined, the Schmid factor reported in this chapter is the highest of the three (in absolute value) for the considered $\{111\}_\gamma$ plane.

To make a more specific link between tensile deformation and microstructure evolution, a series of sequential EBSD experiments were performed. In these experiments, sub-size tensile samples (small enough to fit inside the

SEM chamber) were prepared (Figure 6.2) and pre-strained by 15% in tension. The gauge section of this sample was then electropolished and three areas for each sample were then defined and marked with microhardness indents. A high resolution EBSD scan was then made in each of these areas, prior to the material being strained in tension a further 5%. After straining, this area was again measured by EBSD without any further preparation. This allowed for exactly the same area to be observed after the two levels of strain. Due to surface roughness, it was found that the results deteriorated significantly between the first and second measurement. Attempting a third measurement on the same area without re-preparation resulted in very low indexing rates (e.g. 30–70% misindexed phase).
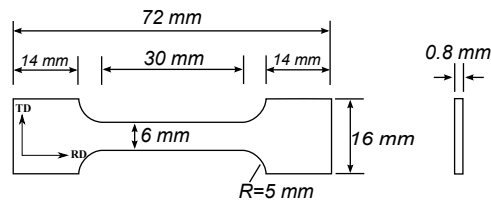
Figure 6.2: Geometry of small tensile coupons used for sequential EBSD.

Finally, TEM observations were made on selected samples after different levels of deformation following the sample preparation procedure defined in section 4.2.2.

6.3 Microstructure Evolution in Uniaxial Tension: Large Grain Size Limit

This section starts with an overview of the behaviour of coarse grained samples deformed in uniaxial tension. This condition is most similar to the majority of data in the literature and therefore allows for comparisons with existing data.

6.3.1   General Overview of Microstructure Evolution as a Function of Strain

As expected based on the results from the last chapter, a strong evolution of the microstructure of the large grain sized samples (D=28 µm) was observed as a function of tensile strain. Figure 6.3 illustrates the evolution from the austenite being the majority phase (5% strain) to α'-martensite being the majority phase (41% strain).

(a) $\epsilon = 5\%$ (b) $\epsilon = 10\%$

(c) $\epsilon = 41\%$
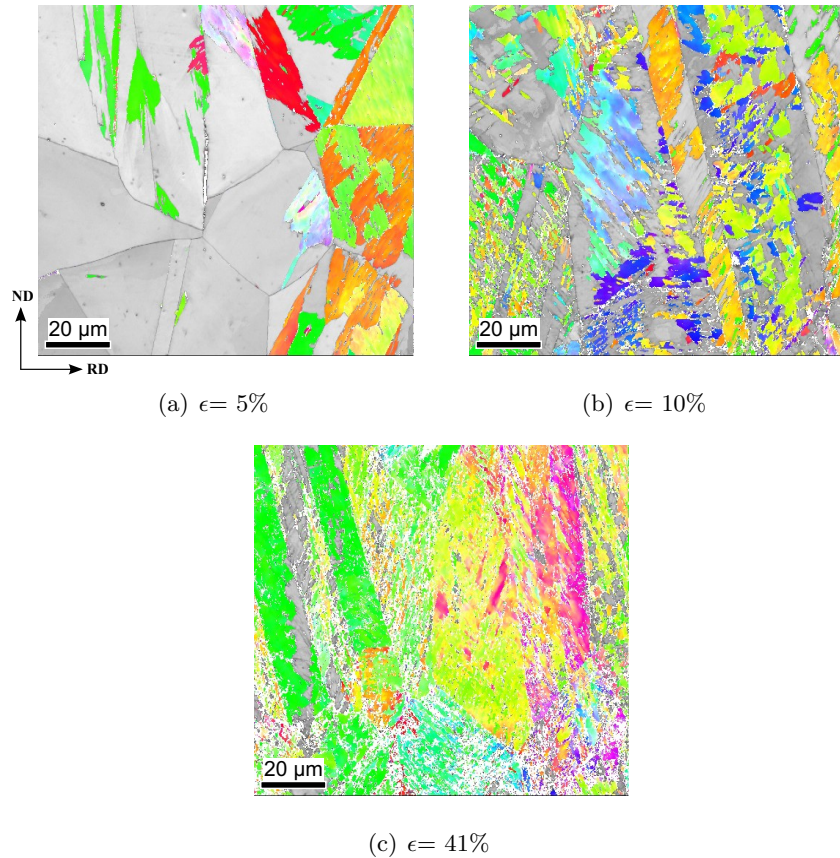
Figure 6.3: A series of three EBSD maps measured on samples (D=28 µm) deformed to the three indicated levels of strain. The qualitative evolution from an austenitic microstructure to a martensitic microstructure is clearly evident.

At a qualitative level, one can see that, in each map, at least a small amount of α'-martensite is present in each grain. The α'-martensite in these maps presents a Kurdjumov-Sachs (K-S) orientation relationship with the surrounding austenite, consistent with the majority of observations in the literature [74, 110, 233]. At 10% and 41% strain, one can observe that most grains have more than one variant of α'-martensite present (as indicated by the different colours of martensite), though many fewer than the 24 possible from crystallographic considerations. At 10% and 41% strain, one can see dark straight features in the band contrast maps for the austenite phase. The presence of ϵ-martensite is not readily apparent from maps at this resolution, however, evidence for its existence will be presented below.

The α'-martensite observed in the EBSD maps appears in different morphologies. In some locations, the α' martensite appears as "blocky" plates (as in Figure 6.4(a)), though the presence of straight, sharp facets on these features suggests the influence of crystallography. In other areas, the martensite appears much narrower, appearing in parallel bands across the grains (as in Figure 6.4(b)).
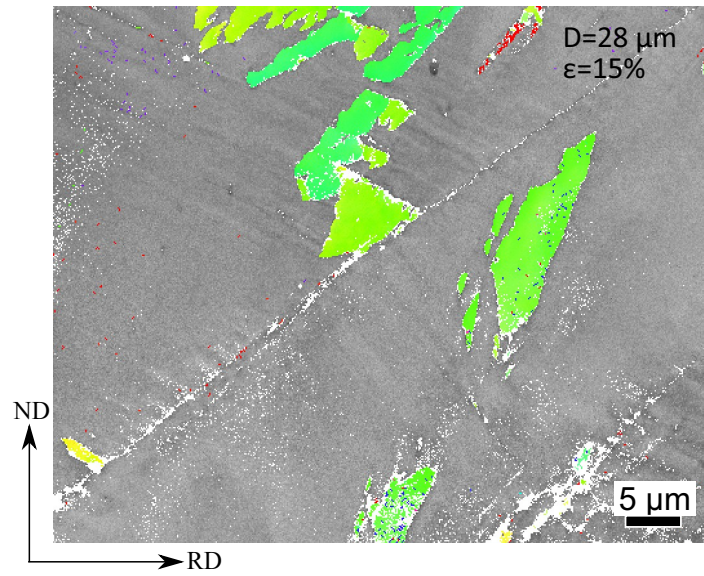
(a)
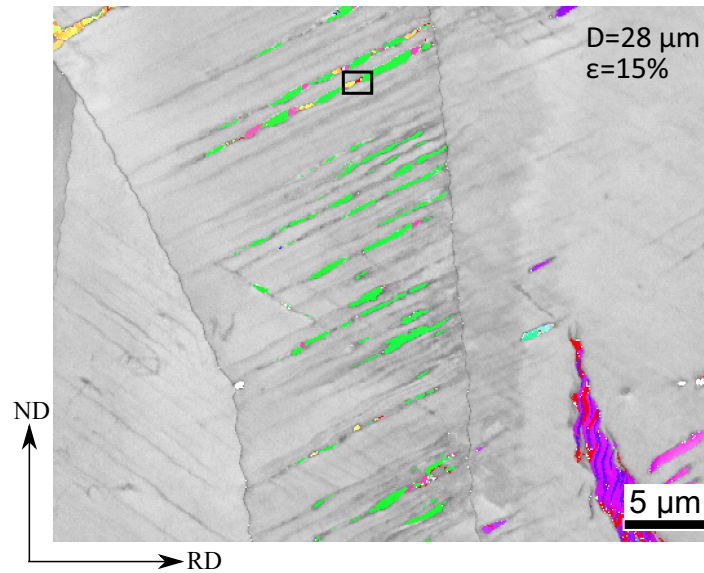
(b)

Figure 6.4: Orientation maps illustrating two different morphologies of α'-martensite. In (a), the α'-martensite (green in colour) appears "blocky", while in (b) it appears in bands within the grain (here, an annealing twin).

6.3.2 Relationship between Martensite Morphology and Crystallography

The appearance of the α'-martensite observed in these maps suggests a link to the underlying crystallography of the transformation. For example, it was found that the thin, parallel α'-martensite plates were usually associated with bands of low band contrast observed in the austenite matrix. The map presented on Figure 6.4(b), taken from a sample strained 15% in tension, illustrates the presence of thin, parallel α' plates within, and parallel to, these lines of low band contrast.
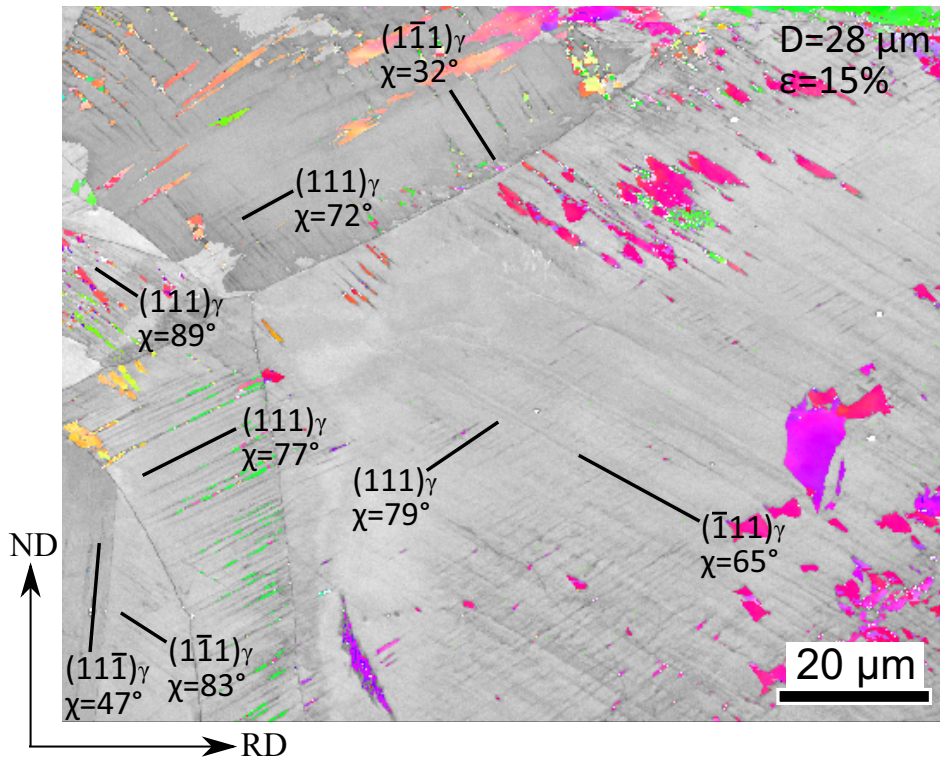
Figure 6.5: Orientation map showing a few grains of austenite in the 28 µm condition, deformed to 15% strain in uniaxial tension. Some planar features are underlined, together with their corresponding plane and their inclination angle (denoted χ) towards TD.

111

Figure 6.5 shows the same sample as shown in Figure 6.4(b) but at a lower magnification. By performing trace analysis within this map it was found that the low band contrast features are consistent with the trace of $\{111\}_\gamma$ planes (see the $\{111\}_\gamma$ traces in Figure 6.5). Moreover, it was found that the vast majority of these $\{111\}_\gamma$ are highly inclined with respect to the surface of the EBSD sample, as illustrated in Figure 6.6.
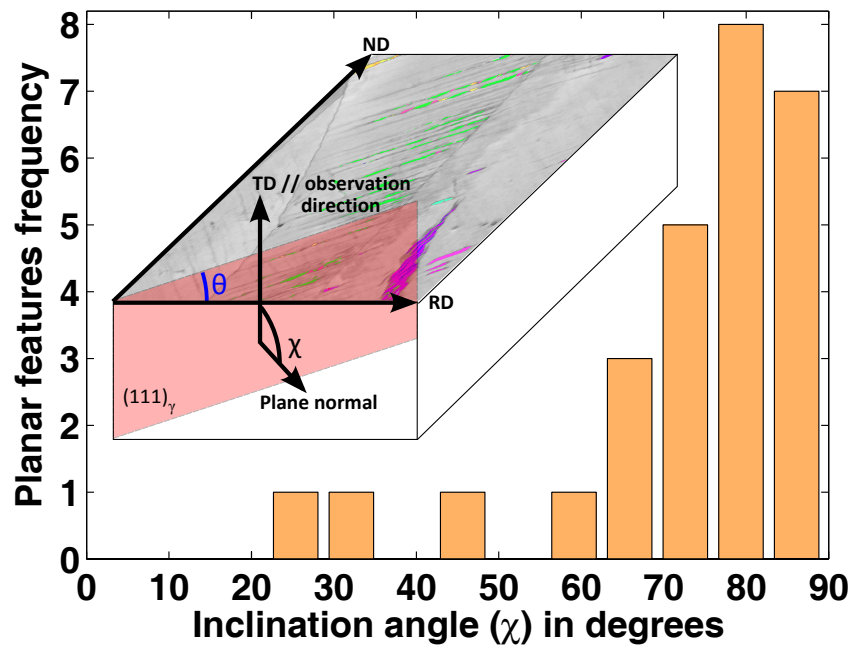
Figure 6.6: Angle of inclination of $\{111\}_\gamma$ traces observed to correspond to low band contrast lines in EBSD maps. These measurements come from 25 grains. The inset figure illustrates the relationship between a $\{111\}_\gamma$ plane (coloured in pink) and its trace and defines the angle of inclination, χ.

The above results show that the observed lines of low band contrast correspond to the trace made between one $\{111\}_\gamma$ plane and the polished surface of the sample, these traces being particularly visible when the associated $\{111\}_\gamma$ planes are highly inclined. If one imagines the low band-contrast

regions in these maps to be thin plates, then the unambiguous observation of the plates, regardless of their internal structure, is easier when they are inclined edge-on ($\chi \approx 90°$) than when they are parallel to the surface of the sample. In the case where the plates are parallel to the surface of the sample, two factors will tend to degrade the measurement. First, if the plates are very thin, then it is likely that the signal from the sample will be dominated by that of the austenite matrix. Second, given that the signal for EBSD arises only from within the first few nanometers of the sample surface [234] and that the volume fraction of plates is low, then the probability of finding a plate within the measurement volume will decrease rapidly with angle of inclination.

When the plates are "edge on" and a sufficiently small probe is used, a more distinct pattern may emerge, though the surrounding matrix may still dominate the signal. This would lead to low band contrast, consistent with what is observed here. This is consistent with what has been reported in the case of materials containing fine deformation twins [235–237].

(a) (b) (c)
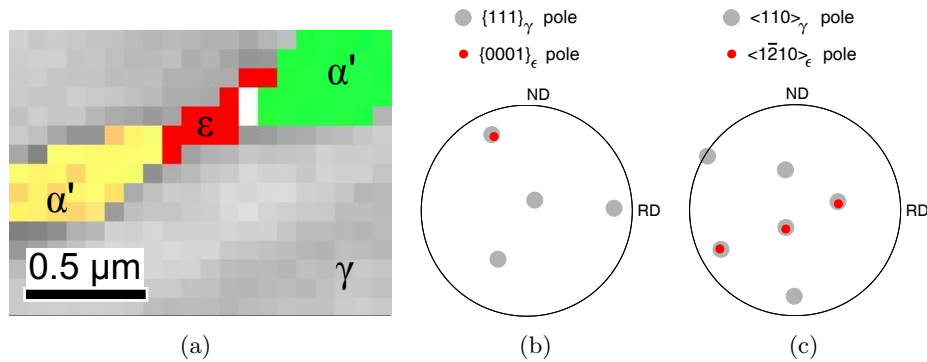
Figure 6.7: (a) Magnified view of the area underlined in Figure 6.4(b), showing the presence of ϵ-martensite. (b) and (c) show the Burgers orientation relation in this grain between γ and the ϵ-phase observed. (b) represents the $\{0001\}_\epsilon$ pole figure superimposed on the $\{111\}_\gamma$ pole figure and (c) represents the $\langle 1\bar{2}10 \rangle_\epsilon$ pole figure superimposed on the $\langle 110 \rangle_\gamma$ pole figure.

To investigate the cause of the low band contrast along the traces of the $\{111\}_\gamma$ planes, a closer examination of the measured data has been made.

Focusing on Figure 6.4(b), several small regions indexed as ϵ-martensite (0.3–0.5% in area fraction) were found within the low band contrast lines. Figure 6.7 shows one region, taken from the highlighted box in Figure 6.4(b), of pixels indexed as ϵ-martensite. Confidence in these measured fragments was provided by the fact that the orientation relationship between the ϵ-martensite points and the surrounding austenite coincides with the Burgers orientation relationship, as expected from the literature [50, 73–75]. Moreover, trace analysis shows that the ϵ-martensite's $(0001)_\epsilon$ plane is parallel to the $\{111\}_\gamma$ whose trace coincides with the line of low band contrast. This is consistent with the view that the observed fragment of ϵ-martensite is actually in the form of a very thin plate whose habit plane is parallel to the $\{111\}_\gamma$ plane whose trace is observed [80].

To confirm the hypothesis of ϵ-martensite in the form of thin plates in the deformed microstructure of the coarse grained samples, TEM observations were performed on samples at low levels of strain ($\sim 5\%$ tensile strain). Figure 6.8 shows a region containing planar faults that gave rise to extra spots in the selected area diffraction pattern, consistent with ϵ-martensite.

6.3.3 Schmid Analysis of $\{111\}_\gamma$ Planes Associated with Trace Analysis

As noted in the literature review (section 2.2.3), previous studies have suggested that ϵ-martensite obeys the Schmid law [86]. This interpretation would be consistent with a mechanism of ϵ-martensite formation associated with the passing of partial dislocations on every other $\{111\}_\gamma$ $\langle 112 \rangle_\gamma$ slip system (cf. section 2.2.3) leading to the shear plane ($\{111\}_\gamma$) being parallel to the $\{0001\}_\epsilon$ plane of the ϵ-martensite. Although the EBSD results above do not provide evidence that ϵ-martensite exists along each of the low band contrast features in the maps, several examples of the correlation between the latter and ϵ-martensite were observed. Here, it is hypothesized that the low band contrast features are a result of non-indexed ϵ-martensite plates, much like fine deformation twins in other steels [145, 233].

Based on the discussion above, one would expect the majority of low
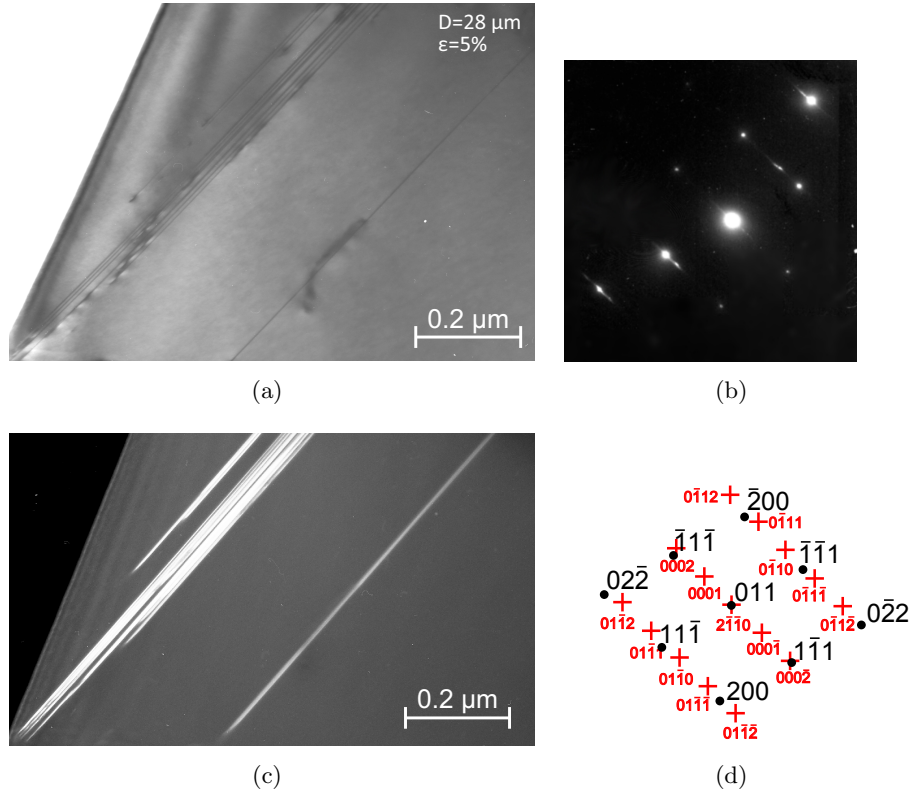
Figure 6.8: (a) Bright field TEM micrograph of a grain showing a set of planar features (b) Selected area diffraction pattern exhibiting extra spots characteristic of ϵ-martensite . (c) Dark field image of the same grain, using the $\langle 0\bar{1}10 \rangle_\epsilon$ reflection underlined in (b). (d) Theoretical positions of the reflections corresponding to (b).

band contrast traces in the EBSD maps to correspond to $\{111\}_\gamma$ $\langle 112 \rangle_\gamma$ slip systems having high Schmid factors. Calculation of Schmid factors in this case is not unambiguous since the $\langle 112 \rangle_\gamma$ direction involved in the formation of ϵ-martensite cannot be fully determined [9].

The 15 grains shown in Figure 6.9, whose orientations are given in Table 6.1, were examined to identify the $\{111\}_\gamma$ planes associated with the low band contrast features. In parallel, the Schmid factors for each $\{111\}_\gamma$

---

[9] Shear on the three $\langle 112 \rangle_\gamma$ directions of a given $\{111\}_\gamma$ plane all give the same variant of ϵ-martensite [50].
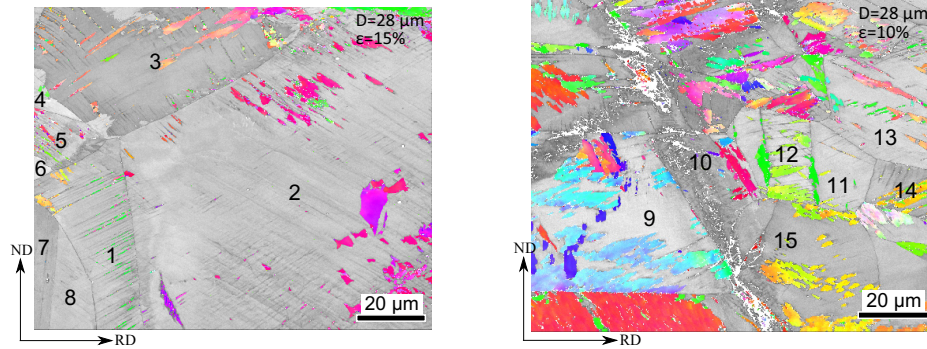
Figure 6.9: Two low magnification orientation maps used for the Schmid analysis detailed in Table 6.2.

$\langle 112 \rangle_\gamma$ system in the 15 grains were calculated, the results being tabulated in Table 6.2. In this same table, those $\{111\}_\gamma$ planes observed to be associated with low band contrast bands are highlighted in bold. The results show that 10 grains out of the 15 grains analyzed had planar faults on the $\{111\}_\gamma$ plane with the highest Schmid factor.

As noted in the literature review (section 2.3), the Patel-Cohen calculation of interaction energy has been recently adopted [10, 50, 160] in an attempt to predict variant selection in strain-induced martensitic transformations. Humbert *et al.* [50] have applied this methodology to predict the expected variants of ϵ-martensite preceding the formation α'-martensite. One can readily show that, in the case of the formation of ϵ-martensite in tension, the interaction energy predicted from the Patel-Cohen model is proportional to the Schmid factor for the $\{111\}_\gamma \langle 112 \rangle_\gamma$ system for the $\gamma \rightarrow \epsilon$ transformations (for details, see Appendix B). Thus, the results above are fully consistent with the interaction energy hypotheses in that the selection of ϵ-martensite on systems with high Schmid factor is equivalent to the formation of ϵ-martensite having the high interaction energies.

116

Grain	Euler angles of γ			Euler angles of α'			Plane matching Condition	Direction matching Condition	Interaction Energy (J m^{-3})	Ranking
	ϕ_1	Φ	ϕ_2	ϕ_1	Φ	ϕ_2				
1	54	38	76	162	19	66	$(111)_\gamma//(101)_{\alpha'}$	$[0\bar{1}1]_\gamma//[\bar{1}11]_{\alpha'}$	0.018	3
				40	34	40	$(111)_\gamma//(011)_{\alpha'}$	$[0\bar{1}1]_\gamma//[1\bar{1}1]_{\alpha'}$	-0.031	-
				219	40	51	$(111)_\gamma//(101)_{\alpha'}$	$[10\bar{1}]_\gamma//[111]_{\alpha'}$	-0.034	-
				230	4	88	$(1\bar{1}1)_\gamma//(011)_{\alpha'}$	$[110]_\gamma//[11\bar{1}]_{\alpha'}$	-0.031	-
2	139	45	7	209	48	48	$(1\bar{1}1)_\gamma//(\bar{1}01)_{\alpha'}$	$[011]_\gamma//[111]_{\alpha'}$	0.038	2
				275	51	41	$(1\bar{1}1)_\gamma//(1\bar{1}0)_{\alpha'}$	$[011]_\gamma//[111]_{\alpha'}$	0.026	4
				156	41	42	$(111)_\gamma//(101)_{\alpha'}$	$[\bar{1}01]_\gamma//[\bar{1}11]_{\alpha'}$	-0.023	-
3	103	34	18	110	24	55	$(111)_\gamma//(101)_{\alpha'}$	$[0\bar{1}1]_\gamma//[11\bar{1}]_{\alpha'}$	-0.032	-
				355	24	36	$(111)_\gamma//(011)_{\alpha'}$	$[1\bar{1}0]_\gamma//[11\bar{1}]_{\alpha'}$	0.01	4
				121	30	46	$(111)_\gamma//(101)_{\alpha'}$	$[10\bar{1}]_\gamma//[\bar{1}11]_{\alpha'}$	0.038	1
4	63	35	63	195	15	30	$(1\bar{1}1)_\gamma//(\bar{1}01)_{\alpha'}$	$[110]_\gamma//[1\bar{1}1]_{\alpha'}$	0.009	4
				61	26	23	$(111)_\gamma//(011)_{\alpha'}$	$[0\bar{1}1]_\gamma//[1\bar{1}1]_{\alpha'}$	-0.034	-
5	324	24	9	30	50	46	$(\bar{1}11)_\gamma//(110)_{\alpha'}$	$[0\bar{1}1]_\gamma//[\bar{1}11]_{\alpha'}$	-0.018	-
				325	17	56	$(111)_\gamma//(101)_{\alpha'}$	$[0\bar{1}1]_\gamma//[11\bar{1}]_{\alpha'}$	0.036	1
				183	29	57	$(111)_\gamma//(011)_{\alpha'}$	$[10\bar{1}]_\gamma//[1\bar{1}1]_{\alpha'}$	-0.006	-
9	133	34	50	152	33	77	$(1\bar{1}1)_\gamma//(0\bar{1}1)_{\alpha'}$	$[10\bar{1}]_\gamma//[\bar{1}11]_{\alpha'}$	-0.019	-
				133	45	9	$(11\bar{1})_\gamma//(0\bar{1}1)_{\alpha'}$	$[101]_\gamma//[111]_{\alpha'}$	-0.014	-
				31	28	52	$(\bar{1}11)_\gamma//(0\bar{1}1)_{\alpha'}$	$[101]_\gamma//[111]_{\alpha'}$	0.028	2
				218	32	59	$(\bar{1}11)_\gamma//(110)_{\alpha'}$	$[01\bar{1}]_\gamma//[\bar{1}11]_{\alpha'}$	0.52	1
				242	21	37	$(1\bar{1}1)_\gamma//(\bar{1}01)_{\alpha'}$	$[011]_\gamma//[111]_{\alpha'}$	0.051	2
10	73	14	51	24	21	58	$(\bar{1}11)_\gamma//(\bar{1}01)_{\alpha'}$	$[01\bar{1}]_\gamma//[1\bar{1}1]_{\alpha'}$	-0.038	-
11	283	34	34	3	36	63	$(\bar{1}11)_\gamma//(110)_{\alpha'}$	$[01\bar{1}]_\gamma//[\bar{1}11]_{\alpha'}$	-0.037	-
				277	42	86	$(11\bar{1})_\gamma//(\bar{1}01)_{\alpha'}$	$[101]_\gamma//[1\bar{1}1]_{\alpha'}$	-0.011	-
12	82	41	56	85	29	8	$(111)_\gamma//(011)_{\alpha'}$	$[10\bar{1}]_\gamma//[11\bar{1}]_{\alpha'}$	-0.039	-
13	304	37	19	305	29	60	$(111)_\gamma//(101)_{\alpha'}$	$[0\bar{1}1]_\gamma//[11\bar{1}]_{\alpha'}$	0.046	1
				148	54	34	$(111)_\gamma//(011)_{\alpha'}$	$[0\bar{1}1]_\gamma//[11\bar{1}]_{\alpha'}$	-0.0077	-
				152	10	78	$(\bar{1}11)_\gamma//(0\bar{1}1)_{\alpha'}$	$[101]_\gamma//[111]_{\alpha'}$	0.036	2
14	291	44	21	1	44	70	$(\bar{1}11)_\gamma//(110)_{\alpha'}$	$[110]_\gamma//[1\bar{1}1]_{\alpha'}$	0.035	1
				238	5	66	$(\bar{1}11)_\gamma//(\bar{1}01)_{\alpha'}$	$[110]_\gamma//[111]_{\alpha'}$	-0.035	-
15	300	41	15	301	27	59	$(111)_\gamma//(101)_{\alpha'}$	$[0\bar{1}1]_\gamma//[11\bar{1}]_{\alpha'}$	0.043	1
				147	44	24	$(\bar{1}11)_\gamma//(101)_{\alpha'}$	$[0\bar{1}1]_\gamma//[11\bar{1}]_{\alpha'}$	-0.036	-

Table 6.1: Identification of the plane/direction matching conditions between γ and α'. 15 grains of austenite (each containing 0–5 α' variants) were analyzed. The Euler angles were determined in Bunge's convention with x_1//RD, x_2//ND and x_3//TD. The interaction energy used to rank the different variants is calculated based on Humbert's methodology [50], as detailed in Appendix B.

		(111)				($\bar{1}11$)				($1\bar{1}1$)				($\bar{1}\bar{1}1$)		
	χ	$[\bar{2}11]$	$[1\bar{2}1]$	$[11\bar{2}]$	χ	$[211]$	$[\bar{1}\bar{2}1]$	$[\bar{1}1\bar{2}]$	χ	$[21\bar{1}]$	$[121]$	$[1\bar{1}\bar{2}]$	χ	$[2\bar{1}1]$	$[\bar{1}21]$	$[\bar{1}\bar{1}\bar{2}]$
1	77°	**0.12**	**0.24**	**0.37**	14°	0.07	0.15	0.08	56°	**0.38**	**0.25**	**0.13**	79°	0.10	0.18	0.08
2	73°	**0.35**	**0.05**	**0.40**	67°	**0.34**	**0.39**	**0.05**	4°	0.07	0.03	0.03	71°	**0.36**	**0.17**	**0.19**
3	73°	**0.11**	**0.22**	**0.33**	45°	0.07	0.16	0.09	32°	**0.40**	**0.25**	**0.15**	81°	0.13	0.17	0.03
4	85°	**0.10**	**0.24**	**0.34**	21°	0.06	0.13	0.07	50°	0.41	0.26	0.14	78°	0.14	0.20	0.06
5	89°	**0.39**	**0.03**	**0.43**	57°	0.33	0.34	0.00	21°	0.13	0.08	0.06	66°	0.41	0.13	0.27
6	87°	**0.09**	**0.24**	**0.33**	24°	0.05	0.11	0.06	48°	**0.42**	**0.28**	**0.15**	79°	0.18	0.22	0.04
7	73°	**0.06**	**0.01**	**0.05**	14°	**0.22**	**0.41**	**0.19**	58°	0.07	0.01	0.08	81°	0.25	0.50	0.23
8	82°	0.43	0.10	0.34	81°	**0.45**	**0.35**	**0.10**	21°	0.33	0.16	0.17	50°	0.49	0.26	0.23
9	73°	**0.21**	**0.07**	**0.14**	70°	**0.43**	**0.36**	**0.08**	39°	0.31	0.04	0.27	43°	0.43	0.43	0.01
10	90°	**0.10**	**0.32**	**0.42**	23°	0.01	0.02	0.01	50°	0.36	0.29	0.07	74°	0.11	0.30	0.19
11	86°	**0.19**	**0.15**	**0.34**	43°	**0.19**	**0.34**	**0.15**	28°	0.25	0.13	0.13	86°	0.08	0.04	0.04
12	84°	**0.13**	**0.12**	**0.25**	31°	0.15	0.35	0.19	40°	0.34	0.14	0.19	89°	0.03	0.04	0.07
13	81°	**0.25**	**0.11**	**0.36**	55°	0.27	0.40	0.13	16°	**0.12**	**0.05**	**0.06**	77°	0.22	0.14	0.08
14	75°	**0.13**	**0.10**	**0.23**	50°	**0.17**	**0.39**	**0.21**	22°	0.31	0.12	0.19	88°	0.00	0.10	0.10
15	74°	**0.19**	**0.14**	**0.33**	54°	**0.20**	**0.36**	**0.16**	18°	0.24	0.12	0.13	84°	0.09	0.06	0.02

Table 6.2: All possible Schmid factors (counted positive) corresponding to the twelve $\{111\}_\gamma \langle 112 \rangle_\gamma$ slip systems, in 15 grains. The $\{111\}_\gamma$ planes containing the planar faults are shown in bold. It can be seen that, in 10 grains out of 15, those features appeared on the planes with highest Schmid factor.

6.3.4 Formation of α'-Martensite and Variant Selection

As discussed in section 2.2.1, various hypotheses for the mechanism of formation of α'-martensite have been presented in the literature. In this section, the formation of α'-martensite is explored by examining the morphology, crystallography and spatial distribution of this phase. The crystallography is of particular interest since, as noted above, many fewer than the maximum number of 24 possible crystallographic variants are observed to form in a given grain. The particular selection of variants should relate to the mechanism of transformation.

In Figure 6.7, a local region from the grain shown in Figure 6.4(b) was highlighted where austenite, α'-martensite and ϵ-martensite all co-exist. The orientation relationship observed for the three phases was identified to be very close [10] to:

$$\{111\}_\gamma//\{0002\}_\epsilon//\{011\}_{\alpha'} \tag{6.2}$$

$$\langle 110 \rangle_\gamma // \langle 2\bar{1}10 \rangle_\epsilon // \langle 111 \rangle_{\alpha'} \tag{6.3}$$

corresponding to the Burgers orientation relationship between austenite and ϵ-martensite and to the Kurdjumov-Sachs (K-S) orientation relationship between γ and α'-martensite. These orientation relationships have been commonly observed before (e.g. [111, 238]) and have been used as evidence for a co-ordinated transformation from austenite to ϵ-martensite to α'-martensite [50, 239].

To help explore the crystallographic relationship between phases, a detailed analysis of several austenite grains has been made. The grain shown in Figure 6.4(b) and redrawn in Figure 6.10 illustrates one example of an analyzed grain where four α'-martensite variants are observed along with one (indexed) ϵ-martensite variant. Three of the α'-variants (numbered #1–3) are seen to co-exist on the same $\{111\}$ plane as the ϵ-martensite. These three variants (green, pink and yellow) can be distinguished based on the colour code of Figure 6.1 showing the crystallographic direction aligned with RD.

---

[10] There is always a small amount of spread in orientation relationship associated with the fact that the phases are plastically deformed.

A fourth α'-martensite variant (labeled as #4) appears on a second $\{111\}$ plane parallel to a low band contrast trace. Although variant #1 and #4 share the same colour in this map ($\langle 110 \rangle$ close to RD), they are not equivalent in orientation.

In Figure 6.10, the crystallographic orientation relationship between the three phases are represented in the form of pole figures. The top two pole figures reproduce the superimposed austenite and ϵ-martensite pole figures previously shown in Figure 6.7. In the subsequent pole figures, the close-packed planes ($\{111\}_\gamma$ superimposed with $\{011\}_{\alpha'}$) and the close-packed directions of austenite and α'-martensite ($\langle 110 \rangle_\gamma$ superimposed with $\langle 111 \rangle_{\alpha'}$) are presented for each of the four α'-martensite variants. The plane and direction parallelisms defined by these pole figures allow one to distinguish different K-S variants.

Consider first the plane matching condition $\{111\}_\gamma$ // $\{011\}_{\alpha'}$ represented in the left most column of pole figures in Figure 6.10. One can see that α'-martensite variants #1–3 all have a $\{011\}_{\alpha'}$ plane parallel to the same $(111)_\gamma$ plane. This $(111)_\gamma$ plane is parallel to the $\{0001\}_\epsilon$ plane and both have their trace parallel to one set of low band contrast features in the map. Consistent with the discussion in the previous section, this $\{111\}_\gamma$ // $\{011\}_{\alpha'}$ // $\{0001\}_\epsilon$ plane has the second highest Schmid factor for $\{111\}_\gamma$ $\langle 112 \rangle_\gamma$ slip.

Variant #4, forms with the plane matching condition corresponding to the $(1\bar{1}1)_\gamma$ plane (the plane having the highest Schmid factor for $\{111\}_\gamma$ $\langle 112 \rangle_\gamma$ slip) rather than the $(111)_\gamma$ plane. The trace of the $(1\bar{1}1)_\gamma$ plane is parallel to the second set of low band contrast features observed in this grain.
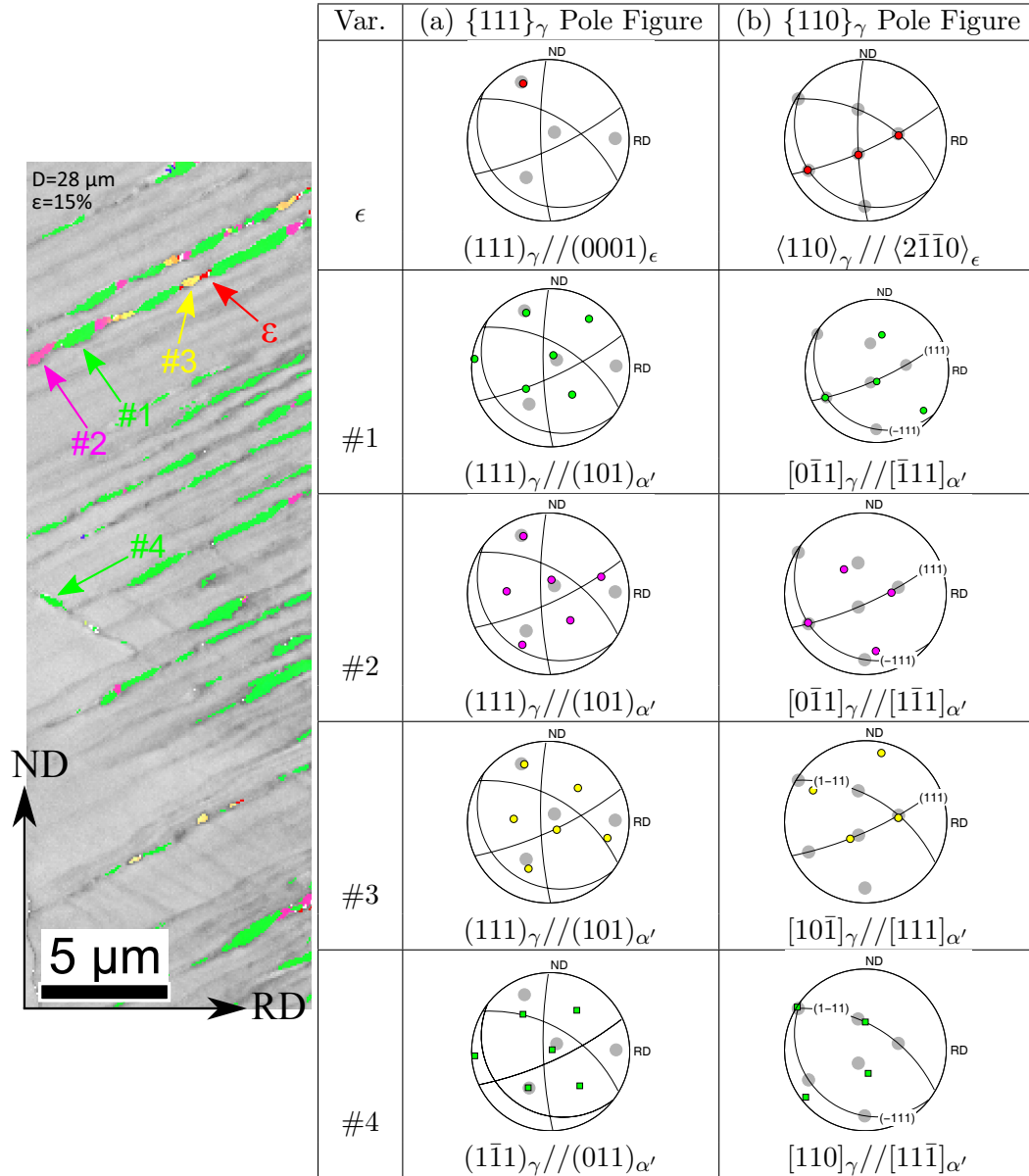
Figure 6.10: Superimposed (a) $\{111\}_\gamma$ and $\{110\}_{\alpha'}$ pole figures and (b) $\{110\}_\gamma$ and $\{111\}_{\alpha'}$ pole figures, showing the orientation relationship of the four identified variants of α'-martensite as observed in grain 1. Only the two $\{111\}_\gamma$ intersecting planes giving rise to the considered variant of α' are represented on the $\{110\}_\gamma$ pole figure.

To provide a more statistical analysis, the 32 α'-variants observed in the fifteen grains shown in Figure 6.9 have been analyzed. The orientations of the austenite grains and the α'-martensite variants are given in Table 6.1. Figure 6.11(a) shows the maximum Schmid factors for $\{111\}_\gamma \langle 112\rangle_{\alpha'}$ slip considering the specific $\{111\}_\gamma$ planes satisfying the plane matching condition in the K-S orientation relationship. Based on the plane matching condition $\{111\}_\gamma$ // $\{0001\}_\epsilon$ // $\{011\}_{\alpha'}$ and the above discussion concerning the tendency for ϵ-martensite to form on $\{111\}_\gamma$ planes having high Schmid factors, it should be expected that the $\{111\}_\gamma$ // $\{011\}_{\alpha'}$ planes should also have a high Schmid factor. One can indeed see a statistical preference for the formation of α'-martensite on planes having a high Schmid factor in Figure 6.11(b), with 78% of observed planes having either the highest or second highest Schmid factor within the grain.
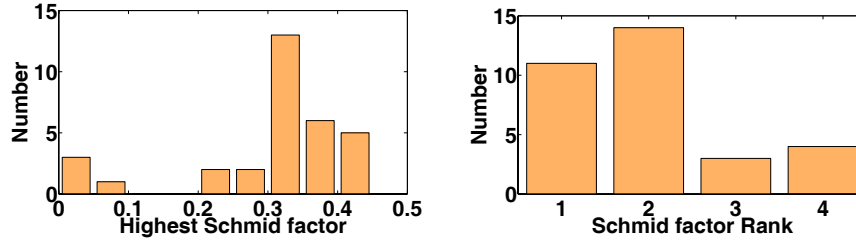
Figure 6.11: (a) Observed distribution of Schmid factors for $\{111\}_\gamma \langle 112\rangle_\gamma$ slip on the $\{111\}_\gamma$ planes corresponding to the plane matching condition in the K-S orientation relationship. (b) Rank of the corresponding Schmid factors, from highest (1) to lowest (4).

These results support the view that α'-martensite forms on pre-existing ϵ-martensite plates, which have formed by the glide of $\{111\}_\gamma \langle 112\rangle_\gamma$ dislocations on slip systems having high Schmid factors. Correspondingly, the plane matching condition between austenite and α'-martensite should be predictable based on a prediction of most active austenite slip systems. This view corresponds very well with the previous TEM observations of Suzuki *et al.* [111] who observed a similar tendency for the plane matching condition in the K-S orientation relationship to correspond to $\{111\}_\gamma$ planes having high Schmid factors. Suzuki *et al.* argued that the presence of α'-martensite
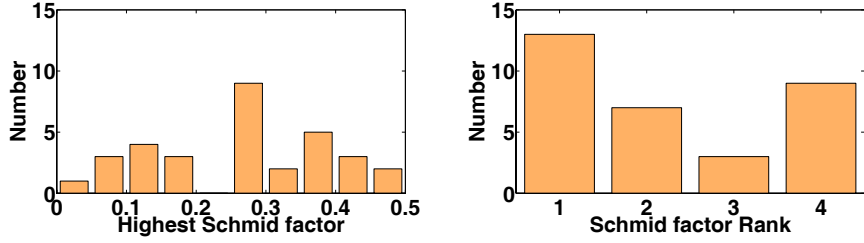
Figure 6.12: (a) Observed distribution of Schmid factors for $\{111\}_\gamma \langle 110 \rangle_\gamma$ slip on the intersecting $\{111\}_\gamma$ planes defined in Figure 6.13. (b) Rank of the corresponding Schmid factors, from highest (1) to lowest (4).

on planes with low Schmid factor increased with increasing fraction of α'-martensite, suggesting that the complex stress state imposed by the already formed α'-martensite would alter the local stress state from the macroscopic stress state assumed in the Schmid factor calculations.

The plane matching condition discussed above is necessary but not sufficient to determine the crystallographic variant of α'-martensite formed. A second condition that can be used to unambiguously identify different variants is that of direction matching (i.e. the parallelism between close-packed directions in austenite and α'-martensite, $\langle 110 \rangle_\gamma // \langle 111 \rangle_{\alpha'}$). For example, the α'-martensite variants (#1–3) in Figure 6.10 share the same plane matching condition but each can be uniquely identified as they have different direction matching conditions.

As noted above, the Patel-Cohen interaction energy method for variant selection has been recently applied to the prediction of the $\gamma \rightarrow \epsilon$, $\gamma \rightarrow \alpha'$ and $\epsilon \rightarrow \alpha'$ transformations [10, 50, 160]. Here, this method is used to examine the specific α'-martensite variants in Table 6.1 assuming that the transformation proceeds from $\gamma \rightarrow \epsilon \rightarrow \alpha'$ and that the plane matching condition in the K-S orientation relationship can be predicted based on the Schmid factor argument presented above. Thus, the Patel-Cohen interaction energy (based on the methodology presented by Humbert *et al.* [50], cf. Appendix B for a detailed description of the methodology) has been calculated for all possible variants of α'-martensite in a grain. Only those variants with high, positive values of the interaction energy would be ex-

pected to form [50]. The results of the interaction energy calculations for each of the observed variants are shown in Table 6.1. Out of 32 observed α'-martensite variants, 17 are predicted to have negative interaction energies, meaning that they should be energetically unfavourable and those would not be predicted to form.

The limitations of the interaction energy approach for predicting specific α'-martensite variants was discussed previously by Suzuki *et al.* [111] who pointed out that only one of two variants having anti-parallel common directions (e.g. variants #1 and #2 in Figure 6.10) will tend to be favoured by the interaction energy. Despite this, Suzuki *et al.* observed several cases where both variants were observed experimentally consistent with the observations presented here where anti-parallel variants were observed in grains 1, 9 and 14 when only one of the two variants is predicted to be energetically favourable.

In the recent work of Malet *et al.* [161], an alternative geometrical argument was made in order to predict observed variants. In this work, the α'-martensite was observed to form largely at the intersection between ϵ-martensite plates. In this case, the common plane condition of the K-S orientation relationship was satisfied with one of the two ϵ-martensite plates while the common direction condition was defined by the line of intersection between the two ϵ-martensite plates, a $\langle 110 \rangle_\gamma$ direction. In the work of Suzuki *et al.* [111], similar observations were made, though in that case the α'-martensite was triggered by the intersection of dislocations on one glide plane with a fault band (ϵ-martensite) on a second $\{111\}_\gamma$ plane. Again, the common direction condition of the α'-martensite was found predominantly to be that defined by the line of intersection between the two $\{111\}_\gamma$ planes. These observations are common with other mechanisms proposed for α'-martensite nucleation that involve intersecting $\{111\}_\gamma$ planes, for example the Olson-Cohen model for nucleation at intersecting ϵ-martensite plates [37].

In contrast to the work of Malet *et al.* [161], there is no evidence in the materials studied here for nucleation at ϵ-martensite intersections. Instead, a more likely situation would be that observed by Suzuki *et al.* [111] where

124

slip on a $\{111\}_\gamma$ plane intersected an ϵ-martensite plate (parallel to a second $\{111\}_\gamma$ plane) and that this event triggers the nucleation of α'-martensite in the ϵ-martensite plate. The geometry implied by this process is illustrated in Figure 6.13. The intersecting plane is the $\{111\}_\gamma$ plane that shares the K-S common direction with the K-S common plane.
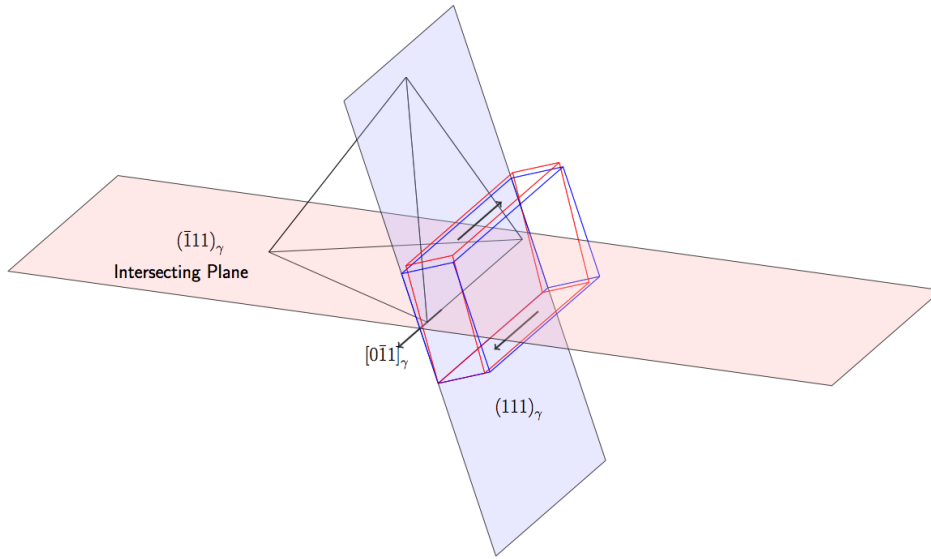
Figure 6.13: Schematic showing the geometry at a $\gamma/\alpha'/\epsilon$ interface. In particular, this shows how the direction parallelism and the plane parallelism from the K-S orientation relationship define a second austenite plane, the intersecting plane. The transformation strain needed to change ϵ-martensite (blue box) to α'-martensite (red parallelepiped) is dominated by a shear strain which is illustrated on the box at the point of intersection between the habit plane of the ϵ-martensite (light blue plane) and the intersecting plane (light red plane).

The above considerations of slip on the intersecting plane leading to the nucleation of α'-martensite on an intersected ϵ-martensite plate would suggest the possibility that the direction matching condition in the K-S orientation relationship could be predicted by looking for candidate intersecting planes with high slip activity. In order to check this hypothesis, the "intersecting" planes for the 32 variants of α'-martensite in Figure 6.9

have been identified and their Schmid factors calculated [11], the results being presented in Figure 6.12. Compared to the Schmid factors for the $\{111\}_\gamma$ plane satisfying the plane matching condition, the intersecting planes appear to correlate less strongly to a high Schmid factor. Only 62% of the intersecting planes were found to have the first or second highest Schmid factor compared to 78% for the plane matching condition. One of the possible reasons for this is that the intersecting plane must be different from the $\{111\}_\gamma$ plane satisfying the plane matching condition. This means that it is more likely that the intersecting plane will necessarily be one of the $\{111\}_\gamma$ planes having the lower Schmid factor.

Returning to the specific grain shown in Figure 6.10, one finds that variant #3 can be associated with the $\{111\}_\gamma$ planes having the first and second highest Schmid factors (specifically $(111)_\gamma$ as the plane matching condition and $(1\bar{1}1)_\gamma$ as the intersecting plane). This variant, however, is observed to be one of the minority variants within the grain. Variants #1, #2 and #4, on the other hand, all share $(\bar{1}11)_\gamma$ as intersecting plane. This plane has the lowest maximum Schmid factor amongst the four $\{111\}_\gamma$ planes in this grain.

To summarize the above results, it appears possible to predict the plane matching condition of the K-S orientation relationship based on the observation that the variants which form tend to have a high Schmid factor for the $\{111\}_\gamma$ plane which is parallel to the corresponding $\{110\}_{\alpha'}$ plane in the α'-martensite. The prediction of the direction matching condition does not seem to reliably correlate with either a condition based on interaction energy, nor with a condition based on a maximum Schmid factor on an intersecting plane. As pointed out by Suzuki *et al.* [111], there are a large number of possible dislocation reactions that one could consider leading to a specific α'-martensite variant. Not all of these necessitate slip on the intersecting plane as defined above. More detailed work is needed to identify the specific mechanisms leading to the selection of the direction matching condition in the formation of α'-martensite.

---

[11] The Schmid factors used here are for $\{111\}_\gamma \langle 110 \rangle_\gamma$ slip. The results are qualitatively the same if $\{111\}_\gamma \langle 112 \rangle_\gamma$ slip is assumed.

6.4   The Effect of Grain Size on the Strain-Induced Formation of Martensite

In section 5.5.2, it was shown that the macroscopic kinetics of α'-martensite formation exhibited a non-monotonic grain size dependence over the range of grain sizes prepared in this study. In this section, the microstructures associated with these different grain sizes will be compared in order to examine possible reasons for this behaviour. In particular this section will focus on contrasting the largest grain size (D=28 µm) and smallest grain size (D=0.5 µm) samples.

(a) $D = 0.5$ µm $- \epsilon = 0.20$ (b) $D = 2.2$ µm $- \epsilon = 0.15$

(c) $D = 28$ µm $- \epsilon = 0.15$
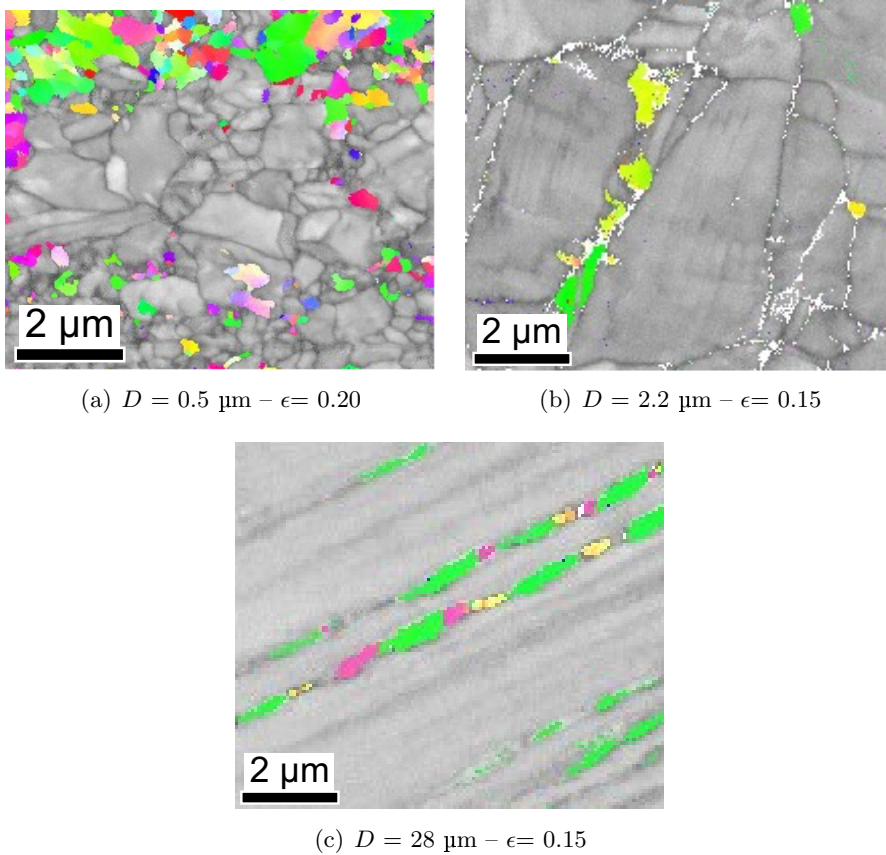
Figure 6.14: Spacing between observed plates (ϵ or faults bands) when the grain size is varied.

Figure 6.14 illustrates the microstructures of samples having grain sizes of D=0.5 µm, 2.2 µm and 28 µm, all viewed at (approximately) the same magnification, after similar levels of strain. Significant changes can be seen in the morphology and spatial distribution of α'-martensite within these maps. Most clearly, one can see that, by D=0.5 µm, the grain size is of a similar order of magnitude as the α'-martensite spacing in the case of the D=28 µm grain size sample. Thus, whereas in the case of the coarse grained material several α'-martensite variants were observed in each austenite grain, in the case of the D=0.5 µm samples, each grain typically contains only one or two α'-martensite variant.

(a)   (b)
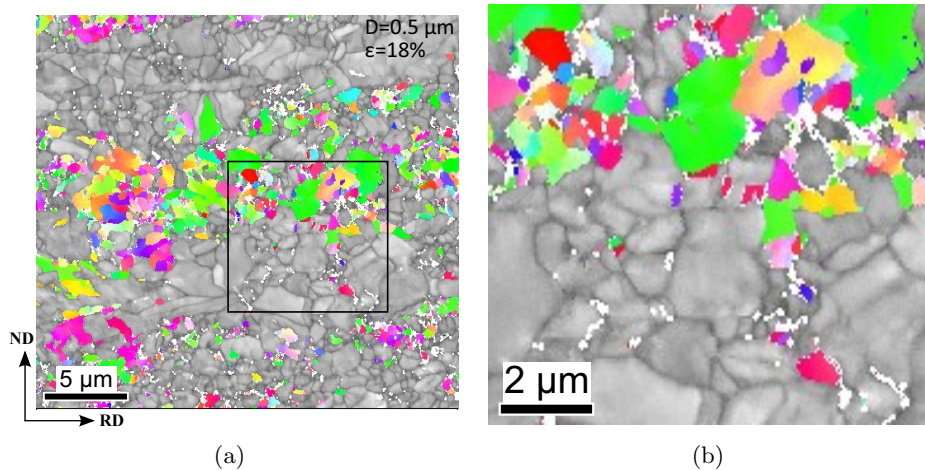
Figure 6.15: Orientation maps of the D=0.5 µm grain size condition, deformed at 18% strain in tension. (b) shows a higher magnification view of the highlighted area from (a), illustrating the lack of low index quality bands in the austenite in contrast to the observations in coarse grain size (e.g. Figure 6.5).

Figure 6.15 examines in more detail the microstructure of a D=0.5 µm sample, revealing several other features of note. First, from the lower magnification image of Figure 6.15(a), one has the impression that α'-martensite has preferentially formed within a band of austenite grains that are parallel to the prior rolling direction. Indeed this observation was made in several cases and can be linked to the observation of nickel segregation presented in

128

section 4.7.

Figure 6.16 shows a correspondence between nickel segregation (appearing lighter in Figure 6.16(a)) and the areas that have remained austenitic according to the EBSD map in Figure 6.16(b). As was previously noted, the effect of this segregation is more apparent for the fine grain sized materials owing to the similar scale of the segregation bands and the grain size.

(a)   (b)
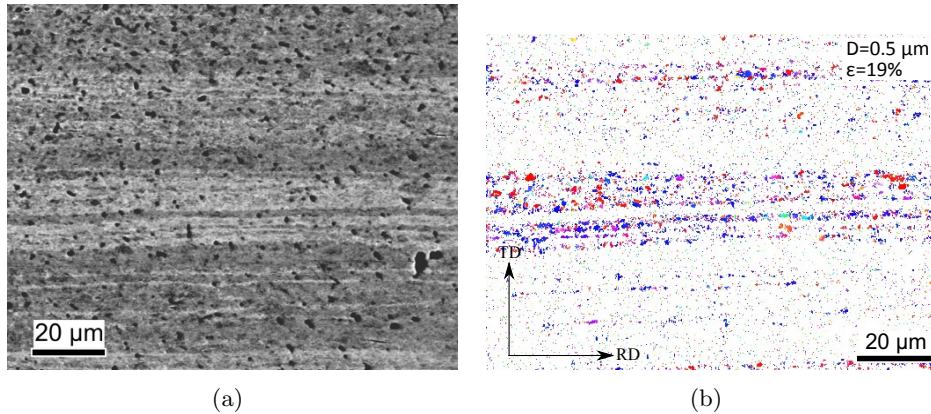
Figure 6.16: Nickel segregation corresponding to the region analyzed in Figure 4.8. (a) Back-scattered electron imaging in the SEM, showing the nickel-rich regions in lighter colours. (b) Austenite orientation map of the same area showing the islands which remained austenitic.

Returning to Figure 6.15 there are several other features that differ, compared to the coarse grained materials. Comparing Figure 6.15 to Figure 6.14(c), one notices that the low band contrast traces observed in the coarse grained samples are not apparent in the band contrast maps from the fine grained samples. Given the discussion in section 6.3, this would suggest a lack of ϵ-martensite in the case of the $D=0.5$ µm samples. This is consistent with the macroscopic X-ray diffraction results from section 5.11, which also showed no evidence for ϵ-martensite in samples with $D=0.5$ µm. TEM samples prepared from a fine-grained sample deformed 5% in tension were also observed. Figure 6.17 shows a low magnification view of the microstructure along with a selected area diffraction pattern which shows rings characteristic of austenite and α'-martensite, but not of ϵ-martensite.

A higher magnification view of an area from a different region in Figure 6.18 shows no ϵ-martensite, although extended faults and fine twins are observed.
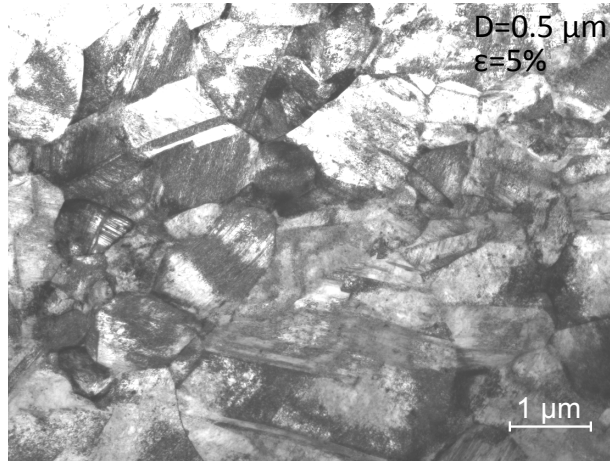
(a)
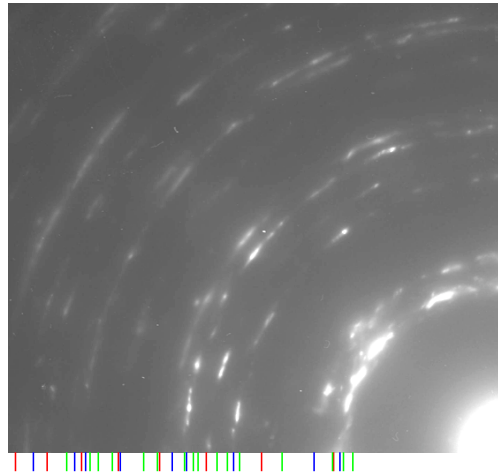
(b)

Figure 6.17: (a) Low magnification bright field image of a fine grained sample deformed to 5% strain. (b) Selected area diffraction pattern of the region viewed in (a). The lines under the diffraction pattern show the expected position of rings for austenite (blue), α'-martensite (red) and ϵ-martensite (green). No clear evidence for diffraction from ϵ-martensite could be found.
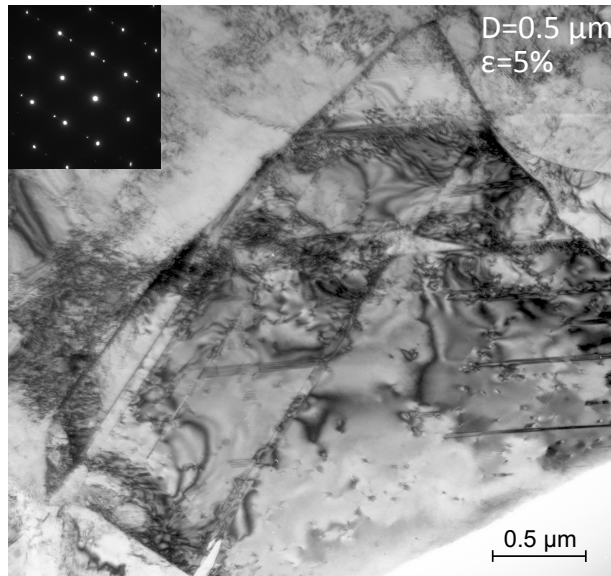
(a)
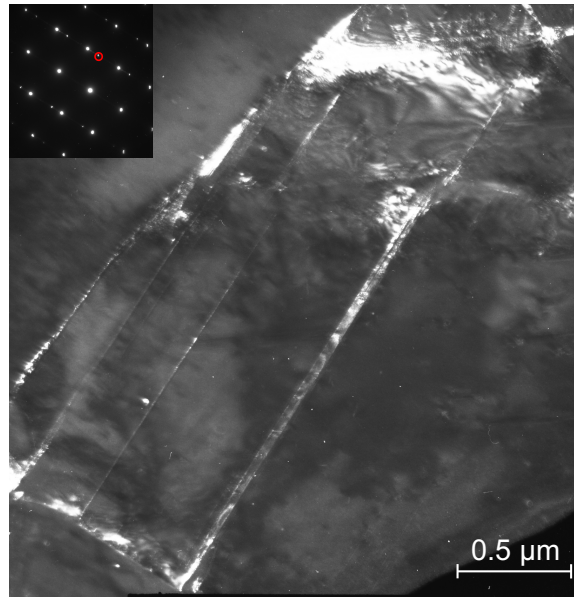
(b)

Figure 6.18: (a) Bright field image of a grain oriented close to $[110]_\gamma$ parallel to the beam direction, exhibiting stacking faults along with a set of fine twins (determined based on the extra spots in the accompanying selected area diffraction pattern). The faults and twins appear to emanate from grain boundaries. (b) Dark field image showing one set of twins.

131

It was argued in section 6.3 that the formation of α'-martensite occurs by the sequence $\gamma \rightarrow \epsilon \rightarrow \alpha'$. Based on the results presented here for the case of D=0.5 µm, this sequence cannot occur due to the absence of ϵ-martensite. In this case, an alternative mechanism leading to the direct transformation from austenite to α'-martensite needs to be envisaged.

In an attempt to identify more clearly the formation and propagation of α'-martensite in the D=0.5 µm condition, a series of sequential deformation experiments were performed. The results of this sequential mapping is shown in Figure 6.19 where the same area is viewed after tensile strains of 0.15 and 0.2. In Figure 6.19(a), a number of α'-nuclei are highlighted, all existing at austenite grain boundaries. In this case, it appears that the nucleation of α'-martensite is triggered by events at austenite grain boundaries. In the map of the same region following re-straining (Figure 6.19(b)), one observes an increase in α'-martensite fraction. In some areas, this has occurred with a sudden growth of martensite nearly completely filling prior austenite grains, while in other instances the small martensite nuclei observed in Figure 6.19(a) appear to propagate outwards and along grain boundaries.

Compiling together the data collected from several maps similar to those shown in Figure 6.19, one can examine the distribution of disorientation angles between austenite and α'-martensite both in the case of the coarse grained (D=28 µm) and fine grained (D=0.5 µm) samples, as shown in Figure 6.20. Here, one can see that both samples show a peak corresponding to the K-S orientation relationship. However, only 26% of the total α'/γ boundary length does not show the K-S orientation relationship in the case of the coarse grained samples, while 60% of the boundary length in the fine grained material was non-K-S. These non-K-S misorientations are due to K-S oriented α'-martensite which is situated at a grain boundary, the disorientation angle now being characterisitic of the relationship between α'-martensite and the neighbouring austenite grain.
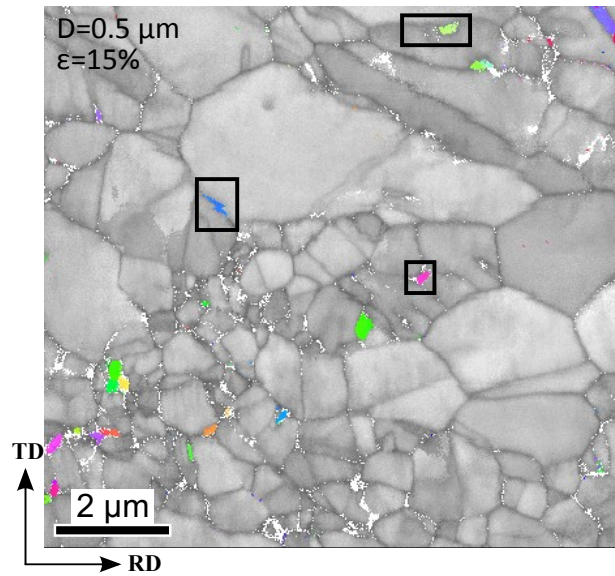
(a)
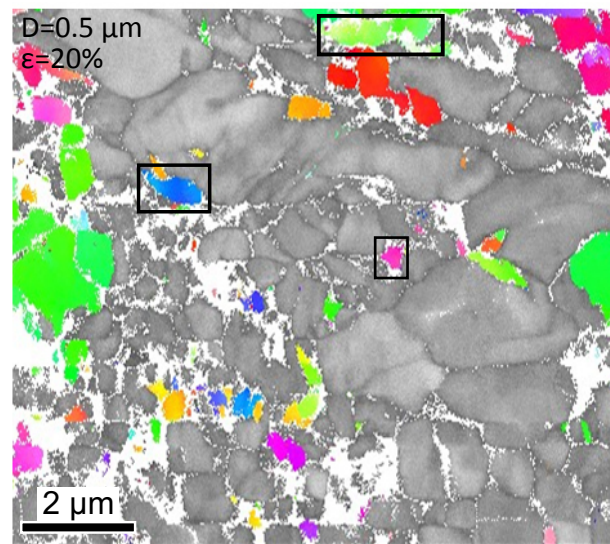
(b)

Figure 6.19: Sequential orientation mapping performed for a true strain of (a) 0.15 and (b) 0.2 where several grain boundary nuclei of α'-martensite have been highlighted. Many of these nuclei appear to grow when the strain is increased from 0.15 to 0.2.
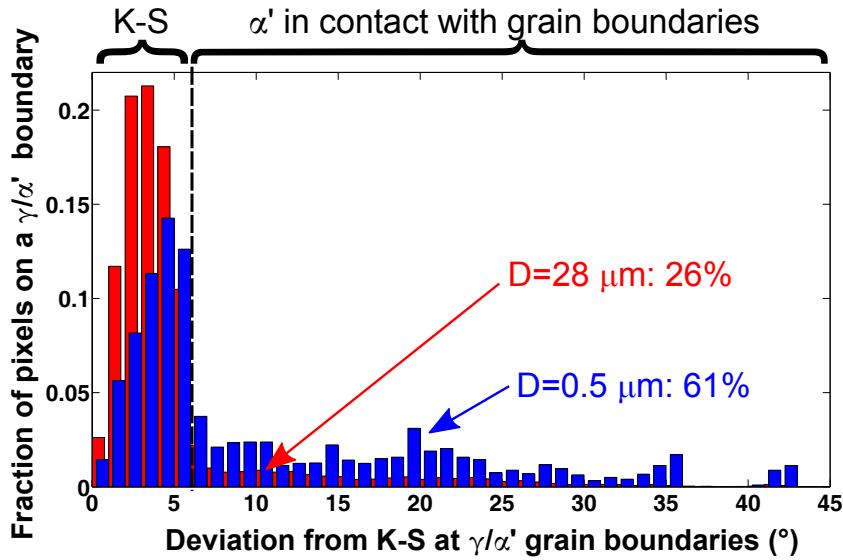
Figure 6.20: Fraction of grain boundaries versus boundary disorientation taken from EBSD maps corresponding to samples with $D=28$ µm and $D=0.5$ µm. The fraction of boundary length that has a disorientation of greater than 6° from the ideal K-S orientation is 26% in the case of coarse grained samples while it is 61% in the case of fine grained samples.

The difference in formation mechanism for α'-martensite in fine grained and coarse grained samples appears to also influence the morphology of the α'-martensite plates. In coarse grained samples, where nucleation is linked to planar ϵ-martensite plates, the α'-martensite appears to have a planar morphology. In the fine grained material, where nucleation appears to be linked to grain boundaries, the α'-martensite appears much less crystallographic and more irregular in shape. No planar α'-martensite was found in the fine grained austenite.

Given the apparent importance of grain boundaries as sites for the nucleation of α'-martensite in fine grained samples, a question that arises is whether grain boundary character is important. In particular the role of annealing twin boundaries is of particular importance given the crystallographic similarity between twin and ϵ-martensite boundaries (cf. section 2.2.3). It was reported in the work of Spencer that annealing twin bound-

aries were one location for α'-martensite nucleation [72]. In order to examine the possible influence of grain boundary character on preferred nucleation of α'-martensite, EBSD data from deformed fine grained samples were analyzed with specific reference to orientation relationship of the α'-martensite with its surrounding austenite matrix. In Figure 6.19, only 3 of 30 α'-martensite nuclei appear to be in contact with austenite annealing twin boundaries. To provide better statistics, the disorientation distribution from several maps has been examined to look for evidence of particular α'-martensite / austenite twin boundary relationships. The K-S orientation relationship can be described in terms of a disorientation angle ($\theta = 42.8°$) about a common crystallographic direction ($n = [0.97\ 0.17\ 0.17]$). Twin boundaries in austenite also present a specific crystallographic orientation described by the axis/angle combination of $\theta = 60°$ and $n = [1\ 1\ 1]$. A plate of α'-martensite nucleated on an annealing twin boundary will have a K-S orientation relationship with one of the austenite grains, and a second specific orientation relationship with the adjacent twin. This specific relationship can be described by the axis/angle combination of $\theta = 42.8°$ and $n = [0.82\ 0.47\ 0.32]$. This relationship has the same disorientation angle as the ideal K-S orientation relationship and therefore will not appear as a distinct peak in Figure 6.20. The K-S/Twin relationship does, however, have a different axis compared to the ideal K-S relationship. Therefore, plotting the disorientation data in Frank-Rodrigues space should allow for differentiation between the exact K-S relationship and K-S/Twin related α'-martensite and austenite. Figure 6.21 shows Frank-Rodrigues space[12] for the same data as used in Figure 6.20, where the data has been plotted showing only the surface corresponding to an intensity of 10 times the mean intensity. The ideal K-S orientation relationship is clearly seen at $r = [0.38\ 0.07\ 0.07]$. However, no peak in intensity is observed corresponding to the location associated with the K-S/Twin relationship, its ideal location ($r = [0.32\ 0.18\ 0.13]$) being indicated by the blue circle. These results seem to suggest that there is

---

[12] Frank-Rodrigues space represents orientations or misorientations as points at the end of a vector that is defined as $r = \tan{(\theta/2)}n$ where n and θ are the axis and angle describing the orientation relationship.

no particular (statistical) significance of annealing twin boundaries on the nucleation of α'-martensite. In fact, beyond the peak in Figure 6.21 corresponding to the K-S orientation relationship, no other strong peaks in the Frank-Rodrigues space could be identified suggesting no special relationship between particular boundaries and α'-martensite nucleation.
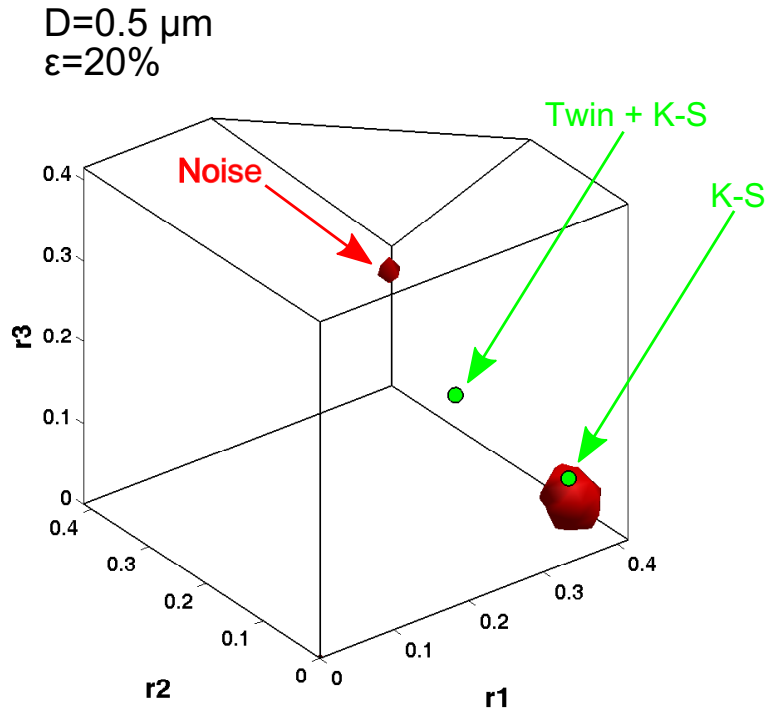
Figure 6.21: Locus of the grain boundary misorientation, represented in the Frank-Rodrigues space. No particular cluster of orientations can be found at the twinning relation. The intensity observed close to $r = [0.41\ 0.41\ 0.17]$ are small misorientations due to misindexing. Note that, due to the symmetry, $r = [0.41\ 0.41\ 0.17]$ is a location equivalent to $r = [0\ 0\ 0]$ [221].

The results above do not prove direct nucleation on grain boundaries but do seem to indicate that nucleation occurs either at or close to grain boundaries in the case of fine grained austenite. Indeed, even in the case of the coarse grained samples, careful observation reveals many α'-martensite plates that interact with grain boundaries (e.g. Figure 6.5). Recent work

by other authors has also suggested differences between the behaviour in fine grained and coarse grained samples. In the work of Yang *et al.*, a possible change of the nucleation mechanism for α'-martensite in a 304L grade deformed by ECAP was suggested [110]. Different morphologies of α' martensite have also been described for austenite grain sizes below 1 µm [110, 240]. In grade 301LN, while the intersections of so-called "shear bands" were observed to be at the origin of laths of α'-martensite in the coarse-grained material, the formation of microtwins (occasionally associated with short stacking faults) was observed to prevail in the submicron grain condition [240].

From EBSD data such as that shown in Figure 6.22, one can estimate the characteristic scale of both austenite and α'-martensite based on the average equivalent area diameter (EQAD) of the phases. The evolution of this quantity is plotted as a function of the true strain in Figure 6.23.
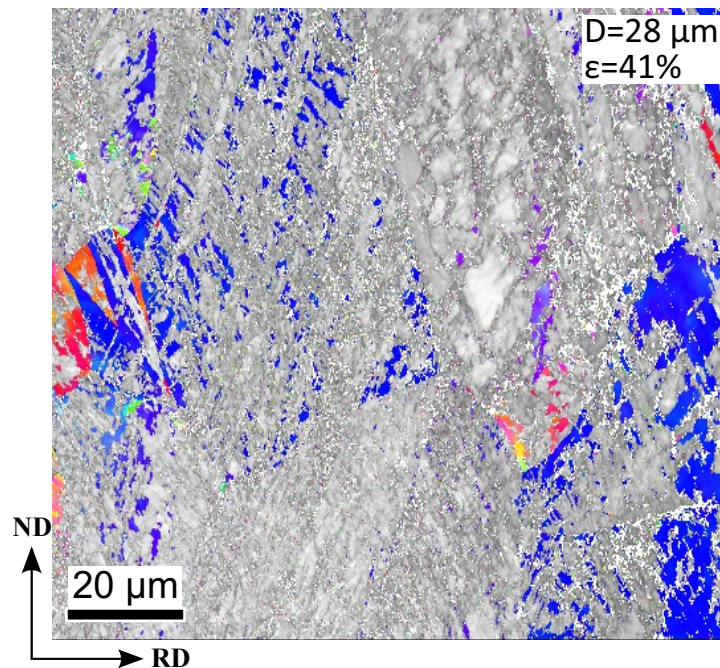
Figure 6.22: Austenite orientation map of a coarse-grained coupon deformed 41% in uniaxial tension.

(a) $D = 0.5$ µm

(b) $D = 2.2$ µm

(c) $D = 28$ µm
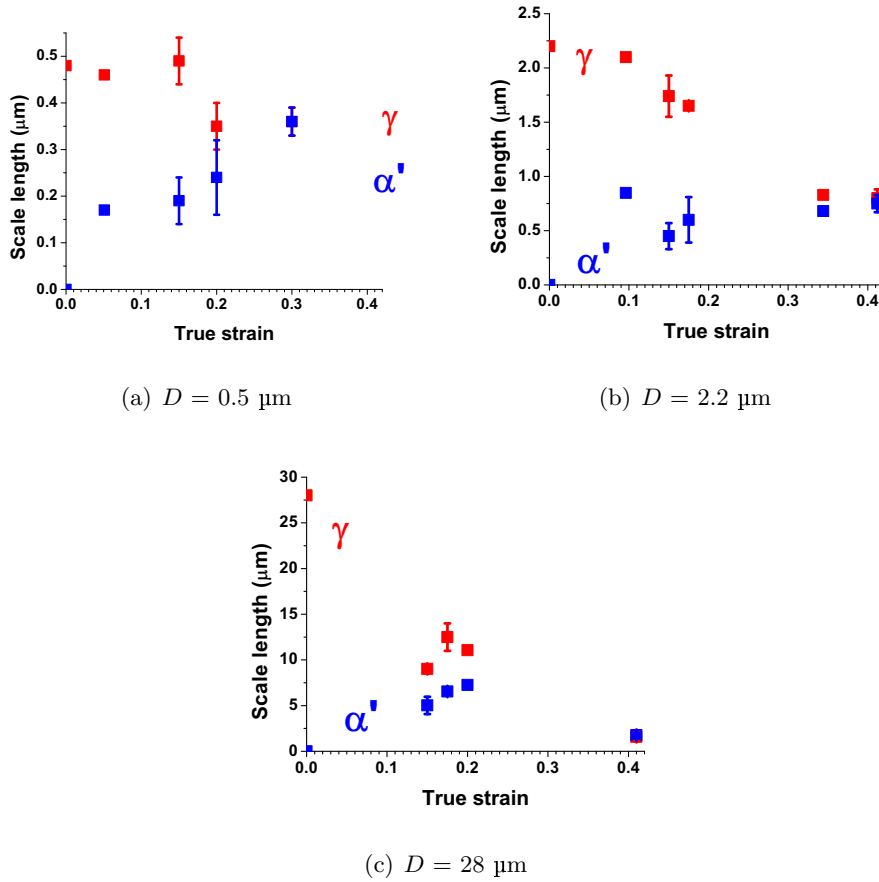
Figure 6.23: Evolution of the length scale of the microstructure, evaluated from EBSD, in (a) the 0.5 µm condition, (b) the 2.2 µm condition, (c) the 28 µm condition. The scale of both phases was evaluated from the EQAD on different EBSD micrographs.

In Figure 6.23(a), one can see that the EQAD of the austenite and α'-martensite in the material having $D = 0.5$ µm vary only slightly during testing. This is consistent with the observations made in, for example Figure 6.19, which showed that individual austenite grains are consumed by no more than 3 or 4 (and in many cases only 1) α'-martensite nuclei. It is also interesting to note that in Figure 6.19 an apparent growth of pre-existing α'-martensite variants occurred. The results in Figure 6.23(a) show that,

while some apparent increase in the average size of α'-martensite nuclei occurs during straining, the change in average size with strain is relatively small.

In Figure 6.23(b) and (c), a slightly different situation can be seen. Here, a substantial refinement of the austenite is observed with straining, again consistent with many α'-martensite nuclei forming in each grain. In the case of D=28 µm, the size of the remaining austenite islands after a strain of 0.4 is on the order of 1 µm. In both cases of D=2.2 µm and D=28 µm, the scale of both α'-martensite and ϵ-martensite converge by the a strain of 0.4. The size of α'-martensite islands, however, is relatively constant in both the cases of D=2.2 µm and D=28 µm, with the average α'-martensite size increasing from 0.3 to 0.7 to 7.2 for grain sizes of D=0.5, 2.2 and 28 µm respectively. One does, however, note a decrease in the average size of α'-martensite nuclei between strains of 0.2 and 0.4 for a starting austenite grain size of D=28 µm. Interestingly, at strains below 0.2, the average austenite size is larger than that α'-martensite size. As the strain is increased, however, the size of the austenite continues to decrease. Given that new α'-martensite can only form within remaining austenite islands, the average size of α'-martensite islands must also decrease.

The above results would indicate that the transformation kinetics are dominated by the rate of nucleation of α'-martensite, which forms with an approximately strain independent (but austenite grain size dependent) size. This latter point can be understood on the basis that the size of α'-martensite formed will be controlled by microstructural features within the material. As the α'-martensite cannot cross austenite grain boundaries (without destroying the preferred K-S orientation relationship) the largest possible size of α'-martensite should be the starting austenite grain size. However, other features such as ϵ-martensite, stacking faults, other α'-martensite variants will also act as obstacles to α'-martensite. In the case of the fine grain sizes (D=0.5 µm and D=2.2 µm), it is more likely that an α'-martensite variant can traverse the entire grain before being stopped. In contrast, one would expect more obstacles per grain in the coarse grain limit and therefore more nuclei per grain for a given volume fraction of

α'-martensite.
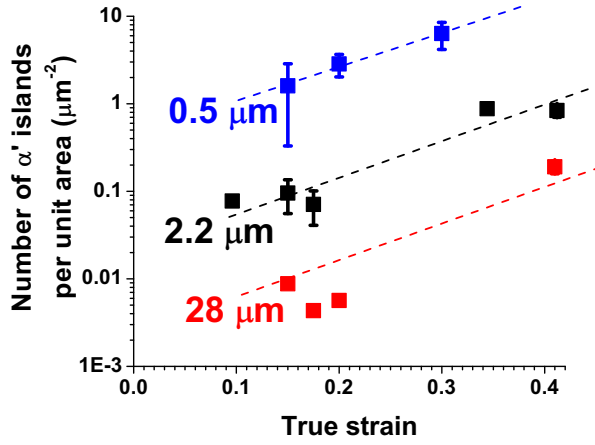
(a)
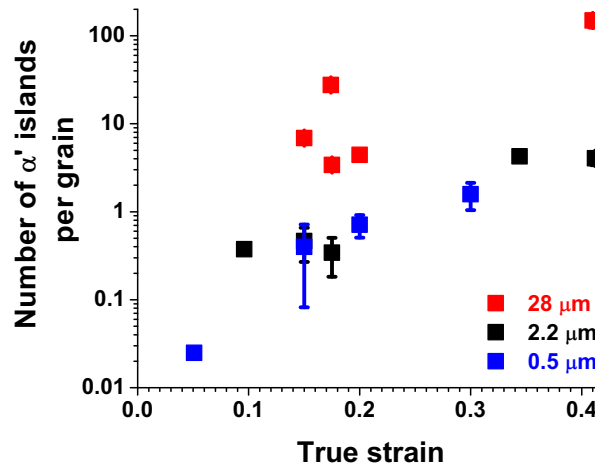
(b)

Figure 6.24: Evolution of (a) the surfacic rate of α' nucleation, (b) the rate per grain, for the three conditions of grain size studied. The error bars, when they exist, illustrate the variation measured from different orientation maps of the same condition.

One can investigate the grain size and strain dependence of the number of α'-nuclei by further interrogating the measured EBSD maps. The number of unique α'-martensite islands observed per unit observation area is plotted in Figure 6.24(a). This figure shows a much higher nuclei density in the fine grained materials compared to the coarse grained materials, however, if the data is plotted as the number of nuclei per grain then one sees that the values for grain sizes of D=0.5 µm and 2.2 µm are very similar while D=28 µm is higher as would be expected from the description above.

6.5 Microstructure Evolution in Simple Shear

D=0.5 µm D=28 µm
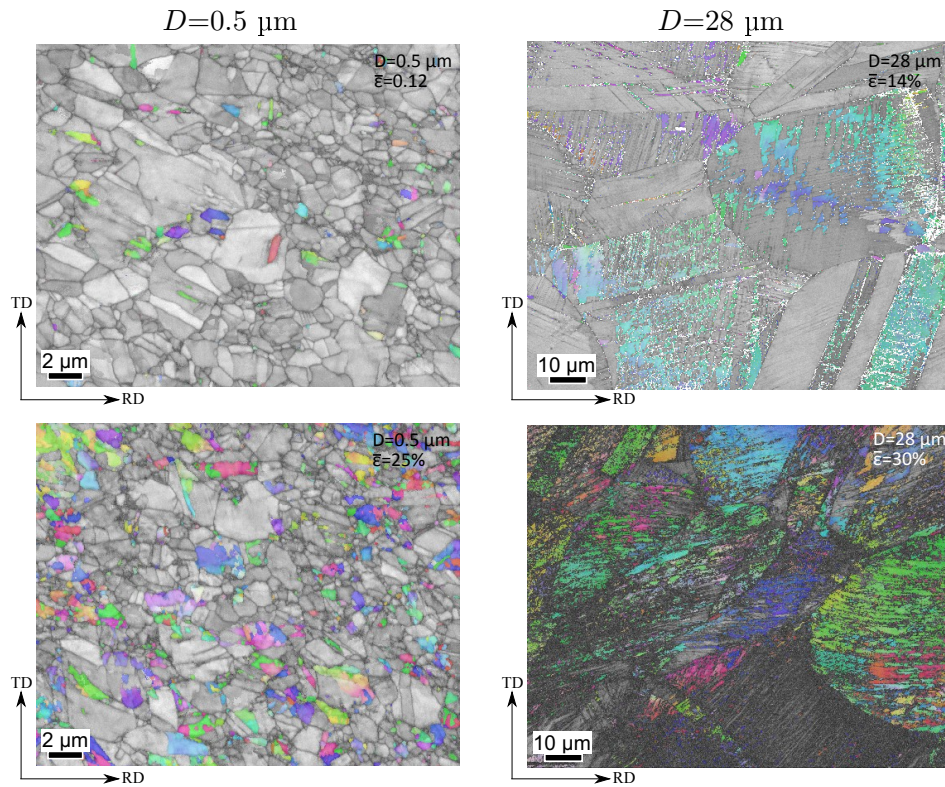
Figure 6.25: EBSD inverse pole figure maps of α'-martensite (colour) overlaid on band contrast maps for austenite illustrating the microstructure of samples deformed in simple shear.

141

The macroscopic transformation kinetics presented in section 5.5.2 showed that the rate of formation of α'-martensite in tension and shear are very similar when compared on the basis of Von Mises equivalent strain. Particularly, the kinetics are nearly identical up to strains of 0.2–0.3. Above these levels of strain, the rate of transformation in shear tended to be lower than in tension. Following from the results presented above, the microstructure of samples deformed in simple shear can be compared directly with those deformed in tension. Consistent with the results presented in section 5.5.2, few differences in the morphology or crystallography of α'-martensite could be found in samples deformed in shear versus tension (Figure 6.25).

As in tension, ϵ-martensite was indexed lying along traces of low band contrast leading to α'-martensite with similar morphologies, sizes and crystallographic orientation relationship as observed in tension. Figure 6.25 shows the variation of the microstructure sheared to different levels of strain. Though the macroscopic kinetics of α'-martensite transformation appear different in tension compared to shear, no significant microstructural differences could be found to correlate with this macroscopic behaviour.

6.6 The Link Between Macroscopic Transformation Kinetics and Microstructure

The results of this section illustrate the complexity of the austenite to α'-martensite transformation in these grades of steel. In the limit of large grain size, it was observed that the transformation primarily takes place by nucleation from ϵ-martensite plates, though some grain boundary nucleation may occur. While the formation of ϵ-martensite plates appears to depend on the magnitude of the applied stress, no good correlation between the applied stress and the formed α'-martensite could be found. As noted before, this may be due to the fact that one must consider the local state of stress rather than the global state of stress when applying criteria such as those applied above. These results, do however, raise questions about the application of interaction energy based methods for the prediction of α'-martensite

formation under the conditions considered here.

The strongest trend observed here is the correlation between the grain size, macroscopic transformation kinetics and the role of ϵ-martensite. It was argued here that refining the starting austenite grain size decreases the fraction of ϵ-martensite formed and therefore the rate of α'-martensite formed. Such a decrease in ϵ-martensite formation with decreasing grain size can be argued in a simple way. The O-C model presented in section 2.4 starts from a simple model for the kinetics of "shear band" formation. In the material studied here, these shear bands can be identified with plates of ϵ-martensite. The parameter α in Equation 2.6 can be re-written explicitly in terms of the volume of an ϵ-martensite plate and the number rate of formation of ϵ-martensite plates,

$$\frac{1}{1-f^\epsilon}\frac{df^\epsilon}{d\epsilon} = \bar{v}_\epsilon\frac{dN_v^\epsilon}{d\epsilon} \tag{6.4}$$

where N_v^ϵ is the number of ϵ-martensite plates per unit volume. If the epsilon plates are assumed to be circular plates of constant thickness t, then one can re-write Equation 6.4 as,

$$\frac{1}{1-f^\epsilon}\frac{df^\epsilon}{d\epsilon} = t\lambda_\epsilon^2\frac{dN_v^\epsilon}{d\epsilon} \tag{6.5}$$

where the size of the ϵ-martensite plates will be determined by the austenite grain size (i.e. $\lambda_\epsilon = D$). For larger grains, the plates may not be able to cross an entire austenite grain due to features such as other ϵ-martensite plates formed in another part of a grain, α'-martensite and dislocation cell walls, as seen in, e.g. Figure 6.5 and Figure 6.14.

Assuming that $dN_v^\epsilon/d\epsilon$ is independent of austenite grain size, Equation 6.5 would predict a rapid decrease in the rate of formation of ϵ-martensite with decreasing grain size. One might, however, argue that grain boundary nucleation of ϵ-martensite may become dominant with a decrease in grain size. In this case, the grain size dependence of the number density of nuclei would depend on the grain boundary surface area to volume ratio,

$$\frac{dN_v^\epsilon}{d\epsilon} \propto \frac{1}{D} \tag{6.6}$$

meaning that overall,

$$\frac{1}{1-f^\epsilon}\frac{df^\epsilon}{d\epsilon} \propto D \tag{6.7}$$

While the simple explanation given above qualitatively describes the decrease in the rate of formation of ϵ-martensite, and therefore a decrease in the rate of formation of α'-martensite, with decreasing austenite grain size, it does not explain the observed increase in the rate of α'-martensite formation for $D < 1$ µm. It was argued above that this change in α'-martensite transformation rate was due to a change in dominant mechanism of transformation from being dominated by nucleation on ϵ-martensite plates to being dominated by nucleation on austenite grain boundaries. In this case, one might expect that the rate of grain boundary nucleation of α'-martensite should vary with the grain boundaries' surface area to volume ratio $(1/D)$.

Such a grain size dependence qualitatively predicts the trends observed in Figure 5.12, with the minimum rate of transformation occurring for D=1 µm. Such a model, however, tends to strongly over predict the magnitude of the grain size effect on the macroscopic kinetics. This points out a number of important questions.

As noted above, in the limit of large D, α'-martensite appears to nucleate from pre-existing ϵ-martensite plates. However, it was also shown (Figure 6.24) that there was a strong refinement of the size of the austenite phase with strain and the formation of α'-martensite. Based on the above arguments, this should lead to a decreasing rate of formation of ϵ-martensite in the remaining austenite. Indeed, it may lead to the complete suppression of ϵ-martensite formation in the finest austenite regions.

Similarly, in the case of the finest grain sized material, it was observed that nucleation early in the deformation occurred on grain boundaries. These nuclei, however, were often observed to be smaller than the austenite grain size (Figure 6.19). Such a situation could lead to a rapid and

144

complete consumption of all grain boundary nucleation sites as $f^{\alpha'}$ tends to 1.

These two observations point to the fact that another mechanism for the formation of α'-martensite that does not require ϵ-martensite or austenite grain boundaries must exist. In Figure 6.19, it was observed that α'-martensite appeared to "grow" between two sequential images. Similar, though less conclusive, observations were made on sequential deformation experiments made on coarse grained samples. Such an observation may point to a further mechanism for the formation of α'-martensite either by a true growth of pre-existing nuclei (much as in the case of isothermal martensite [46]) or by a form of nucleation just ahead of pre-existing α'-martensite islands. Owing to the difficulty of resolving fine details of the microstructures of these samples at high strain, no detailed observations on this mechanism could be made.

Finally, it is interesting to note that there were no perceptible changes in the morphology or geometry of samples tested in simple shear compared to tension, regardless of grain size. The fact that the interaction energy was not capable of predicting the variants of α'-martensite formed in tension supports the idea that the macroscopic stress state is less important than what has been recently suggested on the basis of the Patel and Cohen model [241]. Indeed, it is perhaps not surprising that this model, originally developed to describe the effects of an elastic (i.e. nearly uniform) stress on the transformation of thermal martensite does not adequately capture the effects of stress on the transformation kinetics in a plastically deforming material where large stress concentrations may occur at, for example, dislocation pileups or grain boundaries.

Based on the results presented above, the original O-C model (including grain size dependence) is not capable of predicting the results obtained here. However, it remains valuable as an empirical model for describing the presented data. In this way, some of the ideas presented above have been used to modify the O-C model so that the observed grain size dependence of $df^{\alpha'}/d\epsilon$ can be captured. First, the fraction of shear bands (f^{sb}) described in the O-C model is replaced here with the volume fraction of ϵ-martensite

(f^ϵ). Considering the comments made above, it is assumed that the rate of formation of ϵ-martensite ($df^\epsilon/d\epsilon$) can be written as:

$$\frac{1}{1-f^\epsilon}\frac{df^\epsilon}{d\epsilon} = \alpha \tag{6.8}$$

where α is the rate of the $\gamma \rightarrow \epsilon$ transformation, assumed to be independent of strain. An empirical fit was adopted so that α has the grain size dependence described above, i.e.

$$\alpha = \frac{p}{D} + qD^r \tag{6.9}$$

where p, q and r have been taken to fit the experimental data displayed in Figure 5.13. Following Olson and Cohen [81], the rate of α'-martensite is taken as:

$$\frac{1}{1-f^{\alpha'}}\frac{df^{\alpha'}}{d\epsilon} = \beta\left(f^\epsilon\right)^n \tag{6.10}$$

where β is taken to be grain size independent, but temperature and stress state dependent. The integrated form of this equation is the same as the O-C equation presented in Equation 2.11, with the difference that the α-parameter is now dependent on grain size according to Equation 6.9. For convenience, n is fixed for all conditions as it was found to be possible to fit all α' formation kinetics considering $n = 5$. The best fit values of p, q and r are given in Table 6.3, considering β and n to be independent of grain size.

Deformation mode	p	q	r	β	n
Uniaxial Tension	0.42	3.41	0.08	4.52	5
Simple Shear	0.42	3.41	0.08	3.40	5

Table 6.3: Values retained for the modified Olson-Cohen model.

Using those values, the obtained fits to the kinetics are presented in Figure 6.26, while the non-monotonic grain-size dependence of α is plotted in Figure 6.27. This is viewed as a purely empirical model that will be used in chapter 8 when a model for the macroscopic mechanical behaviour

is presented.

(a)   (b)
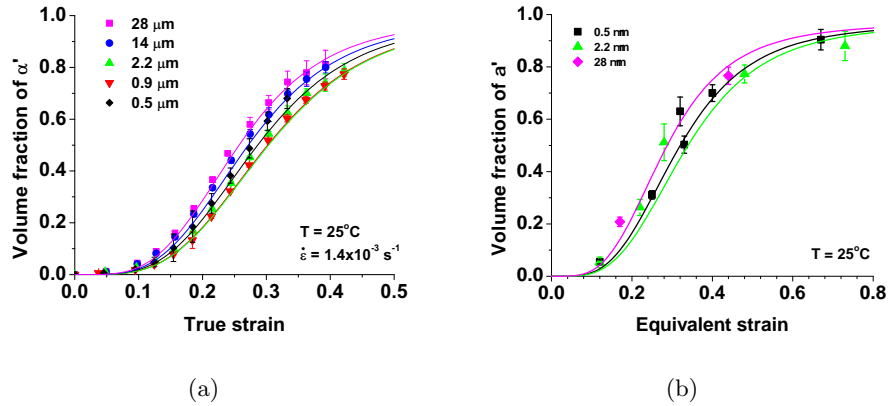
Figure 6.26: Application of equations 6.8 to 6.10 to reproduce the measured kinetics of formation of α'-martensite, (a) in uniaxial tension, (b) in simple shear.
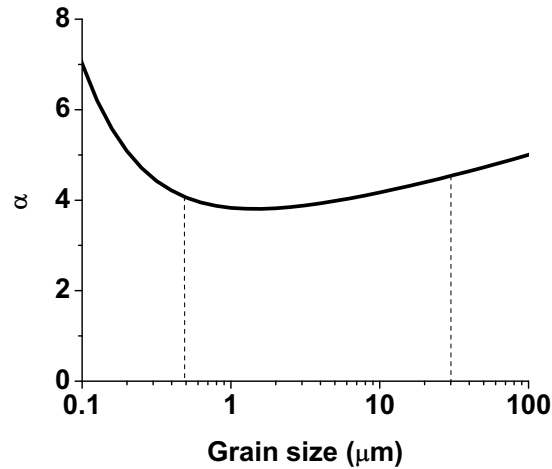
Figure 6.27: Variation of the α-parameter as a function of grain size, in present empirical model. The validity of this fit is limited to 0.5 µm $\leq D \leq$ 30 µm.

6.7 Summary

In this section, the detailed microstructural evolution occurring during the straining of samples having different grain sizes in tension and shear have been summarized. The key findings are that the transformation is nucleated at ϵ-martensite (coarse grain size) and grain boundaries (small grain size). It has been argued that a third mechanism must also exist in order to explain the continued formation of α'-martensite in the absence of ϵ-martensite or austenite grain boundaries. The grain size dependence of the transformation kinetics can be qualitatively understood in terms of the grain size dependence of the formation of ϵ-martensite as well as the increasing density of grain boundary nuclei with decreasing grain size. This picture would lead to the non-monotonic transformation kinetics observed here, for which an empirical model is proposed. Owing to the failure of criteria based on the macroscopic stress to predict the formation of individual α'-martensite nuclei, further work is needed to help provide insight into the mechanisms that lead to nucleation of α'-martensite during straining.

Chapter 7

A Novel Method of Estimating the Stresses in α'-Martensite

7.1 Introduction

In chapter 5, the bulk mechanical properties of 301LN stainless steel measured in tension and shear were presented. To develop a physically based description for these results, one must understand the contributions coming from the individual phases [242]. The complexity of this for the present material comes from the fact that three phases can co-exist (austenite, ϵ-martensite, α'-martensite) and that the fraction of these phases is continuously evolving with strain. In the previous two chapters it has been shown that ϵ-martensite exists only as a minority phase (if it is formed at all). Owing to this observation, and to simplify the following discussion, the mechanical behaviour of 301LN will be attributed to the austenite and the α'-martensite phases only, the possible effect of ϵ-martensite being neglected. This approach is the one that has been generally adopted in the description of metastable austenitic stainless steels in the literature [34, 207].

Understanding the contributions to the mechanical response arising from the austenite and α'-martensite phases requires some estimation of the stresses carried by these two phases *in situ*. Measurements of the *in situ* partitioning of stresses between γ and α' during co-deformation of austenitic stainless steels have previously been made using diffraction-based techniques (e.g. neutron, X-ray) [13, 194, 195, 243, 244]. While powerful, these

techniques have limitations, not the least of which is the need for access to major facilities in the case of experiments requiring a neutron or synchrotron source.

This chapter presents an alternative method for the estimation of the stress partitioning in metastable austenitic stainless steels by means of the magnetomechanical effect. It will be shown that this relatively simple technique gives results that are in excellent agreement with the results of neutron diffraction and X-ray diffraction measurements on the same grade of stainless steel. Moreover, the results of these measurements give important information required for the interpretation of the overall mechanical response in terms of the behaviour of the individual phases.

7.2 Magnetostriction and the Magnetomechanical Effect

Magnetostriction describes the shape change of a ferromagnetic material during the process of magnetization [245]. Under an applied magnetizing field H, favourably oriented magnetic domains will tend to grow by means of magnetic domain wall migration and/or domain rotation. This occurs so as to reduce the magnetic energy at the expense of increased elastic strain energy in the crystal. In the case of linear magnetostriction, sometimes referred to as the Joule effect, a ferromagnetic sample magnetized in a uniform field will undergo a strain denoted as λ. Normally, it is the value of λ measured at magnetic saturation (λ_s) that is reported in the literature. The magnetostriction strain, is actually a tensor, λ_s being the component of the magnetostriction strain observed parallel to the direction of magnetization. Linear magnetostriction is volume conserving so that the principal components of the magnetostriction strain obey $\lambda_1 + \lambda_2 + \lambda_3 = 0$. Magnetostriction is a function of imposed magnetic field, the magnetic properties of the material being magnetized and also the crystallographic direction parallel to the axis of magnetization. In the case of pure iron, the magnetostriction coefficients at saturation parallel to the $\langle 100 \rangle$ and $\langle 111 \rangle$ directions

are $\lambda_{\langle 100 \rangle} = 15 \times 10^{-6}$ and $\lambda_{\langle 111 \rangle} = -21 \times 10^{-6}$, i.e. magnetization parallel to $\langle 100 \rangle$ leads to an extension of the material while magnetization parallel to $\langle 111 \rangle$ leads to contraction parallel to this direction. An untextured polycrystal behaves isotropically, the magnetostriction coefficient of iron in this case being equal to $\lambda_{iso} = -7 \times 10^{-6}$.

From an engineering point of view, magnetostriction is a well known phenomenon that is central to many technologies [246]. For instance, magnetostriction is used in the production of high frequency actuators as well as in magnetic sensors. The most well-known engineering consequence of magnetostriction is that it is the source of the "hum" coming from electrical transformers.
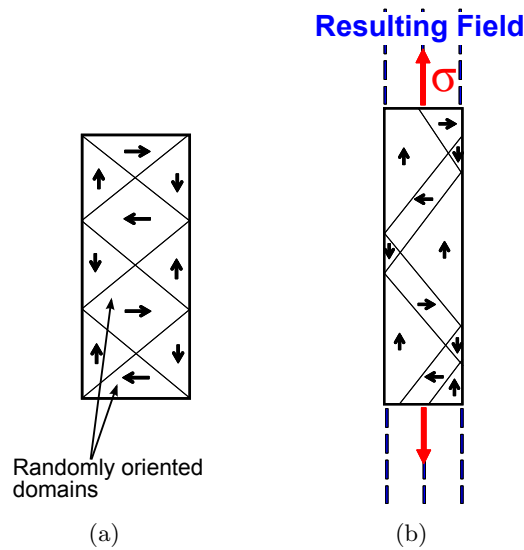
Figure 7.1: Schematic representation of the Villari effect. (a) In the absence of a mechanical stress, the magnetic domains tend to display randomly-oriented magnetization and the overall magnetic field is zero. (b) Once submitted to a mechanical stress, those favourably oriented start expanding to the detriment of others, thus creating a magnetic field.

In this study, it is the inverse effect, often called the magnetomechanical effect, that is of interest. While magnetostriction describes the straining of a ferromagnetic sample due to an imposed magnetic field, the magnetome-

chanical effect describes the change in magnetization induced by an applied stress. Other names are used in conjunction with the magnetomechanical effect. Piezomagnetism is sometimes used to describe this effect, while the term Villari effect is commonly used to describe the changes in the magnetic susceptibility at low magnetization due to an imposed stress or strain.

An imposed elastic strain (stress) couples to magnetic domains in a ferromagnetic material causing those domains that are favourably oriented to grow by means of domain wall migration and (to a lesser extent) domain rotation. This occurs to reduce the total combined magnetic and elastic energy of the system. Figure 7.2 shows the magnetization of an initially demagnetized sample of a low carbon steel under different levels of applied stress [247].
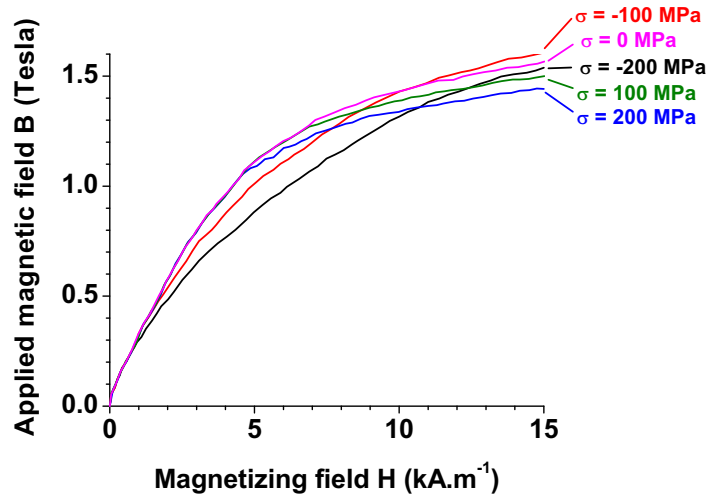
Figure 7.2: Variation of the anhysteretic magnetization curves with true stress, as measured in a Fe-2%Mn steel. Adapted from [247].

The effect is clearly complex as the magnetomechanical effect does not only change the saturation magnetization but also the apparent magnetic susceptibility. The origins of this effect are complex and difficult to describe analytically since it arises from electronic phenomena at the atomistic scale.

Jiles *et al.* have developed a methodology based on thermodynamic arguments giving the result that the effect of an imposed stress can be taken as being equivalent to an extra "effective" applied magnetic field [248]. This effective field can be written as,

$$H_\sigma = \frac{3}{2}\frac{\sigma}{\mu_0}\left(\frac{d\lambda}{dM}\right)_\sigma \tag{7.1}$$

where $M = B/\mu_0 - H$ is the magnetization, σ is the applied stress and μ_0 is the permeability. The calculation of $d\lambda/dM$ requires a knowledge of λ as a function of both M and σ. Analytical models describing this functional dependence are not generally available. Jiles *et al.* have taken an empirical approach to describing λ as a function of M and σ [248], these results showing good agreement with the anhysteritic behaviour shown in Figure 7.2.

Although less well understood compared to magnetostriction, the magnetomechanical effect has been used practically in a number of sensor technologies, including the estimation of stresses within engineering components (see e.g. [246]).

As described in Appendix A and section 4.2.1, a magnetic sensor (Feritscope MP30) has been used to estimate the volume fraction of ferromagnetic α'-martensite in this thesis. Other authors using the same approach have noted that the measurements of α'-martensite made in this way should be carefully analyzed to avoid the magnetomechanical effect arising from stresses in the α'-martensite phase [34, 249–251]. In a limited number of cases, however, the application of the magnetomechanical effect to estimating stresses in ferromagnetic materials has been explored. Kaleta *et al.* explored the possibility of using the magnetomechanical effect as a way of assessing fatigue life for samples where the cyclic strains are very small (stresses close to the fatigue limit) [252]. It was shown that the magnetic measurements could be well correlated to the fatigue life. Moreover, it was shown that a measurement of the magnetizing field strength (H) correlated well with the stress carried by a sample of pure nickel.

The recent work of Post *et al.* [70] is notable in that it marks a first

attempt at using the variation in magnetic induction with applied stress as an estimator for the stresses in strain-induced α'-martensite. In this case, a sensor was attached to a tensile sample and measurements of induced voltage difference between two sensing coils was used to estimate the fraction of α'-martensite. It was found, however, that the same sample had a different magnetic response if the induction was performed under load or on unloading. A systematic decrease in induction was observed with higher strain and volume fraction of α'-martensite. Post *et al.* [70] used the signal measured under load compared to samples under no load as a way of correcting the induction measurement so as to be able to have a measure of the fraction of α'-martensite during continuous loading of the sample. In this work, it was implied that the effect of the stress on the magnetic induction was due to the hydrostatic component of the macroscopically imposed stress state, though in reality the stress state in the α'-martensite will not be the same as that imposed macroscopically. As discussed above the magneto-elastic coupling arising from the magnetomechanical effect in strong ferromagnetic materials (such as α'-martensite) is not purely dilational. Moreover, the stress-state within the individual α'-martensite nuclei should vary strongly from the macroscopic state of stress (particularly at low volume fractions of α'-martensite). Despite these issues, the results of Post *et al.* are very encouraging as one could argue that the measured variation in magnetic induction with stress in α'-martensite, if appropriately calibrated, could be used as a scalar estimate of the *in situ* stresses carried by α'-martensite during the deformation of a metastable austenitic stainless steel. In this chapter, an attempt to make this correlation is presented.

7.3 Experimental Techniques

In these experiments, the variation of Feritscope signal (directly related to the magnetic induction measurements made by Post *et al.* [70]) have been made during the tensile deformation of 301LN. Unless otherwise specified, the geometry of the tensile coupons is the one which appears in Figure 5.1, and the deformation setup is the one defined section 5.2.1, both for room-

temperature and 80°C tensile loadings. The Feritscope measurements were made according to the procedure described in section 4.2.1. Six measurements were made in the gage length of the sample for each condition measured in order to assess the uniformity of the measurement.

As noted above, the magnetomechanical effect is very complex and, at present, only semi-empirical relations exist to describe it. Moreover, the Feritscope used in these experiments does not produce a simple axial magnetic field of uniform strength [216]. Indeed, the Feritscope induces a spatially non-uniform field in the sample to be measured. Given all of these complexities, a simplified empirical procedure has been used in an attempt to calibrate the effect of applied stress on the Feritscope response. This involved the production of a sample containing approximately 100% martensite as a reference sample from which to calibrate the stress sensitivity of the results.

The reference sample was produced by performing a tensile test to the point of necking in a bath of liquid nitrogen at -196°C). In this case the rate of work-hardening in the sample was very large (Figure 7.4) and, therefore, to avoid the spreading of plasticity into the grip section the width of the grip area had to be increased compared to the sample geometry described in Figure 5.1. This new sample geometry is given in Figure 7.3.
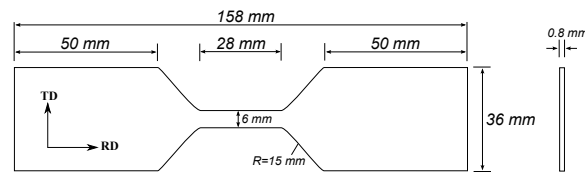
Figure 7.3: Geometry of the tensile coupons used at cryogenic temperatures.

Tensile samples for low temperature testing were prepared from rolled sheet and annealed following the annealing procedure required to produce a 28 μm average grain size (condition E in Table 4.2). The tensile curve from this test (Figure 7.4) exhibits an upper and lower yield stress, as well as a plateau indicating strain localization. As mentioned in section 2.5.1, this feature is common for low temperature testing of this grade of austenitic stainless steels [10].

Figure 7.4: Tensile stress-strain curve of the D=28 µm test coupon at cryogenic temperature.

The volume fraction of α'-martensite in this reference sample was measured using the Feritscope and found to be equal to 91%. This compares to a maximum of 81% α'-martensite measured at the onset of necking in a sample tested at room temperature.

7.4 Estimation of Stress Carried by α'-Martensite via the Magnetomechanical Effect

The magnitude of the magnetomechanical effect on Feritscope measurements is illustrated in Figure 7.5(a), where the results of Feritscope measurements are plotted for two tensile loading experiments [13] made on samples having an austenitic grain size D=28 µm. The results for other conditions of grain size will be discussed in section 7.5. In the first experiment, the test was interrupted and the sample periodically unloaded (to 0 MPa stress) and a

---

[13] The experimental setup for shear testing did not allow for *in situ* measurement using the Feritscope during testing. Thus, only results for uniaxial tension are shown here.

Figure 7.5: (a) Evolution of the Feritscope signal during straining, with measurements performed on two samples, under load and unloaded. The error bars show the range of the signal measured by the Feritscope during six measurements. (b) Corresponding stress-strain data, with the actual measurement points indicated.

Feritscope measurement made. In the second experiment, a sample of the same material was tested in the same way, being interrupted at the same levels of strain but instead of unloading, the sample was held under load at a fixed actuator position and Feritscope measurements were made. For the measurements under load, the tensile tests had to be interrupted with the tensile machine in displacement control. During these holds the load was observed to drop by 10–12% (relative to the stress at the point where the test was stopped) because of stress relaxation. The results presented below are all plotted with respect to the stress measured at the point where the test was stopped.

While, overall, the two curves in Figure 7.5 are similar, both exhibiting a sigmoidal shape characteristic of the transformation kinetics, they begin to diverge above a true strain of approximately 0.2. These results are qualitatively very similar to the results presented by Post *et al.*[70] and indicate an increasing importance of the magnetomechanical effect with increasing macroscopic stress and transformed fraction. Here, the results obtained in the macroscopically unloaded state (F_S^0) are used to estimate the volume fraction of α′-martensite as described in section 5.5.2. Even when the two-

157

phase austenite/α'-martensite mixture is macroscopically in the unloaded state, the individual phases will contain residual stresses. While this could lead to errors in the estimated fraction of α'-martensite due to the magnetomechanical effect even in the macroscopically unloaded state, the results shown below will indicate that the stress effect on Feritscope measurement is negligible for stresses below 600 MPa. A final point on these measurements is that it has been indicated that plastic deformation can also influence the magnetic response of a ferromagnetic material [70]. This can be due to macroscopic texture changes (magnetic anisotropy) as well as through the effect of dislocations on the domain structure. While it is not envisioned that the texture of the α'-martensite changes drastically with deformation in this material [238], it is very difficult to separate the remaining effects of plastic deformation from the effects of stress (elastic deformation) over the range of strains applied to the material. Thus, in this work we consider all changes in Feritscope signal to arise from either changing volume fraction of α'-martensite or to intrinsic stresses in pre-existing α'-martensite.

In order to interpret the results in Figure 7.5(a) in terms of the stress carried by the α'-martensite phase, it is necessary to use the reference sample defined in section 7.3 which contains nearly 100% α'-martensite. This pre-deformed sample was incrementally re-loaded elastically at room temperature. At predetermined levels of elastic strain, Feritscope measurements were made while the sample was held under load. These measurements are shown in Figure 7.6(a), where the raw Feritscope measurement is given without the correction factor described in Appendix A. As can be seen, the Feritscope reading is not very sensitive to stress for low stresses but the signal decreases rapidly with increasing stress. In order to normalize this result with respect to the fraction of α'-martensite in the sample, one can plot the ratio of the Feritscope measurement under load to the Feritscope measurement under no load, i.e. F_s/F_s^0.

In a fully martensitic sample, Figure 7.6(a) should be sufficient to use as a calibration of stress born by the α'-martensite phase as a function of F_s/F_s^0 for any value of pre-strain and therefore any value of F_s^0. In the reference sample considered here, the microstructure is not fully martensitic but (as

(a)   (b)
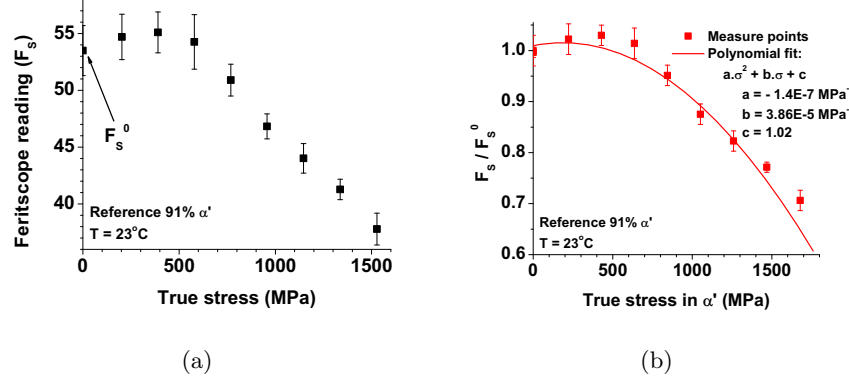
Figure 7.6: (a) Feritscope measurements (F_S) obtained in the reference sample, when reloaded elastically at room temperature. (b) Evolution, in the reference, of F_S normalized by the the Feritscope measurement at zero applied stress (F_S^0) as a function of applied stress. The error bars only show the spread in the F_S measurement.

noted above) was measured to contain $\sim 9\%$ retained austenite. As a first order approximation, it is assumed that the fraction of the stresses borne by the austenite ($(1 - f_{\alpha'})\, \sigma_\gamma$) are small relative to the fraction of the stresses borne by the α'-martensite. The relationship between the macroscopic stress (σ_{ref}) and the stress carried by the martensite ($\sigma_{\alpha'}$) can then be given by the condition for stress equilibrium as,

$$\sigma_{\mathrm{ref}} = f_{\alpha'}\sigma_{\alpha'} + (1 - f_{\alpha'})\, \sigma_\gamma \approx f_{\alpha'}\sigma_{\alpha'} \tag{7.2}$$

and therefore,

$$\sigma_{\alpha'} \approx \sigma_{\mathrm{ref}}/f_{\alpha'} \tag{7.3}$$

The resulting relationship between the Feritscope measurement and the stress $\sigma_{\alpha'}$ is illustrated in Figure 7.6(b). To be able to use this result as a calibration curve for other samples, an empirical polynomial fit has been made to the experimental data, as shown in Figure 7.6(b).

Returning to the data shown in Figure 7.5 it is now possible to estimate the level of stress carried by the α'-martensite using the calibration given

in Figure 7.6(b). As one can see, the sensitivity of this technique is poor at stresses $\sigma_{\alpha'} < 600$ MPa, a result that could reflect the difficulty of moving domain walls below a critical threshold stress [220]. However, for data above this level of stress, the effect of stress on F_s/F_s^0 is significant and easily detectable. By taking the data from the two curves given in Figure 7.5(a) to generate F_s/F_s^0 and using the empirical fit to the data in Figure 7.6(b), one can obtain an estimate for $\sigma_{\alpha'}$ as shown in Figure 7.7(a). The error bars on $\sigma_{\alpha'}$ have been estimated based on the the uncertainty in $f_{\alpha'}$. Though regular measurements of F_s and F_s^0 were made as a function of strain, it was found that reliable estimates of $\sigma_{\alpha'}$ could only be found for measurements above strains of 0.2. Below this level of strain the uncertainty in the Feritscope measurement (as reflected by the variation coming from the 6 measurements on a single sample) overwhelmed the ratio F_s/F_s^0, which is seen in Figure 7.5 to be very small for strains below 0.2.

As will be discussed further in chapter 8, the critical parameter relating to the stress borne by the α'-martensite phase is $f_{\alpha'}\sigma_{\alpha'}$. Plotting $f_{\alpha'}\sigma_{\alpha'}$ rather than $\sigma_{\alpha'}$ has the added advantage that it reduces the significance of the errors noted above when $f_{\alpha'}$ is low. In order to compare $f_{\alpha'}\sigma_{\alpha'}$ with the macroscopic flow stress, both are plotted in Figure 7.7(b). The shape of $f_{\alpha'}\sigma_{\alpha'}$ appears sigmoidal reflecting the evolution of $f_{\alpha'}$ with strain. Both the magnitude and shape of $f_{\alpha'}\sigma_{\alpha'}$ are, however, influenced by $\sigma_{\alpha'}$. This is consistent with the discussion in section 5.6, where it was shown that the macroscopic hardening rate could not be explained by $df_{\alpha'}/d\epsilon$ alone and that some intrinsic hardening of the α'-martensite phase must also be present.

.

7.4.1 Comparison of Results with Other Estimates for Stresses in Martensite

The results presented in Figure 7.7 can be compared to various other experimental methods for estimating the value of $f_{\alpha'}\sigma_{\alpha'}$. Here, such a comparison can be made against estimates arising from an assumed behaviour for austenite and, more reliably, against results arising from neutron diffraction

(a) (b)
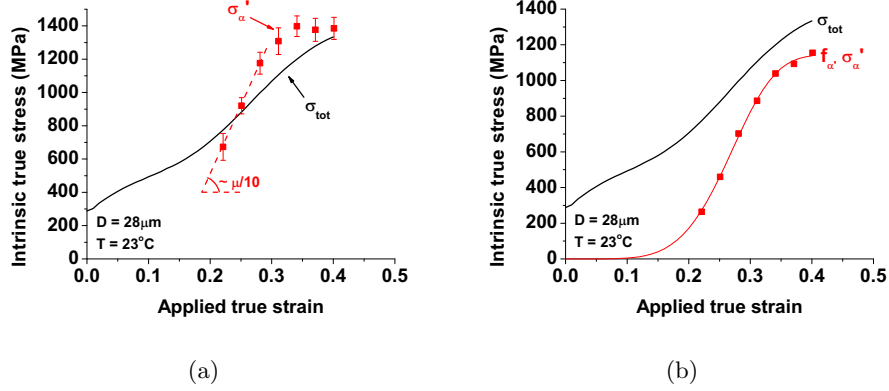
Figure 7.7: (a) Intrinsic stresses measured in the α'-martensite. (b) Same as (a) but multiplied by the volume fraction of considered phase. Points are the actual measurements.

experiments.

In chapter 5, macroscopic tensile curves for 301LN were measured at $80°$C. These results indicated that, after correcting the yield strength for temperature, the hardening rates of the samples tested at $80°$C was nearly identical to the behaviour measured at room temperatures for strains up to approximately 0.15 (i.e. up to the point where $df_{\alpha'}/d\epsilon$ becomes significant). If it is hypothesized that this behaviour can be extrapolated to explain the behaviour of austenite over the full range of strains investigated at room temperature, then an estimate for $f_{\alpha'}\sigma_{\alpha'}$ based on equilibrium of stresses can be obtained as:

$$f_{\alpha'}\sigma_{\alpha'} = \sigma_{tot} - (1 - f_{\alpha'})\,\sigma_\gamma \tag{7.4}$$

The magnitude of $f_{\alpha'}\sigma_{\alpha'}$ estimated in this way based on the $80°$C tensile data from Figure 5.6 is compared to the Feritscope estimate of $f_{\alpha'}\sigma_{\alpha'}$ in Figure 7.8.

While the above analysis requires strong assumptions (both in terms of the estimates in σ_γ as well as in the Feritscope estimated $\sigma_{\alpha'}$), the results show remarkably good agreement. This is particularly true considering that
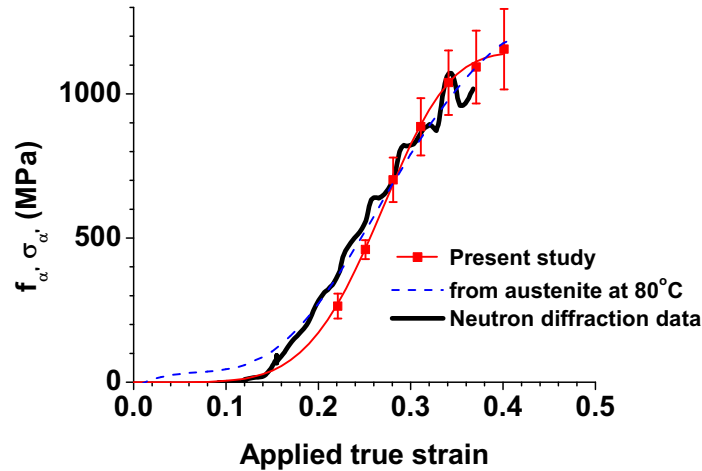
Figure 7.8: Comparison of the fraction of stresses in the α'-martensite obtained from Feritscope measurements compared with neutron diffraction measurements [13] and theoretical stresses obtained from Figure 5.18, by extrapolating the behaviour of the austenite from 80°C tests.

the behaviour of the austenite has had to be extrapolated well beyond where it can be independently measured at room temperature and to strains where the remaining volume fraction of austenite is low.

A second check of the Feritscope estimated $f_{\alpha'}\sigma_{\alpha'}$ can be made in comparison with neutron diffraction measurements. An independent study, by Dufour [13] at the **Université Catholique de Louvain** was undertaken using *in situ* time of flight neutron diffraction measurements during tensile testing of the same steel as studied here. These experiments were performed to estimate the stresses in both austenite and α'-martensite by means of changes in the lattice parameters of the austenite and α'-martensite phases. Rietveldt whole-pattern analysis of neutron diffraction spectra provided the evolution of the lattice parameters for different crystallographic planes of each phases. The determination of a strain-free lattice parameter for the α'-martensite was carried on by different methods, including the X-ray diffraction measurement of internal stresses by the $\sin^2\psi$ method. Knowing

162

the change in unit cell parameters as a function of macroscopic strain allows for an average elastic strain to be estimated (using the stress-free lattice parameter) for both austenite and α'-martensite. Based on the Rietveld analysis, an average behaviour of the phase was used to estimate the average stresses carried by each phase. The details of the calculation of the intrinsic stresses can be found in reference [13].

While the same grade of steel (provided by ArcelorMittal) as analyzed by Dufour was used in this study, the material used by Dufour had been given a small skin pass as a final step in the processing before final coiling. It was found that the macroscopic tensile response of the material studied by Dufour matched very well to the stress-strain response of the material studied here if their data was offset by a 6% strain. This is illustrated in Figure 7.9. Moreover, if the work-hardening rates of the two materials are compared on the basis of stress rather than strain, one finds that they are nearly identical, as one would expect. Thus, in the following comparisons Dufour's data has been corrected by adding 6% strain corresponding to the shift shown in Figure 7.9.

(a) (b)
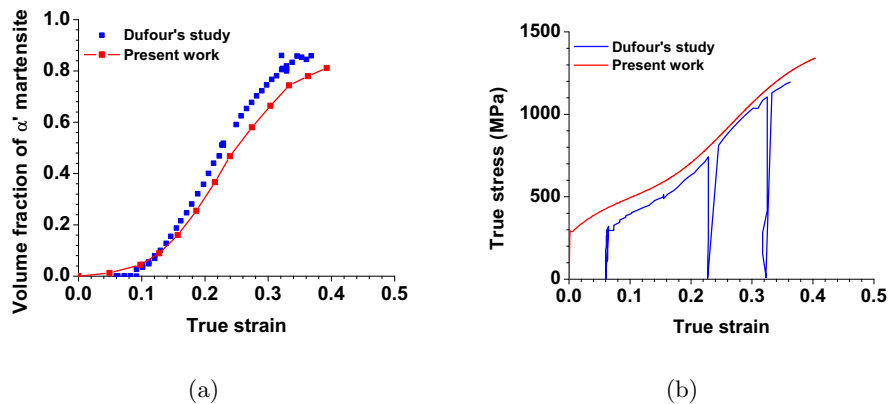
Figure 7.9: Comparison of (a) the $\gamma \rightarrow \alpha'$ transformation kinetics, and (b) overall stress-strain curve in the two grades of 301LN. The data originating from Dufour's work [13] was shifted 6% so that the $\gamma \rightarrow \alpha'$ transformation kinetics would match present study.

The neutron diffraction results from Dufour are reproduced in Figure 7.10,

showing only the average response for the austenite and α'-martensite curves along with the total macroscopic stress. It is notable that the α'-martensite appears under compression at small strains, though the low α'-martensite volume fractions at these levels of strain makes the measurements very sensitive to any sources of error.
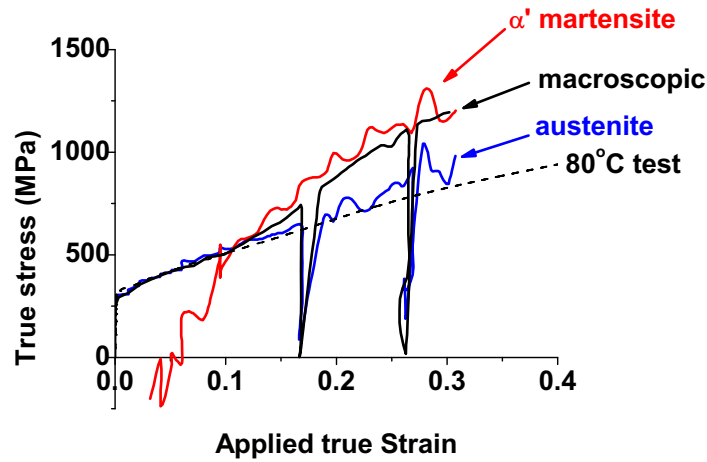
Figure 7.10: Evolution of the average stresses in austenite and martensite, as a function of the applied strain. Adapted from Dufour [13].

Figure 7.8 shows the value of $f_{\alpha'}\sigma_{\alpha'}$ taken from Dufour's data compared with the estimate of $f_{\alpha'}\sigma_{\alpha'}$ from the Feritscope estimates produced here. Again, the agreement between the two methods is excellent. The divergence between the data at low strains and α'-martensite fractions could be attributable to measurement errors from either the Feritscope or neutron diffraction measurements as the uncertainty in both techniques grows rapidly with decreasing volume fraction of α'-martensite. In the neutron diffraction measurements, the measurement of strain, and the resulting calculated stresses, are made independently for the austenite and martensite phases.

While the comparisons made above focused on $\sigma_{\alpha'}$ one can also compare the Feritscope and neutron diffraction measurements on the basis of the behaviour of austenite. In Figure 7.11, the neutron diffraction estimates of

164

σ_γ and $(1 - f_{\alpha'}) \sigma_\gamma$ are compared against these same parameters calculated from the Feritscope estimates of $\sigma_{\alpha'}$. In the case of the Feritscope data, σ_γ and $(1 - f_{\alpha'}) \sigma_\gamma$ have been calculated on the basis of stress equilibrium Equation 5.4. It can be seen that, again, the agreement between the two methods is very good consistent with the above discussion. These results also point to the fact that the neutron diffraction estimated σ_γ is quite similar to the (temperature corrected) stress-strain curve measured at 80°C. This is shown in Figure 7.10.
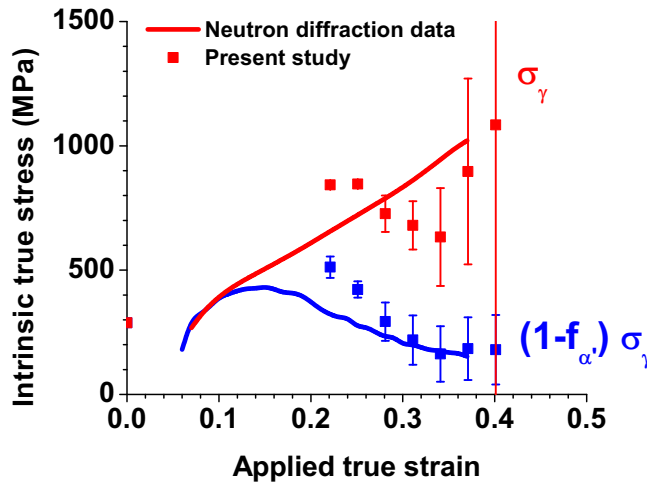
Figure 7.11: Comparison between neutron diffraction [13] and Feritscope measurements of the stresses borne in the austenite.

The good agreement between the estimated stresses borne by α'-martensitic as measured from neutron diffraction, estimated from extrapolation of the behaviour of austenite and from the new magnetic method proposed here suggest that the magnetomechanical effect can provide a route for assessing the mechanical response of an embedded ferromagnetic phase in a complex material such as the one studied here. The robust nature of these results has been checked as well against the data of stresses in α'-martensite measured via *in situ* X-ray diffraction in the work of Talonen [34]. This data set collected on the same grade (301LN, though manufactured by a different

165

company) shows very similar response to that found by Dufour. Moreover, these results also suggest that the estimated behaviour of austenite coming from the extrapolation of data measured at 80°C is close to being correct, at least over the range of strains where $(1 - f_{\alpha'})\,\sigma_\gamma$ is significant compared to $f_{\alpha'}\sigma_{\alpha'}$.

While diffraction based estimates of the stresses are certainly more robust and provide deeper understanding of the deformation behaviour, since they discriminate based on elastic strains along selected crystallographic directions, the relatively inexpensive and simple magnetomechanical method proposed here has been shown to provide useful and complimentary estimates of the load partitioning in a material containing a ferrite-austenite mixture.

7.5 Measurement of Stresses in Samples of Different Grains Sizes and the Impact on Overall Mechanical Response

The procedure described above for the D=28 µm sample has been equally applied to the other four conditions of grain size highlighted in chapter 4. The estimated variation of $f_{\alpha'}\sigma_{\alpha'}$ with strain in these samples is shown in Figure 7.12

One can see in Figure 7.12 that the load borne by the α'-martensite is not strongly depending on the starting austenite grain size, as was previously suggested from the macroscopic data from Figure 5.18. The fact that the behaviour of the α'-martensite is nearly independent of austenite grain size (aside from the effect on transformation kinetics) is not surprising given the results presented in Figure 6.23 where it was shown that the size and morphology of the α'-martensite nuclei, while not exactly the same, were similar for all of the different grain sizes.

Reflecting upon the results given above for $f_{\alpha'}\sigma_{\alpha'}$ in relation to the overall mechanical response of the samples, one can make some general statements regarding the relative importance of austenite and α'-martensite on
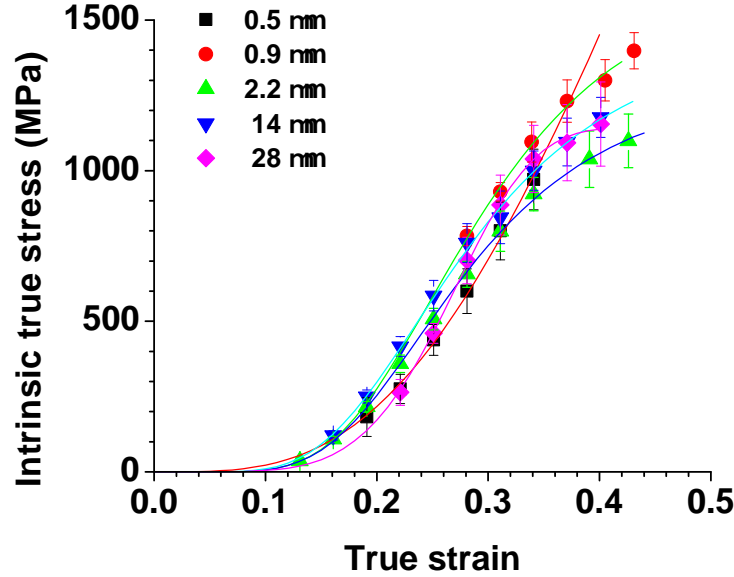
Figure 7.12: Stress evolution in the different condition of grain size. The symbols are the real data points calculated from Feritscope measurements, while the lines are the result from the applied fit.

the work-hardening response. First, it would appear that the contribution from α'-martensite to the work-hardening response is largely determined by the rate of transformation $df_{\alpha'}/d\epsilon$, but that there is a non-negligible hardening rate attributable to the α'-martensite. Assuming the α'-martensite to be a perfectly elasto-plastic material is therefore not appropriate in this case (see section 2.5.2). Careful examination of the $\sigma_{\alpha'}$ curve shown in Figure 7.7 raises some questions, however, given that the initial rate of hardening predicted for the α'-martensite is actually high and sustained at $\sim\mu/10$. Theoretically, one expects the highest rate of work-hardening in cubic metals to be of the order of $\mu/20$, a rate which drops rapidly with strain due to dynamic recovery [202, 253]. This particularity will be discussed in more detail in the following chapter, where it will be argued that this is a consequence of the "dynamic composite" behaviour of the material. Examining

167

the behaviour of $\sigma_{\alpha'}$ further, it is interesting to also note that it is predicted that the stresses in the α'-martensite increase from $\sim$800 MPa at a strain of 0.2 to $\sim$1500 MPa at a strain of 0.4. This would suggest that the flow stress of α'-martensite, at least at small strains, is not much higher than that of the austenite (which can reach $\sim$1000 MPa at a strain of 0.4). Thus, for much of the stress-strain curve the austenite contributes significantly to the overall work-hardening rate.
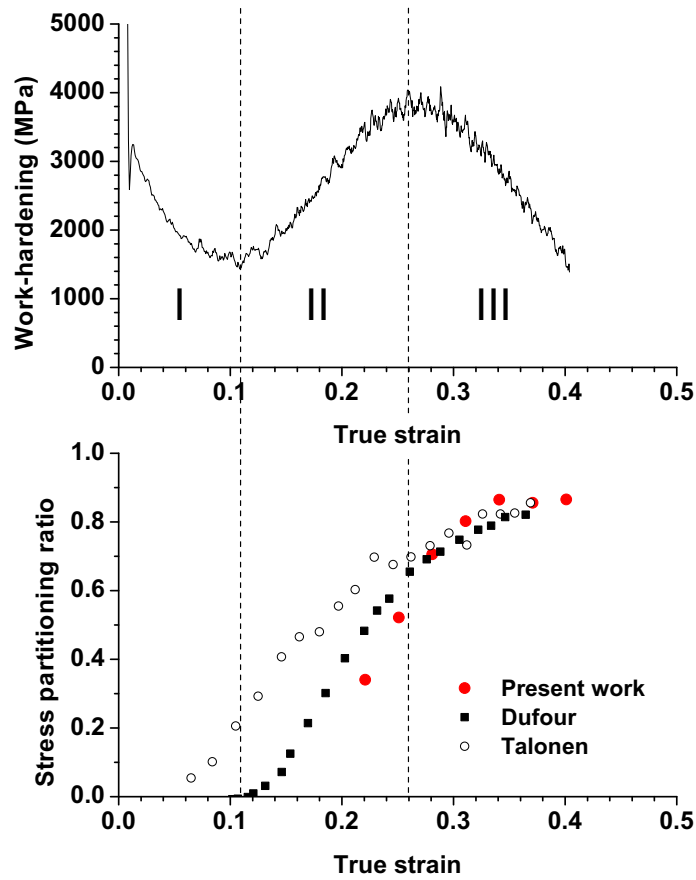
Figure 7.13: Stress partitioning ratio as a function of true strain, making apparent a relation with the three stages of work-hardening. Those are in turn compared to the work of Dufour [13] and Talonen [34].

168

In an attempt to quantify the relative contributions of the α'-martensite and austenite, it is interesting to examine the ratio (r) between the stresses carried by these two phases,

$$r \ = \ \frac{f_{\alpha'}\sigma_{\alpha'}}{\sigma_{tot}} \tag{7.5}$$

$$= \ 1 - \frac{(1 - f_{\alpha'})\,\sigma_{\gamma}}{\sigma_{tot}} \tag{7.6}$$

This quantity is plotted for the sample with D=28 μm in Figure 7.13. It can be deduced from this plot that the austenite dominates the tensile stress-strain response below 0.20 true strain, while above 0.35 true strain, 80% of the total stress is borne by α'-martensite. This point is important as it suggests that the possible effects arising from austenite scale refinement on its mechanical response with increasing $f_{\alpha'}$ will not be dominant, and can perhaps be ignored. This could explain why the extrapolation of the austenite flow stress measured at 80°C provides a reasonable description of the austenite behaviour without accounting for any strain dependent scale refinement (as considered by Talonen to be dominant [34]). For strains between 0.2 and 0.35, the contributions from both phases influence the hardening behaviour to a similar amount. These three domains can be linked to the three work-hardening stages described in section 5.6.

7.6 Summary

In this chapter, a novel way of using the magnetoelastic effect to estimate the stresses borne α'-martensite has been presented. While the use of this effect has been previously employed in sensors and an effect similar to the one presented here was observed by Post *et al.* [70], it is believed that this work represents the first attempt at making quantitative predictions of stress partitioning based on this effect.

Although the analysis presented here is very simple, neglecting the potential for multiaxial states of stress or for residual stresses and lacking a

precise description of the underlying physics of the magnetomechanical effect, it has been shown that the calbration and analysis procedure used here compared very well with measurements on the same steel made using diffraction by Talonen [34] and Dufour [13]. In agreement with these diffraction experiments, the measure reflects the variation in importance of the austenite and α'-martensite behaviour as a function of strain. Moreover, the results presented here confirm that the mechanical behaviour of the austenite is similar to the mechanical response of austenite measured at 80°C.

The results of this work also help to provide important details needed for the construction of a physically based mechanical model for the tensile response of this alloy. It shows, for example, that the contribution of austenite and α'-martensite to the total flow stress of the material can be separated into three regimes, the first dominated by austenite, the last dominated by α'-martensite and the intermediate range of strains being controlled by both phases in similar proportions. The behaviour of α'-martensite, while largely controlled by $df_{\alpha'}/d\epsilon$, itself has an intrinsic hardening rate. This hardening rate is surprisingly high and sustained up to relatively large strains where it begins to saturate. In the next chapter a description for this behaviour is presented which attempts to capture the fact that the measured response of α'-martensite reflects a range of behaviours resulting from the progressive nature of the formation of α'-martensite.

Chapter 8

Modelling of the Mechanical Response of 301LN

8.1 Introduction

It has been shown in chapters 5 and 7 that the mechanical behaviour has strong contributions from both austenite and α'-martensite. Based on the results presented in chapter 7, it is possible to develop a description for the bulk mechanical response based on the measured mechanical response of the individual phases. In section 2.5.3, it was noted that two different approaches to the modelling of the mechanical response of austenitic stainless steels can be found in the literature. The mechanics-based models, such as the one previously highlighted by Iwamoto and Tsuta [169], tend to be complex, including many empirical parameters allowing for the inclusion of strain path and stress state effects. On the other hand, material-based models such as those developed by Olson [58], Spencer [112], Bouquerel [207] and Talonen [34], tend to use simpler one-dimensional descriptions of mechanical response while focusing more heavily on capturing physical aspects of the microstructural contributions to strength. In the present work, an attempt has been made to develop a description more aligned with the latter group of models.

8.2 Review of Mechanical Response and Previous Microstructural Based Models

In chapter 7, it was shown that the behaviour of austenite back-extrapolated from both diffraction and from the magnetic method proposed in this thesis was consistent with the behaviour of austenite measured at 80°C when the yield strength was corrected for temperature. In particular, this appears very consistent when one views the early stages of deformation prior to the formation of significant fractions of α'-martensite. In this case, the work-hardening rates of the curves measured at room temperature and at 80°C are very similar. Previous models (e.g. [207] and [34]) have highlighted the fact that plastic incompatibility between the austenite and α'-martensite along with the scale refinement of the austenite (cf. Figure 6.23) should lead to extra hardening of the austenite due to the formation of geometrically necessary dislocations. This would seem incompatible with the assertion made above that the behaviour of austenite measured at 80°C (where little α'-martensite forms) appears to be the same as that at room temperature. Figure 7.13 however shows that the relative importance of austenite to the work-hardening and flow stress drops rapidly with strain such that at a strain of ~0.3, the austenite contributes only 20% to the overall flow stress. This is clearly seen if one examines the estimated value of $(1 - f_{\alpha'})\,\sigma_\gamma$ shown in Figure 7.11. The sensitivity of the overall behaviour of the material to the description of the austenite at higher levels of strain (where extra strengthening due to geometrically necessary dislocations will be important) is expected to be low, in this case. This may help to explain why it is possible to extrapolate the behaviour of the austenite measured at 80°C to large strains without needing to account for extra hardening.

In the case of α'-martensite, various proposals have been made for its behaviour in the literature. Bouquerel [207] treated it has a monolithic phase and described it as obeying a Voce type hardening law. Others, e.g. Talonen [34], have treated the α'-martensite as a rigid, non-plastically deforming phase. Under this assumption, the mechanical response of the material has been attributed to the hardening arising from the dislocation content in

austenite. Neither of these cases appears to capture the response of the α'-martensite found here. Examination of Figure 7.7 reveals the behaviour of α'-martensite to be complex. The behaviour of α'-martensite shows an extremely large rate of apparent hardening between the strains of 0.2 and 0.3. Between these strains, the stress carried by α'-martensite appears to rise linearly with a slope of $\sim \mu/10$ where μ is the shear modulus of the martensite. In cubic metals, the maximum rate of hardening due to dislocations is generally found to be of the order of $\mu/20$, this occurring at the onset of general yield in a well annealed material [202, 253]. One must be careful as the behaviour of α'-martensite in Figure 7.7 is plotted against the macroscopic strain. In reality the stains carried by α'-martensite and austenite could be very different. The apparent hardening rate of α'-martensite in Figure 7.7 could be written as:

$$\frac{d\sigma_{\alpha'}}{d\epsilon} = \frac{d\sigma_{\alpha'}}{d\epsilon_{\alpha'}} \frac{d\epsilon_{\alpha'}}{d\epsilon} \tag{8.1}$$

where ϵ is the macroscopic strain and $\epsilon_{\alpha'}$ is the strain carried by α'. In order for $d\sigma_{\alpha'}/d\epsilon_{\alpha'}$ to be smaller than $d\sigma_{\alpha'}/d\epsilon$, $d\epsilon_{\alpha'}/d\epsilon$ needs to be larger than 1, meaning that the strain in α'-martensite would have to be higher than the macroscopic strain. If α'-martensite is considered to be the hardest of the two phases, then it would be expected to have a lower strain compared to the macroscopic strain. Thus, non-uniform strain partitioning would appear not able to explain this behaviour. The sustained high apparent hardening rate of the α'-martensite suggests that another mechanism must be accounted for.

An important aspect of the mechanical response of austenitic stainless steels is that they behave as a "dynamic composite" in that the microstructure is gradually converting from austenite to α'-martensite. The behaviour shown in Figure 7.7 can therefore be misleading, as it has to be viewed as an **average behaviour** of α'-martensite formed at various levels of strain. This is a point which has not been adequately explored in previous models for the mechanical response of dynamically transforming materials (e.g. TRIP, TWIP steels) and will form the basis of the model developed below.

8.3 A Dynamic Composite Model for 301LN Stainless Steel

The approach taken here, motivated by the results presented in chapters 5 and 7, is to describe the behaviour of the material not as a mixture between two monolithic materials, but as an n-phase composite composed of austenite and a continuous distribution of α'-martensites, the behaviour of the martensite depending on the strain at which it has been formed. In developing the basic components of this model, the data for the coarse grained (D=28 µm) sample deformed in tension will be treated first. Both the bulk mechanical response presented in chapter 5 as well as the behaviour of the individual phases chapter 7 are used to fit the model. A vital component to the model is a good description of the kinetics of the $\gamma \rightarrow \alpha'$ transformation. For simplicity, the basic O-C equation (Equation 2.11) has been fit to the experimental data as shown in Figure 5.12. The deformation of the material in this model is considered based on an equivalent stress and strain basis and is therefore one-dimensional. In the model, strain is assumed uniform through all phases. More sophisticated homogenization schemes (such as the β-model [254] or the iso-work approach [255]) could be applied, however, this choice does not change the physical nature of the model presented.

8.3.1 Behaviour of Austenite

The work-hardening response of the austenite has simply been fit to this experimental data using a Voce law:

$$\sigma_\gamma = \sigma_{\gamma 0} + \sigma_{\gamma s} \left(1 - \exp(-\frac{\theta_{\gamma 0}}{\sigma_{\gamma s}} \epsilon) \right) \tag{8.2}$$

in which $\sigma_{\gamma 0}$, $\theta_{\gamma 0}$ and $\sigma_{\gamma s}$ respectively stand for the yield stress, initial hardening rate and scaling stress of the austenite. The physical meaning of these hardening parameters is shown schematically in Figure 8.1.

A Voce law has been selected as the parameters in this model (i.e. $\theta_{\gamma 0}$ and $\sigma_{\gamma s}$) can be attributed to dislocation based hardening mechanisms in fcc

materials [202, 253] through a Kocks-Mecking approach. The temperature dependence of the yield strength of this alloy can also be described based on the recent model presented by Allain *et al.* [174], as shown in Figure 2.20. In the present case, for simplicity, the yield strength of the tensile curve measured at 80°C has simply been adjusted to fit the yield strength of the samples tested at room temperature. The form of the Voce law used does not include a term accounting for geometrically necessary dislocations. Such a term could be included but, as discussed above, the sensitivity of the results to the inclusion of this term are considered small.
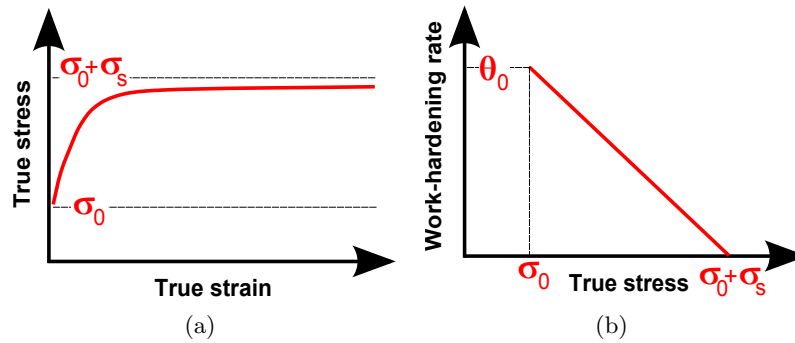
Figure 8.1: Schematic representation of the parameters appearing in Equation 8.2.

8.3.2 Behaviour of α'-Martensite

The model developed here is applied incrementally such that the fraction of the total stress carried by austenite, $(1 - f_{\alpha'})\,\sigma_\gamma$, and α'-martensite $f_{\alpha'}\sigma_{\alpha'}$ are computed at fixed increments of the strain $(d\epsilon)$. The increment of α'-martensite formed in this strain increment $(df_{\alpha'})$ is also calculated for each increment of strain. Each $df_{\alpha'}$ increment of α'-martensite formed is treated as a separate phase in the calculation.

Critical to the explanation of the behaviour observed in Figure 7.7 is the assumption that each increment of α'-martensite formed is an elasto-plastic element and that the α'-martensite, when formed, is in compression by an amount denoted as $\sigma_{\alpha'00}$. As previously discussed in sections 2.2.1 and 6.3.4,

175

the formation of α'-martensite from austenite involves a shear strain, as well as an expansion along one direction, and contraction along the two perpendicular directions. Overall, the transformation occurs with an increase in volume from austenite to α'-martensite. The net result of this process is that the formation of α'-martensite should lead to a local unloading of the material while also giving rise to an extra amount of "transformation strain". Various detailed micromechanical models have been previously built to examine the combination of these two effects (see e.g. [256, 257]). In simpler one-dimensional models, this complex situation is often considered either in terms of an extra transformation strain added to the macroscopic strain due to the transformation (e.g. [112]) at fixed stress, or the formed phase is considered to be under compression at fixed (uniform) strain (see e.g. [257], for a discussion of these limits). In the present case, the latter description has been selected as it matches better to the results shown in Figure 7.7 and is consistent with the assumption of uniform strains. This behaviour is consistent with the neutron diffraction measurements presented in Figure 7.10, which suggest that the α'-martensite is under compression at small strains [13].

Once formed, each incremental element of α'-martensite is assumed to load elastically in tension until it reaches the stress $\sigma_{\alpha'0}$. Above this level of stress it is assumed to deform plastically, where each α'-martensite element is assumed to obey a Voce law. Therefore, the constitutive behaviour for martensite can be described by:

$$\sigma_{\alpha'} = \begin{cases} \sigma_{\alpha'00} + E_{\alpha'}\epsilon & \text{for } \sigma_{\alpha'} < \sigma_{\alpha'0} \\ \sigma_{\alpha'0} + \sigma_{\alpha's}\left(1 - \exp(-\frac{\theta_{\alpha'0}}{\sigma_{\alpha's}}\epsilon)\right) & \text{for } \sigma_{\alpha'} > \sigma_{\alpha'0} \end{cases} \qquad (8.3)$$

with $E_{\alpha'}$ being the Young modulus of α'-martensite, estimated to be 200 GPa (e.g. [13]). Based on this constitutive model for each α'-martensite element, the high initial hardening rate in Figure 7.7 is explained to be due to the injection, at each step of deformation, of new α'-martensite elements which are initially in compression and which have to load elastically to their yield stress. Thus, the high hardening rate can be interpreted as a sort of extended

elasto-plastic transition.

At each step of the calculation, the material will consist of n elements of α'-martensite, each carrying a different level of stress. The total contribution to the stress from the α'-martensite is the sum of the contributions of the n different islands of α' which were formed at each time step weighted by their individual volume fractions:

$$\sigma_{\alpha'}^{tot} = \sum_{i=1}^{n} df_{\alpha'}^{n-i} \cdot \sigma_{\alpha'}^{i} \tag{8.4}$$

in which the exponent refers to the step when α' was formed.

Finally, macroscopic equilibrium imposes that:

$$\sigma = (1 - f_{\alpha'})\sigma_{\gamma} + \sigma_{\alpha'}^{tot} \tag{8.5}$$

8.3.3 Choice of the Parameters

As already noted, some of the parameters used in the model can be derived from experimental measurements. This is the case for the yield stress and work-hardening rate of the austenite as well as the kinetics of the $\gamma \to \alpha'$ phase transformation, extracted from Figure 5.12 or Figure 5.15. The grain size, and yield strength of austenite derived from experiments are given in Table 8.1 as are the parameters for the O-C model for the $\gamma \to \alpha'$ kinetics.

	Yield stress of	Uniaxial Tension		
Grain size	Austenite	O-C parameters		
D	$\sigma_{\gamma 0}$	α	β	n
0.5 µm	670 MPa	4.06	4.52	5
0.9 µm	610 MPa	3.85	4.52	5
2.2 µm	440 MPa	3.83	4.52	5
14 µm	370 MPa	4.28	4.52	5
28 µm	280 MPa	4.52	4.52	5

Table 8.1: Input parameters directly determined from tensile experiments. The yield stresses were determined from Figure 5.4, while the kinetics were taken from Table 6.3.

The parameters for the Voce law used to describe austenite have been fit to the behaviour of 301LN measured at 80°C and are shown in Table 8.2. It should be noted that $\theta_{\gamma 0} \approx \mu_\gamma / 30$ and $\theta_{\alpha' 0} \approx \mu_{\alpha'} / 20$, where μ_γ and $\mu_{\alpha'}$ are the shear moduli of austenite and α'-martensite. These values are consistent with the theory of work-hardening of polycrystals [202, 253]. The only temperature-dependence of this parameter comes from the temperature-dependence of the shear modulus. In the range of temperature considered here (e.g. from -196°C to 150°C), θ_0 can be considered independent of temperature. On the other hand, the scaling stress $\sigma_{\gamma s}$ is expected to be temperature-dependent.

The four parameters corresponding to the martensitic mechanical behaviour have been determined by fitting to the bulk mechanical response as well as the evolution of $f_{\alpha'}\sigma_{\alpha'}$ given in Figure 7.12. It was found that the two hardening parameters for α'-martensite ($\theta_{\alpha' 0}$ and $\sigma_{\alpha' s}$) had a relatively small impact on the overall stress-strain response of the material. On the other hand, the values of $\sigma_{\alpha' 00}$ and $\sigma_{\alpha' 0}$ were found to strongly influence the predicted behaviour. The selected values of all those parameters are presented in Table 8.2.

Austenite (γ)		Martensite (α')			
$\theta_{\gamma 0}$	$\sigma_{\gamma s}$	$\sigma_{\alpha' 00}$	$\sigma_{\alpha' 0}$	$\theta_{\alpha' 0}$	$\sigma_{\alpha' s}$
2500 MPa	1000 MPa	-2200 MPa	1050 MPa	3500 MPa	900 MPa

Table 8.2: Adjustable input parameters, used to model uniaxial tension.

The respective behaviours of each phase using the parameters from Table 8.2 are represented in Figure 8.2. It can be seen from this plot that the choice of the hardening parameters for α'-martensite is compatible with the yield stress measured at room temperature on a sample of 301LN which had been previously cryorolled. Because cryorolling results in samples containing nearly 100% α'-martensite (cf. Figure 4.2), the yield stress of such a sample defines an upper limit for the flow stress of α', upon specified strain route. This argument is consistent with the low work-hardening, as observed on cryorolled specimens experimentally deformed in shear. Figure 8.2 suggests

that this maximum flow stress is different from uniaxial tension to simple shear. This last point will be revisited in section 8.3.6.
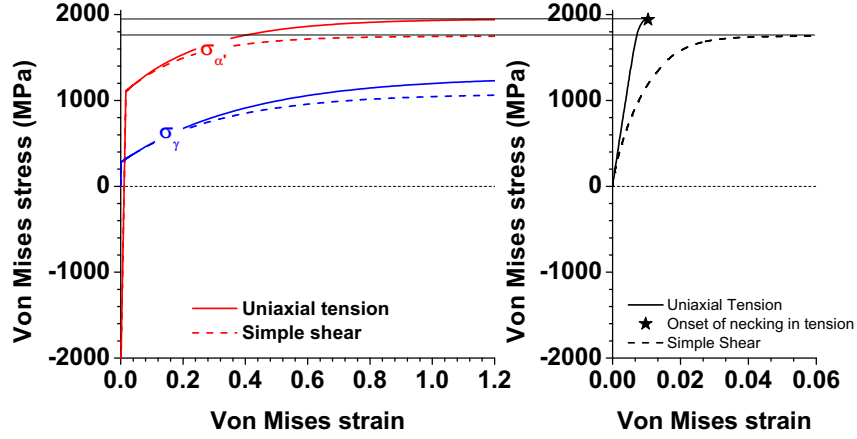
Figure 8.2: (a) Simulated stress-strain behaviour of the two single phases γ and α'. For this model, the scaling stresses of the α'-martensite were obtained from the experimental stress-strain curve of cryorolled material shown in (b).

8.3.4 Discussion of Model Results for $D{=}28$ µm in Uniaxial Tension

The results of the model fit to the sample having $D{=}28$ µm is shown in Figure 8.3. One can see that the model reasonably predicts both the macroscopic stress-strain response as well as the Feritscope measured variation of $f_{\alpha'}\sigma_{\alpha'}$.

The various contributions to the macroscopic work-hardening behaviour can be identified more easily if one examines the rate of work-hardening based on the derivative of Equation 5.5,

$$\frac{d\sigma}{d\epsilon} = \underbrace{(1 - f_{\alpha'})\frac{d\sigma_\gamma}{d\epsilon}}_{\text{Term 1}} + \underbrace{\frac{df_{\alpha'}}{d\epsilon} \cdot (\sigma_{\alpha'} - \sigma_\gamma)}_{\text{Term 2}} + \underbrace{f_{\alpha'} \cdot \frac{d\sigma_{\alpha'}}{d\epsilon}}_{\text{Term 3}} \qquad (8.6)$$

179

(a)   (b)
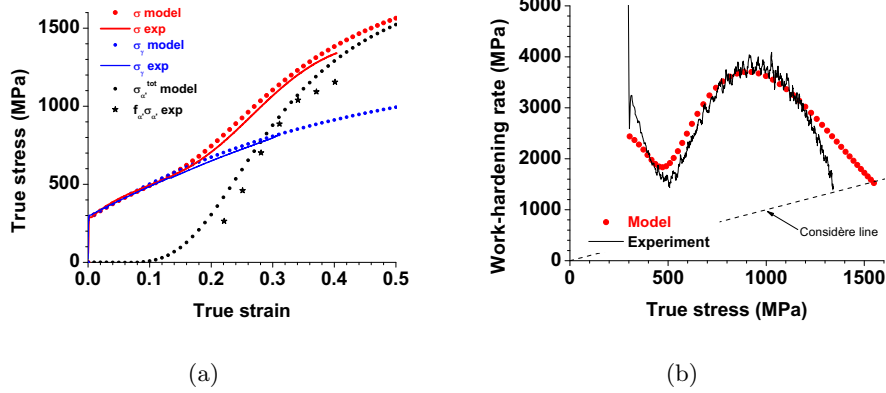
Figure 8.3: (a) Simulated stress-strain curves of the D=28 µm condition deformed in uniaxial tension. Those are compared to the experimental stress-strain curves obtained from Figure 5.4 for the γ/α' aggregate and from Figure 5.7 for the austenite. The simulated stress in α'-martensite (Equation 8.4) is compared to the experimental stresses determined from Feritscope measurements (Figure 7.8). (b) Comparison of the simulated and experimental work-hardening curves.

The three terms highlighted in the above equation describe the work-hardening of the austenite (Term 1), the rate of the $\gamma \rightarrow \alpha'$ phase transformation and the mechanical contrast between austenite and martensite (Term 2), and the apparent work-hardening arising from the net behaviour of the α'-martensite (Term 3). These three components of the work-hardening rate are compared in Figure 8.4.

For strains between 0 to 0.10, work-hardening is dominated by the mechanical behaviour of the austenite (Term 1). This corresponds to the stage I as identified in chapters 5 and 7. The inflection characteristic of the TRIP effect is the dominant feature of stage II. It can be seen that this corresponds to the transition during which Terms 2 (related to the rate of the phase transformation) and 3 (related to the apparent work-hardening of α') start becoming more important than the work-hardening of the austenite. In the last work-hardening stage (stage III), Term 1 becomes negligible and Term 3 has the largest contribution. A consequence of this observation is that the
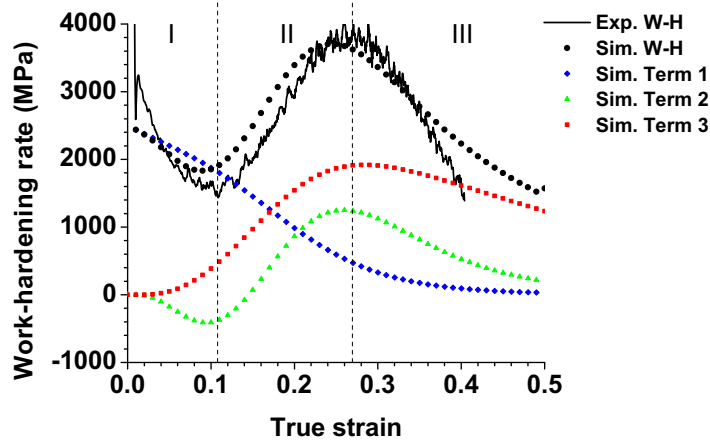
Figure 8.4: Representation of the three work-hardening (W-H) terms, as defined in Equation 8.6, obtained from simulation. The sum of these three terms is in turn compared to the work-hardening measured experimentally.

kinetics of the $\gamma \rightarrow \alpha'$ phase transformation only dominates in stage II, an effect already highlighted in the discussion on stress partitioning evolution (Figure 7.13). A final point on this plot is that Term 2 becomes negative in the early stages of deformation due to the fact that the stress carried by austenite is initially higher than that carried by α'-martensite. This can have an important consequence when the austenite has a high yield strength (i.e. fine grain sized samples) as will be discussed in sections 8.3.5 and 8.4.

8.3.5 Application of Model to the Grain Size Dependence of Mechanical Response

As shown by the tensile tests carried out at elevated temperature (Figure 5.6), the grain size apparently has little impact on the work-hardening rate of austenite. This is also confirmed by the early stages of deformation at room temperature where, as discussed above, the work-hardening rate is dominated by the behaviour of austenite.

(a) 14 µm

(b) 2.2 µm

(c) 0.9 µm
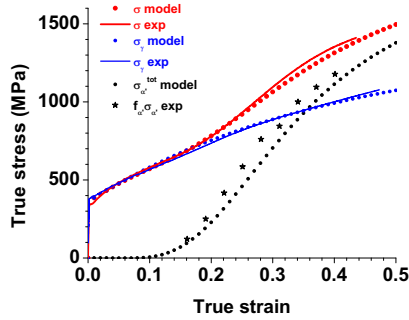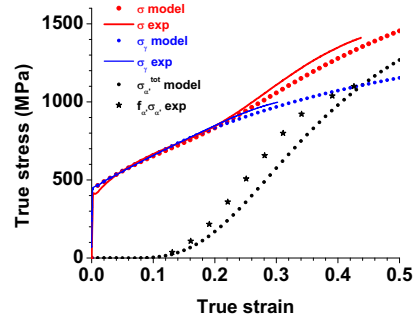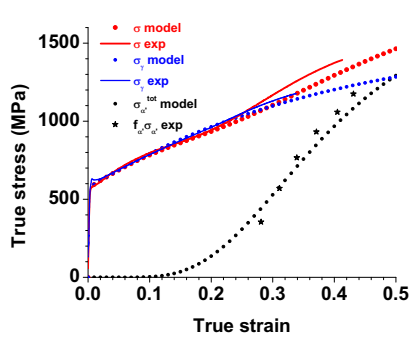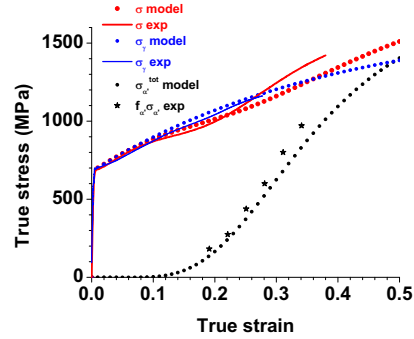
(d) 0.5 µm

Figure 8.5: Influence of the grain size on the simulated tensile curves. Those are compared to the experimental stress-strain curves obtained from Figure 5.4 for the γ/α' aggregate and from Figure 5.7 for the austenite. The simulated stress in α'-martensite (Equation 8.4) is compared to the experimental stresses determined from Feritscope measurements (Figure 7.12).

This effect is seen in Figure 5.5 where the hardening rates for the initial portion (Stage I) of the curves collapse on top of one another if the yield strength is subtracted from the stress axis of the plot. According to the results shown in Figure 7.12, the mechanical behaviour of the α'-martensite has been taken to be independent of the austenite grain size. Based on these two observations, it has been assumed that the hardening parameters for each phase in Table 8.2 are independent of grain size, at least in the

range of grain size considered here (0.5 µm $< D <$ 50 µm). Consequently, the austenite grain size is considered to only affect the mechanical properties through the kinetics of the $\gamma \rightarrow \alpha'$ transformation and the yield stress of austenite, all parameters are easily obtained from experiment.

The results of the predicted mechanical response as a function of grain size are shown in Figure 8.5, the individual contributions to the work-hardening rate being shown in Figure 8.6.

(a) 14 µm

(b) 2.2 µm

(c) 0.9 µm

(d) 0.5 µm
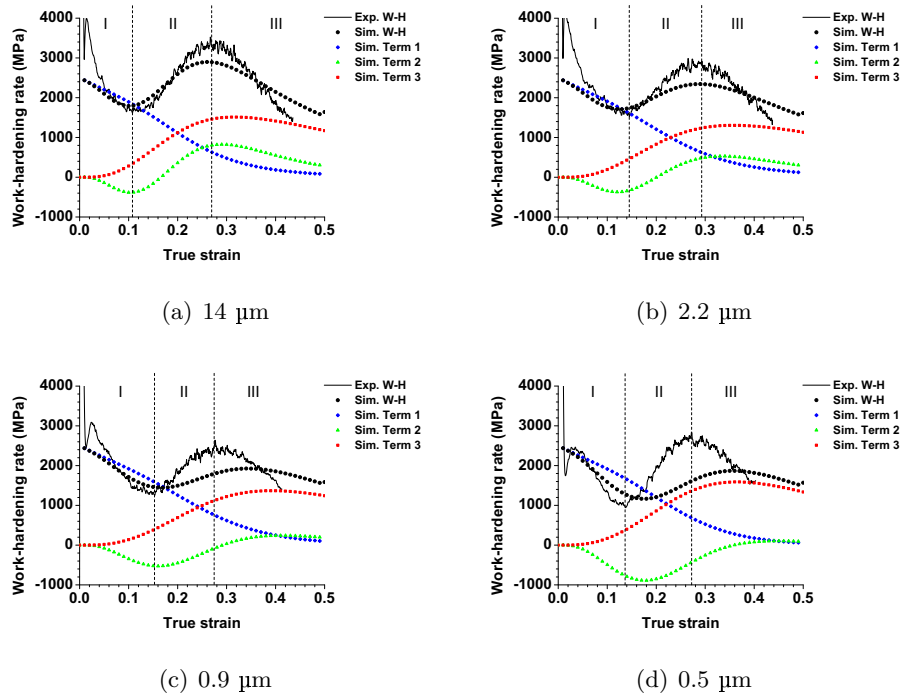
Figure 8.6: Grain size dependence of the three work-hardening (W-H) terms, as defined in Equation 8.6, obtained from simulation.

It can be seen that changing the austenite grain size mainly effects the contribution of Term 2, which includes the difference in stress carried by austenite and α'-martensite. The increase of peak work-hardening (peak B, according to the nomenclature used in Figure 5.16) with grain size is primarily due to the difference between the flow stress of austenite and α'-

martensite.

An important effect that comes from Term 2 is its dependence on $(\sigma_{\alpha'} - \sigma_\gamma)$. As one can see in Figure 8.6, this term becomes increasingly negative in the early stages of deformation as grain size is decreased. This is because of the increasing yield strength of austenite relative to the α'-martensite (whose properties have been assumed independent of austenite grain size). The end result is that, as the grain size of austenite is refined, the influence of the formation of α'-martensite can actually be to soften the material. This is observed, for example, in the case of the D=0.5 µm condition where the flow stress of austenite lies above that of the macroscopic material.

Another important point concerning Term 2 is the importance of the $\gamma \to \alpha'$ kinetics. A weak change in transformation kinetics results in a large difference in the predicted stress-strain curve. One example to illustrate this point is given in Figure 8.7 in which the transformation kinetics of the 28 µm condition have been computed assuming the transformation kinetics of the D=2.2 µm condition. It is clear that even small errors in the prediction of the transformation kinetics can have large effects on the predicted mechanical response. In the case considered here, the use of the kinetics for the D=2.2 µm condition leads to a reduction of 150 MPa in the true stress at necking.
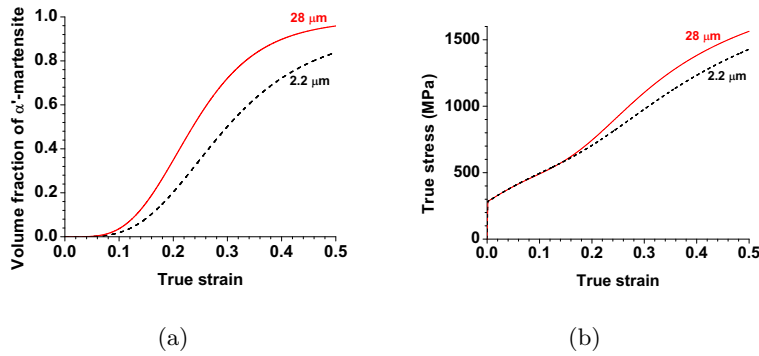
Figure 8.7: Sensitivity of the kinetics on the tensile behaviour. Comparison of (a) kinetics and (b) simulated tensile curves, using in one case the kinetics of the 28 µm condition, and in the other case, the kinetics of the 2.2 µm condition.

8.3.6 Application of Model to the Mechanical Response in Shear

It was shown in chapter 5 that the mechanical response in shear was initially very similar to the mechanical response in tension (compared on the basis of Von Mises equivalent stress and strain) but that, as the strain and fraction of α'-martensite increased, the flow stress for the two strain paths increasingly deviated from one another. It was also shown that the $\gamma \rightarrow \alpha'$ transformation kinetics were similar for the two strain paths over the initial stages of deformation but that the rate of transformation slowed more rapidly in the case of the shear tests than in the case of tension.

In an attempt to adapt the model developed for tension to the case of shear, some modifications are necessary. First, the O-C parameters need to be changed to describe the kinetics of the $\gamma \rightarrow \alpha'$ transformation observed experimentally (cf. Figure 5.15). Second, the hardening parameters are also required to be adapted to the variation of strain path. A first example of this can be found in the work of Allain focusing on the deformation mechanisms of Fe-Mn steels, in the absence of $\gamma \rightarrow \alpha'$ phase transformation [87]. In this work, discrepancies were observed between the mechanical properties of austenite measured along uniaxial tension and pure shear, these being explained by the difference in texture evolution and the fact that the equivalent strain (according to Von Mises) does not take into account the rotation of principal axes (this point will be revisited in the end of this section). A second example, in terms of the mechanical properties of α' only, was presented in Figure 8.2. The mechanical behaviours of cryorolled materials, plotted in terms of Von Mises equivalents, suggest that the scaling stresses of α'-martensite need to be smaller in shear than in tension. These scaling stress can be calculated using the fact that the maximum flow stress of a cryorolled specimen along a specific strain path is equal to $\sigma_{\alpha'0} + \sigma_{\alpha's}$. The actual values deduced from Figure 8.2 show that the scaling stress of α' is decreased from 900 to 700 MPa.

Since the change from uniaxial tension to simple shear tends to lower the flow stress of both austenite and α'-martensite, the overall effect on the

flow stress of austenitic stainless steels is also a decrease in flow stress, a trend consistent with the experiments reported in references [146, 186].

In order to account for these changes, the scaling stress of austenite $\sigma_{\gamma0}$ was lowered from 1000 to 800 MPa, while that of α' $\sigma_{\alpha'0}$ was also decreased from 900 to 700 MPa, according to Figure 8.2. All other parameters, particularly the initial hardenings, were left unchanged. The full list of parameters is detailed in Table 8.4. The model results in Figure 8.8.

		Simple Shear		
Grain size	Austenite	O-C parameters		
D	$\sigma_{\gamma0}$	α	β	n
0.5 µm	670 MPa	4.06	3.4	5
2.2 µm	440 MPa	3.83	3.4	5
28 µm	280 MPa	4.52	3.4	5

Table 8.3: Input parameters directly determined from simple shear experiments. The yield stresses were the same as those determined in uniaxial tension, while the kinetics were taken from Table 6.3.

Austenite (γ)		Martensite (α')			
$\theta_{\gamma0}$	$\sigma_{\gamma s}$	$\sigma_{\alpha'00}$	$\sigma_{\alpha'0}$	$\theta_{\alpha'0}$	$\sigma_{\alpha's}$
2500 MPa	800 MPa	-2200 MPa	1050 MPa	3500 MPa	700 MPa

Table 8.4: Adjustable input parameters, used to model simple shear. When compared to tension, only the scaling stresses were changed in agreement with the experimental data from Figure 8.2.
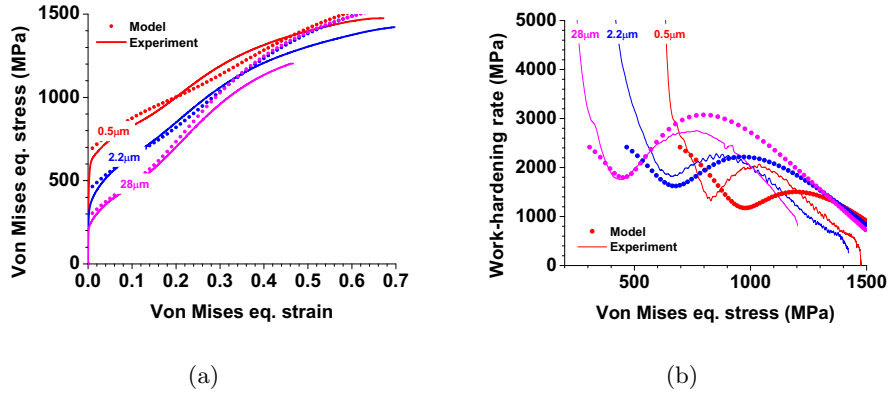
Figure 8.8: Comparison of the simple shear simulated curves with the experimental ones. The divergence between model and experiment is attributed to the different texture evolution

It can be noticed that the shear behaviour above 40% true strain differs when one compares experiment and model predictions. This feature could be a reflection of the difficulty to capture strains using the Von Mises equivalent strain. Indeed, the equivalent strain was already reported to overestimate the true strains in simple shear [258, 259]. The underlying reason is that the Von Mises strain does not account for the incremental rotation of the principal axes. This effect would help explain the results observed here, since an overestimation of the strains results in an overestimation of both α'-martensite fraction and equivalent individual stresses. All these effects tend to an overestimation of the overall flow stress of the composite material, as observed in Figure 8.8.

8.4 Application of Model to Literature Data

If the model presented here is to be of general applicability, it should be possible to extend it to explain the mechanical behaviour at different temperatures, and for different alloys. As was mentioned earlier in this thesis, the work carried out here was performed in parallel with a second study focused on the effects of temperature and strain rate on the same alloy

[146, 186]. The effects of strain rate, as discussed in section 2.3, mainly come from self-heating of the sample. These non-isothermal conditions are difficult to model as they require a model for the temperature as a function of strain (time) in the sample. It is, however, possible to compare the model developed here with the data collected under isothermal conditions.

It was assumed, in section 8.3.3, that temperature does not significantly influence the work-hardening rate of austenite in the range $20°C$ to $80°C$. In reality, the work-hardening response of austenite should be a function of temperature primarily through the $\sigma_{\gamma s}$ term (related to dynamic recovery) and to a much smaller extent through $\theta_{\gamma 0}$ (through the temperature dependence of the shear modulus). Similarly, the flow stress and hardening rate of α'-martensite should also be a function of temperature. As a simple check on the robustness of the model developed here, a simple comparison between the data collected by Nanga [146, 186] has been made assuming that the work-hardening behaviours of austenite and α'-martensite were temperature independent. Consequently, the temperature dependence was considered only in relation to the yield strength of austenite and the rate of $\gamma \rightarrow \alpha'$ transformation. The rate of $\gamma \rightarrow \alpha'$ transformation has been captured using a fit to the O-C model, as for the results presented above. The results of this simulation are shown in Figure 8.9.

(a)
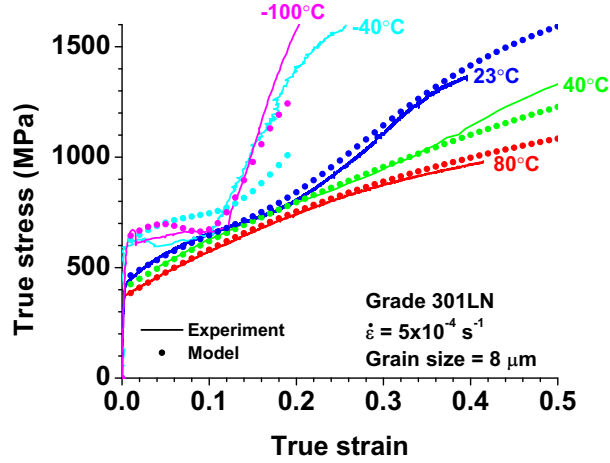
T	$\sigma_{\gamma 0}$	O-C values		
(°C)	(MPa)	α	β	n
−100	620	4.3	57.7	4.5
−40	600	4.6	14.4	4.5
23	440	3.2	12.7	4.5
40	400	3.9	0.9	4.5
80	360	3.0	0.1	4.5
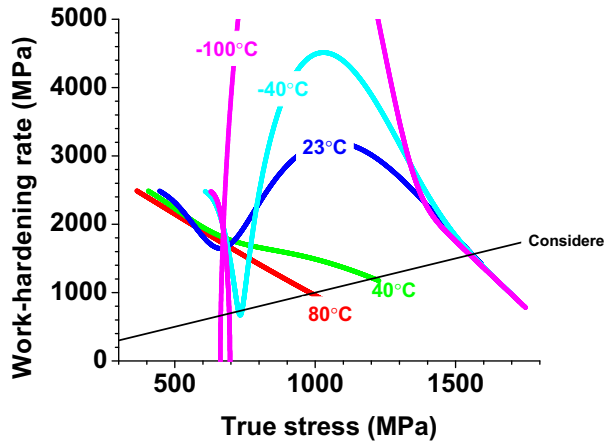
(b)

Figure 8.9: Results of the mechanical model applied to the data collected by Nanga [146, 186]. (a) Simulated stress-strain curves and (b) simulated work-hardening curves, for uniaxial tension. For the two lowest temperatures, the simulated work-hardening curves start laying below the Considère line at the exact moment when strain localization is observed.

Despite the fact that the temperature dependence of the flow stress of

austenite and α'-martensite have been excluded in Figure 8.9, the model predictions capture the behaviour well. Indeed, the model has also been successfully applied to the data from the work of Talonen where measurements were made over a similar temperature range on a similar grade of 301LN stainless steel [34].

Interestingly, the model predicts the observed localization (similar to the propagation of a Lüders band) at $-40°$C and $-100°$C from Nanga's data. This comes from the increasing difference in flow stress between austenite and α'-martensite and therefore an increasing negative contribution from Term 2 in Equation 8.6. At low temperature, this negative contribution to the work-hardening rate results in the Considère criterion (Equation 2.17) being satisfied early in the stress-strain curve (Figure 8.9(b)). Yet, as Term 2 rises and becomes positive with increasing fraction of α'-martensite, the instability is ended and uniform straining is continued again.

This effect of strain localization has similarly been observed during the present study for a sample deformed in liquid nitrogen (cf. Figure 7.4). Aside from tension, it is also possible to induce Lüdering if the grain size is sufficiently reduced or if the austenite is sufficiently work-hardened without the formation of α'-martensite. Indeed, the tensile sample having D=0.5 µm ($\sigma_{\gamma 0}$=670 MPa) nearly reaches this condition as illustrated by Figure 8.5. A second example of a high yield stress resulting in strain localization is detailed below.

A sample was produced with a very fine grain size (high yield strength) by cryorolling 301LN followed by annealing at $750°$C during 30 minutes. This treatment generated a partially recrystallized microstructure ($\sim$80% recrystallized), resulting in a yield stress of 970 MPa. The starting microstructure of this material was free of α'-martensite in the as-annealed state. As expected, the tensile curve of this material presented sharp discontinuous yielding followed by a long plateau ($\sim$24% of strain) of strain localization (Figure 8.10(b)).

<div align="center">(a)   (b)</div>
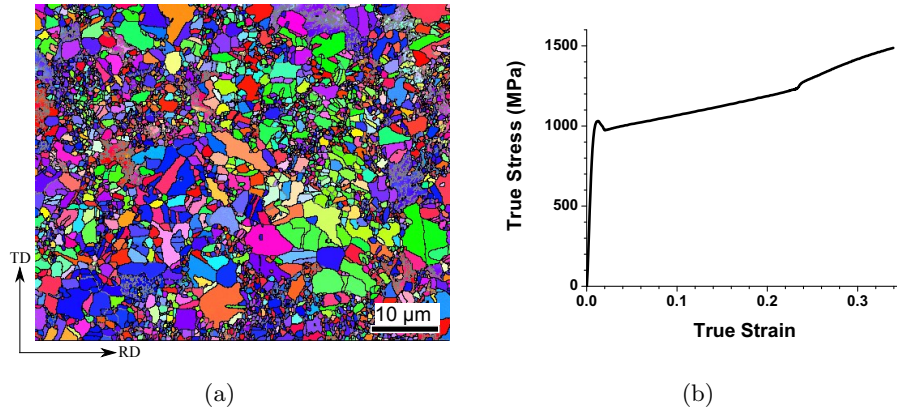
Figure 8.10: (a) Orientation map showing the microstructure of 301LN after cryorolling and annealing at 750°C. It can clearly be seen that the austenite is not fully recrystallized. (b) Stress-strain curve of the condition exhibiting the microstructure shown in (a), during room-temperature uniaxial tension. The tensile curve shows a long plateau (24% strain) characteristic of strain localization.

The observation of strain localization has previously been discussed in the literature. In the work of Spencer [72], the formation of apparent Lüders bands at low temperature was attributed to a a high rate of transformation, resulting in a large contribution to the strain (at constant stress) from the transformation strain. This explanation is similar to the one given here, since, as discussed above, the assumption of an extra transformation strain (at constant stress) and an unloading effect (at constant strain) are upper and lower bounds on the true expected behaviour of the material. However, the advantage of the current proposal is that it shows that the rate of transformation does not need to be particularly high in order to induce strain localization. A key factor that must be considered is the relative difference in the flow stress contribution coming from austenite and α'-martensite. Thus, the experimental observations made by Spencer [72] of very large Lüders plateaux following a change of testing condition from room temperature (no α'-martensite formation but work-hardening of austenite) to -196°C (high rate of α'-martensite formation) should be considered in terms of both the rate of $\gamma \rightarrow \alpha'$ transformation as well as the difference in flow stress of

191

austenite and α'-martensite, as suggested by Term 2 in Equation 8.6.

It has also been recently suggested [10] that the formation of strain localization bands in metastable austenitic stainless steels is an indication of a transition from a strain-induced to stress-assisted transformation. While the work here does not preclude the possibility for such a transition, it does show that such a transition is not necessary to explain the observed behaviour.

So far, the proposed model has been applied only to a 301LN grade of stainless steel. This grade has the advantage, compared to other grades, that it is relatively unstable and therefore forms a high fraction of α'-martensite by testing at room temperature. Similar effects, however, can be seen in other grades tested at low temperatures.

Spencer *et al.* performed tests on a 316L grade of stainless steel at low temperatures [72]. Since no α'-martensite is formed in 316L at room temperature, the stress-strain curve at $25°C$ is a good estimate for the mechanical behaviour of the austenite. Comparing the results of tensile testing at room temperature on 316L with that on 301LN tested at $80°C$ revealed that the behaviours were quite similar. The Voce parameters required to fit the behaviour of austenite in 316L at this temperature, are given in Figure 8.11. As in other cases, the experimental $\gamma \rightarrow \alpha'$ transformation kinetics reported by Spencer have been fit to an O-C model for the various test temperatures, and the yield strength of the austenite has been matched to the experimental curves. The behaviour of the austenite and α'-martensite have been taken to be the same as that used for the 301LN alloy described above, except for the yield stress of the α'-martensite, which was increased from 1050 MPa to 1550 MPa to better reproduce the experimental stress-strain curve in Figure 8.11.

(a)
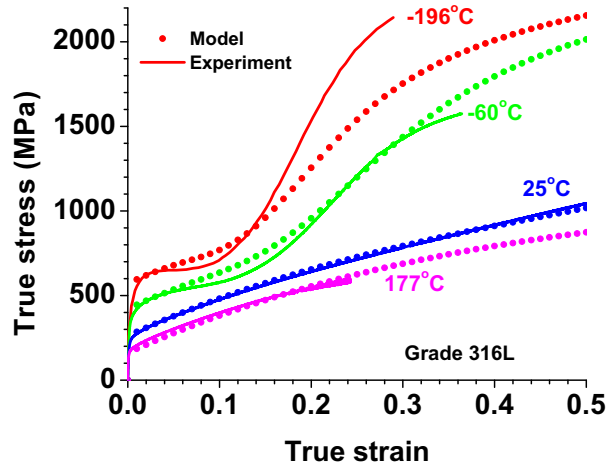
T	$\sigma_{\gamma 0}$	O-C values		
(°C)	(MPa)	α	β	n
−196	550	4.5	9.6	4.5
−60	420	3.9	5.8	4.5
25	260	0.4	65	4.5
177	160	0.0	0.0	4.5
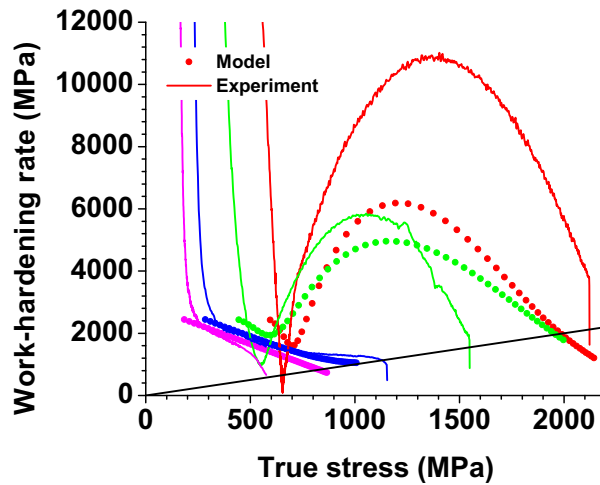
|	
$\sigma_{\gamma s}$	1000 MPa
$\theta_{\gamma 0}$	2500 MPa
$\sigma_{\alpha' s}$	900 MPa
$\theta_{\alpha' 0}$	3500 MPa
$\sigma_{\alpha' 00}$	−2200 MPa
$\sigma_{\alpha' 0}$	1550 MPa

(b)

Figure 8.11: Results of the mechanical model applied to the data collected by Spencer on grade 316L [72]. (a) Simulated stress-strain curves and (b) simulated work-hardening curves, for uniaxial tension.

Once again, the model provides a good qualitative prediction for the

experimental tensile response. In the case of testing at $-196°$C, one sees that the maximum stress at necking is not properly captured. This can be corrected if the value of $\sigma_{\alpha's}$ is made to be a function of temperature such that the α'-martensite strength increases with decreasing temperature as one would expect.

8.5 Defining an Average α'-Martensite Behaviour in the Dynamic Composite Model

In the model presented above, it is necessary to treat each new increment of α'-martensite formed in a given increment of applied strain as a separate phase with its own stress and strain. Each of these α'-martensite elements must be tracked individually in terms of the strain that they have undergone and therefore the stress that they carry. It would be much easier if the average behaviour of the α'-martensite could be defined directly based on the current volume fraction of α'-martensite. One way of doing this in such a dynamic composite has been recently proposed by Bouaziz *et al.* [260]. The key point is that, while each of the pre-existing $df_{\alpha'}$ should see the same increment of imposed strain ($d\epsilon$), the newly formed α'-martensite is formed with no strain. Now, consider an average increment of strain $\langle d\epsilon \rangle$ applied to all elements of α'-martensite equally. This will also lead to an average strain, $\langle \epsilon \rangle$ in the α'-martensite. Equating these two approaches gives:

$$f_{\alpha'}\left(\langle \epsilon \rangle\right) + df_{\alpha'}\left(0\right) = \left(f_{\alpha'} + df_{\alpha'}\right)\left[\langle \epsilon \rangle + \langle d\epsilon \rangle\right] \tag{8.7}$$

This can be simplified to:

$$\langle d\epsilon \rangle = \frac{f_{\alpha'} - df_{\alpha'}}{f_{\alpha'}}\left[\langle \epsilon \rangle + d\epsilon\right] - \langle \epsilon \rangle \tag{8.8}$$

Neglecting the second order terms, one can write:

$$\langle d\epsilon \rangle = d\epsilon - \frac{df_{\alpha'}}{f_{\alpha'}}\langle \epsilon \rangle \tag{8.9}$$

This allows one to calculate, for a given applied strain increment $d\epsilon$, an

average strain increment for α'-martensite that accounts for the formation of $df_{\alpha'}$ at each step of the calculation having zero strain. In this way, one can track only the average strain in the α'-martensite $\langle \epsilon \rangle$ rather than individual strains for each of the $df_{\alpha'}$ formed. This has significant advantage in terms of the simplicity of calculating the incremental material response.

The results of applying this method to the model developed above is illustrated in Figure 8.12 and compared to the full approach described above. The results are nearly identical as expected. While only shown here for the case of a single grain size, this simplified average approach works equally well for all of the other conditions of grain size, temperature and composition described above.
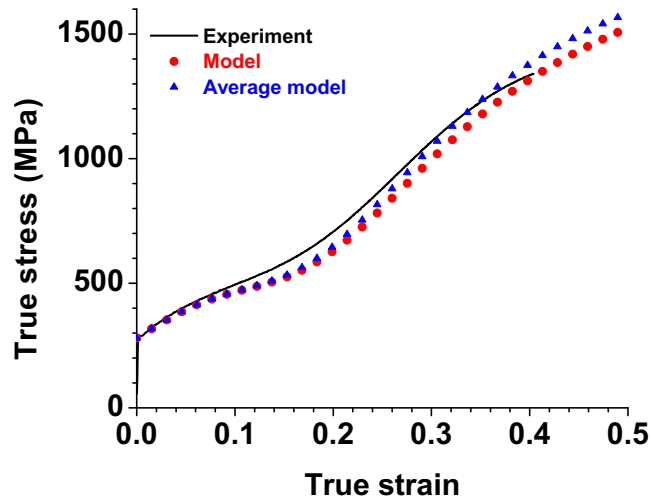
Figure 8.12: Comparison of both approaches applied to simulate the tensile curve of the 28 µm condition.

8.6 Summary

The novelty of the approach described in this chapter resides in the description of the mechanical behaviour of the α'-martensite via a n-phase

195

composite model, stressing the difference in work-hardening between freshly formed and more ancient α'-martensite. One of the assets of this model is its ability to describe, with minimal number of adjustable parameters, the grain size dependence and the temperature dependence of the mechanical properties of grade 301LN. In particular, the model succeeds in explaining the strain localization occurring at low temperatures or in a partially recrystallized sample. The extension to other austenitic grades seems possible as well, as shown by the comparison of the simulation with Spencer's results. Complex strain paths may be more challenging to model, given the uncertainty of describing a deformation by its Von Mises equivalents. In this case, incorporating the model within a more rigorous mechanical framework (e.g. crystal plasticity calculations) would avoid this problem.

Chapter 9

Conclusion

9.1   Summary and Key Results

The aim of this thesis, as defined in chapter 2, was to implement a physically-based model for the mechanical response of 301LN stainless steel able of capturing the effects of grain size, strain path and deformation temperature. Beyond this, the work presented here has helped to advance our basic understanding of the relationship between the mechanical response and microstructure in these complex materials. Here is how these objectives were accomplished in present work.

A particularly important outcome of this work is the observation of the effect of austenite grain size on the strain-induced martensitic phase transformations. As highlighted in the literature review (chapter 2), until now, there had been no single study with systematic observations on the trends related to the rate of transformation with grain size refinement, particularly with grain sizes in the nanometric scale. The results of this work shows that the effect of starting austenite grain size on the transformation kinetics is not large (much smaller than that predicted from the classical O-C model) but that this change in the kinetics does have a large effect on the predicted mechanical response (see e.g. Figure 8.7). Also interesting was the fact that the grain size dependence of the transformation kinetics were not monotonic, first decreasing with grain size then increasing with grain size, the change in trend occurring for $D \approx 1$ µm. It was found that this transition occurred at around the same grain size range where ϵ-martensite was found to be suppressed. Thus, it has been hypothesized that the decreasing rate of $\gamma \rightarrow \alpha'$ transformation corresponds to a decreasing proportion of ϵ-martensite to serve as nucleation sites for the α'-martensite. The increase

197

in the rate of transformation with further grain size refinement (below $D \approx 1$ µm) was suggested to be linked to a change in nucleation mechanism. In particular, for sufficiently fine grains, it was observed that the transformation may nucleate preferentially at grain boundaries (in the absence of ϵ-martensite).

The effect of strain path on the mechanical response and transformation kinetics were also monitored by comparing the results of tests in uniaxial tension and simple shear. As with the effect of grain size, the experimental data available in the literature (cf. chapter 2) does not present a consistent picture with respect to the effect of stress state and strain path. Consistent with other work [151], it was found that the effect of shear is to reduce the **apparent** rate of formation of α'-martensite, when tension and shear tests were compared on the basis of Von Mises equivalent strain. It has been argued here that the use of the Von Mises equivalent strain (and similarly the Von Mises equivalent stress) is not appropriate for making direct comparisons between the data as they ignore the effects of plastic anisotropy. It has been suggested here that the difference between shear and tension, both in terms of the transformation kinetics and mechanical response, could possibly be resolved if one were to account for texture and its evolution (e.g. via crystal plasticity simulations). This goes against traditional models which have argued for the predominance of triaxiality [171]. Detailed observations on the crystallography of the $\gamma \rightarrow \epsilon \rightarrow \alpha'$ transformation, however, also lead to questions about the importance of the macroscopic stress state on the transformation kinetics. In the case of tension, no clear correlation could be found between the interaction energy for the $\epsilon \rightarrow \alpha'$ transformation and the specific variants selected during this transformation based on the imposed stress. Attempts to correlate to slip activity were similarly unsuccessful. On the other hand, it was shown that the interaction energy and Schmid factors (which are shown to be proportional to one another) were well-correlated to the observed variants of ϵ-martensite.

The estimation of the stresses borne in the α'-martensite during tensile loading by the technique based on the magnetomechanical effect presented in chapter 7, compared well with measurements performed using

well-established diffraction techniques [13, 34]. A clear advantage for this technique is its relative simplicity both in terms of equipment required and the processing of data. With this technique, it was demonstrated that the hardening of the austenite, when the alloy was deformed at room temperature, was well approximated by deformation at 80°C, despite the fact that significant scale refinement occurs within the austenite due to the formation of α'-martensite. It was suggested that this scale refinement does not make a large contribution to the macroscopic flow stress because of the diminishing fraction of austenite with strain. In this sense, it was argued that it is most relevant to discuss the contributions of the individual phases as $f_{\alpha'}\sigma_{\alpha'}$ and $(1 - f_\gamma)\,\sigma_\gamma$ rather than as $\sigma_{\alpha'}$ or σ_γ. These quantities were found to be of prime importance in validating the model proposed in chapter 8.

The unique feature of the model presented in chapter 8 is in its incorporation of a "dynamic composite effect", where consideration is given to "fresh" α'-martensite being formed at each increment of strain. To our knowledge, this approach has not been previously adopted, most microstructurally based models considering monolithic behaviour for the α'-martensite phase. The other key feature is the requirement that α'-martensite forms with a compressive stress. This effect, arising from the transformation strain associated with the phase transformation, has previously been accounted for by means of an extra (positive) transformation strain associated with each new fraction of α'-martensite formed. This "dynamic composite" effect contributes to the hardening coming from the elastic loading of the freshly formed α'-martensite. This phenomenon helps to explain the observed high work-hardening behaviour of the α'-martensite. The input parameters of this model have been held to a minimum, with most being identifiable from experiments, the only parameters requiring adjustment being those defining the constitutive law of α'-martensite, i.e. $\sigma_{\alpha'00}$, $\sigma_{\alpha'0}$ and $\theta_{\alpha'0}$, these having relatively low sensitivity to the overall response.

The model is capable of predicting grain size and temperature dependence of the flow stress as well as the response in shear. Notably, it was successful in predicting the apparition of tensile instabilities. Previously, such instabilities have been attributed to very high rates of α'-martensite

199

transformation and large transformation strains [72]. Here, it is proposed that, under certain circumstances, the α'-martensite can lead to a softening as its contribution to the flow stress is lower than that of the austenite.

With weight reduction and improved crashworthiness in mind, grain size strengthening processing routes have been examined with growing interest by steel industries and manufacturers. Such thermo-mechanical routes have been shown to be easily applicable to austenitic stainless steels in which martensite reversion enables substantial grain size refinement, e.g. [213]. On a macroscopic level, the gain brought by grain size refinement is mostly reflected on the yield strength of the material, the results of present study showing that its ultimate tensile strength and uniform elongation would be similar for all grain sizes. More specifically, in grade 301LN, grain refinement below $\sim$0.5 µm will not be beneficial in forming operations, due to the strain localization which appears when the yield strength of austenite is too high. Specifically, in this grade, localization occurred when the yield stress of the austenite was raised above $\sim$700 MPa, regardless of whether the strengthening was due to temperature reduction or grain size refinement. The model for the development of such tensile instability, as proposed in this study, should therefore constitute a valuable tool when forming operations are envisaged.

The modelling presented here also demonstrated the importance of the rate of transformation on the mechanical properties, with a weak change in the kinetics of α'-martensite formation translating to a large difference in tensile stress at necking (of the order of 150 MPa in Figure 8.7). Hence, the advantage of monitoring the volume fraction of α'-martensite *in situ* during forming operations. The Feritscope used in present study could be an appropriate tool to perform such measurements. However, as shown in Figure 7.5, the Feritscope measurements require correction due to the fact that the α'-martensite is not free of stresses. This has been raised previously as a point of concern when using magnetic techniques for measurement of α'-martensite fraction [34]. It was shown, here, that for uniaxial stresses lower than $\sim$600 MPa (a value to adapt to the considered deformation route), corrections due to stress can be neglected. Another possible

use of the Feritscope method presented in chapter 7 is in the evaluation of residual stresses. Evaluating the usefulness of this technique for assessing residual stresses in deep drawn parts could be very useful, particularly when considered in relation to problems such as delayed cracking [261].

Finally, it was noted in chapter 1 that one of the key limitations to the implementation of austenitic stainless steel sheet in formed parts comes from a lack of "knowledge" about its behaviour. This thesis provides significant new insights both into the behaviour of this specific alloy, as well as in the coupling between phase transformations and mechanical properties more generally in austenitic stainless steels and therefore helps push towards a better "knowledge" of behaviour for these steels.

9.2 Future Work

This thesis showed the difficulty to model the grain size dependence of the kinetics of $\gamma \rightarrow \alpha'$ transformation (the equations proposed in section 6.6 tending to over predict the kinetics, although they capture the non-monotonic effect). The mechanisms of formation of α', notably the reduction in ϵ-martensite with scale refinement and the other mechanisms that may not involve nucleation on ϵ-martensite or grain boundaries demand deeper analysis before a complete model of the kinetics of α' formation can be advanced. One of the questions that needs to be resolved clearly is the influence of stress (rather than strain) on the transformation kinetics. It has been recently proposed [262] that experiments should be performed where the material is pre-strained at a temperature where no transformation takes place followed by deformation at a lower temperature where transformation can occur. In this way, the effect of hardening of the austenite (increasing its yield stress) by plastic deformation can affect the subsequent transformation kinetics. Finally, with regards to the transformation kinetics, it was shown here that the formation of ϵ-martensite could be explained based on the macroscopic stress, but that the specific variants of α'-martensite could not based upon the concept of interaction energy nor based upon slip system activity. This is an area that needs much work as a good physical expla-

nation for the transformation kinetics requires a clear understanding of the dominant mechanisms of nucleation of α'-martensite. Further detailed microscopy is needed to identify these mechanisms and to provide statistics for evaluating the different hypotheses that exist in the literature.

With regard to the mechanical model derived in chapter 8, an important requirement of the model is that the α'-martensite forms in compression. This part of the model could be validated, for instance, by X-ray microbeam diffraction experiments [263]. Another possible route to assess the importance of the mechanical contrast between the phases would be by measurement of the Bauschinger effect. Such experiments on 301LN have been performed and will be analyzed to compare with the predictions of the model developed here.

A natural next step to refine the model developed here would be to incorporate it within the framework of crystal plasticity so that the variation of crystallographic textures along different strain paths can be considered. As noted already in this thesis, the important differences in work-hardening rates of austenite between tension and shear cannot be captured by a simple Von Mises yield surface. Incorporation into such a model would also allow for arbitrary stress states and strain paths without the need for an assumption about the yield surface. Ideally, this model could then be used to simulate the kinetics of phase transformation and the deformation curve along plane strain deformation, a common deformation route in industrial practice.

Finally, as seen in chapter 8, very few parameters need to be varied in the mechanical model developed here to account for the mechanical behaviour of other grades of materials presenting the TRIP effect. The knowledge of the evolution of those parameters with some thermodynamics variables (e.g. stacking fault energy and Gibbs energies of the phases) would be an important contribution in terms of alloy design to tailor the chemical composition of a material to match a predetermined range of specifications. This requires that more experiments be performed on alloys of known chemistry to evaluate the effects of solute on the overall mechanical response.

Bibliography

[1] "Ultralight steel auto body, ulsab final report," tech. rep., American Iron and Steel Institute, Washington, D.C., March 1998.

[2] J. H. Schmitt, "New trends in austenitic stainless steel flat products for structural applications," in *4th Stainless Steel Science and Market Congress*, 2002.

[3] R. Armstrong *Canadian Metallurgical Quarterly*, vol. 13, p. 187, 1974.

[4] N. Ohkubo, "Effect of alloying elements on the mechanical properties of the stable austenitic stainless steel.," *ISIJ International*, vol. 34, no. 9, pp. 764–772, 1994.

[5] F. Danoix and P. Auger, "Atom probe studies of the Fe-Cr system and stainless steels aged at intermediate temperature: A review," *Materials Characterization*, vol. 44, no. 1-2, pp. 177–201, 2000.

[6] C. N. Hsiao, C. S. Chiou, and J. R. Yang, "Aging reactions in a 17-4 PH stainless steel," *Materials Chemistry and Physics*, vol. 74, no. 2, pp. 134–142, 2002.

[7] C. L. Xie and E. Nakamachi, "Design of texture for improved formability of high-strength steel," *Materials Science and Engineering A*, vol. 340, no. 1-2, pp. 130–138, 2003.

[8] M. Sarwar and R. Priestner, "Influence of ferrite-martensite microstructural morphology on tensile properties of dual-phase steel," *Journal of Materials Science*, vol. 31, no. 8, pp. 2091–2095, 1996.

[9] H. Takuda, K. Mori, T. Masachika, E. Yamazaki, and Y. Watanabe, "Finite element analysis of the formability of an austenitic stainless steel sheet in warm deep drawing," *Journal of Materials Processing Technology*, vol. 143–144, pp. 242–248, 2003. Proceedings of the International Conference on the Advanced Materials Processing Technology, 2001.

[10] E. PerdahcIoglu, H. Geijselaers, and M. Groen, "Influence of plastic strain on deformation-induced martensitic transformations," *Scripta Materialia*, vol. 58, no. 11, pp. 947–950, 2008.

[11] S. Rajasekhara, *Development of Nano/Sub-micron Grain Structures in Metastable Austenitic Stainless Steels*. PhD thesis, The University of Texas, Austin, U.S.A., 2007.

[12] C.-S. Yoo, Y.-M. Park, Y.-S. Jung, and Y.-K. Lee, "Effect of grain size on transformation-induced plasticity in an ultrafine-grained metastable austenitic steel," *Scripta Materialia*, vol. 59, no. 1, pp. 71 – 74, 2008.

[13] P. Dufour, "Détermination des propriétés micromécaniques d'un acier TRIP par diffraction de neutrons et par corrélation directe d'images digitales," Master's thesis, Université Catholique de Louvain, Belgium, 2007.

[14] S. Nanga, *Comportement et Transformations Martensitiques de deux aciers inoxydables austénitiques: effets de la temperature, de la vitesse et du chargement.* PhD thesis, École Nationale Supérieure des Mines de Paris, France, 2008.

[15] P. Lacombe, B. Baroux, and G. Beranger, eds., *Stainless Steels.* Les editions de physique - Les Ulis, France, 1993.

[16] A. J. Sedriks, *Corrosion of Stainless Steels*, ch. 2: Composition, Structure and Mechanical Properties, pp. 18–21. second edition ed., 1996.

[17] D. T. Llewellyn, "Work-hardening effects in austenitic stainless steels," *Journal of Materials Science & Technology*, vol. 13, no. 5, pp. 389–400, 1997.

[18] *ASM Handbook*, ch. Properties and Selection: Irons, Steels, and High-Performance Alloys - Section Wrought Stainless steels. ASM International, 2002.

[19] "British-Adopted European Standard BS EN 10088-1:2005 - Stainless steels. List of stainless steels."

[20] J. Charles, "The new 200-series: an alternative answer to Ni surcharge? Risks or opportunities?," *La Revue de Métallurgie-CIT*, pp. 308–317, 2007.

[21] M. Byrnes, M. Grujicic, and W. Owen, "Nitrogen strengthening of a stable austenitic stainless steel," *Acta Metallurgica*, vol. 35, no. 7, pp. 1853–1862, 1987.

[22] *Thermo-Calc, database TCFE 2000, S-version*, 2000.

[23] D. Bancroft, E. L. Peterson, and S. Minshall, "Polymorphism of iron at high pressure," *Journal of Applied Physics*, vol. 27, no. 3, pp. 291–298, 1956.

[24] T. Takahashi and W. Bassett, "High-pressure polymorph of iron," *Science*, vol. 145, no. 3631, pp. 483–486, 1964.

[25] L. Dougherty, G. Gray, E. Cerreta, R. McCabe, R. Field, and J. Bingert, "Rare twin linked to high-pressure phase transition in iron," *Scripta Materialia*, vol. 60, no. 9, pp. 772–775, 2009.

[26] J. Friedel, *Dislocations.* Pergamon Press, Oxford, 1964.

[27] D. Hull and D. J. Bacon, *Introduction to Dislocations.* Butterworth-Heinemann, 2001.

[28] L. Bracke, *Deformation Behaviour of Austenitic Fe-Mn Alloys by Twinning and Martensitic Transformation.* PhD thesis, Ghent University, Netherlands, 2007.

[29] S. Tavares, J. Pardal, M. G. da Silva, H. Abreu, and M. da Silva, "Deformation induced martensitic transformation in a 201 modified austenitic stainless steel," *Materials Characterization*, vol. 60, no. 8, pp. 907–911, 2009.

[30] L. Rémy, *Maclage et transformation martensitique cfc → hc induite par déformation plastique dans les alliages austénitiques à basse énergie de défaut d'empilement des systèmes Co-Ni et Fe-Mn-Cr-C*. PhD thesis, Université de Paris-Sud, Orsay, France, 1975.

[31] R. Schramm and R. Reed, "Stacking fault energies of seven commercial austenitic stainless steels," *Metallurgical and Materials Transactions A*, vol. 6, no. 7, pp. 1345–1351, 1975.

[32] F. B. Pickering, "Physical metallurgical development of stainless steels," in *Proc. Conf. Stainless Steels, Gothenburg* (E. G. Dunlop, ed.), 1984.

[33] F. Lecroisey and A. Pineau, "Martensitic transformations induced by plastic deformation in the Fe-Ni-Cr-C system," *Metallurgical and Materials Transactions B*, vol. 3, no. 2, pp. 391–400, 1972.

[34] J. Talonen, *Effect of strain-induced α' martensite transformation on mechanical properties of metastable austenitic stainless steels*. PhD thesis, Aalto University School of Science and Technology (TKK), Finland, 2007.

[35] L. E. Murr, *Interfacial Phenomena in Metals and Alloys*. Addison-Wesley Pub. Co., 1975.

[36] J. P. Hirth, "Thermodynamics of stacking faults," *Metallurgical Transactions B*, vol. 1, no. 9, pp. 2367–2374, 1970.

[37] G. B. Olson and M. Cohen, "A general mechanism of martensitic nucleation. part I: General concepts and fcc-hcp transformation," *Metallurgical and Materials Transactions A*, vol. 7, no. 12, pp. 1897–1904, 1976.

[38] S. Allain, J. P. Chateau, O. Bouaziz, S. Migot, and N. Guelton, "Correlations between the calculated stacking fault energy and the plasticity mechanisms in Fe-Mn-C alloys," *Materials Science and Engineering A*, vol. 387-389, pp. 158–162, 2004.

[39] P. J. Ferreira and P. Müllner, "A thermodynamic model for the stacking-fault energy," *Acta Materialia*, vol. 46, no. 13, pp. 4479–4484, 1998.

[40] R. Bunshah and R. Mehl, "Rate of propagation of martensite," *Transactions of the AIME*, vol. 197, pp. 1251–1258, 1953.

[41] D. A. Porter and K. E. Easterling, *Phase Transformations in Metals and Alloys*. London: Chapman & Hall, 2nd edition ed., 1993.

[42] R. Grange and H. Stewart, "The temperature range of martensite formation," *Transactions of the AIME*, vol. 167, pp. 467–497, 1946.

[43] P. Maxwell, A. Goldberg, and J. Shyne, "Stress-assisted and strain-induced martensites in Fe-Ni-C alloys," *Metallurgical and Materials Transactions B*, vol. 5, no. 6, pp. 1305–1318, 1974.

[44] I. Y. Georgieva and I. I. Nikitina, "Isothermal and athermal martensitic transformations," *Metal Science and Heat Treatment*, vol. 14, no. 5, pp. 452–458, 1972.

[45] Z. Nishiyama, *Martensitic Transformation*. Academic Press, London, 1978.

[46] A. Borgenstam and M. Hillert, "Nucleation of isothermal martensite," *Acta Materialia*, vol. 48, no. 11, pp. 2777–2785, 2000.

[47] J. Patel and M. Cohen, "Criterion for the action of applied stress in the martensitic transformation," *Acta Metallurgica*, vol. 1, no. 5, pp. 531–538, 1953.

[48] E. Bain, "The nature of martensite," *Transactions of the AIME*, vol. 70, p. 2546, 1924.

[49] J. J. Jonas, Y. He, and S. Godet, "The possible role of partial dislocations in facilitating transformations of the Nishiyama-Wassermann type," *Scripta Materialia*, vol. 52, no. 3, pp. 175–179, 2005.

[50] M. Humbert, B. Petit, B. Bolle, and N. Gey, "Analysis of the $\gamma \rightarrow \epsilon \rightarrow \alpha'$ variant selection induced by 10% plastic deformation in 304 stainless steel at -60°C," *Materials Science and Engineering A*, vol. 454-455, pp. 508–17, 2007.

[51] H. Bhadeshia, *Worked examples in the Geometry of Crystals*, ch. 3, pp. 26–27. The Institute of Materials, London, 2001.

[52] P. Mangonon and G. Thomas, "The martensite phases in 304 stainless steel," *Metallurgical and Materials Transactions B*, vol. 1, no. 6, pp. 1577–1586, 1970.

[53] M. Andersson, R. Stalmans, and J. Ågren, "Unified thermodynamic analysis of the stress-assisted $\gamma \rightarrow \epsilon$ martensitic transformation in Fe-Mn-Si alloys," *Acta Materialia*, vol. 46, no. 11, pp. 3883–3891, 1998.

[54] H. Funakubo, *Shape Memory Alloys*. Gordon and Breach Science Publishers, 1987.

[55] K. Otsuka and C. Wayman, *Shape Memory Materials*. Cambridge University Press, 1998.

[56] H. Yu, "A new model for the volume fraction of martensitic transformations," *Metallurgical and Materials Transactions A*, vol. 28, no. 12, pp. 2499–2506, 1997.

[57] K. Tsuzaki, Y. Natsume, and T. Maki, "Transformation reversibility in Fe-Mn-Si shape memory alloy," *Journal de Physique IV*, vol. 5, pp. 409–414, 1995. International Conference on Martensitic Transformations (ICOMAT).

[58] G. B. Olson and M. Azrin, "Transformation behavior of TRIP steels," *Metallurgical and Materials Transactions A*, vol. 9, no. 5, pp. 713–721, 1978.

[59] G. F. Bolling and R. H. Richman, "The influence of stress on Martensite-start temperatures in Fe-Ni-C alloys," *Scripta Metallurgica*, vol. 4, no. 7, pp. 539–543, 1970.

[60] G. B. Olson and M. Cohen, "A mechanism for the strain-induced nucleation of martensitic transformations," *Journal of the Less Common Metals*, vol. 28, no. 1, pp. 107–118, 1972.

[61] J. Talonen, P. Aspegren, and H. Hänninen, "Comparison of different methods for measuring strain induced α' martensite content in austenitic steels," *Materials Science And Technology*, vol. 20, no. 12, pp. 1506–1512, 2004.

[62] M. Dickson *Journal of Applied Crystallography*, vol. 2, p. 176, 1969.

[63] H. M. Rietveld, "A profile refinement method for nuclear and magnetic structures," *Journal of Applied Crystallography*, vol. 2, no. 2, pp. 65–71, 1969.

[64] A. Albinati and B. T. M. Willis, "The Rietveld method in neutron and X-ray powder diffraction," *Journal of Applied Crystallography*, vol. 15, no. 4, pp. 361–374, 1982.

[65] R. D. Arnell *J. Iron Steel Inst.*, vol. 206, pp. 1035–1036, 1968.

[66] R. W. Cheary and Y. Ma-sorrell *J. Mater. Sci.*, vol. 35, pp. 1105–1113, 2000.

[67] M. Radu, J. Valy, A. Gourgues, F. L. Strat, and A. Pineau, "Continuous magnetic method for quantitative monitoring of martensitic transformation in steels containing metastable austenite," *Scripta Materialia*, vol. 52, no. 6, pp. 525–530, 2005.

[68] S. Hecker, M. Stout, K. Staudhammer, and J. Smith, "Effects of strain state and strain rate on deformation-induced transformation in 304 stainless steel. Part I: Magnetic measurements and mechanical behavior," *Metallurgical and Materials Transactions A*, vol. 13, no. 4, pp. 619–626, 1982.

[69] L. Zhao, N. H. van Dijk, E. Brück, J. Sietsma, and S. van der Zwaag, "Magnetic and X-ray diffraction measurements for the determination of retained austenite in TRIP steels," *Materials Science and Engineering A*, vol. 313, no. 1-2, pp. 145–152, 2001.

[70] J. Post, H. Nolles, K. Datta, and H. Geijselaers, "Experimental determination of the constitutive behaviour of a metastable austenitic stainless steel," *Materials Science and Engineering A*, vol. 498, no. 1-2, pp. 179–190, 2008.

[71] A. K. De, D. C. Murdock, M. C. Mataya, J. G. Speer, and D. K. Matlock, "Quantitative measurement of deformation-induced martensite in 304 stainless steel by X-ray diffraction," *Scripta Materialia*, vol. 50, pp. 1445–1449, 2004.

[72] K. Spencer, *The Work-Hardening of Austenitic Stainless Steel, applied to the Fabrication of High-Strength Conductors*. PhD thesis, McMaster University, Canada, 2004.

[73] W. G. Burgers *Physica*, vol. 1, p. 561, 1934.

[74] G. Stone and G. Thomas, "Deformation induced alpha' and epsilon martensites in Fe-Ni-Cr single crystals," *Metallurgical and Materials Transactions B*, vol. 5, no. 9, pp. 2095–2102, 1974.

[75] T.-H. Lee, E. Shin, C.-S. Oh, H.-Y. Ha, and S.-J. Kim, "Correlation between stacking fault energy and deformation microstructure in high-interstitial-alloyed austenitic steels," *Acta Materialia*, vol. 58, no. 8, pp. 3173–3186, 2010.

[76] L. Rémy and A. Pineau, "Twinning and strain-induced fcc → hcp transformation in the Fe-Mn-Cr-C system," *Materials Science and Engineering B*, vol. 28, no. 1, pp. 99–107, 1977.

[77] H. Idrissi, L. Ryelandt, M. Véron, D. Schryvers, and P. Jacques, "Is there a relationship between the stacking fault character and the activated mode of plasticity of Fe-Mn-based austenitic steels?," *Scripta Materialia*, vol. 60, no. 11, pp. 941–944, 2009.

[78] J. Brooks, M. Loretto, and R. Smallman, "Direct observations of martensite nuclei in stainless steel," *Acta Metallurgica*, vol. 27, no. 12, pp. 1839–1847, 1979.

[79] J. Putaux and J. Chevalier, "HREM study of self-accomodated thermal ϵ martensite in an Fe-Mn-Si-Cr-Ni shape memory alloy," *Acta Materialia*, vol. 44, pp. 1701–1716, 1996.

[80] K. Verbeken, N. Van Caenegem, and D. Raabe, "Identification of epsilon martensite in a Fe-based shape memory alloy by means of EBSD," *Micron*, vol. 40, no. 1, pp. 151–156, 2009.

[81] G. B. Olson and M. Cohen, "Kinetics of strain-induced martensitic nucleation," *Metallurgical and Materials Transactions A*, vol. 6, no. 4, pp. 791–795, 1975.

[82] J. W. Brooks, M. H. Loretto, and R. E. Smallman, "In-situ observations of the formation of martensite in stainless steel," *Acta Metallurgica*, vol. 27, no. 12, pp. 1829–1838, 1979.

[83] Seeger *Zeitschrift fur Metallkunde*, vol. 47, p. 653, 1956.

[84] H. Fujita and S. Ueda, "Stacking faults and f.c.c. (γ) → h.c.p. (ϵ) transformation in 18/8-type stainless steel," *Acta Metallurgica*, vol. 20, no. 5, pp. 759–767, 1972.

[85] B. Jiang, X. Qi, S. Yang, W. Zhou, and T. Y. Hsu, "Effect of stacking fault probability on $\gamma \to \epsilon$ martensitic transformation and shape memory effect in Fe-Mn-Si based alloys," *Acta Materialia*, vol. 46, no. 2, pp. 501–510, 1998.

[86] P. Hedström, U. Lienert, J. Almer, and M. Odén, "Elastic strain evolution and ϵ-martensite formation in individual austenite grains during in situ loading of a metastable stainless steel," *Materials Letters*, vol. 62, no. 2, pp. 338–340, 2008.

[87] S. Allain, *Caractérisation et modélisation thermomécaniques multi-échelles des mécanismes de déformation et d'écrouissage d'aciers austénitiques à haute teneur en manganèse. Application à l'effet TWIP.* PhD thesis, INP Lorraine, Metz, France, 2004.

[88] G. Blanc, R. Tricot, and R. Castro, "Transformations martensitiques dans les aciers inoxydables austénitiques Fe-Cr-Ni. Relation entre les paramètres de la phase ϵ et les mécanismes de la transformation.," *Revue de la Métallurgie*, vol. 70, no. 7-8, pp. 527–541, 1973.

[89] W. L. Fink and E. D. Campbell *Transactions of the American Society for Steel Treating*, vol. 9, p. 717, 1926.

[90] N. Sljakov, G. Kurdjumov, and N. Goufdob *Z. Phys.*, vol. 45, p. 384, 1927.

[91] C. S. Roberts, "Effect of carbon on the volume fractions and lattice parameters of retained austenite and martensite," *Transactions of the AIME*, vol. 197, pp. 203–204, 1953.

[92] G. Krauss, "Deformation and fracture in martensitic carbon steels tempered at low temperatures," *Metallurgical and Materials Transactions B*, vol. 32, no. 2, pp. 205–221, 2001.

[93] L. Xiao, Z. Fan, and Z. Jinxiu, "Lattice parameter variation with carbon content of martensite (I)," *Physical Review*, vol. 52, no. 14, pp. 9970–9978, 1995.

[94] J. A. Venables, "Martensite transformation in stainless steel," *Philosophical Magazine*, vol. 7, no. 73, pp. 35–44, 1962.

[95] J. Breedis and L. Kaufman, "The formation of hcp and bcc phases in austenitic iron alloys," *Metallurgical and Materials Transactions B*, vol. 2, no. 9, pp. 2359–2371, 1971.

[96] J. Dash and H. M. Otte, "The martensite transformation in stainless steel," *Acta Metallurgica*, vol. 11, no. 10, pp. 1169–1178, 1963.

[97] L. E. Murr, K. Staudhammer, and S. Hecker, "Effects of strain state and strain rate on deformation-induced transformation in 304 stainless steel. Part II: Microstructural study," *Metallurgical and Materials Transactions A*, vol. 13, pp. 627–635, 1982.

[98] J.-Y. Choi and W. Jin, "Strain-induced martensite formation and its effect on strain-hardening behavior in the cold-drawn 304 austenitic stainless steels," *Scripta Materialia*, vol. 36, no. 1, pp. 99–104, 1997.

[99] H. Fujita and T. Katayama, "In-situ observation of strain-induced $\gamma \rightarrow \epsilon \rightarrow \alpha'$ and $\gamma \rightarrow \alpha'$ martensitic transformations in Fe-Cr-Ni alloys," *Material Transactions of the Japanese Institute of Metals*, vol. 33, no. 3, pp. 243–252, 1992.

[100] V. Tsakiris and D. V. Edmonds, "Martensite and deformation twinning in austenitic steels," *Materials Science and Engineering A*, vol. 273-275, pp. 430–436, 1999.

[101] T. Inamura, K. Takashima, and Y. Higo, "Crystallography of nanometre-sized α'-martensite formed at intersections of mechanical γ twins in an austenitic stainless steel," *Philosophical Magazine*, vol. 83, no. 8, pp. 935–954, 2003.

[102] N. Nakada, H. Ito, Y. Matsuoka, T. Tsuchiyama, and S. Takaki, "Deformation-induced martensitic transformation behavior in cold-rolled and cold-drawn type 316 stainless steels," *Acta Materialia*, vol. 58, no. 3, pp. 895–903, 2010.

[103] P. Mangonon and G. Thomas, "Structure and properties of thermal-mechanically treated 304 stainless steel," *Metallurgical and Materials Transactions B*, vol. 1, no. 6, pp. 1587–1594, 1970.

[104] X. Wang, "Private communication." 2010.

[105] C. Sinclair, "A molecular dynamics study of deformation induced phase transformations at fault band intersections," in *15th International Conference on Strength in Materials (ICSMA)*, 2009.

[106] N. Gey, B. Petit, and M. Humbert, "Electron backscattered diffraction study of ϵ/α'-martensite martensitic variants induced by plastic deformation in 304 stainless steel," *Metallurgical And Materials Transactions A*, vol. 36, no. 12, pp. 3291–3299, 2005.

[107] Y.-K. Lee and C.-S. Choi, "Effects of thermal cycling on the kinetics of the $\gamma \rightarrow \epsilon$ martensitic transformation in an Fe-17%Mn alloy," *Metallurgical and Materials Transactions A*, vol. 31, no. 11, pp. 2735–2738, 2000.

[108] G. B. Olson and M. Cohen, "A general mechanism of martensitic nucleation. part II: fcc→bcc and other martensitic transformations," *Metallurgical and Materials Transactions A*, vol. 7, no. 11, pp. 1905–1914, 1976.

[109] J. Guimaraes and S. F. De Oliveira, "Work-hardening and martensitic transformation in Fe-27% Ni-0.23%C at 263 K," *Scripta Metallurgica*, vol. 13, no. 7, pp. 537–542, 1979.

[110] G. Yang, C. Huang, S. Wu, and Z. Zhang, "Strain-induced martensitic transformation in 304L austenitic stainless steel under ECAP deformation," *Acta Metallurgica Sinica*, vol. 45, no. 8, pp. 906–911, 2009.

[111] T. Suzuki, H. Kojima, K. Suzuki, T. Hashimoto, and M. Ichihara, "An experimental study of the martensite nucleation and growth in 18/8 stainless steel," *Acta Metallurgica*, vol. 25, no. 10, pp. 1151–1162, 1977.

[112] K. Spencer, J. D. Embury, K. T. Conlon, M. Véron, and Y. Bréchet, "Strengthening via the formation of strain-induced martensite in stainless steels," *Materials Science and Engineering A*, vol. 387-89, pp. 873–881, 2004.

[113] W.-S. Lee and C.-F. Lin, "The morphologies and characteristics of impact-induced martensite in 304L stainless steel," *Scripta Materialia*, vol. 43, no. 8, pp. 777 – 782, 2000.

[114] L. Bracke, L. Kestens, and J. Penning, "Transformation mechanism of α' martensite in an austenitic Fe-Mn-C-N alloy," *Scripta Materialia*, vol. 57, no. 5, pp. 385–388, 2007.

[115] A. Das, S. Sivaprasad, M. Ghosh, P. Chakraborti, and S. Tarafder, "Morphologies and characteristics of deformation induced martensite during tensile deformation of 304 LN stainless steel," *Materials Science and Engineering A*, vol. 486, no. 1-2, pp. 283–286, 2008.

[116] C. Huang, G. Yang, Y. Gao, S. Wu, and S. Li, "Investigation on the nucleation mechanism of deformation-induced martensite in an austenitic stainless steel under severe plastic deformation," *Journal of Materials Research*, vol. 22, no. 3, pp. 724–729, 2007.

[117] K. Spencer, M. Véron, K. Yu-Zhang, and J. D. Embury, "The strain induced martensite transformation in austenitic stainless steels. part 1: Influence of temperature and strain history," *Materials Science And Technology*, vol. 25, no. 1, pp. 7–17, 2009.

[118] H.-S. Yang and H. Bhadeshia, "Austenite grain size and the martensite-start temperature," *Scripta Materialia*, vol. 60, no. 7, pp. 493–495, 2009.

[119] A. Bogers and W. Burgers, "Partial dislocations on the {110} planes in the bcc lattice and the transition of the fcc into the bcc lattice," *Acta Metallurgica*, vol. 12, no. 2, pp. 255–261, 1964.

[120] C. Sinclair and R. Hoagland, "A molecular dynamics study of the fcc → bcc transformation at fault intersections," *Acta Materialia*, vol. 56, no. 16, pp. 4160–4171, 2008.

[121] C. Hayzelden, K. Chattopadhyay, J. Barry, and B. Cantor, "Transmission electron microscopy observations of the f.c.c.-to-h.c.p. martensite transformation in Co-Ni alloys," *Philosophical Magazine A*, vol. 63, no. 3, pp. 461–470, 1991.

[122] S. C. H.-S. W. J. R. Y. . H. K. D. H. Bhadeshia, "Mechanical stabilisation of austenite," *Materials Science and Technology*, vol. 22, pp. 641–644, 2006.

[123] V. Kouznetsova and M. Geers, "Modeling the interaction between plasticity and the austenite-martensite transformation," *International Journal for Multiscale Computational Engineering*, vol. 5, no. 2, pp. 129–140, 2007.

[124] M. Umemoto and W. Owen, "Effects of austenitizing temperature and austenite grain size on the formation of athermal martensite in an iron-nickel and an iron-nickel-carbon alloy," *Metallurgical and Materials Transactions B*, vol. 5, no. 9, pp. 2041–2046, 1974.

[125] B. H. Jiang, L. Sun, R. Li, and T. Y. Hsu, "Influence of austenite grain size on $\gamma \to \epsilon$ martensitic transformation temperature in Fe-Mn-Si-Cr alloys," *Scripta Metallurgica et Materialia*, vol. 33, no. 1, pp. 63–68, 1995.

[126] T. Durlu, "Effect of austenite grain size on ϵ martensite formation in an Fe-Mn-Mo alloy," *Journal of Materials Science Letters*, vol. 16, no. 4, pp. 320–321, 1997.

[127] Y. Inokuti and B. Cantor, "Splat-quenched Fe–Ni alloys," *Scripta Metallurgica*, vol. 10, no. 7, pp. 655–659, 1976.

[128] Y. Inokuti and B. Cantor, "Overview 15: The microstructure and kinetics of martensite transformations in splat-quenched Fe and Fe-Ni alloys – II," *Acta Metallurgica*, vol. 30, no. 2, pp. 343–356, 1982.

[129] A. Hamada, P. Sahu, S. Ghosh Chowdhury, L. Karjalainen, and T. Levoska, J.And Oittinen, "Kinetics of the $\gamma \to \epsilon$ martensitic transformation in fine-grained Fe-26Mn-0.14C austenitic steel," *Metallurgical And Materials Transactions A*, vol. 39, pp. 462–465, 2008.

[130] K. Tao, H. Choo, H. Li, B. Clausen, J.-E. Jin, and Y.-K. Lee, "Transformation-induced plasticity in an ultrafine-grained steel: An in situ neutron diffraction study," *Applied Physics Letters*, vol. 90, no. 10, p. 101911, 2007.

[131] J.-H. Jun and C.-S. Choi, "Variation of stacking fault energy with austenite grain size and its effect on the Ms temperature of $\gamma \rightarrow \epsilon$ martensitic transformation in Fe-Mn alloy," *Materials Science and Engineering A*, vol. 257, no. 2, pp. 353–356, 1998.

[132] T. Maki, Y. Tomota, and I. Tamura, "Effect of grain size on the transformation-induced plasticity in metastable austenitic Fe-Ni-C alloy," *Journal of the Japanese Institute of Metals*, vol. 38, pp. 871–876, 1974.

[133] E. Jimenez-Melero, N. van Dijk, L. Zhao, J. Sietsma, S. Offerman, J. Wright, and S. van der Zwaag, "Martensitic transformation of individual grains in low-alloyed TRIP steels," *Scripta Materialia*, vol. 56, no. 5, pp. 421–424, 2007.

[134] K. Nohara, Y. Ono, and N. Ohashi, "Composition and grain-size dependencies of strain-induced martensitic transformation in metastable austenitic stainless steels," *The Iron and Steel Institute of Japan (ISIJ)*, vol. 63, pp. 212–222, 1977.

[135] R. H. Leal and J. Guimaraes, "Microstructure evolution during mechanically induced martensitic transformation in Fe-33%Ni-0.1%C," *Materials Science and Engineering*, vol. 48, no. 2, pp. 249–254, 1981.

[136] J. Gonzales, R. Aranda, and M. Jonapá, "The influence of grain size on the kinetics of strain induced martensite in type 304 stainless steel," in *Applications of stainless steel '92, Stockholm, Sweden*, pp. 1009–1016, 1992.

[137] W. Jeong, D. Matlock, and G. Krauss, "Effects of tensile-testing temperature on deformation and transformation behavior of retained austenite in a 0.14C-1.2Si-1.5Mn steel with ferrite-bainite-austenite structure," *Materials Science and Engineering A*, vol. 165, no. 1, pp. 9–18, 1993.

[138] S. K. Varma, J. Kalyanam, L. E. Murr, and V. Shrinivas, "Effect of grain size on deformation-induced martensite formation in 304 stainless steel and 316 stainless steel during room temperature tensile testing," *Journal of Materials Science Letters*, vol. 13, no. 2, pp. 107–111, 1994.

[139] A. Pétein, *On the Interaction between strain-induced Phase Transformations and Mechanical Properties in Mn-Si-Al Steels And Ni-Cr Austenitic Stainless Steels*. PhD thesis, Université Catholique de Louvain, Belgium, 2007.

[140] V. Shrinivas, S. K. Varma, and L. E. Murr, "Deformation-induced martensitic characteristics in 304 and 316 stainless steels during room-temperature rolling," *Metallurgical and Materials Transactions A*, vol. 26, pp. 661–671, 1995.

[141] A. De, J. Speer, D. Matlock, D. Murdock, M. Mataya, and R. Comstock, "Deformation-induced phase transformation and strain-hardening in type 304 austenitic stainless steel," *Metallurgical and Materials Transactions A*, vol. 37, no. 6, pp. 1875–1886, 2006.

[142] T. Angel, "Formation of martensite in austenitic stainless steels - effects of deformation, temperature, and composition," *Journal of Iron & Steel Institute*, vol. 177, pp. 165–174, 1954.

[143] K. Mumtaz, S. Takahashi, J. Echigoya, L. Zhang, Y. Kamada, and M. Sato, "Temperature dependence of martensitic transformation in austenitic stainless steel," *Journal of Materials Science Letters*, vol. 22, no. 6, pp. 423–427, 2003.

[144] R. Kubler, *Étude du comportement des aciers à effet TRIP : approches micromécaniques et phénoménologiques. Application à la mise en forme.* PhD thesis, Université Paul Verlaine de Metz, France, 2004.

[145] J. Talonen, H. Hänninen, P. Nenonen, and G. Pape, "Formation of shear bands and strain-induced martensite during plastic deformation of metastable austenitic stainless steels," *Acta Materialia*, vol. 55, no. 18, pp. 610–6118, 2007.

[146] S. Nanga, A. Pineau, B. Tanguy, L. Nazé, and P.-O. Santacreu, "Plasticity and strain-induced martensitic transformation in two austenitic stainless steels," in *International Conference on Martensitic Transformations (ICOMAT)*, 2008.

[147] V. Talyan, R. H. Wagoner, and J. K. Lee, "Formability of stainless steel," *Metallurgical And Materials Transactions A*, vol. 29, no. 8, pp. 2161–2172, 1998.

[148] H. N. Han, C. G. Lee, C.-S. Oh, T.-H. Lee, and S.-J. Kim, "A model for deformation behavior and mechanically induced martensitic transformation of metastable austenitic steel," *Acta Materialia*, vol. 52, no. 17, pp. 5203–5214, 2004.

[149] S. G. S. Raman and K. A. Padmanabhan, "Tensile deformation-induced martensitic transformation in AISI 304LN austenitic stainless steel," *Journal of Materials Science Letters*, vol. 13, pp. 389–392, 1994.

[150] J. Talonen, P. Nenonen, G. Pape, and H. Hänninen, "Effect of strain rate on the strain-induced $\gamma \rightarrow \alpha'$ martensite transformation and mechanical properties of austenitic stainless steels," *Metallurgical and Materials Transactions A*, vol. 36, no. 2, pp. 421–432, 2005.

[151] A. A. Lebedev and V. V. Kosarchuk, "Influence of phase transformations on the mechanical properties of austenitic stainless steels," *International Journal of Plasticity*, vol. 16, no. 7-8, pp. 749–767, 2000.

[152] T. Iwamoto, T. Tsuta, and Y. Tomita, "Investigation on deformation mode dependence of strain-induced martensitic transformation in TRIP steels and modelling of transformation kinetics," *International Journal of Mechanical Sciences*, vol. 40, no. 2-3, pp. 173–182, 1998.

[153] G. W. Powell, E. R. Marshall, and W. A. Backofen, "Strain-hardening of austenitic stainless steel," *ASM Transactions*, vol. 50, pp. 478–497, 1958.

[154] M. Kato and T. Mori, "Orientation of martensite formed in Fe-23Ni-5Cr crystals under uniaxial stress along [001]," *Acta Metallurgica*, vol. 25, no. 8, pp. 951–956, 1977.

[155] P. Jacques, Q. Furnémont, T. Pardoen, and F. Delannay, "On the role of martensitic transformation on damage and cracking resistance in TRIP-assisted multiphase steels," *Acta Materialia*, vol. 49, no. 1, pp. 139–152, 2001.

[156] P. Jacques, Q. Furnémont, F. Lani, T. Pardoen, and F. Delannay, "Multiscale mechanics of TRIP-assisted multiphase steels. Part I: Characterization and mechanical testing," *Acta Materialia*, vol. 55, no. 11, pp. 3681–3693, 2007.

[157] DeMania, "The influence of martensitic transformation on the formability of 304L stainless steel sheet," Master's thesis, Massachusetts Institute of Technology, 1995.

[158] D. Mohr and J. Jacquemin, "Large deformation of anisotropic austenitic stainless steel sheets at room temperature: Multi-axial experiments and phenomenological modeling," *Journal of the Mechanics and Physics of Solids*, vol. 56, no. 10, pp. 2935–2956, 2008.

[159] E. PerdahcIoglu, H. Geijselaers, and J. Huétink, "Influence of stress state and strain path on deformation-induced martensitic transformations," *Materials Science and Engineering A*, vol. 481–482, pp. 727–731, 2008.

[160] S. Kundu and H. Bhadeshia, "Transformation texture in deformed stainless steel," *Scripta Materialia*, vol. 55, no. 9, pp. 779–781, 2006.

[161] L. Malet, C. Sinclair, P. Jacques, and S. Godet, "Grain scale analysis of variant selection during the $\gamma \rightarrow \epsilon \rightarrow \alpha'$ phase transformation in austenitic steels," in *PTM*, 2010.

[162] D. C. Ludwigson and J. A. Berger, "Plastic behaviour of metastable austenitic stainless steels," *Journal of Iron & Steel Institute*, vol. 207, pp. 63–69, 1969.

[163] W. W. Gerberich, G. Thomas, E. R. Parker, and V. F. Zackay vol. 3, pp. 849–899, ASM, Metals Park, 1970.

[164] J. R. C. Guimaraes, "The deformation-induced martensitic reaction in polycrystalline Fe-30.7Ni-0.06C," *Scripta Metallurgica*, vol. 6, p. 795, 1972.

[165] K. Sugimoto, M. Kobayashi, and S. Hashimoto, "Ductility and strain-induced transformation in a high-strength transformation-induced plasticity-aided dual-phase steel," *Metallurgical Transactions A*, vol. 23, no. 11, pp. 3085–3091, 1992.

[166] I. Pychmintsev, R. Savrai, B. De Cooman, and O. Moriau, "High strain rate behaviour of TRIP-aided automotive steels," in *Proceedings of the International Conference on TRIP-aided high strength ferrous alloys, GRIPS, Aachen:Mainz*, pp. 299–302, 2002.

[167] H. C. Shin, T. K. Ha, W. J. Park, and Y. W. Chang, "Deformation-induced martensitic transformation under various deformation modes," *Key Engineering Materials*, vol. 223, no. 236, pp. 667–672, 2003.

[168] C. Guntner and R. Reed, "The effect of experimental variables including the martensitic transformation on the low-temperature mechanical properties of austenitic stainless stees," *ASM Transactions*, vol. 55, pp. 399–419, 1962.

[169] T. Iwamoto and T. Tsuta, "Computational simulation of the dependence of the austenitic grain size on the deformation behavior of TRIP steels," *International Journal of Plasticity*, vol. 16, no. 7-8, pp. 791–804, 2000.

[170] R. G. Stringfellow, *Mechanics of Strain-induced Transformation Toughening in Metastable Austenitic Stainless Steels*. PhD thesis, Massachusetts Institute of Technology, U.S.A., 1990.

[171] R. G. Stringfellow, D. M. Parks, and G. B. Olson, "A constitutive model for transformation plasticity accompanying strain-induced martensitic transformations in metastable austenitic steels," *Acta Metallurgica et Materialia*, vol. 40, no. 7, pp. 1703–1716, 1992.

[172] J. Serri, M. Martiny, and G. Ferron, "A numerical analysis of the formability of unstable austenitic steels," *Journal of Materials Processing Technology*, vol. 164-165, pp. 1241–1247, 2005. AMPT/AMME05 Part 2.

[173] U. F. Kocks, "Laws for work-hardening and low-temperature creep," *Journal of Engineering Materials and Technology - Transactions of the ASME*, pp. 76–85, 1976.

[174] S. Allain, O. Bouaziz, and J. Chateau, "Thermally activated dislocation dynamics in austenitic FeMnC steels at low homologous temperature," *Scripta Materialia*, vol. 62, no. 7, pp. 500–503, 2010.

[175] E. Hall, "The deformation and ageing of mild steel," *Proceedings of the Physical Society B*, vol. 64, pp. 747–753, 1951.

[176] N. Petch, "Ductile fracture of polycrystalline α-iron," *Philosophical Magazine*, vol. 1, pp. 186–190, 1956.

[177] S. Rajasekhara, P. J. Ferreira, L. P. Karjalainen, and A. Kyrolainen, "Hall-Petch behaviour in ultra-fine grained AISI 301LN stainless steel," *Metallurgical and Materials Transactions A*, vol. 38, no. 6, pp. 1202–1210, 2007.

[178] A. Di Schino, M. Barteri, and J. M. Kenny, "Effects of grain size on the properties of a low nickel austenitic stainless steel," *Journal of Materials Science*, vol. 38, no. 23, pp. 4725–4733, 2003.

[179] B. Kashyap and K. Tangri, "On the hall-petch relationship and substructural evolution in type 316L stainless steel," *Acta Metallurgica et Materialia*, vol. 43, no. 11, pp. 3971–3981, 1995.

[180] S. M. G. Singh, K.K.; Sangal, "Hallpetch behaviour of 316L austenitic stainless steel at room temperature," *Materials Science and Technology*, vol. 18, no. 2, pp. 165–172, 2002.

[181] S. Brochet, *Compréhension du rôle de la microstructure d'aciers inoxydables austénitiques à grains fins sur le comportement en fatigue*. PhD thesis, Université des Sciences et Technologies de Lille, France, 2007.

[182] M. A. Meyers and C. K. Kumar, *Mechanical Metallurgy: Principles and applications*, ch. 14: Grain size Strengthening, pp. 494–514. Prentice-Hall Inc., 1984.

[183] A. W. Thompson, "Effect of grain size on work hardening in nickel," *Acta Metallurgica*, vol. 25, pp. 83–86, 1977.

[184] T. Lebedkina, M. Lebyodkin, J.-P. Chateau, A. Jacques, and S. Allain, "On the mechanism of unstable plastic flow in an austenitic Fe-Mn-C TWIP steel," *Materials Science and Engineering, A*, vol. 519, no. 1-2, pp. 147–154, 2009.

[185] K. Renard, S. Ryelandt, and P. Jacques, "Characterisation of the Portevin-Le Châtelier effect affecting an austenitic TWIP steel based on digital image correlation," *Materials Science and Engineering, A*, vol. 527, no. 12, pp. 2969–2977, 2010.

[186] S. Nanga, A. Pineau, B. Tanguy, and P.-O. Santacreu, "Strain-induced martensitic transformations in two austenitic stainless steels: macro-micro behaviour," in *17th European Conference on Fracture (ECF17)*, 2008.

[187] R. A. Varin, B. Mazurek, and D. Himbeault, "Discontinuous yielding in ultrafine-grained austenitic stainless steels," *Materials science and Engineering*, vol. 94, pp. 109–119, 1987.

[188] K. Singh, "Strain hardening behaviour of 316L austenitic stainless steel," *Materials Science and Technology*, vol. 20, no. 9, pp. 1134–1142, 2004.

[189] B. P. Kashyap and K. Tangri, "Hall-Petch relationship and substructural evolution in boron containing type 316L stainless steel," *Acta Materialia*, vol. 45, no. 6, pp. 2383–2395, 1997.

[190] X. Feaugas and H. Haddou, "Grain-size effects on tensile behavior of nickel and AISI 316L stainless steel," *Metallurgical and Materials Transactions A*, vol. 34, no. 10, pp. 2329–2340, 2003.

[191] C. W. Sinclair, H. Proudhon, and J. D. Mithieux, "Work-hardening in a fine grained austenitic stainless steel," *Materials Science Forum*, vol. 539-543, pp. 4714–4719, 2007.

[192] D. Rousseau, G. Blanc, R. Tricot, and A. Gueussier, "Structure stability under deformation and at low temperatures for austenitic stainless steels with Cr-Ni," *Mem. Sci. Revue de la Métallurgie*, vol. 67, no. 5, p. 315, 1970.

[193] P.-O. Santacreu, J.-C. Glez, G. Chinouilh, and T. Frohlich, "Behaviour model of austenitic stainless steels for automotive structural parts," *Steel Research International*, vol. 77, pp. 686–691, 2006.

[194] K. Spencer, K. T. Conlon, Y. Bréchet, and J. D. Embury, "The strain induced martensite transformation in austenitic stainless steels. part 2: Effect of internal stresses on mechanical response," *Materials Science And Technology*, vol. 25, no. 1, pp. 18–28, 2009.

[195] M. R. Berrahmoune, *Martensitic transformation and delayed cracking phenomenon in the 301LN unstable austenitic steel*. PhD thesis, ENSAM, Metz, France, 2006.

[196] T. Narutani, "Effect of deformation-induced martenic transformation on the plastic behavior of metastable austenitic stainless steel," *Material Transactions of the Japanese Institute of Metals*, vol. 30, no. 1, pp. 33–45, 1989.

[197] A. Molinari, "Extensions of the self-consistent tangent model," *Modelling and Simulation in Materials Science & Engineering*, vol. 7, no. 5, pp. 683–697, 1999.

[198] L. Bardella, "An extension of the secant method for the homogenization of the nonlinear behavior of composite materials," *International Journal of Engineering Science*, vol. 41, no. 7, pp. 741–768, 2003.

[199] Y. Benveniste, "A new approach to the application of Mori-Tanaka's theory in composite materials," *Mechanics of Materials*, vol. 6, no. 2, pp. 147–157, 1987.

[200] C. Garion, B. Skoczen, and S. Sgobba, "Constitutive modelling and identification of parameters of the plastic strain-induced martensitic transformation in 316L stainless steel at cryogenic temperatures," *International Journal of Plasticity*, vol. 22, no. 7, pp. 1234–1264, 2006.

[201] Y. Tomita and T. Iwamoto, "Constitutive modelling of trip steel and its application to the improvement of mechanical properties," *International Journal of Mechanical Sciences*, vol. 37, no. 12, pp. 1295–1305, 1995.

[202] U. F. Kocks and H. Mecking, "Physics and phenomenology of strain-hardening: the fcc case," *Progress in Materials Science*, vol. 48, pp. 171–273, 2003.

[203] N. Tsuchida, Y. Tomota, H. Moriya, O. Umezawa, and K. Nagai, "Application of the Kocks-Mecking model to tensile deformation of an austenitic 25Cr-19Ni steel," *Acta Materialia*, vol. 49, no. 15, pp. 3029–3038, 2001.

[204] S. Allain, J. P. Chateau, and O. Bouaziz, "A physical model of the twinning-induced plasticity effect in a high manganese austenitic steel," *Materials Science and Engineering A*, vol. 387-389, pp. 143–147, 2004.

[205] O. Bouaziz and N. Guelton, "Modelling of TWIP effect on work-hardening," *Materials Science and Engineering A*, vol. 319-321, pp. 246–249, 2001.

[206] O. Bouaziz, S. Allain, and C. Scott, "Effect of grain and twin boundaries on the hardening mechanisms of twinning-induced plasticity steels," *Scripta Materialia*, vol. 58, no. 6, pp. 484–487, 2008.

[207] J. Bouquerel, K. Verbeken, and B. C. de Cooman, "Microstructure-based model for the static mechanical behaviour of multiphase steels," *Acta Materialia*, vol. 54, no. 6, pp. 1443–1456, 2006.

[208] R. Rodriguez and I. Gutierrez, "Unified formulation to predict the tensile curves of steels with different microstructures," *Materials Science Forum*, vol. 426-432, pp. 4525–4530, 2003.

[209] A. Di Schino, M. Barteri, and J. M. Kenny, "Development of ultra fine grain structure by martensitic reversion in stainless steel," *Journal of Materials Science Letters*, vol. 21, no. 9, pp. 751–753, 2002.

[210] H. W. Zhang, Z. K. Hei, G. Liu, J. Lu, and K. Lu, "Formation of nanostructured surface layer on AISI 304 stainless steel by means of surface mechanical attrition treatment," *Acta Materialia*, vol. 51, no. 7, pp. 1871–1881, 2003.

[211] K. Tomimura, S. Takaki, and Y. Tokunaga, "Reversion mechanism from deformation induced martensite to austenite in metastable austenitic stainless steels," *ISIJ International*, vol. 31, pp. 1431–1437, 1991.

[212] A. F. Padilha, R. L. Plaut, and P. R. Rios, "Annealing of cold-worked austenitic stainless steels," *ISIJ International*, vol. 43, no. 2, pp. 135–143, 2003.

[213] A. Poulon-Quintin, S. Brochet, J. B. Vogt, J. C. Glez, and J. D. Mithieux, "Fine grained austenitic stainless steels: The role of strain induced α' martensite and the reversion mechanism limitations," *ISIJ International*, vol. 49, no. 2, pp. 293–301, 2009.

[214] R. Misra, S. Nayak, P. Venkatasurya, V. Ramuni, M. Somani, and L. Karjalainen, "Nanograined/ultrafine-grained structure and tensile deformation behavior of shear phase reversion-induced 301 austenitic stainless steel," *Metallurgical and Materials Transactions A*, vol. 41, no. 8, pp. 2162–2174, 2010.

[215] F. Forouzan, A. Najafizadeh, A. Kermanpur, A. Hedayati, and R. Surkialiabad, "Production of nano/submicron grained AISI 304L stainless steel through the martensite reversion process," *Materials Science and Engineering A*, vol. 527, no. 27-28, pp. 7334–7339, 2010.

[216] F. T. Inc., *Feritscope MP30E - Operator's Manual*, 2006.

[217] R. Bozorth, *Ferromagnetism*, ch. 2: Factors affecting Magnetic Quality, pp. 14–19. Van Nostrand, 1951.

[218] K. M. Olsen and R. C. Stoffers, "Effect of carbon content on the magnetic properties of iron-30 % cobalt-15 % chromium alloys," *Journal Of Applied Physics*, vol. 42, no. 4, pp. 1792–1793, 1971.

[219] E. du Trémolet de Lacheisserie, *Magnetostriction, Theory and Applications of Magnetoelasticity*, ch. 3: Magnetoelasticity of Soft Ferromagnets: The Physical Effects, pp. 198–211. CRC Press, 1993.

[220] S. Chikazumi, *Physics of Magnetism*, ch. 8: Magnetostriction, pp. 161–185. John Wiley & Sons, Inc., 1964.

[221] V. Randle and O. Engler, *Texture Analysis: Macrotexture, Microtexture & Orientation Mapping*, ch. 6: The Kikuchi Diffraction Pattern, pp. 148–151. Gordon and Breach Science Publishers, 2000.

[222] S. Takaki, S. Tanimoto, and Y. Tokunaga, "Grain refining of austenitic stainless steels by α'-reversion to γ-reversion," *Transactions of the Iron and Steel Institute of Japan*, vol. 25, no. 9, pp. B223–B223, 1985.

[223] R. Ueji, N. Tsuji, Y. Minamino, and Y. Koizumi, "Ultragrain refinement of plain low carbon steel by cold-rolling and annealing of martensite," *Acta Materialia*, vol. 50, no. 16, pp. 4177–4189, 2002.

[224] B. Raeisinia, *Modelling the Effect of Grain Size Distribution on the Mechanical Response of Metals*. PhD thesis, The University of British Columbia, Vancouver, Canada, 2008.

[225] A. Ramirez, J. Lippold, and S. Brandi, "The relationship between chromium nitride and secondary austenite precipitation in duplex stainless steels," *Metallurgical and Materials Transactions A*, vol. 34, no. 8, pp. 1575–1597, 2003.

[226] *ASM Handbook Online*, ch. 8: Mechanical Testing and Evaluation. ASM International, 2000.

[227] C. G'Sell, S. Boni, and S. Shrivastava, "Application of the plane simple shear test for determination of the plastic behaviour of solid polymers at large strains," *Journal of Materials Science*, vol. 18, pp. 903–918, 1983.

[228] E. Rauch and C. G'Sell, "Flow localization induced by a change in strain path in mild steel," *Materials Science and Engineering A*, vol. 111, pp. 71–80, 1989.

[229] P.-Y. Manach, *Étude du comportement thermomécanique d'alliages à mémoire de forme Ni-Ti*. PhD thesis, Institut National Polytechnique de Grenoble, France, 1993.

[230] P. Y. Manach and N. Couty, "Elastoviscohysteresis constitutive law in convected coordinate frames: application to finite deformation shear tests," *Computational Mechanics*, vol. 28, no. 1, pp. 17–25, 2002.

[231] I. Tamura, T. Maki, and H. Hato *Trans. ISIJ*, vol. 10, p. 163, 1970.

[232] O. Instruments, "HKL - Channel 5 User manual," 2007.

[233] K. Datta, R. Delhez, P. Bronsveld, J. Beyer, H. Geijselaers, and J. Post, "A low-temperature study to examine the role of ϵ-martensite during strain-induced transformations in metastable austenitic stainless steels," *Acta Materialia*, vol. 57, no. 11, pp. 3321–3326, 2009.

[234] J. Goldstein, D. E. Newbury, D. C. Joy, and C. E. Lyman, *Scanning Electron Microscopy and X-ray Microanalysis*, vol. 1, ch. 3: Electron Beam – Specimen Interactions, pp. 75–86. Springer; 3rd edition, 2003.

[235] D. Barbier, N. Gey, N. Bozzolo, S. Allain, and M. Humbert, "EBSD for analysing the twinning microstructure in fine-grained TWIP steels and its influence on work hardening," *Journal of Microscopy*, vol. 235, pp. 67–78, 2009.

[236] X. Liang, J. McDermid, O. Bouaziz, X. Wang, J. Embury, and H. Zurob, "Microstructural evolution and strain hardening of Fe-24Mn and Fe-30Mn alloys during tensile deformation," *Acta Materialia*, vol. 57, no. 13, pp. 3978–3988, 2009.

[237] I. Gutierrez-Urrutia, S. Zaefferer, and D. Raabe, "Electron channeling contrast imaging of twins and dislocations in twinning-induced plasticity steels under controlled diffraction conditions in a scanning electron microscope," *Scripta Materialia*, vol. 61, no. 7, pp. 737–740, 2009.

[238] B. Petit, *Étude du comportement mécanique et des modifications de texture et de microstructure induites par la transformation de phase $\gamma \rightarrow \alpha'$ sous contrainte d'un acier AISI 304. Aspects expérimentaux et modélisations.* PhD thesis, Université Paul Verlaine de Metz, France, 2006.

[239] C. Cayron, F. Barcelo, and Y. de Carlan, "The mechanisms of the fcc-bcc martensitic transformation revealed by pole figures," *Acta Materialia*, vol. 58, no. 4, pp. 1395–1402, 2010.

[240] R. Misra, Z. Zhang, Z. Jia, M. Somani, and L. Karjalainen, "Probing deformation processes in near-defect free volume in high strength-high ductility nanograined/ultrafine-grained metastable austenitic stainless steels," *Scripta Materialia*, vol. 63, no. 11, pp. 1057–1060, 2010.

[241] H. Geijselaers and E. PerdahcIoglu, "Mechanically induced martensitic transformation as a stress-driven process," *Scripta Materialia*, vol. 60, no. 1, pp. 29 – 31, 2009.

[242] J. D. Embury and C. W. Sinclair, "The mechanical properties of fine-scale two-phase materials," *Materials Science and Engineering A*, vol. 319-321, pp. 37–45, 2001.

[243] K. Tao, J. J. Wall, H. Li, D. W. Brown, S. C. Vogel, and H. Choo, "In situ neutron diffraction study of grain-orientation-dependent phase transformation in 304L stainless steel at a cryogenic temperature," *Journal of Applied Physics*, vol. 100, no. 12, p. 123515, 2006.

[244] P. Hedström, L. E. Lindgren, J. Almer, U. Lienert, J. Bernier, M. Terner, and M. Odén, "Load partitioning and strain-induced martensite formation during tensile loading of a metastable austenitic stainless steel," *Metallurgical And Materials Transactions A*, vol. 40, no. 5, pp. 1039–1048, 2009.

[245] R. Bozorth, *Ferromagnetism*, ch. 13: Stress and magnetostriction, pp. 595–712. Van Nostrand, 1951.

[246] B. Westermo and L. Thompson, "Magnetic strain measurement methodology for structural damage assessment and monitoring," in *Advances in Instrumentation, Proceedings*, vol. 47, pp. 1295–1303, 1992.

[247] D. Jiles and D. Atherton, "Theory of the magnetisation process in ferromagnets and its application to the magnetomechanical effect," *Journal of Physics D*, vol. 17, pp. 1265–1281, 1984.

[248] D. C. Jiles, "Theory of the magnetomechanical effect," *Journal of Physics D*, vol. 28, pp. 1537–1547, 1995.

[249] M. Smaga, F. Walther, and D. Eifler, "Deformation-induced martensitic transformation in metastable austenitic steels," *Materials Science and Engineering A*, vol. 483-484, pp. 394–397, 2008. 14th International Conference on the Strength of Materials (ICSMA).

[250] A. M. Beese, D. Mohr, and P.-O. Santacreu, "Isotropic phase transformation in anisotropic stainless steel 301LN sheets," in *European Symposium on Martensitic Transformations (Esomat)*, 2009.

[251] A. M. Beese, "Quantification of phase transformation in stainless steel 301LN sheets," Master's thesis, Massachusetts Institute of Technology, 2009.

[252] J. Kaleta and J. Zebracki, "Application of the Villari effect in a fatigue examination of nickel," *Fatigue & Fracture Of Engineering Materials & Structures*, vol. 19, no. 12, pp. 1435–1443, 1996.

[253] H. Mecking and U. F. Kocks, "Kinetics of flow and strain-hardening," *Acta Metallurgica*, vol. 29, pp. 1865–1875, 1981.

[254] G. Cailletaud and K. Sai, "A polycrystalline model for the description of ratchetting: Effect of intergranular and intragranular hardening," *Materials Science and Engineering A*, vol. 480, no. 1-2, pp. 24–39, 2008.

[255] O. Bouaziz and P. Buessler, "Iso-work increment assumption for heterogeneous material behavior modelling," *Advanced Engineering Materials*, vol. 6, no. 1-2, pp. 79–83, 2004.

[256] L. Delannay, P. Jacques, and T. Pardoen, "Modelling of the plastic flow of TRIP-aided multiphase steel based on an incremental mean-field approach," *International Journal of Solids and Structures*, vol. 45, no. 6, pp. 1825–1843, 2008.

[257] L. Mazzoni-Leduc, T. Pardoen, and T. Massart, "Strain gradient plasticity analysis of transformation induced plasticity in multiphase steels," *International Journal of Solids and Structures*, vol. 45, no. 20, pp. 5397–5418, 2008.

[258] A. Rolett, *Strain Hardening at Large Strains in Aluminum Alloys*. PhD thesis, Drexel University, Philadelphia, U.S.A., 1987.

[259] S. Shrivastava, J. Jonas, and G. Canova, "Equivalent strain in large deformation torsion testing : Theoretical and practical considerations," *Journal of the Mechanics and Physics of Solids*, vol. 30, no. 1-2, pp. 75–90, 1982.

[260] O. Bouaziz, C. W. Sinclair, and M. Gouné, "An improved approach for the description of the behaviour of dynamic composites," 2009.

[261] M. Berrahmoune, S. Berveiller, K. Inal, and E. Patoor, "Delayed cracking in 301LN austenitic steel after deep drawing: Martensitic transformation and residual stress analysis," *Material Science and Engineering A*, vol. 438-440, pp. 262 – 266, 2006.

[262] A. Das, P. C. Chakraborti, S. Tarafder, and H. K. D. H. Bhadeshia, "Analysis of deformation induced martensitic transformation in stainless steels," *Materials Science and Technology*, vol. 27, pp. 366–370, 2011.

[263] D. Stephan and K. Richter, "Fast local stress measurement by the x-ray microbeam diffraction technique using an annular proportional counter," *Crystal Research and Technology*, vol. 16, pp. 57–61, 1981.

[264] A. M. Beese and D. Mohr, "Identification of the direction-dependency of the martensitic transformation in stainless steel using in situ magnetic permeability measurements," 2010.

[265] S. Kundu and H. Bhadeshia, "Crystallographic texture and intervening transformations," *Scripta Materialia*, vol. 57, no. 9, pp. 869–872, 2007.

Appendix A

Calibration of the Feritscope in Grade 301LN

This appendix defines the calibration necessary to adapt the Feritscope measurements to the volume fractions of α'-martensite actually present in grade 301LN after straining. The present calibration was performed towards volume fractions measured by Rietveld fitting of X-ray diffraction spectra, a method already used in the past for phase quantification in austenitic stainless steels [139].

This calibration was performed on only one condition of grain size, namely the D=28 µm condition. Given that the size of α'-martensite varies little when the austenitic grain size is varied, it was assumed that the calibration curve could be applied to all grain size conditions of 301LN presented in this work.

Rectangular strips ($\sim$ 100 mm $\times$ 20 mm $\times$ 0.8 mm) were strained in uniaxial tension, the tensile direction corresponding to the prior rolling direction. The X-ray diffraction spectra were acquired using the Bruker D8 diffractomer presented in section 5.2.3, with no texture correction. Those spectra are presented in Figure A.1.

Six Feritscope measurements were performed on each samples, according to the procedure described in section 4.2.1. An average Feritscope reading (denoted as FS_0 [14]) and a dispersion were calculated. The correlation between Feritscope measurements and Rietveld calculation of α'-martensite appear in Figure A.2.

---

[14] The notation emphasizes the fact that the measurement is performed under no applied stress.
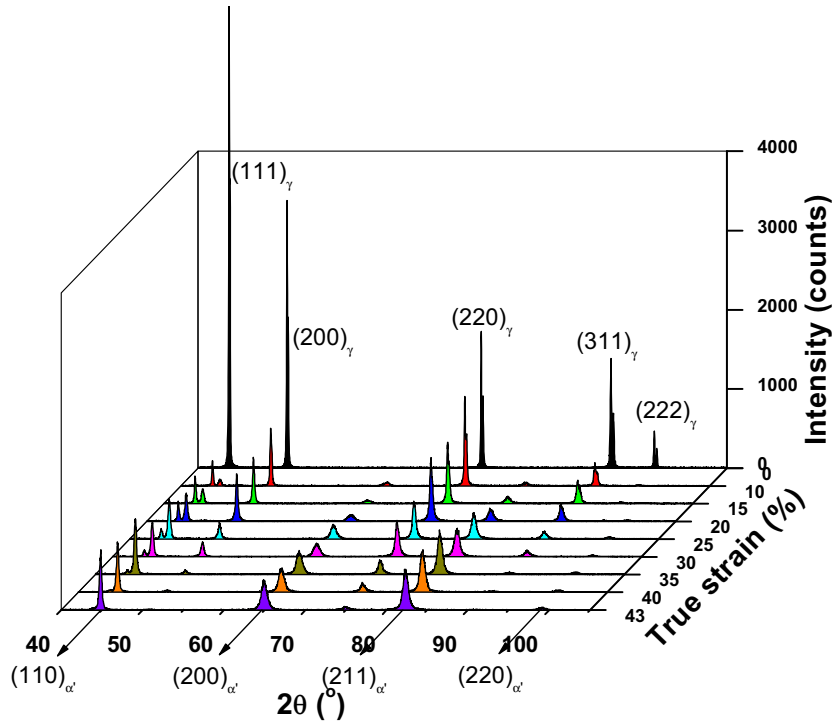
Figure A.1: X-ray diffraction patterns illustrating the change in the proportion of phases when the strain is increased.
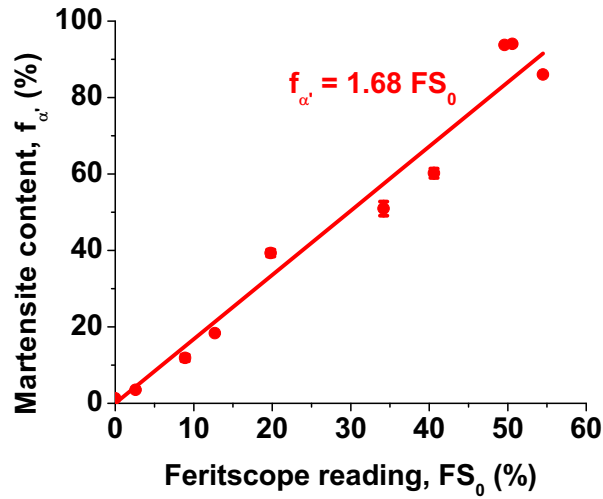
Figure A.2: Calibration curve of the Feritscope towards Rietveld refinement of X-Ray Diffraction spectra.

Figure A.2 shows that the relation between the Feritscope readings and the actual volume fraction ($f_{\alpha'}$) can be described by the linear equation:

$$f_{\alpha'} = 1.68 \times FS_0 \tag{A.1}$$

which was already verified in grade 301LN [61, 250, 264].

The calibration was performed for Feritscope readings ranging from 0 to 60% only. The Feritscope may suffer from saturation of the magnetic signal for higher volume fractions [72], consequently, such high volume fractions need to be treated with caution.

Appendix B

The Patel-Cohen Model for Variant Selection

Here we summarize the methodology for computing the interaction energy as outlined by Humbert *et al.* [50]. A more detailed description can be found in this reference.

The interaction energy as defined by Patel and Cohen [47] can be written as,

$$W = \sigma \epsilon \tag{B.1}$$

where σ is the macroscopically imposed stress tensor and ϵ is the transformation strain associated with the transformation between austenite and ϵ-martensite or austenite and α'-martensite. As suggested by Kundu and Bhadeshia [265], the factor of 0.5 introduced by Humbert *et al.* has been dropped. In the case of a uniaxial tensile test, σ is written as,

$$\sigma = \begin{pmatrix} \sigma_{11} & 0 & 0 \\ 0 & 0 & 0 \\ 0 & 0 & 0 \end{pmatrix} \tag{B.2}$$

The deformation gradient associated with the austenite to ϵ-martensite transformation can be written as [50]

$$D^{\gamma \to \epsilon} = \begin{pmatrix} 1 & 0 & 1/\sqrt{2} \\ 0 & 1 & 0 \\ 0 & 0 & 1 \end{pmatrix} \tag{B.3}$$

where the x direction is parallel to a $\langle 112 \rangle_\gamma$ (shearing direction) and z

is parallel to a $\langle 111 \rangle_\gamma$.

In the case of the austenite to α'-martensite transformation the deformation gradient can be written as,

$$D^{\gamma \to \alpha'} = \begin{pmatrix} \frac{a_{\alpha'}\sqrt{3}}{2a_\epsilon} & -\frac{a_{\alpha'}}{6a_\epsilon} & 0 \\ 0 & \frac{a_{\alpha'}\sqrt{8}}{3a_\epsilon} & 0 \\ 0 & 0 & \frac{a_{\alpha'}\sqrt{2}}{c_\epsilon} \end{pmatrix} \tag{B.4}$$

where x is parallel to the common close packed directions in the austenite and α'-martensite and z is perpendicular to the close packed planes of the austenite and α'-martensite. Also, $a_\epsilon = 0.254$ nm, $c_\epsilon = 0.415$ nm, and $a_{\alpha'} = 0.287$ nm correspond to the lattice parameters of ϵ-martensite and α'-martensite respectively, the values being taken from Humbert [50].

To convert the above deformation gradients to strain tensors one can write $\epsilon = 1/2 \left(D + D^T \right)$ where the superscript T denotes transpose.

In order to calculate the interaction energy, one must re-write both the imposed stress and the transformation strain in the same coordinate frame. In the case of Humbert *et al.*, this was chosen to be the macroscopic frame of reference associated with the tensile test. One can, however, calculate this within the frame of reference that the transformation strains are written in. In the specific case of the ϵ-martensite transformation occurring during a tensile test, this has obvious advantages.

The transformation strain associated with the austenite to ϵ-martensite transformation is a pure shear (i.e. $\epsilon_{13} = \epsilon_{31} = \left(2\sqrt{2} \right)^{-1}$ and all other $\epsilon_{ij} = 0$) when calculated in the frame of reference coinciding with the $x = b = \langle 112 \rangle_\gamma$, $z = n = \langle 111 \rangle_\gamma$ coordinate system defined above. A macroscopic tensile stress σ can be resolved onto this slip system as, $\tau = (\sigma n) \cdot b$ giving the interaction energy as,

$$W^{\gamma \to \epsilon} = (\sigma n) \cdot b \epsilon_{13} \tag{B.5}$$

Given that the transformation strain is fixed at that the applied tensile stress (σ_{11}) is a constant, then this can be re-written as,

$$W^{\gamma \rightarrow \epsilon} = m\sigma_{11}\epsilon_{13} \tag{B.6}$$

where m is the Schmidt factor for the $\{111\}_\gamma \langle 112 \rangle_\gamma$ slip system in question. Thus, the Patel-Cohen interaction energy is directly proportional to the Schmid factor for the austenite to ϵ-martensite transformation.